Systematic Investigation of Intermolecular Interactions in NEXAFS Spectroscopy

A Thesis Submitted to the College of

Graduate and Postdoctoral Studies

in Partial Fulfillment of the Requirements

for the Degree of Doctor of Philosophy

in the Department of Chemistry

University of Saskatchewan

Saskatoon

By

Sahan Daksitha Perera Neelakanni Mudiyanselage

March 2019

Permission to Use

In presenting this thesis in partial fulfillment of the requirements for a postgraduate degree from the University of Saskatchewan, I agree that the Libraries of this University may make it freely available for inspection. I further agree that permission for copying of this thesis in any manner, in whole or in part, for scholarly purposes may be granted by Professor S. G. Urquhart who supervised my thesis work or, in his absence, by the Head of the Department of Chemistry or the Dean of the College of Graduate Studies and Research. It is understood that any copying or publication or use of this thesis or parts thereof for financial gain shall not be allowed without my written permission. It is also understood that due recognition shall be given to me and to the University of Saskatchewan in any scholarly use that may be made of any material in my thesis. Request for permission to copy or to make other use of material in this thesis in whole or in part should be addressed to:

Head
Department of Chemistry
University Of Saskatchewan
Saskatoon, Saskatchewan
Canada S7N 5C9

OR

Dean
College of Graduate and Postdoctoral Studies
University of Saskatchewan
116 Thorvaldson Building, 110 Science Place
Saskatoon, Saskatchewan S7N 5C9
Canada

Abstract

Near Edge X-ray Absorption Fine Structure (NEXAFS) spectroscopy can be used to study molecular packing and order in organic materials, but only if the spectroscopic effects of intermolecular interactions are well understood. This work aims to contribute to an improved general understanding of the roles of intermolecular interactions on NEXAFS spectroscopy by studying the effects of Rydberg quenching on the degree of Rydberg-valence mixing in saturated molecules and π-π interactions of unsaturated molecules. The effects of π-π interactions were systematically studied by using paracyclophane (PCP) molecules, in which the benzene/benzene separation distance can be systematically varied through the length of the spacer between benzene rings. The effects of Rydberg quenching on the degree of Rydberg-valence mixing in saturated molecules were systematically studied as a function of different crystalline polymorphs (orthorhombic and monoclinic) and chain lengths of *n*-alkane single crystals.

The effects of π-π interactions with varied spacing between co-facial benzene rings in PCPs are observed and these intermolecular effects can be used to study molecular packing and order in unsaturated materials. This work explores the strengths and significances of the effects of π-π interactions on NEXAFS spectroscopy as a function of benzene-benzene separation distances.

The effects of Rydberg quenching on the degree of Rydberg-valence mixing to the NEXAFS spectra are not significant between different *n*-alkanes crystalline polymorphs. However, linear dichroism effects were observed for these different *n*-alkane crystalline polymorphs. For a given a crystal structure (orthorhombic or monoclinic), the relative intensities of the two C-H peaks (287-288 eV) and the energy of the C-H band (287-288 eV) changed when X-ray linear horizontal polarization was aligned along the principal axes (X,Y) of individual crystals. In addition to the observed linear dichroism, the room temperature NEXAFS spectra of orthorhombic alkanes becomes broader as the alkane chain length decreased. This broadening of NEXAFS spectra is believed to be the result of increased molecular disorder and nuclear motion at room temperature. Nuclear motion effects refers to the energetically accessible molecular conformations present at the experimental temperature. In summary, this work is a significant contribution to the development a more comprehensive understanding of the influences of intermolecular interactions on NEXAFS spectroscopy.

Acknowledgements

First and foremost, I would like to thank to my supervisor, Professor Stephen G. Urquhart, for his endless teaching, exceptional guidance and faith in me throughout this project. The experience which I gained through this wonderful synchrotron based research project will surely enlighten my research career in colours.

I would like to acknowledge to the members of my Advisory Committee Professors Robert Scott, Andrew Grosvenor, and Yansun Yao for their endless support and guidance throughout my program.

I am thankful to the present group members; Amara Zuhaib and Sadegh Shokatian, and past group members; Dr. Mitra Masnadi, Curtis Senger, and Dr Andrew Ritchie of Professor Urquhart lab to their commitment to me during this program.

I am grateful to the Department of Chemistry, University of Saskatchewan and Canadian Light Source which are supported by NSERC, NRC, CIHR, and the Province of Saskatchewan, for providing more advance experimental source throughout this project.

Special thanks goes to my undergraduate teaching laboratory managers; Drs. Adrian Clark and Alexandra Bartole-Scott for their endless support and faith in me throughout the program.

Further I would like to thank Soft X-ray microscopy (SM) beam line scientist in the Canadian Light Source, Dr Jian Wang, for his endless support throughout this project.

Finally I would like to express my deepest gratitude to my wonderful wife, and family members from both sides for their encouragement and trust on me throughout the program.

Table of Contents

List of Figures

Chapter 1

Chapter 3

Chapter 4

Chapter 5

Chapter 8

Chapter 9

Appendix

List of Tables

Chapter 2

Chapter 3

Appendix

List of Abbreviation

AEY	Auger Electron Yield
AO	Atomic Orbitals
BE	Binding Energy
BM	Bending Magnets
BO	Born-Oppenheimer
DFT	Density Functional Theory
TP-DFT	Transition Potential Density Functional Theory
ECP	Effective Core-Potential
EPU	Eliiptically Polarized Undualtor
eV	Electron Volt
EXAFS	Extended X-ray Absorption Spectroscopy
E_{XC}	Exchange Correlation Energy
FZP	Fresnel Zone Plate
GGA	Generalized Gradient Approximation
HF	Hartree-Fock
HV	High Vacuum
ID	Insertion Device
IP	Ionization Potential
KS	Kohn-Sham
ΔKS	Delta Kohn-Sham
LCAO	Linear Combination of Atomic Orbitals
LCGTO	Linear Combination of Gaussian-Type Orbital
LD	Linear Dichroism
LDA	Local Density Approximation
Linac	Linear Accelerator
LUMO	Lowest Unoccupied Molecular Orbital
MD	Molecular Dynamics
MEMS	Micro-Electro-Mechanical-Systems
MO	Molecular Orbital

NA	Numerical Aperture
NEXAFS	Near Edge X-ray Absorption Fine Structure
NMR	Nuclear Magnetic Resonance
OM	Optical Microscopy
OSA	Order Sorting Aperture
P	Ellipticity
PAN	Polyacrylonitrile
PBE	Perdew-Burke-Ernzerhof
PCP	Paracyclophane
PC	Polycarbonate
PEY	Partial Electron Yield
PGM	Plane Grating Monochromator
P3HT	Poly(3-hexylthiophene-2,5-diyl)
PMT	Photo Multiplier Tube
PUret	Polyurethane
PUrea	Polyurea
PVMK	Poly(vinyl methyl ketone)
PαMS	Poly(α-methyl styrene)
P2VP	Poly(2-vinyl pyridine)
SE	Schrödinger Equation
SGM	Spherical Grating Monochromator
SM	Soft X-ray Microscopy
SMD	Single Matrix Diagonalization
STEX	Static Exchange
RF	Radiofrequency
Δt	Lifetime
TDM	Transition Dipole Moment
TEY	Total Electron Yield
TV	Term Value
UHV	Ultra High Vacuum

V_{ext}	Static External Potential
V_{eff} (r)	Effective Potential
V_{xc} (r)	Exchange Correlation Potential
V_{H} (r)	Hartree Potential
XAS	X-ray Absorption Spectroscopy

List of Symbols and Nomenclature

c	Speed of Light (2.99782×10^{8} m s^{-1})
e	Electron Charge (1.602×10^{-19} C)
$\overline{E}$	Electric Field Vector of Polarized X-rays
f	Oscillator Strength
h	Planck Constant (6.62607×10^{-34} m^2 kg s^{-1})
ħ	$h/2\pi$
m_e	Mass of Electron (9.11×10^{-31} kg)
mon	Monoclinic
N_A	Avogadro Number (6.023×10^{23})
o-rh	Orthorhombic
λ	Wavelength
μ	Dipole Operator
ψ	Wave Function/ Eigen function
π	3.142
ρ	Density
ρ_0	Electron Density
Z	Nuclear Charge

Chapter 1 Introduction

Near Edge X-ray Absorption Fine Structure (NEXAFS) spectra of organic materials are predominantly sensitive to intramolecular effects, that is, to the electronic structure and bonding structure of a molecule. Most NEXAFS studies of organic materials focus on chemical analyses, such as chemical compositional analyses,[1-7] functional group analyses,[1-2, 8-10] and orientation analyses,[11-19] etc. In contrast to these *intra*molecular effects (bonding, chemical speciation, orientation etc.), *inter*molecular effects (e.g. those due to neighbouring molecules) have not been heavily explored using NEXAFS spectroscopy.

Several types of intermolecular effects are known, such as hydrogen bonding,[20] quenching of Rydberg states,[21] and dynamic stabilization of a core exited state.[22] For instance, in the NEXAFS spectrum of water, hydrogen bonding in liquid water affects its NEXAFS spectra, making it profoundly different from the gas phase spectrum of water.[20] In Leetma *et al*,[20] the authors show that the hydrogen bonding network in liquid water contributes to the shape of its XAS spectrum. Gillies *et al*.[21] have studied intermolecular interactions in simple alkanes and found significant changes in Rydberg-valence mixing between the gas and solid phase NEXAFS spectra.[21] Ruhl *et al.*[22] have studied benzene clusters and observed energy shifts between solid clusters phase and the gas phase. These energy shifts were attributed to dynamic stabilization effects in the solid.[22] All these studies are evidence to the sensitivity of NEXAFS to intermolecular interactions. A complete understanding of intermolecular interactions has not yet been achieved and the area of study has been therefore relatively unexplored. If intermolecular effects were better understood, NEXAFS spectroscopy could be used to study molecular packing and order in organic molecules. This work focused on the π-π interactions of unsaturated molecules (first research objective) and effects of Rydberg quenching on degree of Rydberg-valence mixing in saturated molecules (second research objective). In pursuing the second research objective, it was found that the effects of Rydberg quenching on the degree of Rydberg-valence mixing in saturated molecules (*n*-alkanes) as a function of crystal structure and chain length is not significant to the NEXAFS spectra. Consequently, new sets of ideas such as effects of nuclear motion contributions to the NEXAFS spectra were explained within the context of the second research objective.

The following ideas will be discussed in the introduction of this dissertation:

- The principles of NEXAFS spectroscopy.

- The sensitivity of this spectroscopic tool to the structure and orientation of organic molecules.
- Two main concepts of this project: effects of intermolecular interactions and nuclear motion contributions.
- Finally, potential uses for NEXAFS spectroscopy in the study of intermolecular interactions and nuclear motion contributions will be discussed generally, as well as within the context of the stated research objectives.

1.1 X-ray Absorption Spectroscopy (XAS)

X-ray absorption attenuates the intensity of the X-rays transmitted through a sample. Variation in X-ray absorption cross section as a function of incident photon energy is shown in **Figure 1.1**.[23]

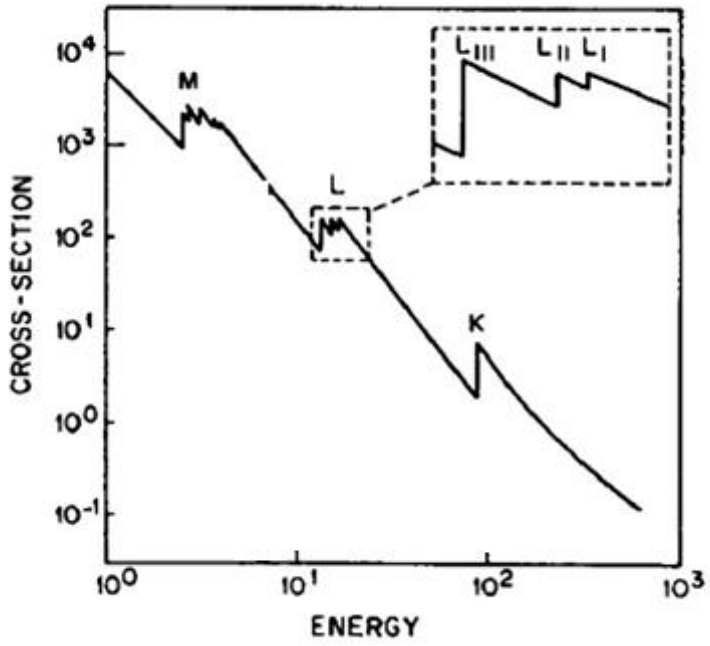

Figure 1.1: X-ray absorption cross section as a function of photon energy. Figure reprinted from Reference 23 with permission.

According to **Figure 1.1**, the X-ray absorption cross section is inversely proportional to the X-ray photon energy. This means that high energy photons are less likely to be absorbed and penetrate further into a sample.[23-25] However, when the incident photon energy is sufficient to

overcome the ionization potential (IP) of a core electron, the X-ray absorption cross section increases abruptly at this energy and then decreases monotonically beyond the core edge. These abrupt discontinuities in absorption cross section are known as the absorption edges. Absorption edges are classified according to the origin of the core excited electron. For instance, if an electron is ionized from a 1s shell, the absorption edge is called a K edge, if ionized from the 2s, $2p_{1/2}$, or $2p_{3/2}$ edge, it is will be referred to as a L_I, L_{II}, of L_{III} edge, respectively. Moreover, the locations of absorption edges depend on IP of the absorbing core electron. The IP of an electron is defined as the minimum energy required to ionize an electron to the continuum of states above the vacuum level.[26] IP is also known as Binding Energy (BE).[26] IPs are specific to the elements (atomic number Z) present in the absorber.[24-26] For instance, the core 1s orbital (K edge) IP of carbon is 284 eV, nitrogen is 409 eV, and oxygen is 530 eV.[27-28]

X-ray Absorption Cross Section

The X-ray absorption probability of a system can be described by either the X-ray absorption cross section or the optical oscillator strength. The absorption cross-section is the number of electrons excited per unit time divided by the number of incident photons per unit time per unit area.[26] Within the dipole approximation, the X-ray absorption cross section can be defined as:[26]

$$\sigma_x = \frac{4\pi\hbar^2 e^2 1}{m^2\ \hbar c\ \hbar\omega}\left\langle \psi_f \left| \bar{E}\cdot\mu \right| \psi_i \right\rangle^2 \rho_f\ (\bar{E}) \qquad \textbf{Equation 1.1}$$

Where σ_x is the X-ray absorption cross-section, h is the Planck constant, $\hbar$ is $h/2\pi$, $\hbar\omega$ is the photon energy of the X-ray radiation, c is the speed of light, e is the electron charge, m_e is the mass of electron, $\bar{E}$ is the electric field vector of the X-rays, $\bar{\mu}$ is the dipole operator, ψ_f is the wave function of the final state, ψ_i is the wave function of the initial state, and ρ_f is the energy density of the final state. In brief, **Equation 1.1** describes the probability of the transition of an electron from an initial state (ψ_i) to a final state (ψ_f).

Equation 1.1 is the main equation used to compute X-ray absorption spectra. The optical oscillator strength (f) can be extracted from the X-ray absorption cross-section, σ_x, as shown below.[26]

$$\sigma_{x(E)} = C\frac{df}{d\overline{E}} \qquad \textbf{Equation 1.2}$$

Where C=2π2e2ħ/mc. The variable *f* is an energy integral of the X-ray absorption cross section and a measure of resonance intensity in X-ray absorption spectroscopy.[26] X-ray absorption transition intensities can be expressed as *f* numbers and are calculated as:[26]

$$f = \frac{2}{\mathrm{m}\hbar\omega}\left\langle \psi_{\mathrm{f}}\middle|\overline{E}.\mu\middle|\psi_{\mathrm{i}}\right\rangle^{2} \qquad \textbf{Equation 1.3}$$

Using the calculated *f* in **Equation 1.3**, X-ray absorption cross section from **Equation 1.2** can be modified as:

$$\sigma_{\mathrm{x}}(\overline{E}) = \frac{2\pi^2 e^2 \hbar}{mc} f\rho_f(\overline{E}) \qquad \textbf{Equation 1.4}$$

Overall, XAS can be divided into two regions: the Extended X-ray Absorption Fine Structure (EXAFS) region and the NEXAFS region. EXAFS lies beyond ~ 50 eV above the XAS absorption edge. EXAFS is useful for determining the types of, numbers of, and distances between the neighboring atoms attached to the absorbing atom.[29] The EXAFS technique was not used in this work and will not be discussed further. NEXAFS corresponds to the spectral region extending from a few eV below the absorption edge up to approximately 50 eV above the absorption edge. The NEXAFS region is sensitive to chemical bonding, functionality, and orientation. This research is aimed at *enhancing* the current understanding how NEXAFS spectroscopy can be applied to organic molecules, particularly with respect to intermolecular interactions and the nuclear motion contributions.

1.2 Near Edge X-ray Absorption Fine Structure Spectroscopy (NEXAFS)

NEXAFS spectroscopy measures the photo-absorption cross-section associated with the excitation and photoionization of core electrons induced upon X-ray absorption.[10] A schematic diagram of the core excitation processes for an isolated atom (A) and a diatomic molecule (AB) is given in **Figure 1.2**.[30] During core excitation, a core hole is created when an electron is removed from a core orbital, which deshieldes the nucleus. As a result, the Coulombic attraction between the deshielded nucleus and the rest of the electrons is increased, affecting the energies of all of the orbitals, including the unoccupied orbitals.[26, 31] Resonances in NEXAFS spectra can occur at energies either below or above the IPs (vacuum level in **Figure 1.2**), and create fine structures near

the absorption edge (see bottom image of **Figure 1.2**). Due to the core hole effect, the energy of transitions observed in NEXAFS spectroscopy do not match calculated ground state MO energies.[31]

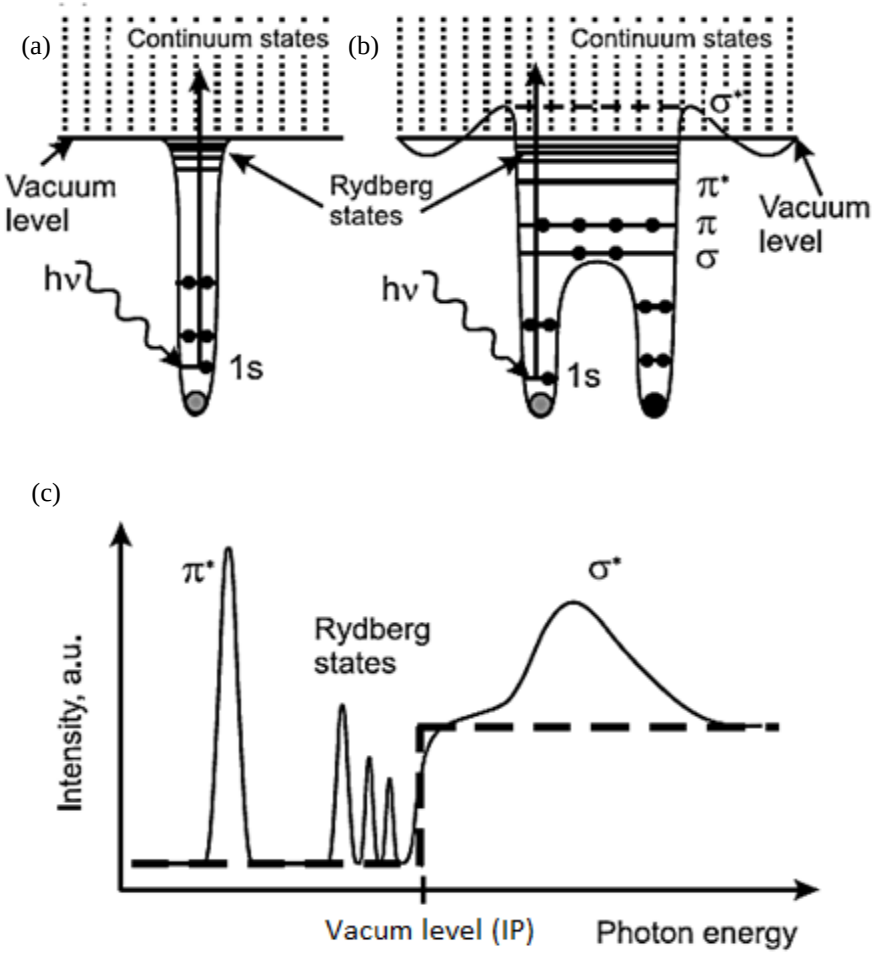

Figure 1.2: Schematic diagram of (a) core excitation process of an isolated atom, and (b) core excitation process of a diatomic molecule, and (c) is a core excitation spectra. Figure adapted from Reference 30 with permission.

In the NEXAFS spectrum of an atom, Rydberg transitions will appear just below the IP and a continuum of empty states will appear above the IP.[26] Rydberg transitions are atomic-like features formed by the excited electron interacting with the positively charged nucleus.[26, 30] Molecules also have unoccupied valence MOs (σ* and π* character), and therefore will show transitions to π* and σ* MOs at energies above and below the IP (see **upper right image in Figure 1.2**).[26]

Using the IP as a boundary, resonances observed in a molecular NEXAFS spectrum roughly fall into two categories. One category of transition includes those due to the excitations of core electrons (1s) into bound orbitals. These are pre-edge transitions and orbital character could be either Rydberg, π*, or sometimes σ*, depending on the symmetry and energy of the unoccupied orbital.[25, 30] The other category of transition includes those due to the excitation of a core electron (1s) into an unbound orbitals or into the continuum, above the IP. Unbound orbitals usually have a σ* character.[25, 30]

The natural width of a resonance is determined by the lifetime of the final state.[26] The correlation between the lifetime of the final state (Δt_f) and the observed spectral width (ΔE) of a NEXAFS feature can be obtained from the Heisenberg uncertainty principle.[26]

$$\Delta E \,.\, \Delta t_f = \frac{h}{2\pi} \qquad \textbf{Equation 1.5}$$

When discussing X-ray absorption spectra, it is convenient to separate the contributions to Δt_f. The Δt_f is contributed by two factors. One is the lifetime of the excited electron within the molecular potential (Δt_e) and other is the lifetime of the core hole state (Δt_{ch}).[26]

$$\frac{1}{\Delta t_f} = \frac{1}{\Delta t_e} + \frac{1}{\Delta t_{ch}} \qquad \textbf{Equation 1.6}$$

According to **Equation 1.5**, final states with long lifetimes generate sharp peaks in the NEXAFS spectra as the time uncertainty is larger. The major types of resonances observed in NEXAFS spectroscopy of organic molecules are discussed below.

1.2.1 Core → π* Transitions

Core to π* resonances only exist in unsaturated molecules. The final levels of these transitions are the antibonding counterparts of the π bonding MO.[32] These transitions are usually the lowest energy features present in the NEXAFS spectra (see **Figures 1.2 and 1.3** for π* transition examples).[26] For a π* resonance, the lifetime of the core excited state is mostly determined by the decay of the core hole, and it usually has long lifetime.[26] Therefore, π* features are usually narrow and intense (see **Figure 1.3**).[9, 26]

The intensity, shape, and position of a π* resonance is sensitive to the π-bond order and chemical environment of the unsaturated system. This is shown with an example in **Figure 1.3**. **Figure 1.3** depicts the carbon 1s NEXAFS spectra for polyacrylonitrile (PAN), poly(α-methyl

styrene) (PαMS), and poly(2-vinyl pyridine) (P2VP).[9] As shown in **Figure 1.3**, the intensity of a π* resonance is affected by the number of π-bonds.[9] The triply bonded $\pi^*_{C\equiv N}$ resonance (~287 eV) of PAN is more intense than the doubly bonded $\pi^*_{C=C}$ resonances (~285 eV) of PαMS and P2VP (see **Figure 1.3**).[9] The strong intensity of the π* feature in PAN is due to there being two degenerate π* MOs in the C≡N functional group.[9]

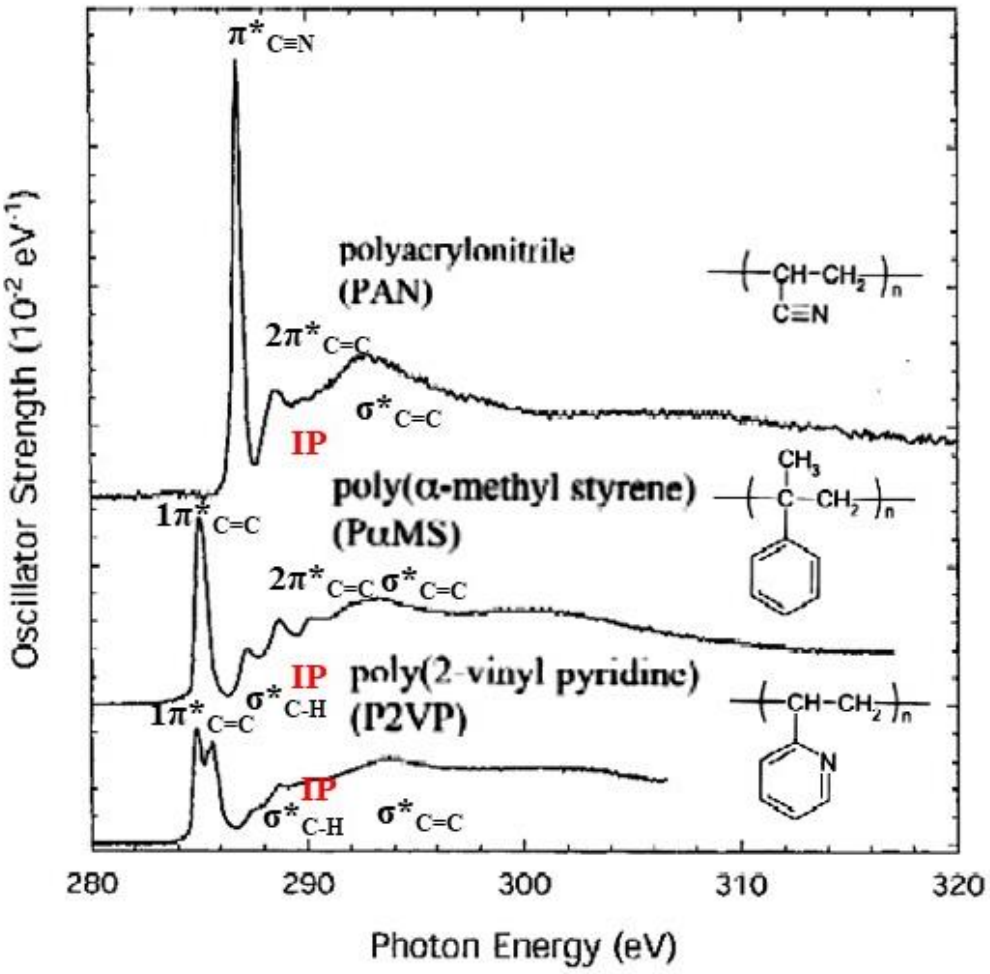

Figure 1.3: Carbon 1s NEXAFS spectra of polyacrylonitrile (PAN), poly(α-methyl styrene) (PαMS), and poly(2-vinyl pyridine) (P2VP). Figure reprinted from Reference 9 with permission.

The positions and shapes of π* resonances are affected by the π bonding environment. For example, in **Figure 1.3**, the P2VP polymer has a pyridine ring and PαMS has a benzene ring. The inequivalent carbon atoms in these two π bonding environments change the shape and position of the lowest π* resonance (~285 eV).[9] The inductive effect of the nitrogen heteroatom in the pyridine ring of P2VP, presumably due to core level shifts affects its lowest $\pi^*_{C=C}$ peak by splitting the

peak into a doublet and thereby reducing the peak intensities.[9] This inductive effect in the lowest $\pi^*_{C=C}$ peak is not observed in the PαMS spectrum since it does not have a heteroatom in its ring.[9]

1.2.2 Core → σ* Transitions

Unlike core → π* transitions, core → σ* transitions are not limited to unsaturated molecules. The σ* resonances usually appear above the IP, but they can appear below the IP in molecules that have weaker σ bonds (see σ^*_{C-H} transitions of the P2VP and PαMS in **Figure 1.3**). The energy width of a σ* resonance is determined by the lifetime (see **Equation 1.5**) of the quasi-bound electronic state [$C1s^{-1}$, σ*]. The quasi-bound state is metastable and has a faster decay time than the usual bound states (π* or Rydberg).[26] Hence, σ* resonances are broader compared to π* resonances.[26]

1.2.3 Core → Rydberg Transitions

Rydberg orbitals are sharp but weak atomic like features that appear below the IP in atomic and molecular NEXAFS spectra (see **Figure 1.2**).[33] For core → Rydberg transitions, all the nuclei and non-excited electrons appear to the excited electron as a single entity with a +1 charge; the excited electron "sees" a hydrogenic nucleus.[24, 26, 32-33] The energies of the Rydberg orbitals of a molecule follows the Rydberg formula.[24, 32-33]

$$TV = IP - E_n = \frac{R}{(n-\delta_l)^2} \qquad \textbf{Equation 1.7}$$

Where *TV* is the term value [*IP* - Transition Energy (E_n)], *R* is the Rydberg energy (13.6 eV), δ_l is the quantum defect associated with the angular-momentum quantum number *l*.[33] These quantum defects are stronger with the lower value of the angular-momentum quantum number *l* such as *s* orbitals.[34] For example, δ_l values for carbon atom (Z=6) for *s*, *p*, *d*, and *f* orbitals are 0.9784, 0.5801, 0.0080, and 0.0001 respectively.[34]

1.2.4 Identification of the Probable Behaviour (Rydberg or Valence) of a Transition

When core electron is excited, the excited electron will have a smaller interaction with other valence electrons if it lands in a Rydberg orbital as these orbitals are generally further from the nucleus and other valence electrons. The excited electron interacts more strongly with other electrons if it lands in a valence orbital as these orbitals are generally closer to the nucleus.[35] The probable behaviour of a given transition can be identified by comparing the calculated excitation energy difference between the singlet (spin-paired electrons) and triplet (two spin-aligned

electrons) excited states [ΔE(S-T)].[35] For a given transition, the greater the ΔE(S-T), the more valence character is present. This can be explained as follows. When an electron is closer to the nucleus (like a valence electrons), the Pauli exclusion principle indicates that there will be a stronger repulsion in triplet state than in the singlet state. Therefore, the closer the two spin-aligned electrons are, the stronger the coulombic interactions, making the difference between the singlet and triplet excitation energies bigger. As a general guideline, if the transition has a calculated singlet-triplet energy difference greater than 0.05 eV, that transition has a greater probability of exhibiting valence behaviour.[35]

1.2.4.1 Mixed Rydberg-Valence Transition

Rydberg-valence mixing can be observed if Rydberg and valence transitions occur in the same energy region of the spectra and if their symmetries are matched with each other. For an example, Rydberg-valence mixing is observed in the NEXAFS spectra of molecules with C-H bonds. In this case, the symmetries and energies of the Rydberg orbitals match with the symmetries and energies of the hydrogen derived antibonding C-H orbitals (valence) and fulfill the requirements for Rydberg-valence mixing.[21, 26, 32, 35-36] The degree of $\sigma^*_{C\text{-}H}$ mixing in this case increases with the number of C-H bonds attached to the core excited carbon atom.[21, 35]

For a given molecule, the degree of Rydberg-valence mixing can vary for different transitions. For an example, in small gaseous alkanes, Gillies *et al*.[35] found that carbon 1s → 3s Rydberg transitions demonstrate more valence character than carbon 1s → 3p transitions. This is due to the strong orbital overlap of the *s* symmetry of the Rydberg orbital and the valence electrons. However, some transitions show pure Rydberg behaviour. For an example, transitions on the central carbon in neopentane do not show any Rydberg-valence mixing due to the lack of C-H bonds in the central atom. In this case, calculated excitation energy differences between the singlet and triplet excited states for corresponding transitions are very small and less than 0.05 eV.[21] Therefore, these transitions do not have any valence ($\sigma^*_{C\text{-}H}$) character to mix with the Rydberg orbitals.[21]

Before explaining how NEXAFS spectroscopy is applied, the different ways of expressing molecular transitions (core → π* or core → σ* etc.) in core excitation processes will be described. **Figure 1.4** shows different ways that can be used to describe the nitrogen 1s → π* core excitation feature in the core excitation process for a unsaturated molecule like N_2 .[32]

1.2.5 Different Ways of Expressing Molecular Transitions in Core Excitation Process

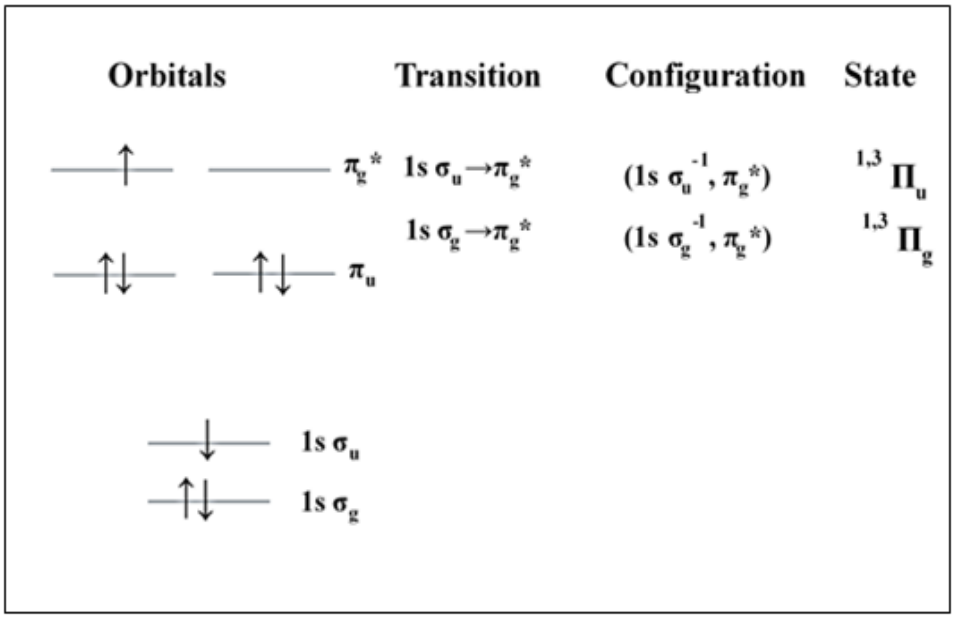

Figure 1.4: Different ways of expressing the nitrogen 1s → π* core excitation feature in the unsaturated molecule like N_2. Figure reprinted from Reference 32 with permission.

First, the terms used to describe core excited states will be explained. A state is described by a wave function that contains information regarding the coordinates and motions of all of the electrons in the molecule.[32] Therefore, for a molecular core excitation process, the state picture represents the behaviour of all of the electrons in the molecule. In the state picture, core-excited states can be defined with term symbols, $^{1,3}\Pi_u$ and $^{1,3}\Pi_g$ (see **Figure 1.4**). Using this notation, a spin allowed singlet core-excited state ($^1\Pi$: $\Delta S = 0$) and spin forbidden triplet state ($^3\Pi$: $\Delta S = 1$) can be distinguished. [32] This approach is correct on a fundamental level since all electrons in the molecule involved in any electronic transition, but the state picture is not convenient for describing the features of the core excitation process.[32]

Therefore, for simplicity, spectroscopic features in molecular NEXAFS spectroscopy are usually described as one electron processes. One electron is described as being excited from a core orbital (initial level) to an unoccupied orbital (final level). For instance, the nitrogen 1s → π* transition in N_2 molecule (shown in **Figure 1.4**), can be described by one electron transition from a nitrogen 1s level ($1s\,\sigma_g$ or $1s\,\sigma_u$) to a π_g^* MO. Here, gerade (g) and ungerade (u) are the symmetry notation of the MOs. If the phase is the same after the inversion symmetry operation, the orbital

called gerade and if the phase is different, orbital called as ungerade. According to the one electron picture, the core-excited state in this transition can be named as either (1s σ_u^{-1}, π_g*) or (1s σ_g^{-1}, π_g*) depending on the type of σ orbital used to remove the electron.[32] According to the Laporte rule, allowed transitions must involve a change in parity either g → u or u → g, so the 1s $\sigma_u \rightarrow \pi_{g*}$ transition is allowed by this selection rule.

1.3 Applications of NEXAFS Spectroscopy

1.3.1 Chemical Sensitivity of the NEXAFS Spectroscopy

This section discusses the chemical and functional group sensitivity of NEXAFS spectroscopy. NEXAFS can be used to study chemical composition and bonding in organic molecules.[8-10, 27]

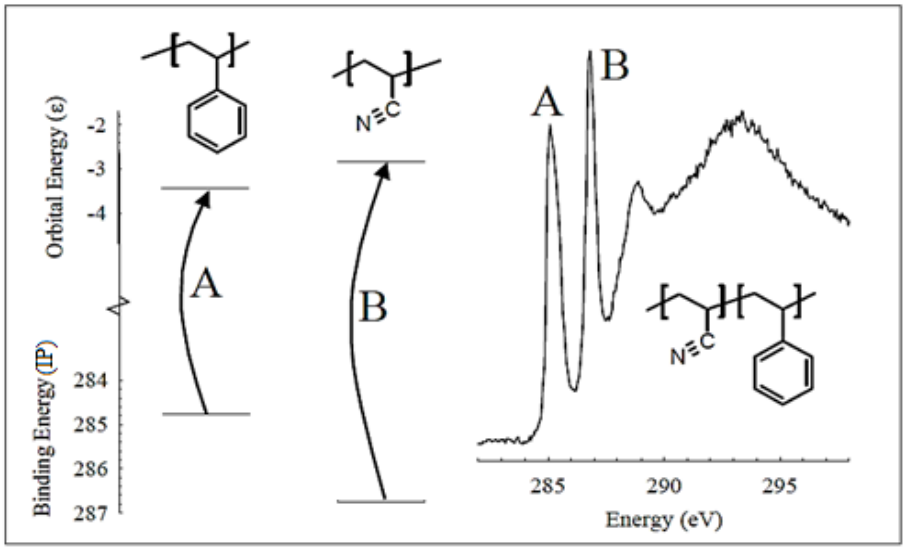

Figure 1.5: Schematic diagram for the NEXAFS spectrum of poly(styrene-*r*-acronitrile). Figure reprinted from Reference 10 with permission.

As shown in **Figure 1.5**, the low energy region (285-288 eV) of the carbon 1s NEXAFS spectrum of poly(styrene-*r*-acronitrile) is dominated by two intense peaks.[10] Peak A (285 eV) is the carbon 1s → $\pi^*_{C=C}$ (phenyl functional group) electronic transition and Peak B (287 eV) is the carbon 1s → $\pi^*_{C\equiv N}$ (acrylonitrile functional group) electronic transition.[10] According to **Figure 1.5**, each transition has a different IPs (initial level) and different unoccupied MO energy (final level), therefore, peaks A and B appear at different energies.[10] This can be explained as follows. For the C≡N group, the carbon is bonded to a nitrogen which makes this carbon atom more electropositive than a carbon atom in a phenyl group. For this reason, the carbon 1s IP of the C≡N group is greater

than that of the carbon 1s IP of the phenyl group (see **Figure 1.5**). The energy of the unoccupied MO in the C≡N group and C=C in the phenyl group is identified from its TV (orbital energy in the **Figure 1.5**).[10, 26] In this case, the *TV* for the $\pi^*_{C\equiv N}$ MO is larger than the $\pi^*_{C=C}$ bond due to the different bonding.[10] Therefore, by considering the effects from both IP and unoccupied orbital *TV* to each transition, the carbon 1s → $\pi^*_{C\equiv N}$ transition energy is greater than the carbon 1s → $\pi^*_{C=C}$ transition energy.[10]

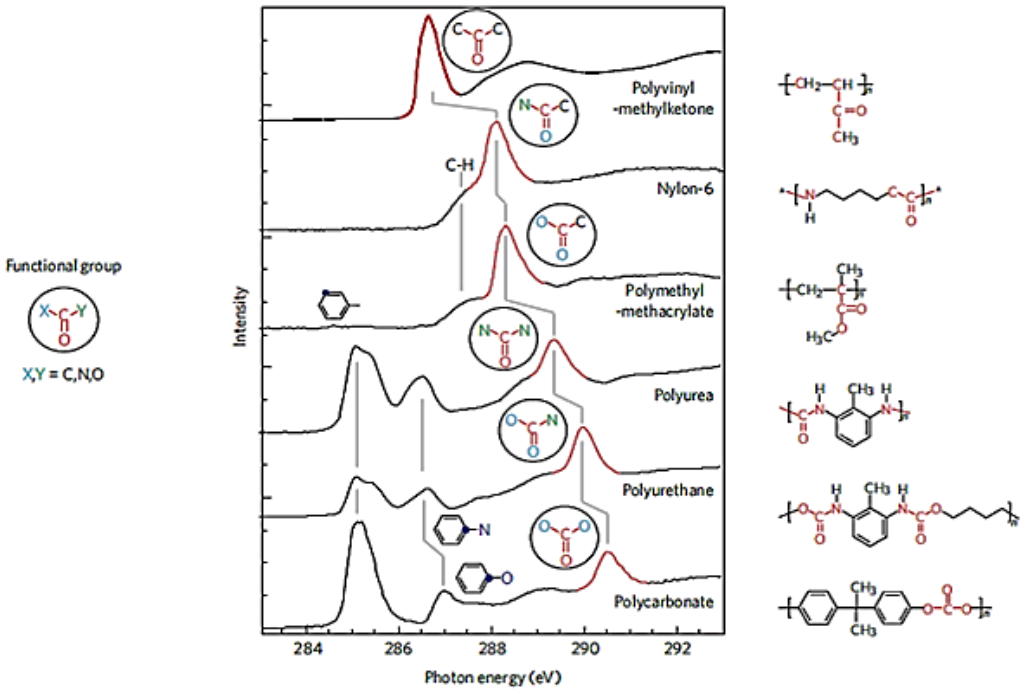

Figure 1.6: Variation in the NEXAFS spectral feature of carbonyl group as a function of different chemical environments (ketone to carbonate). Figure reprinted from Reference 8 with permission.

The chemical sensitivity of NEXAFS spectroscopy can be used to identify functional groups surrounded by different chemical environments (**see Figure 1.6**). As shown in **Figure 1.6**,[8] the carbon 1s NEXAFS spectra of a series of polymers containing the C=O moiety are presented under different bonding environments.[2, 8] In addition to the carbonyl band (288-292 eV), carbon 1s NEXAFS spectra of polycarbonate, polyurethane and polyurea also show bands for unsaturated C=C phenyl group.[2] The band near to the 285-286 eV region corresponds to a carbon 1s (C-H) → $\pi^*_{C=C}$ transition and the band near the 286-287 eV region corresponds to a carbon 1s (C-R) → $\pi^*_{C=C}$ transition. The *R* group in the phenyl ring has a greater inductivity than the *H* group,

therefore, the carbon 1s (C-R) → $\pi^*_{C=C}$ transition appears at a higher energy relative to the carbon 1s (C-H) → $\pi^*_{C=C}$ transition.[2]

In **Figure 1.6**, the carbon 1s → $\pi^*_{C=O}$ peak (highlighted in red) shows a significant energy shift (3.8 eV) between poly(vinyl methyl ketone) and polycarbonate. This energy shift is mainly attributed to the inductive strength of atoms neighbouring the carbonyl carbon.[2, 8] Of the six polymers shown in **Figure 1.6**, the polycarbonate C=O moiety is bonded to the most inductive neighbouring atoms, i.e. both sides of the C=O moiety bonded to electronegative oxygen atoms. Hence, polycarbonate has the highest energy carbon 1s → $\pi^*_{C=O}$ peak.[2, 8] This example demonstrates how NEXAFS spectroscopy can be used to extract information regarding the chemical environments of organic molecules.

1.3.2 Orientation Sensitivity of the NEXAFS Spectroscopy

Electronic transitions in NEXAFS spectroscopy occur as the result of dipole allowed transitions from core orbitals to unoccupied MOs. The previous section showed that different intramolecular properties (chemical and functional group sensitivity) of a molecule can affect the intensity and energy of a given molecular NEXAFS transition. In addition to that, the intensity of a particular transition also depends on the angle between the transition dipole moment (TDM) of the transition and the linear polarization of the X-ray radiation.

Polarization of Light

Light is an electromagnetic wave that is composed of electric ($\bar{E}$) and magnetic ($\bar{H}$) fields. These fields are perpendicular to each other and to the direction of propagation. Light can be unpolarised, demonstrating random fluctuations in the directions of the electric and magnetic fields. However, by constraining the orientation of the electric field and magnetic field, light can be polarized in a specific direction. **Figure 1.7** demonstrates the three main types of light polarization.[37]

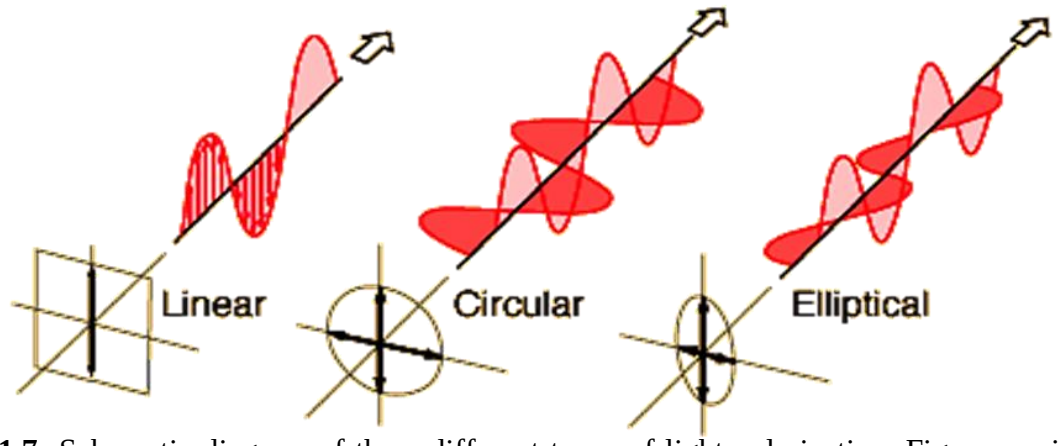

Figure 1.7: Schematic diagram of three different types of light polarization. Figure reprinted from Reference 37 with permission.

The electric field or magnetic field of linearly polarized light is confined to a single plane normal to the direction of propagation (see Linear in **Figure 1.7)**.[37] The electric field of circularly polarized light has a fixed magnitude at each point, but the field rotates in the plane perpendicular to the direction of propagation (see Circular **Figure 1.7**). Circular polarization can be either circular left or circular right, depending on the direction of electric field rotation.[31] In elliptical polarization, two linear components (horizontal and vertical) in the electric field do not have same amplitude, therefore, electric field vector rotates in an elliptical pathway (see Elliptical in **Figure 1.7**). Different X-ray polarizations can be achieved by using X-ray sources such as bending magnets and undulators.

Transition Dipole Moment (TDM)

The TDM of an absorbing molecule is the electric charge distribution difference between its initial and final states, as induced by the electric field vector of the exciting electromagnetic radiation. The strength of a TDM depends on the strength of the interaction between the electron cloud of the absorbing molecule and the electric force of the electromagnetic radiation.[38] The following equation can be used to describe the one-electron TDM (μ_{if}) resulting from the excitation from an initial state (i) to a final state (f) of a molecule [19]

$$\mu_{if} = \langle \psi_i | \mu | \psi_f \rangle$$ **Equation 1.8**

Where, ψ_i and ψ_f are the initial and final state wave functions, and μ is the electric dipole moment operator.[17, 19]

Dipole Selection Rules

The transition between the initial and final state of an atom or molecule is governed by the dipole selection rule. Since the angular momentum number (l) of a photon is one, excitations in atoms follow the atomic selection rule ($\Delta l = \pm 1$). To have a dipole-allowed electronic transition from a 1s atomic orbital (AO) to an unoccupied AO, the unoccupied AO must have a *p* orbital component to satisfy the selection rule ($\Delta l = \pm 1$). Moreover, the direction of the TDM and the *p* component of the unoccupied AO should be in the same direction. This rule is exact for a single atom or diatomic molecules, but it is propensity and not precise for polyatomic molecules because the orbital angular momentums of polyatomic molecules is not strictly defined.[26]

Intensity of a Transition

The angle between the TDM and the electric field vector of the X-ray ($\bar{E}$) determines the intensity of the dipole allowed transition. The intensity of the dipole allowed transition is given in **Equation 1.9**.

$$I \propto \left|\bar{E}\cdot\mu_{if}\right|^2 = |\bar{E}|^2 = \left|\mu_{if}\right|^2 \cos^2\theta$$ **Equation 1.9**

$\bar{E}$ is the electric field vector of the X-ray radiation and θ is the angle between $\bar{E}$ and μ_{if} (see **Equation 1.8** for μ_{if}). The maximum observable intensity (I_{max}) occurs when the two vectors are parallel to one another, and the minimum observable intensity (I_{min}) occurs when the two vectors are normal to one another.

If the degree of linear X-ray polarization is not 100% (as in the case of X-rays produced by bending magnets), the intensity of the dipole allowed transition (**Equation 1.9)** can be affected by the polarization ellipticity. Ellipticity (*P*) describes the degree of linear polarization and can be expressed as:[26]

$$P = \frac{\left|\bar{E}^{//}\right|^2}{\left|\bar{E}^{//}\right|^2 + \left|\bar{E}^{\perp}\right|^2}$$ **Equation 1.10**

In this equation, the horizontal and vertical components of the X-ray electric field are given by the $\overline{E}^{/\!/}$ and $\overline{E}^{\perp}$ terms, respectively, and they are defined as parallel or perpendicular to the electron orbit plane of the synchrotron storage ring.[25-26]

In such situations, the intensities of molecular transitions are affected as,

$$I \propto P\left|\overline{\mathbf{E}}^{\|}\right|^2 \left|\mu_{if}\right|^2 \cos^2\theta + (1-P)\left|\overline{E}^{\perp}\right|^2 \left|\mu_{if}\right|^2 \sin^2\theta \qquad \textbf{Equation 1.11}$$

Here, θ is the angle between $\overline{E}^{/\!/}$ and μ_{if}. According to **Equation 1.11**, the intensity of a particular transition is non-zero when its TDM is normal to the $\overline{E}^{/\!/}$. This is because the transition intensity now includes contributions from the both $\overline{E}^{\perp}$ and $\overline{E}^{/\!/}$ terms, due to ellipticity of the X-ray polarization.[25-26]

However, X-ray sources such as undulators (see §2.4.1.1 and 2.4.1.2 for bending magnets and undulators) are capable of producing 100% pure X-ray linear polarization and this ellipticity problem can often be resolved.

1.3.2.1 Linear Dichroism (LD) in NEXAFS Spectroscopy of *n*-Alkanes

Section 1.3.2 showed that the intensity of a given transition varies with the angle between the TDM of the transition and polarization $\bar{E}$ of the X-ray beam. Therefore, X-ray polarization and angular dependence of the NEXAFS spectra can be used to determine the orientation of the TDM and thus the molecule.[39] LD-NEXAFS is a well-known spectroscopic technique that investigates the molecular orientations and conformations of aligned organic materials.[5, 16-17, 19, 40]

LD-NEXAFS is the anisotropic absorption of linearly polarized X-ray radiation. In order to absorb linearly polarized X-ray radiation, the polarization $\bar{E}$ of the X-ray radiation needs to be aligned with the TDM of the transition. In LD techniques, this can be achieved by either rotating the sample with respect to a beam with a fixed X-ray linear polarization (as shown in **Figure 1.8**)[40] or by rotating the linear X-ray polarization with respect to a sample of fixed position (as shown in **Figure 1.9**)[17].

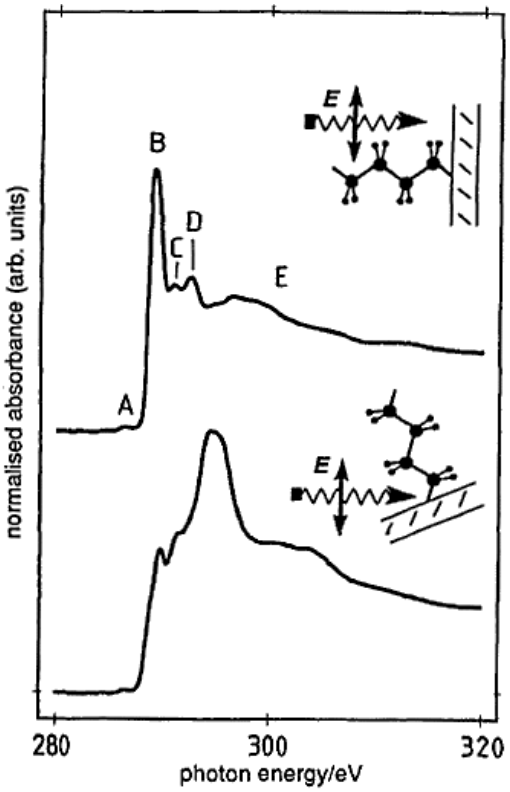

Figure 1.8: The angle dependence of carbon 1s NEXAFS spectra of *n*-$C_{36}H_{74}$ alkane thin films with fixed X-ray polarization vector. Figure reprinted from Reference 40 with permission.

Figure 1.8 illustrates the angular dependence of the most prominent core → σ* transitions (carbon 1s → $\sigma^*_{C\text{-}H}$ and carbon 1s → $\sigma^*_{C\text{-}C}$) in alkane thin films where the chains are oriented normal to the surface. The figure compares the spectra obtained at normal incidence with spectra obtained at glancing incidence angles. At normal incidence, the $\bar{E}$ of the polarized X-ray is parallel to the TDM of the C-H bond and a maximum intensity of the carbon 1s → $\sigma^*_{C\text{-}H}$ transition is observed (peak B in **Figure 1.8**).[40] The situation is reversed at glancing angles, where the $\bar{E}$ of the polarized X-ray is parallel to the TDM of the C-C backbone, in which case the maximum peak intensity observed is for the carbon 1s → $\sigma^*_{C\text{-}C}$ transition (peaks D).[40] In both cases, the X-ray polarization vector is fixed and the LD effect is observed as a result of rotating the sample relative to the fixed polarization. [25-26]

For situations where the X-ray source can deliver linear polarization with arbitrary inclination (elliptically polarized undulator, see §2.4.1.2), the LD effect of NEXAFS spectroscopy can be examined by rotating the X-ray polarization vector with respect to a fixed sample position (see **Figure 1.9**).[17]

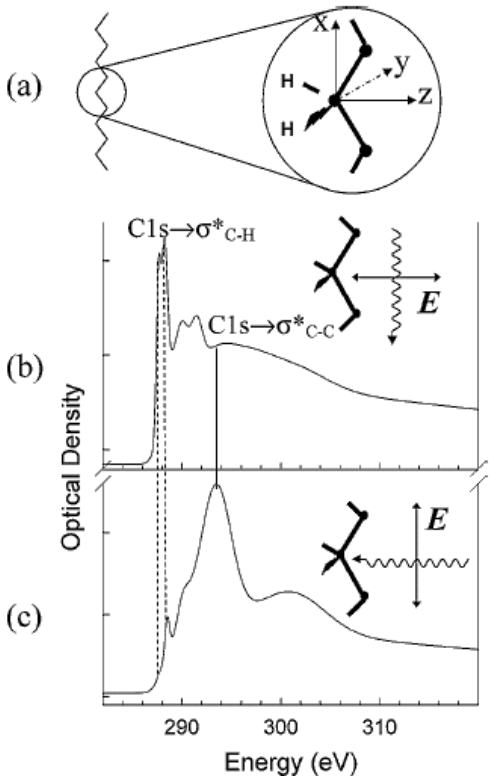

Figure 1.9: (a) Schematic diagram of the geometry of the carbons in alkane chain lengths, (b) carbon 1s NEXAFS spectra of *n*-$C_{60}H_{122}$ when $\bar{E}$ is normal to the chain back bone direction (X axis), and (c) carbon 1s NEXAFS spectra of *n*-$C_{60}H_{122}$ when $\bar{E}$ is parallel to the chain back bone direction (X axis). Figure reprinted from Reference 17 with permission.

In this method, when the $\bar{E}$ of the X-ray beam is parallel to the chain backbone, the maximum intensity is observed for carbon 1s → $\sigma^*_{C\text{-}C}$ transitions, while the $\sigma^*_{C\text{-}H}$ transition intensity is minimized. The situation is reversed, $\sigma^*_{C\text{-}H}$ transitions achieve their highest intensities, when $\bar{E}$ of the X-ray beam is oriented parallel to C-H bond plane.

1.3.3 Intermolecular Effects in NEXAFS Spectroscopy

Intermolecular effects in NEXAFS spectroscopy have not been extensively studied as intramolecular effects for organic molecules.[1-3, 9-10, 14, 16-19, 28, 41-43] Thus, studying and knowing the roles of intermolecular effects in NEXAFS spectroscopy will strengthen knowledge and understanding of the spectral behaviours of condensed (solid and liquid) phase molecules.

Intermolecular effects predominantly arise from conformational changes in the solid phase and perturbations due to the electronic interactions between neighbouring molecules such as quenching of Rydberg character in solid phase.[21] NEXAFS spectroscopy can be used to identify the specific solid state effects caused by these intermolecular interactions. In this study, the effects

of Rydberg quenching on the degree of Rydberg-valence mixing and π-π interactions on the carbon 1s NEXAFS spectra of solid organic molecules are examined.

1.3.3.1 Previous Experimental Approaches

The solid and gaseous phases of carbon 1s NEXAFS spectra of saturated[21] and unsaturated[44-45] molecules demonstrate significant spectral differences, specifically at the low energy region (287-288 eV).

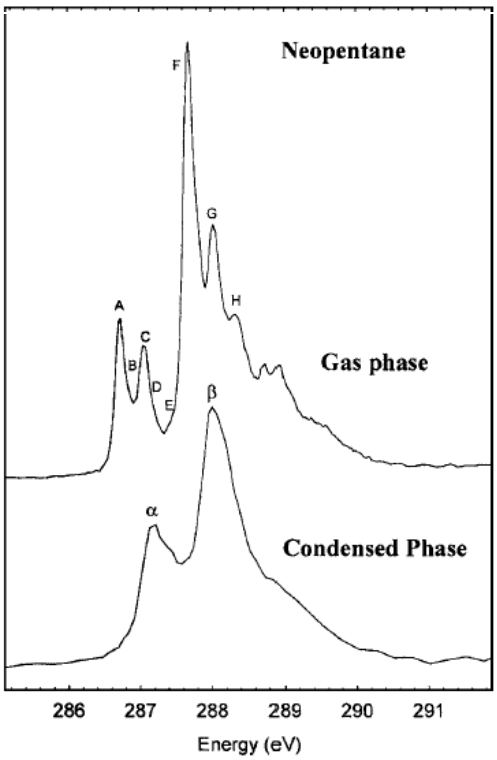

Figure 1.10: Carbon 1s NEXAFS spectra of solid and gas neopentane measured by total ion yield and total electron yield respectively. Figure reprinted from Reference 21 with permission.

For instance, low energy features in the NEXAFS spectrum of solid phase neopentane are broader and shifted to higher energies (blue energy shift) relative to the molecule's gas phase spectrum (see **Figure 1.10**).[21] In **Figure 1.10**, the gas phase neopentane spectrum shows many sharp Rydberg peaks in the 286-289 eV region. These are reduced to two broad peaks in the solid phase spectrum. These spectral differences are due to the solid state effects caused by the intermolecular interactions in the solid phase.

High resolution carbon 1s NEXAFS spectra of simple gas phase alkanes such as methane and propane are dominated by carbon 1s → Rydberg transitions with rich vibronic structures.[35, 46-

[49] Therefore, spectral features of the gas phase alkanes are unambiguously Rydberg in nature. A small degree of $\sigma^*_{C\text{-}H}$ valence character can contribute to excited states if the valence character has the same symmetry as the Rydberg states.[35] Specifically, in molecules with C-H bonds, such as alkanes, Rydberg-valence mixing is possible for spectral transitions oriented along the C-H bonds (see §1.2.2).[35]

Compared to the gas phase spectra, the interpretation of the carbon 1s NEXAFS spectra of solid phase alkanes is controversial.[51-53] Features in the pre-edge region (286–289 eV) of carbon 1s NEXAFS spectra of solid alkanes have traditionally been assigned to carbon 1s $\rightarrow \sigma^*_{C\text{-}H}$ valence transitions.[50-51] However, Bagus *et al.*[52] have argued that carbon 1s → Rydberg transitions are the dominant features in the pre-edge regions of solid alkane spectra. They used high quality *ab initio* calculations of isolated propane molecules to support their assignments. This model is problematic.[21, 52] Although the authors[52] hypothesize that intermolecular interactions can modify Rydberg states in the condensed phase, this calculation of an isolated propane molecules cannot approximate the intermolecular interactions present in the solid phase.[21] Without accounting for the effects of molecular interactions within the condensed phase, it is hard to comment on the nature of the Rydberg characters of the spectra of solid phase molecules.[21] In a separate study, Weiss *et al*.[53] proposed that Rydberg peaks are not quenched upon condensation, but instead move to higher energies in the solid phase. They supported their argument with *ab initio* calculations for propane trimers and septamers.[53] However, trimers and septamers are small, simple clusters and their size does not exceed the radius of the Rydberg orbital in the condensed phase.[21] Therefore, the modeled clusters may lead to anomalous Rydberg states because the excited states in this model might represented a mixed cluster/vacuum environment.[21] Considering these physical inconsistencies, the suggestion by Bagus *et al*.[52] and Weiss *et al*.[53] that solid state organic spectra demonstrate predominately Rydberg characters is contested.[21]

Schöll *et al*.[54] propose that the pre-edge features (287-288 eV) of ordered solid alkanes are not dominated by Rydberg character. Instead their assignments agree with the conclusions of Stöhr *et al*.[50], and they claimed that double peak structure in the pre-edge region of ordered solid alkanes have $\sigma^*_{C\text{-}H}$ character (valence character). Schöll *et al*.[54] study found the appearance of the carbon 1s $\rightarrow \sigma^*_{C\text{-}H}$ resonance (287-288 eV) was directly correlated to the polymer crystallinity, and that quenching effects were observed in the NEXAFS spectra of solid alkanes. The double peak

structure in the carbon 1s → $\sigma^*_{C\text{-}H}$ resonance (287-288 eV) disappears as the crystallinity decreased in the solid polymer structure.

All these studies show a double peak structure in the pre-edge region as the key spectroscopic feature in the NEXAFS spectrum of solid alkanes. A relevant double peak structure was observed by the experimental work of Gillies *et al.*[21] for condensed neopentane as well (see **Figure 1.10**). In Gillies *et al*.[21] work, they propose that this pre-edge feature (double peak structure) of ordered solid alkanes is not dominated by Rydberg character. One of the major differences in Gillies *et al*. [21] work is that he studied both solid and gas phase samples of the same species at the same time.[52-54] Gillies *et al*.[21] work showed that the Rydberg character of the gas phase changes to valence character (carbon 1s → $\sigma^*_{C\text{-}H}$) upon condensation. This is shown in **Figure 1.10**; upon condensation of neopentane, two broad peaks appear in the low energy C-H region (287-288 eV) of the condensed spectra.[21] The Gillies interpretation of solid phase spectrum was based on a solid model calculation that embeds propane molecules into a large cluster of neon atoms. To use this solid model, the researchers made sure that the size of the cluster was big enough to exceed the size of the Rydberg orbital in the solid. Therefore, the Gillies *et al*.[21] spectral interpretation of solid phase spectra should be more accurate than those using no clusters or simple cluster models.[52,53]

Based on calculations of ΔE(S-T) in excited state orbitals (where a greater ΔE(S-T) indicates more valence character), Gillies *et al*.[21] proposed that solid phase core excited states are dominated by valence character. Therefore, Gillies *et al*.[21] proposed that spectral changes in the solid phase spectrum are attributed to the quenching of Rydberg character by interactions of the Rydberg orbitals with neigbouring atoms and emergence of carbon 1s → $\sigma^*_{C\text{-}H}$ character (valence) in the solid state. In summary, these works confirm that different intermolecular interactions (degree of Rydberg-valence mixing) in each phase cause definite spectral changes in their NEXAFS spectra.

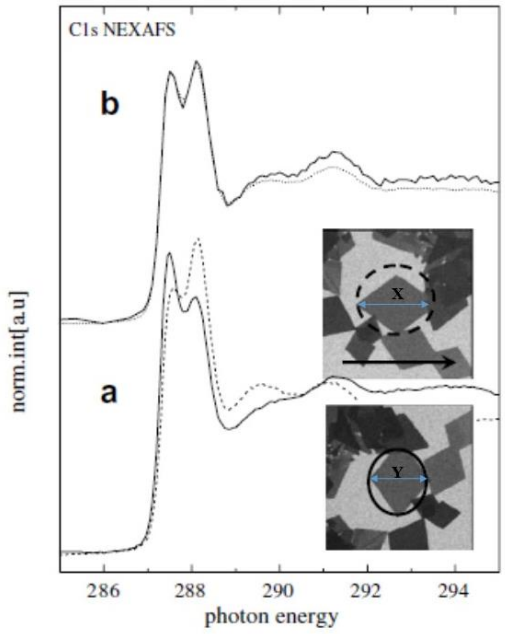

Figure 1.11: (a) Carbon 1s NEXAFS spectra of the *n*-tetracontane (*n*-$C_{40}H_{82}$) crystal in the center of the images recorded by STXM at 288.0 eV. Solid line spectrum represents horizontal linearly polarized light aligned along the Y crystal axis, dashed line spectrum represents horizontal linearly polarized light aligned along the X crystal axis of same crystal after rotation of the sample by 90° (b) Carbon 1s NEXAFS spectrum of *n*-tetracontane (*n*-$C_{40}H_{82}$) crystal recorded with circularly polarized light (solid line), compared to the sum spectrum (dotted line) derived from (a). Figure is reprinted from Reference 55 with permission.

Zou *et al*.[55] studied the strengths of intermolecular interactions in solid alkanes using single crystal carbon 1s NEXAFS spectra of *n*-tetracontane (*n*-$C_{40}H_{82}$) and *n*-nonadecane (*n*-$C_{19}H_{40}$) (see **Figure 1.11** for *n*-tetracontane). Since the double peak structure in the pre-edge region (287-288 eV) is the key feature in the NEXAFS spectra of linear *n*-alkanes, Zou *et al*.[55]studied the relationship between the intensity of the split peak in the carbon 1s → $\sigma^*_{C\text{-}H}$ resonance (287-288 eV) and the crystal orientation along the principle crystal axes (see X and Y in **Figure 1.11**). They found that the relative intensities of the split peak of the carbon 1s → $\sigma^*_{C\text{-}H}$ resonance showed opposite relationship when the in-plane crystal orientation was changed from Y crystal axis direction to X crystal axis direction.[55] Zou *et al*.[55] note that even a small change in the weak van der Waals interactions between the *n*-alkane molecules can change spectral intensity, shape, and linear dichroic signatures in NEXAFS spectra. Moreover, their work proposes that carbon 1s → $\sigma^*_{C\text{-}H}$ transitions in pre-edge features depend on the crystal symmetry rather than the symmetries of the *n*-alkane molecules.[55] While instructive, Zou *et al*.[55] work only considered the orthorhombic crystal structure, and did not account for other possible *n*-alkane crystal polymorphs (monoclinic,

triclinic etc.). In a separate work, Swaraj *et al*.[56] studied how the *n*-alkane NEXAFS spectra change with alkane chain length and carbon backbone parity (eg. odd or even number of carbon atoms in backbone). Swaraj *et al*.[56] proposed that pre-edge features in *n*-alkane spectra are affected by the backbone parity, but not by the *n*-alkane chain length.[56] Their work did not account for crystal polymorphism in the *n*-alkane crystals. Since NEXAFS is sensitive to density, order, and electronic structure, it may be important to consider the crystal polymorph of the *n*-alkane crystal when addressing the effects of intermolecular interactions. Therefore, in this work, we account for single crystal polymorphism, and effects of Rydberg quenching on the Rydberg-valence mixing in saturated molecules (*n*-alkanes) by defining the crystal structures (orthorhombic, monoclinic etc.) and chain lengths of the *n*-alkane single crystals (second research objective).

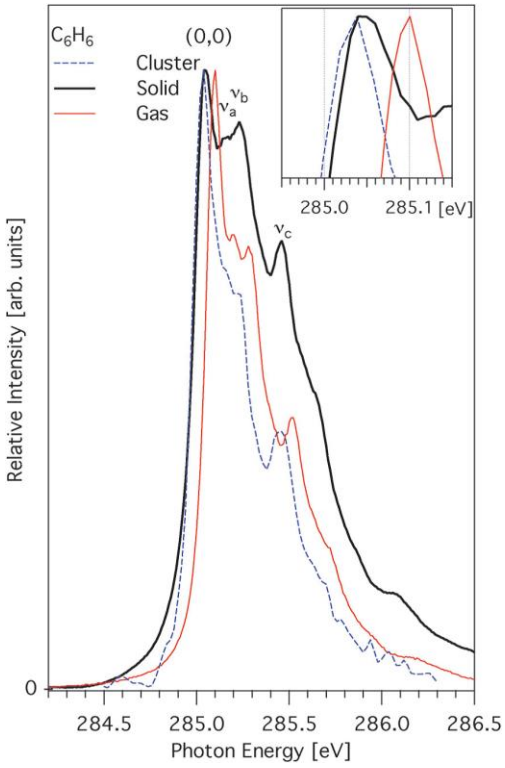

Figure 1.12: Carbon 1s NEXAFS spectra of solid (black), cluster (blue), and, gas (red) phase of naphthalene in the carbon 1s → π* region (284 eV-287 eV). Cluster and solid spectra obtained simultaneously with the gas phase. Figure reprinted from Reference 45 with permission.

As with saturated molecules, the NEXAFS spectra of aromatic molecules are also expected to exhibit different solid state effects. For an example, Flesh *et al*.[22, 45] studied spectral variations in the different phases (gas, cluster, and, solid) of benzene in the carbon 1s → π* transition (see **Figure 1.12**). According to **Figure 1.12**, the π* region (284 eV-286.4 eV) of benzene is dominated

by adiabatic (0,0) transition and three vibronic peaks: v_a, v_b, and v_c. The adiabatic (0,0) peak represents the carbon 1s (C-H) (v=0) → π*(v=0) transition.[45] The v_a and v_c vibration π* peaks are due to excitation to the C-H out-of-plane bending and stretching vibrations of benzene, and the v_b vibration π* peak is due to its aromatic ring vibrations (C-C bond) that accompany the 1s → π* transition.[45] From Flesh *et al*.[22, 45] work, they found that different phases of the benzene molecule exhibited slightly different spectra. The energy positions of the vibration peaks (v_a, v_b, and, v_c) and (0,0) peak of benzene shift to lower energies (55 ± 5 meV) when spectrum goes from the gas phase to the solid phase.[45] The energy shift is most prominent when one compares the peak maxima of the (0,0) peak.[45] Moreover, all these prominent peaks broaden slightly upon the condensation (gas to solid).[45] The origin of this energy shift is a change in the local environment of the excited atom when condensed (dynamic stabilization).[45] In addition, the energy shift observed between the gas and solid phase spectra is sensitive to the interactions of the nearest neighbours of the absorbing atom in each phase, but energy shift is not affected by the long range interactions of the benzene molecules.[45]

Although Flesh *et al*.[22, 45] says that the energy shift in the spectra is sensitive to the interactions of the nearest neighbours of the absorbing atom in each phase, they proposed that the reasons for the shape differences in the carbon 1s → π* transitions in benzene molecule are not due to the different intermolecular interactions present in each phase (solid vs cluster vs gas), because the vibrational structures of the gas, cluster, and solid benzene molecule are all very similar. [22, 45] Flesh *et al*.[22, 45] mentioned that these peak shape changes are the result of electron yield saturation effects that are exclusively present in the solid phase.[45, 57]

Schmidt *et al*.[44] compared solid and gas phase naphthalene spectra. As shown in **Figure 1.13**, the spectral features of solid naphthalene are broader in all regions (A-E) of the carbon 1s NEXAFS spectrum, compared to those of the gas phase.[44] Spectral variations in region A-C are explained below. Based on DFT calculations on isolated naphthalene molecules published by Schmidt *et al*.[44], spectral features in regions A and B are the result of carbon 1s → π* transitions (285.0 eV, 285.2 eV and 285.8 eV), and those transitions originate from the C1, C2, and C3 atoms of naphthalene (see naphthalene in **Figure 1.13**).[44] The authors attribute the broadening of features in regions A and B of the solid phase spectrum to packing effects in the crystalline material.[44]

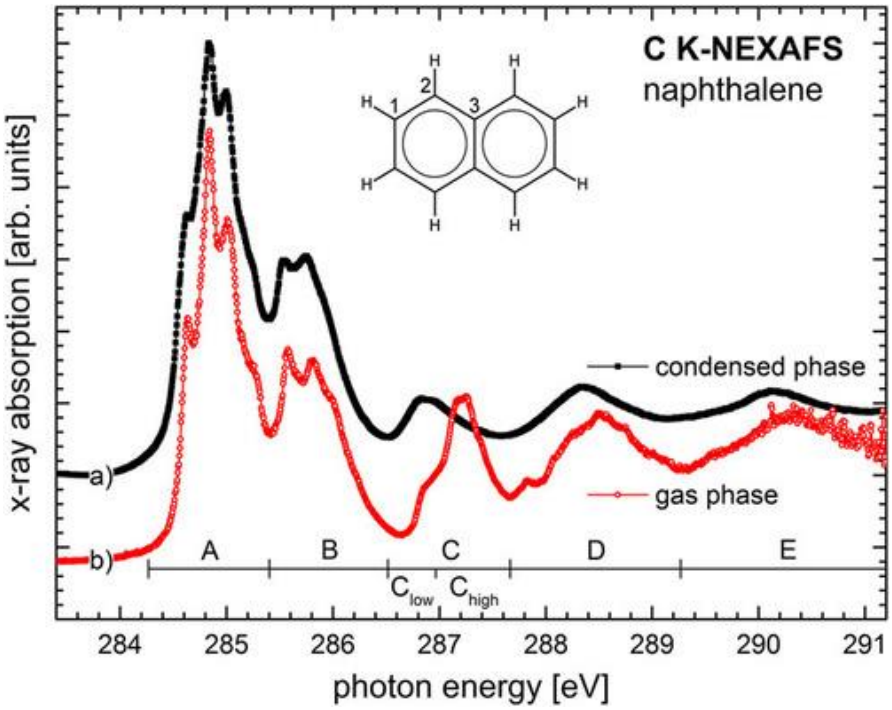

Figure 1.13: Carbon 1s NEXAFS spectra of naphthalene in (a) solid phase, and (b) gas phase. Figure reprinted from Reference 44 with permission.

In Region C, the gas phase naphthalene spectrum (red trace) shows a strong shoulder peak on the low energy (C_{low} in **Figure 1.13**) side, and a split peak (doublet with 287.2 eV and 287.3 eV) on the high energy (C_{high} in **Figure 1.13**) side.[44] In contrast to the gas phase, the solid phase spectrum (black trace) exhibits low spectral intensity in region C and features centered around the 286.8 eV peak.[44] Based on the DFT calculations, Schmidt *et al.*[44] proposed that the spectral features in the C_{low} region are the result of carbon 1s $\rightarrow \pi^*$ transitions (valence), and those in the C_{high} region are the result of mixed Rydberg-valence transitions.[44] The DFT calculations also show that C_{high} region has more diffuse Rydberg character and the Rydberg character in solid phase spectrum in C_{high} is highly affected by the intermolecular interactions and confinement of the solid phase.[44] Therefore, intermolecular interactions leading to Rydberg quenching in solid phase spectrum were observed on the high energy side of region C (C_{high} group). The authors suggest intermolecular interactions and confinement to be the reason for the missing spectral features in the C_{high} region of the solid phase spectrum of naphthalene.[44]

Both the Flesh *et al.*[45] and Schmidt *et al.*[44] studies found distinct spectral changes caused by differences in the intermolecular interactions (Rydberg-valence mixing) of solid and gas phase aromatic molecules. However, how differences in the intermolecular interactions *between solids*

of different structures affect the carbon 1s NEXAFS spectra of unsaturated molecules is still unclear and open to study. Therefore, as a first objective, this research work systematically studied the effects of π-π interactions on *solid phase* spectra by studying paracyclophane (PCP) molecules with different spacer lengths. This research aims to enhance the general understanding of intermolecular effects on NEXAFS spectroscopy by studying the effects of π-π interactions of unsaturated molecules (PCP) and effects of Rydberg quenching on the degree of Rydberg-valence mixing of saturated molecules (*n*-alkanes).

1.3.4 Effects of Nuclear Motion Contribution on NEXAFS Spectra

Identifying the origin for the spectral broadening in molecular NEXAFS spectroscopy is the key to understand the interpretation of the NEXAFS spectra of organic molecules. In §1.3.3, the contributions of Rydberg quenching to the spectral broadening of the NEXAFS spectra of solid organic molecules were discussed.[21, 44]

Spectral broadening in molecular NEXAFS spectroscopy can occur from lifetime effects by Rydberg quenching or environmental effects or from both.[21] Environmental effects include unresolved chemical shifts in vibronic transitions[35, 46] and nuclear motion.[20, 58-61] Nuclear motion contributions were studied in this project in an effort to address the spectral broadening observed in the carbon 1s NEXAFS spectra of short-chain orthorhombic (o-rh) *n*-alkanes.

Nuclear Motion Effects in NEXAFS Spectroscopy

Spectroscopic contributions that originate from energetically accessible vibrations (including zero point motion) and conformations present at experimental temperatures are called nuclear motion effects.[20, 60] Such effects can arise from a variety of vibrations,[35, 46] structural dynamics,[54] or various other kinds of disorders (conformational/structural) in a solid phase.[60-61] Several approaches have been used to address the nuclear motion effects in NEXAFS spectroscopy of organic materials.

1.3.4.1 Previous Approaches

The Prendergast group have examined how nuclear motion contributes to spectral broadening in NEXAFS spectroscopy using molecular dynamics (MD) and Density Functional Theory (DFT) simulations of amino acids and related molecules.[58]

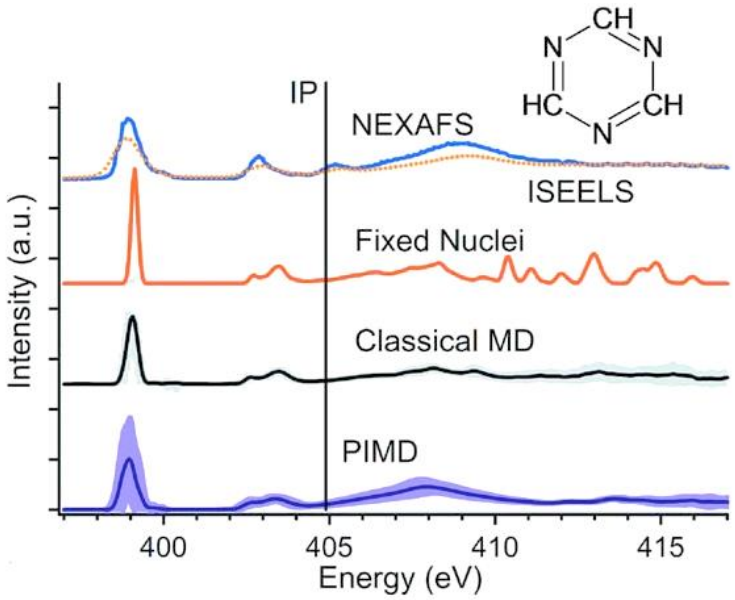

Figure 1.14: Measured and simulated core level spectra of 1,3,5-triazine (s-triazine) at the nitrogen K edge. Figure reprinted from Reference 58 with permission.

The Prendergast group compared the simulated core level spectra generated using the fixed nuclei model (single lowest energy geometry) with those generated from a model incorporating average nuclear degrees of freedom.[58] The later model was obtained by averaging spectral simulations based on structural snapshots obtained from MD simulations. They found that the shapes of the molecular NEXAFS spectra are the result of contributions from both the excited vibration modes and the zero point motions of the molecules.[58]

Figure 1.14 presents a spectral comparison of a measured and simulated core level spectra of 1,3,5-triazine (s-triazine) at the nitrogen K edge.[58] According to **Figure 1.14**, the fixed nuclei spectrum approximation overestimates the intensities of measured s-triazine spectral features, and does not accurately reproduce the energy width of the main spectral features of the measured s-triazine spectrum.[58] Comparatively, MD (both MD and Path Integral Molecular Dynamics (PIMD)) simulations of core level spectra that include nuclear degrees of freedom based on classical thermal motions (classical MD) better represent experimental core-level spectra, relative to computational approaches that leave out nuclear motions of molecules (fixed nuclear approximation).[58] MD and PIMD simulations were able to estimate the intensities and peak widths of the main spectral features of the measured s-triazine spectrum much better than the fixed nuclei approximation.[58] In their work, these MD and PIMD simulations generated distributions of s-

triazine conformations and used them as nuclear coordinates for electronic structure calculations. The vibrational degrees of freedom of the electronic structures generated from this approach are supposed to be more accurate than those considered by conventional approaches, which explore vibrational degrees of freedom within normal mode analysis.[58]

Furthermore, the same authors' MD-DFT simulation work on complex molecular solids, such as glycine, was able to predict that solid-phase vibrational modes would be the origin of temperature dependent broadening effects in NEXAFS spectra.[58] This work showed the importance of considering quantum dynamics when simulating nuclear motion contributions to the spectra of solid organic materials. The same nuclear motion contribution should be present in the NEXAFS spectra of *n*-alkanes.

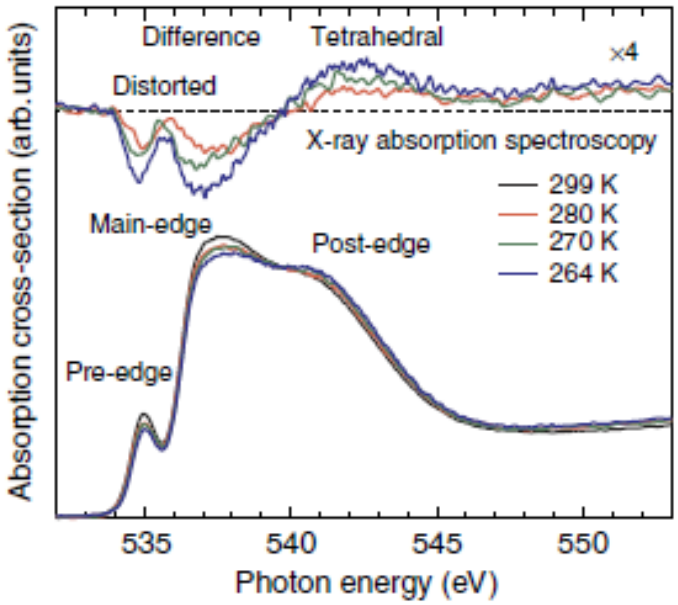

Figure 1.15: XAS spectra of liquid water at various temperatures, obtained in transmission detection mode. Figure reprinted from Reference 59 with permission.

In a separate research program, Lars Pettersson and his group examined the anomalous properties of liquid water as a function of temperature (see **Figure 1.15)**.[59] Pettersson's extensive water studies combined MD studies of liquid and solid water with DFT-based spectral simulations.[59, 61] Pettersson showed how a range of water structures, including high and low density forms associated with the anomalous properties of super cooled liquid water, contribute to the shape of its NEXAFS spectrum.[59] In **Figure 1.15**, the pre-edge (535 eV) and main-edge (537-538 eV) peaks of liquid water are shaped by contributions originating in distorted H-bonds, and

the post edge is shaped by water's strong tetrahedral H-bond structures.[61] This is consistent with the temperature dependence NEXAFS spectra of liquid water as well. The spectral features did not undergo major energy shifts or spectral broadening with increasing temperature.[59] However, there are intensity changes at an almost fixed energy. Specifically, intensity of the main-edge features are enhanced due to the contributions from many forms of water, such as high-density amorphous ice and crystalline high pressure ice.[59, 61] Therefore, the average XAS spectrum of water has contributions from different water geometries. Sampling the contribution of each unique water geometry is important to rationalize the average spectral shape.

There is a lack of experimental data from molecular systems other than water. There is evidence to suggest that molecular disorder associated with the temperature have similarly significant influence on the NEXAFS spectra of condensed alkanes. In this regard, Schöll *et al*.[54] studied the NEXAFS spectra of several polyethylene co-polymers with different degrees of disorder and crystallinity changes with temperature.

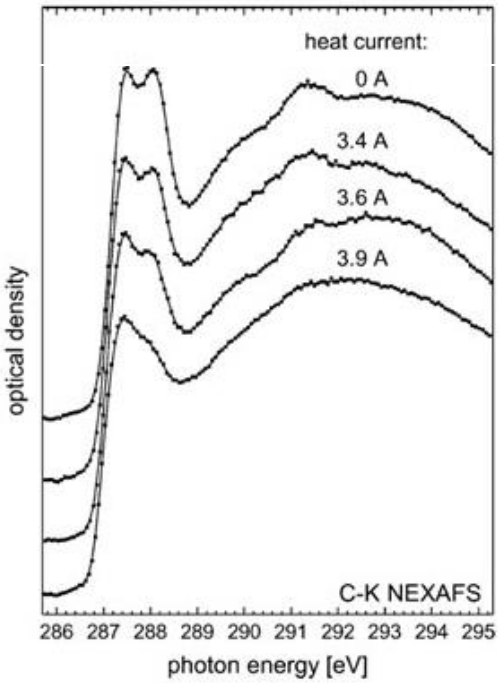

Figure 1.16: Spectral variation in the carbon 1s NEXAFS spectra of polyethylene copolymer as a function of current (temperature). Figure reprinted from Reference 54 with permission.

Schöll *et al*.[54] found spectroscopic features were broader for more disordered copolymers and for the crystalline co-polymer at higher temperatures, especially for temperatures close to the polymer melting points (see **Figure 1.16**). Molecular disorder may appear similar to nuclear

motion and understanding these factors could help enhance our understanding of the spectral broadening observed in molecular NEXAFS spectroscopy.

Since the short chain alkanes used in this research work have relatively low melting points, compared to larger chain alkanes in Schöll *et al.*[55] they are expected to have higher thermal mobilities and molecular defects at room temperature. The spectral broadening observed in the NEXAFS spectra of orthorhombic short chains (orthorhombic spectrum of *n*-$C_{28}H_{58}$) alkanes in **Chapter 5** will be discussed on **Chapters 6** and **7**. In **Chapter 6**, spectral contributions arise from the nuclear motion and molecular disorder in orthorhombic *n*-$C_{28}H_{58}$ to the NEXAFS spectroscopy were studied by using temperature measurements (~298 K (room temperature) vs 93K (liquid nitrogen)) of orthorhombic *n*-$C_{28}H_{58}$ alkane. **Chapter 7** studies the molecular disorder associated with the orthorhombic alkane chain length and their significance in the spectral broadening in NEXAFS spectroscopy.

1.4 Research Objectives

The goal of this thesis is to investigate the relationship between intermolecular effects and NEXAFS spectroscopy. To achieve this goal, this work examines two intermolecular interactions and their effects on the NEXAFS spectra of organic materials. Specifically, it examines the effects of π-π interactions on the NEXAFS spectra of unsaturated organic materials, and the effects of Rydberg quenching on the degree of Rydberg-Valence mixing on the NEXAFS spectra of saturated organic materials.

1.4.1 To Determine the Effects of π-π Interactions on the NEXAFS Spectra of Unsaturated Organic Materials

The effects of π-π interactions on NEXAFS spectroscopy were studied by varying benzene-benzene separation distances in unsaturated molecular systems. Using PCP as a model system, benzene-benzene separation can be varied systematically by varying the length of the spacer moiety that connects the two benzene rings of the PCP molecule. Trends observed in experimental NEXAFS spectroscopy of the PCP materials were reproduced and rationalized using theoretical calculations. Both *ab initio* and DFT calculations were used to rationalize experimental trends. It was found that the DFT calculations did a much better job of interpreting and rationalizing the experimental data of large molecules (PCP molecules) than did the *ab initio* calculations. This dissertation, therefore, only discusses the DFT results.

1.4.2 To Identify the Effects of Rydberg Quenching on the Degree of Rydberg-Valence Mixing on the NEXAFS Spectra of Saturated Organic Materials

The effects of Rydberg quenching on the degree of Rydberg-valence mixing on the NEXAFS spectroscopy of saturated organic molecules were systematically identified by varying molecule chain lengths and crystal structures (orthorhombic vs monoclinic). Using *n*-alkanes as a model system, Rydberg-valence effects (effects caused due to change in valence and Rydberg character in the molecular transitions) correlating to chain length (*n*-$C_{23}H_{48}$, *n*-$C_{24}H_{50}$, *n*-$C_{28}H_{58}$, *n*-$C_{32}H_{66}$ and *n*-$C_{40}H_{82}$) and crystal structure (monoclinic vs orthorhombic) were studied. A great deal of effort was required to maintain the shapes and structures of the *n*-alkanes crystals during data acquisition. Crystals of the shortest chain *n*-alkanes (*n*-$C_{23}H_{48}$ and *n*-$C_{24}H_{50}$) in our system were unstable, and their shapes and crystalline structures could not be maintained because of their smaller crystal sizes and high vapour pressures. Therefore, the study examined longer, more stable *n*-alkane chains (*n*-$C_{28}H_{58}$, *n*-$C_{32}H_{66}$ and *n*-$C_{40}H_{82}$). As the local geometries (subcell structure oriented along the *n*-alkane backbone) are identical in both orthorhombic and monoclinic structures, the degree of Rydberg quenching should be same for each crystalline polymorphs (orthorhombic and monoclinic). Hence NEXAFS spectra should be insensitive to the differences in the Rydberg-valence mixing resulting from varying *n*-alkane crystal structures. However, linear dichroism (LD) effects were observed along the principal crystal axes (specifically along the short crystal axis Y) of the different crystalline environments (orthorhombic and monoclinic) of the *n*-alkanes.

1.4.3 To Recognize the Effects of Nuclear Motion Contribution to the NEXAFS Spectroscopy

In addition to LD effects, the NEXAFS spectra of orthorhombic *n*-$C_{28}H_{58}$ were broader relative to the longer chain orthorhombic *n*-alkanes *n*-$C_{32}H_{66}$ and *n*-$C_{40}H_{82}$. The study was, therefore, extended to address the origins of the spectral broadening of the *n*-alkane o-rh-*n*-$C_{28}H_{58}$. This was done by using two approaches. One is examining the relationship between alkane disorder and alkane chain length (**Chapter 7**), other is examining the nuclear motion effects of the shortest *n*-alkane (*n*-$C_{28}H_{58}$) in our system to its NEXAS spectra (**Chapter 6**). Raman spectroscopy was used to study disorder in the short-chain *n*-alkane. Since nuclear motion effects is similar for all *n*-alkanes, the effect was studied for shortest *n*-alkane (*n*-$C_{28}H_{58}$) in our system. The study was performed by comparing NEXAFS spectra obtained at room temperature (~298 K), where nuclear motions should be significant, to spectra obtained at cryogenic temperatures (~93

K), where nuclear motion should be reduced. From this comparison, spectral changes resulting from the nuclear motions of molecules were identified.

1.5 Outline of Thesis Chapters

Chapter Two will outline the experimental methodologies and techniques used for this work: solution casting sample preparation, optical microscopy, NEXAFS, and Raman spectroscopy.

Chapter Three will discuss the computational approaches used in this research work. Density functional theory (DFT), transition potential density functional theory (TP-DFT), and the delta Kohn-Sham (ΔK-S) method will be discussed in detail. The effects of the two significant intermolecular interactions (π-π interactions and Rydberg-valence mixing) and linear dichroism on NEXAFS spectroscopy will be discussed in detail in **Chapters Four** through **Six**.

Chapter Four will present an analysis of PCP molecules with different aliphatic bridging groups. In this chapter, the effects of the π-π interactions between cofacial aromatic groups on NEXAFS spectra will be investigated. These relationships will be examined systematically by controlling the π-π interactions of the cofacial benzene rings by varying the length of the alkyl bridging groups of the PCP molecules. Experimental trends will then then be explored, reproduced, and rationalized through TP-DFT and ΔK-S computational methods.

In **Chapter Five**, the effects of linear dichroism and the effects of Rydberg quenching on the degree of Rydberg-valence mixing on NEXAFS spectra will be investigated by analyzing the carbon 1s NEXAFS spectra of *n*-alkanes (*n*-$C_{28}H_{58}$, *n*-$C_{32}H_{66}$ and *n*-$C_{40}H_{82}$) and considering their crystal structures (orthorhombic and monoclinic) and chain lengths.

Chapter Six (temperature dependence NEXAFS study of short chain orthorhombic *n*-$C_{28}H_{58}$) and **Chapter Seven** (contributions of molecular disorder to the carbon 1s NEXAFS spectra of short chain *n*-alkanes) investigate the effects of nuclear motion contribution and molecular disorder in the short chain orthorhombic *n*-alkanes on carbon 1s NEXAFS spectra and address the unusual spectral broadening observed in the molecular NEXAFS spectra (orthorhombic *n*-$C_{28}H_{58}$) presented in **Chapter Five**. Addressing the origins of spectral broadening in molecular NEXAFS spectroscopy will improve the scientific community's understanding of the fundamental phenomena underlying the interpretation and modeling of the NEXAFS spectra of

organic molecules. Finally, insights and conclusions drawn from these investigations will be discussed and presented in **Chapter Eight**.

1.6 References

1. Rightor, E. G.; Urquhart, S. G.; Hitchcock, A. P.; Ade, H.; Smith, A. P.; Mitchell, G. E.; Priester, R. D.; Aneja, A.; Appel, G.; Wilkes, G.; Lidy, W. E. Identification and Quantitation of Urea Precipitates in Flexible Polyurethane Foam Formulations by X-ray Spectromicroscopy. *Macromolecules* **2002,** *35* (15), 5873-5882.

2. Urquhart, S.; Ade, H. Trends in the Carbonyl Core (C 1s, O 1s) → π* C= O Transition in the Near-Edge X-ray Absorption Fine Structure Spectra of Organic Molecules. *The Journal of Physical Chemistry B* **2002,** *106* (34), 8531-8538.

3. Lipton-Duffin, J.; Miwa, J. A.; Urquhart, S. G.; Contini, G.; Cossaro, A.; Casalis, L.; Barth, J. V.; Floreano, L.; Morgante, A.; Rosei, F. Binding Geometry of Hydrogen-Bonded Chain Motif in Self-Assembled Gratings and Layers on Ag(111). *Langmuir* **2012,** *28* (40), 14291-14300.

4. Qaqish, S. E.; Urquhart, S. G.; Lanke, U.; Brunet, S. M. K.; Paige, M. F. Phase Separation of Palmitic Acid and Perfluorooctadecanoic Acid in Mixed Langmuir-Blodgett Monolayer Films. *Langmuir* **2009,** *25* (13), 7401-7409.

5. Iyer, G. R. S.; Wang, J.; Wells, G.; Bradley, M. P.; Borondics, F. Nanoscale Imaging of Freestanding Nitrogen Doped Single Layer Graphene. *Nanoscale* **2015,** *7* (6), 2289-2294.

6. Zhong, J.; Zhang, H.; Sun, X.; Lee, S. T. Synchrotron Soft X-ray Absorption Spectroscopy Study of Carbon and Silicon Nanostructures for Energy Applications. *Advanced Materials* **2014,** *26* (46), 7786-7806.

7. Hitchcock, A. P.; Berejnov, V.; Lee, V.; West, M.; Colbow, V.; Dutta, M.; Wessel, S. Carbon Corrosion of Proton Exchange Membrane Fuel Cell Catalyst Layers Studied by Scanning Transmission X-ray Microscopy. *Journal of Power Sources* **2014,** *266*, 66-78.

8. Ade, H.; Stoll, H. Near-Edge X-ray Absorption Fine-Structure Microscopy of Organic and Magnetic Materials. *Nature Materials* **2009,** *8* (4), 281-290.

9. Dhez, O.; Ade, H.; Urquhart, S. G. Calibrated NEXAFS Spectra of Some Common Polymers. *Journal of Electron Spectroscopy and Related Phenomena* **2003,** *128* (1), 85-96.

10. Ade, H.; Urquhart, S. G. NEXAFS Spectroscopy and Microscopy of Natural and Synthetic Polymers. In *Chemical Applications of Synchrotron Radiation: Part I: Dynamics and VUV Spectroscopy Part II: X-Ray Applications*, pp. 285-355. World Scientific: Singapore, **2002**.

11. Ney, A.; Ney, V.; Ollefs, K.; Schauries, D.; Wilhelm, F.; Rogalev, A. X-Ray Linear Dichroism: An Element-Selective Spectroscopic Probe for Local Structural Properties and Valence. *Journal of Surfaces and Interfaces of Materials* **2014,** *2* (1), 14-23.

12. Baio, J. E.; Jaye, C.; Fischer, D. A.; Weidner, T. High-Throughput Analysis of Molecular Orientation on Surfaces by NEXAFS Imaging of Curved Sample Arrays. *ACS Combinatorial Science* **2014,** *16* (9), 449-453.

13. Rossi, G.; d'Acapito, F.; Amidani, L.; Boscherini, F.; Pedio, M. Local Environment of Metal ions in Phthalocyanines: K-Edge X-ray Absorption Spectra. *Physical Chemistry Chemical Physics* **2016,** *18* (34), 23686-23694.

14. Patel, S. N.; Su, G. M.; Luo, C.; Wang, M.; Perez, L. A.; Fischer, D. A.; Prendergast, D.; Bazan, G. C.; Heeger, A. J.; Chabinyc, M. L.; Kramer, E. J. NEXAFS Spectroscopy Reveals the Molecular Orientation in Blade-Coated Pyridal[2,1,3]Thiadiazole-Containing Conjugated Polymer Thin Films. *Macromolecules* **2015,** *48* (18), 6606-6616.

15. Marchetto, H.; Schmidt, T.; Groh, U.; Maier, F. C.; Levesque, P. L.; Fink, R. H.; Freund, H. J.; Umbach, E. Direct Observation of Epitaxial Organic Film Growth: Temperature-Dependent Growth Mechanisms and Metastability. *Physical Chemistry Chemical Physics* **2015,** *17* (43), 29150-29160.

16. Masnadi, M.; Urquhart, S. G. Indirect Molecular Epitaxy: Deposition of *n*-Alkane Thin Films on Au Coated NaCl(001) and HOPG(0001) Surfaces. *Langmuir* **2013,** *29* (21), 6302-6307.

17. Fu, J.; Urquhart, S. G. Effect of Chain Length and Substrate Temperature on the Growth and Morphology of *n*-Alkane Thin Films. *Langmuir* **2007,** *23* (5), 2615-2622.

18. Urquhart, S. G.; Lanke, U. D.; Fu, J. Characterisation of Molecular Orientation in Organic Nanomaterials by X-ray Linear Dichroism Microscopy. *International Journal of Nanotechnology* **2008,** *5* (9-12), 1138-1170.

19. Fu, J.; Urquhart, S. G. Linear Dichroism in the X-ray Absorption Spectra of Linear *n*-Alkanes. *The Journal of Physical Chemistry A* **2005,** *109* (51), 11724-11732.

20. Leetmaa, M.; Ljungberg, M.; Lyubartsev, A.; Nilsson, A.; Pettersson, L. G. Theoretical Approximations to X-ray Absorption Spectroscopy of Liquid Water and Ice. *Journal of Electron Spectroscopy and Related Phenomena* **2010,** *177* (2-3), 135-157.

21. Urquhart, S. G.; Gillies, R. Matrix Effects in the Carbon 1s Near Edge X-ray Absorption Fine Structure Spectra of Condensed Alkanes. *The Journal of Chemical Physics* **2006,** *124* (23), 234704.

22. Bradeanu, I. L.; Flesch, R.; Kosugi, N.; Pavlychev, A. A.; Ruhl, E. Carbon 1s $\rightarrow \pi^*$ Excitation in Variable Size Benzene Clusters. *Physical Chemistry Chemical Physics* **2006,** *8* (16), 1906-1913.

23. Teo, B. K. *EXAFS: Basic Principles and Data Analysis*. Springer Science & Business Media: Berlin, Germany, **2012**.

24. Behyan, S. Development of Surface Sensitivity in Scanning X-ray Microscopy and NEXAFS Spectroscopy of Organosulphur Compounds. PhD Thesis, University of Saskatchewan, Ecommons, **2013**.

25. Fu, J. Linear Dichroism in the NEXAFS Spectroscopy of *n*-Alkane Thin Films. PhD Thesis, University of Saskatchewan, Ecommons, **2006.**

26. Stohr, J. *NEXAFS Spectroscopy*. Springer -Verlag: Berlin, Germany, **1992**.

27. Hahner, G. Near Edge X-ray Absorption Fine Structure Spectroscopy As a Tool to Probe Electronic and Structural Properties of Thin Organic Films and Liquids. *Chemical Society Reviews* **2006,** *35* (12), 1244-1255.

28. Chen, J. G. NEXAFS Investigations of Transition Metal Oxides, Nitrides, Carbides, Sulfides and Other Interstitial Compounds. *Surface Science Reports* **1997,** *30* (1), 1-152.

29. Henderson, G.; Baker, D. R. Synchrotron Radiation: Earth, Environmental and Materials Sciences Applications. Mineralogical Association of Canada: Canada, **2002**.

30. Nefedov, A.; Woll, C. Advanced Applications of NEXAFS Spectroscopy for Functionalized Surfaces. In *Surface Science Techniques*, pp. 277-303. Bracco, G.; Holst, B., Eds. Springer Berlin Heidelberg: Berlin, Germany, **2013**.

31. Otero, E. Soft X-ray Spectroscopy of Organic and Organometallic Molecules and Polymers. PhD Thesis, University of Saskatchewan, Ecommons, **2008.**

32. Urquhart, S. G. Delocalization and Functional Group Fingerprinting in the Core Excitation Spectroscopy of Molecules and Polymers. PhD Thesis, McMaster University, **1997**.

33. Robin, M. B. Higher Excited States of Polyatomic Molecules. Academic Press: New York, USA, **1974**.

34. Theodosiou, C. E.; Inokuti, M.; Manson, S. T. Quantum Defect Values for Positive Atomic Ions. *Atomic Data and Nuclear Data Tables* **1986,** *35* (3), 473-486.

35. Urquhart, S. G.; Gillies, R. Rydberg-Valence Mixing in the Carbon 1s Near-Edge X-ray Absorption Fine Structure Spectra of Gaseous Alkanes. *The Journal of Physical Chemistry A* **2005,** *109* (10), 2151-2159.

36. Kosugi, N. Spin-Orbit and Exchange Interactions in Molecular Inner Shell Spectroscopy. *Journal of Electron Spectroscopy and Related Phenomena* **2004,** *137*, 335-343.

37. Classification of X-ray Polarization. http://hyperphysics.phy-astr.gsu.edu/hbase/phyopt/polclas.html (accessed on 08th March 2018).

38. Masnadi, M. Kinetic and Thermodynamic of *n*-Alkane Thin Film Epitaxial Growth. PhD Thesis, University of Saskatchewan, Ecommons, **2013**.

39. Perera, S. D. Effect of Intermolecular Interactions on the Carbon 1s Near Edge X-ray Absorption Fine Structure (NEXAFS) Spectroscopy of *n*-Alkanes. MSc Thesis, University of Saskatchewan, Ecommons, **2012**.

40. Hastie, G. P.; Johnstone, J.; Roberts, K. J.; Fischer, D. Examination of the Structure and Melting Behaviour of Thin film *n*-Alkanes Using Ultra-Soft Polarised Near-Edge X-ray Absorption Spectroscopy. *Journal of the Chemical Society, Faraday Transactions* **1996,** *92* (5), 783-789.

41. Urquhart, S. G.; Hitchcock, A. P.; Smith, A. P.; Ade, H.; Rightor, E. G. Inner-Shell Excitation Spectroscopy of Polymer and Monomer Isomers of Dimethyl Phthalate. *The Journal of Physical Chemistry B* **1997,** *101* (13), 2267-2276.

42. Hitchcock, A. P.; Dynes, J. J.; Johansson, G.; Wang, J.; Botton, G. Comparison of NEXAFS Microscopy and TEM-EELS for Studies of Soft Matter. *Micron* **2008,** *39* (6), 741-748.

43. Cooney, R. R.; Urquhart, S. G. Chemical Trends in the Near-Edge X-ray Absorption Fine Structure of Monosubstituted and Para-Bisubstituted Benzenes. *The Journal of Physical Chemistry B* **2004,** *108* (47), 18185-18191.

44. Schmidt, N.; Wenzel, J.; Dreuw, A.; Fink, R. H.; Hieringer, W. Matrix Effects in the Carbon 1s Photoabsorption Spectra of Condensed Naphthalene. *The Journal of Chemical Physics* **2016,** *145* (23), 234307.

45. Flesch, R.; Serdaroglu, E.; Blobner, F.; Feulner, P.; Brykalova, X. O.; Pavlychev, A. A.; Kosugi, N.; Ruhl, E. Gas-to-Solid Shift of Carbon 1s Excited Benzene. *Physical Chemistry Chemical Physics* **2012,** *14* (26), 9397-9402.

46. Ma, Y.; Chen, C.; Meigs, G.; Randall, K.; Sette, F. High-Resolution K-Shell Photoabsorption Measurements of Simple Molecules. *Physical Review A* **1991,** *44* (3), 1848-1858.

47. Schirmer, J.; Trofimov, A.; Randall, K.; Feldhaus, J.; Bradshaw, A.; Ma, Y.; Chen, C.; Sette, F. K-Shell Excitation of the Water, Ammonia, and Methane Molecules Using High-Resolution Photoabsorption Spectroscopy. *Physical Review A* **1993,** *47* (2), 1136-1147.

48. Remmers, G.; Domke, M.; Kaindl, G. Vibrationally Resolved Carbon Core Excitations in Alkane Molecules. *Physical Review A* **1993,** *47* (4), 3085-3091.

49. Ueda, K.; Okunishi, M.; Chiba, H.; Shimizu, Y.; Ohmori, K.; Sato, Y.; Shigemasa, E.; Kosugi, N. Rydberg-Valence Mixing in the Carbon 1s Excited States of CH_4 Probed by Electron Spectroscopy. *Chemical Physics Letters* **1995,** *236* (3), 311-317.

50. Stöhr, J.; Outka, D.; Baberschke, K.; Arvanitis, D.; Horsley, J. Identification of C-H Resonances in the K-Shell Excitation Spectra of Gas-Phase, Chemisorbed, and Polymeric Hydrocarbons. *Physical Review B* **1987,** *36* (5), 2976-2979.

51. Hitchcock, A.; Newbury, D.; Ishii, I.; Stöhr, J.; Horsley, J.; Redwing, R.; Johnson, A.; Sette, F. Carbon K-Shell Excitation of Gaseous and Condensed Cyclic Hydrocarbons: C_3H_6, C_4H_8, C_5H_8, C_5H_{10}, C_6H_{10}, C_6H_{12}, and C_8H_8. *The Journal of Chemical Physics* **1986,** *85* (9), 4849-4862.

52. Bagus, P.; Weiss, K.; Schertel, A.; Wöll, C.; Braun, W.; Hellwig, C.; Jung, C. Identification of Transitions into Rydberg States in the X-ray Absorption Spectra of Condensed Long-Chain Alkanes. *Chemical Physics Letters* **1996,** *248* (3-4), 129-135.

53. Weiss, K.; Bagus, P.; Wöll, C. Rydberg Transitions in X-ray Absorption Spectroscopy of Alkanes: The Importance of Matrix Effects. *The Journal of Chemical Physics* **1999,** *111* (15), 6834-6845.

54. Schöll, A.; Fink, R.; Umbach, E.; Mitchell, G.; Urquhart, S.; Ade, H. Towards a Detailed Understanding of the NEXAFS Spectra of Bulk Polyethylene Copolymers and Related Alkanes. *Chemical Physics Letters* **2003,** *370* (5-6), 834-841.

55. Zou, Y.; Araki, T.; Appel, G.; Kilcoyne, A. L. D.; Ade, H. Solid State Effects in the NEXAFS Spectra of Alkane-Based van der Waals Crystals: Breakdown of Molecular Model. *Chemical Physics Letters* **2006,** *430* (4), 287-292.

56. Swaraj, S.; Ade, H. Differences in NEXAFS of Odd/Even Long Chain *n*-Alkane Crystals. *Journal of Electron Spectroscopy and Related Phenomena* **2013,** *191*, 60-64.

57. Nakajima, R.; Stöhr, J.; Idzerda, Y. U. Electron-Yield Saturation Effects in L-Edge X-ray Magnetic Circular Dichroism Spectra of Fe, Co, and Ni. *Physical Review B* **1999,** *59* (9), 6421-6429.

58. Schwartz, C. P.; Uejio, J. S.; Saykally, R. J.; Prendergast, D. On the Importance of Nuclear Quantum Motions in Near Edge X-ray Absorption Fine Structure Spectroscopy of Molecules. *The Journal of Chemical Physics* **2009,** *130* (18), 184109.

59. Nilsson, A.; Pettersson, L. G. The Structural Origin of Anomalous Properties of Liquid Water. *Nature Communications* **2015,** *6*, 8998.

60. Uejio, J. S.; Schwartz, C. P.; Saykally, R. J.; Prendergast, D. Effects of Vibrational Motion on Core-Level Spectra of Prototype Organic Molecules. *Chemical Physics Letters* **2008,** *467* (1-3), 195-199.

61. Fransson, T.; Zhovtobriukh, I.; Coriani, S.; Wikfeldt, K. T.; Norman, P.; Pettersson, L. G. Requirements of First-Principles Calculations of X-ray Absorption Spectra of Liquid Water. *Physical Chemistry Chemical Physics* **2016,** *18* (1), 566-583.

Chapter 2 Experimental

2.1 Sample Candidates

***Linear n-Alkanes*:** Used as a model system to study the effects of Rydberg quenching on the degree of Rydberg-valence mixing on the NEXAFS spectra of saturated molecules. Within this study, the effects of linear dichroism and nuclear motion contribution on the NEXAFS spectra were also examined. The linear *n*-alkanes used in this study are *n*-tetracontane (*n*-$C_{40}H_{82}$, 97+%), *n*-dotriacontane (*n*-$C_{32}H_{66}$, 98%), *n*-octacosane (*n*-$C_{28}H_{58}$, 99%), *n*-tetracosane (*n*-$C_{24}H_{50}$, 99%), and *n*-tricosane (*n*-$C_{23}H_{48}$, 99%). The two shortest chain *n*-alkanes, *n*-tetracosane (*n*-$C_{24}H_{50}$, 99%) and *n*-tricosane (*n*-$C_{23}H_{48,}$ 99%), were purchased from Sigma-Aldrich and the rest were purchased from Alfa Aesar. All *n*-alkanes were used as received without further purification.

***[n,n] Paracyclophanes (PCPs)*:** Used as a model system to study the effects of π-π interactions on the NEXAFS spectra of unsaturated molecules. The [n,n]PCPs used in this research work were [2,2]PCP (Sigma-Aldrich 97%), [5,5]PCP (Sigma-Aldrich), and [3,3]PCP (>95%). [3,3]PCP was obtained from Prof. Henning Höpf (Technische Universität Braunschweig, Germany, 2014). The structures of both [2,2] and [3,3]PCP were confirmed by Nuclear Magnetic Resonance (NMR) spectroscopy (see **A.1**). However, the NMR spectrum of the commercially available [5,5] PCP did not match its chemical structure (see **A.1**). Therefore, the [5,5]PCP sample was not used in this work.

2.2 Sample Preparation

n-Alkanes

The effects of Rydberg quenching on the degree of Rydberg-valence mixing on NEXAFS spectra were studied as a function of *n*-alkane chain length in well-defined crystalline polymorphs (orthorhombic and monoclinic). Isolating different crystalline polymorphs for each *n*-alkane was necessary for the project. The *n*-alkane powders are usually polycrystalline. Based on that, the starting materials (powder form of *n*-alkanes) are likely to give a mixture of crystalline structures for specific *n*-alkane chain lengths. Therefore, *n*-alkane single crystals were prepared from the starting *n*-alkane powder in order to obtain alkane with well-defined crystalline polymorphs. Specific crystalline polymorphs of each *n*-alkane chain length were identified via the internal angles of the *n*-alkane single crystals by optical microscopy. Solution casting was used to prepare dispersed arrays of *n*-alkane single crystals. For each *n*-alkane chain length, the solution casting

solvent and evaporation temperatures were optimized in order to preferentially isolate orthorhombic and monoclinic crystals of each *n*-alkane. Solution casting sample preparation conditions for each *n*-alkane are shown in **Table 2.1**.

Table 2.1: Sample preparation conditions for *n*-alkane crystals.

n-Alkane	Solvent	Substrate for Spectroscopic Measurements	Crystal Structure	*Solvent Evaporation Temperature
n-$C_{40}H_{82}$	Toluene	100 nm Si_3N_4 window	Orthorhombic	~ 8 °C
			Monoclinic	~ 25 °C
n-$C_{32}H_{66}$	Isopropyl alcohol	100 nm Si_3N_4 window	Orthorhombic	~ 8 °C
			Monoclinic	~ 25 °C
n-$C_{28}H_{58}$	Isopropyl alcohol	100 nm Si_3N_4 window	Orthorhombic	~ 8 °C
			Monoclinic	~ 25 °C
n-$C_{24}H_{50}$	Methanol	30 nm SiO layer on 100 nm Si_3N_4 window	Triclinic[#]	~ 8 °C
n-$C_{23}H_{48}$	Methanol	30 nm SiO layer on 100 nm Si_3N_4 window	Orthorhombic[#]	~ 8 °C

Notes: * The temperature ~ 8 °C was obtained inside the refrigerator and the temperature ~ 25 °C is the room temperature. [#]The crystal morphologies studied are unstable at room temperature, therefore, crystal structures for *n*-$C_{24}H_{50}$ and *n*-$C_{23}H_{48}$ alkanes were obtained from the literature.[1]

For solution casting, *n*-alkanes were first dissolved in a suitable solvent with a mass/volume ratio of 1.0 mg/2.00 ml and stirred at 50 °C. A drop of the solution was then placed on a 100 nm low stress Si_3N_4 window (Norcada Inc.), and the solvent subsequently evaporated as shown in **Figure 2.1**.

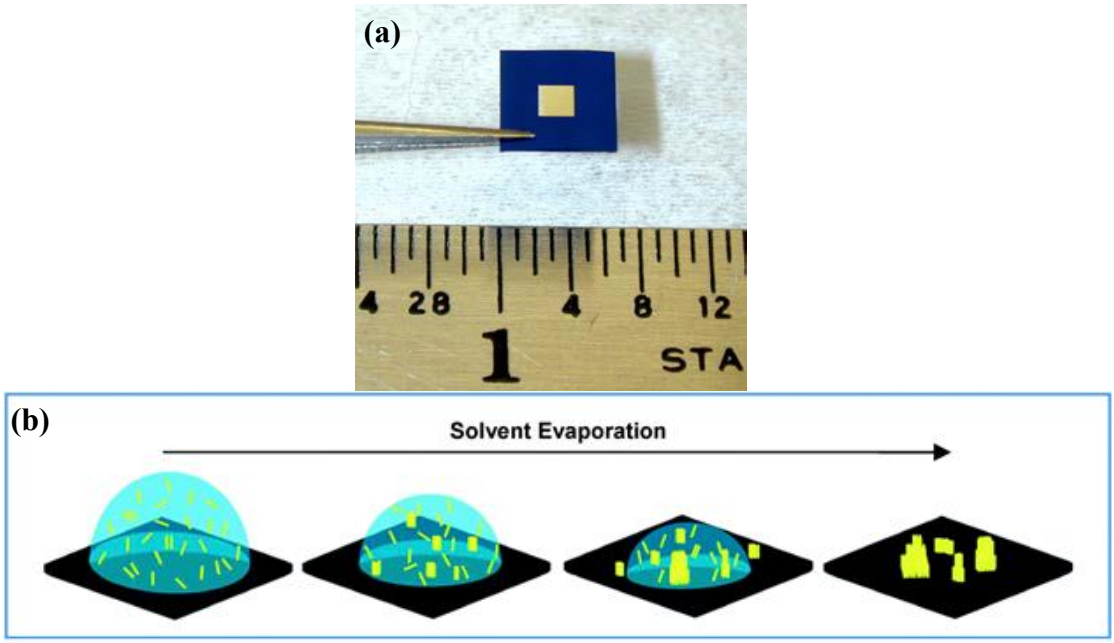

Figure 2.1: (a) Image of a typical Si_3N_4 window used as a substrate for *n*-alkane crystals. (b) Illustration of *n*-alkane crystals formed from the solution casting method.

[n,n]PCP

The effects of π-π interactions on NEXAFS spectra were studied as a function of benzene-benzene separation distance in PCP molecules. Structures of the PCP molecules studied are shown in **Figure 4.3** in **Chapter 4**. For a given PCP molecule, benzene-benzene separation distance is fixed and the benzene-benzene separation distance is obtained from the published literature.[2-4] [n,n] PCPs samples were prepared by pressing PCP powders onto clean indium foil substrates (5 × 5 mm squares).

2.3 Sample Characterization by Optical Microscopy (OM)

In this work, a standard optical reflection microscope (Nikon Eclipse ME600, with a Q-Imaging CCD camera) was used for initial characterization (shapes, orientations, morphologies, and internal angles of crystals) of *n*-alkane single crystals. In an optical microscope with a camera, the objective lens and camera lens are the two main lenses involved in the formation of a specimen image. A schematic diagram of an optical microscope is shown in **Figure 2.2**.

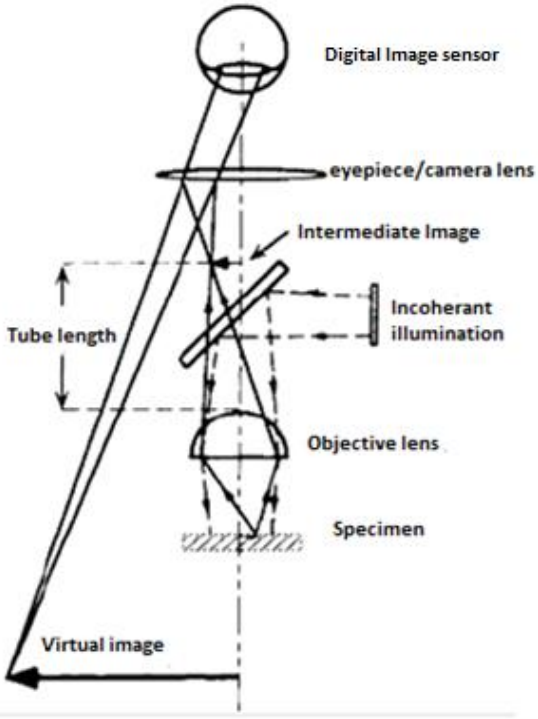

Figure 2.2: Schematic diagram of a standard optical reflection microscope. Figure reprinted from Reference 6 with permission.

As shown in **Figure 2.2**, a specimen is illuminated by a light source through the objective lens. The objective lens gathers that light to form an inverted image of the specimen (intermediate image). The intermediate image is then magnified by the camera lens, attached to the optical microscope, and forms a virtual image of the specimen on the digital imaging sensor. [5-6]

The spatial resolution of the optical microscope has a crucial impact on image quality. Spatial resolution is defined in **Equation 2.1**.

$$d_{min} = 1.22 \times \left(\frac{\lambda}{2NA}\right) \qquad \textbf{Equation 2.1}$$

In **Equation 2.1**, d_{min} is the smallest distance between the two points on a specimen that can be distinguished by the observer as separate entities. λ is the wavelength of illuminating light. *NA* is the numerical aperture of the objective lens ($NA = n\sin\alpha$ where n is the refractive index of medium between objective lens and specimen, and α is the half maximum angle from which the objective lens can collect light from the specimen). *NA* measures the ability of lens to gather light and resolve fine specimen details at a fixed objective distance. The spatial resolution and brightness of an image can be improved by using a larger numerical aperture.[6] The contrast of an image can be

manipulated by using many optical microscopy techniques, such as through the use of bright field, dark field, fluorescence, and polarization image modes.[7]

Bright Field Polarized Optical Microscopy

Optical microscope images used for this work were obtained under bright field polarized image mode.[6-7] A schematic diagram of polarized OM is shown in **Figure 2.3**.

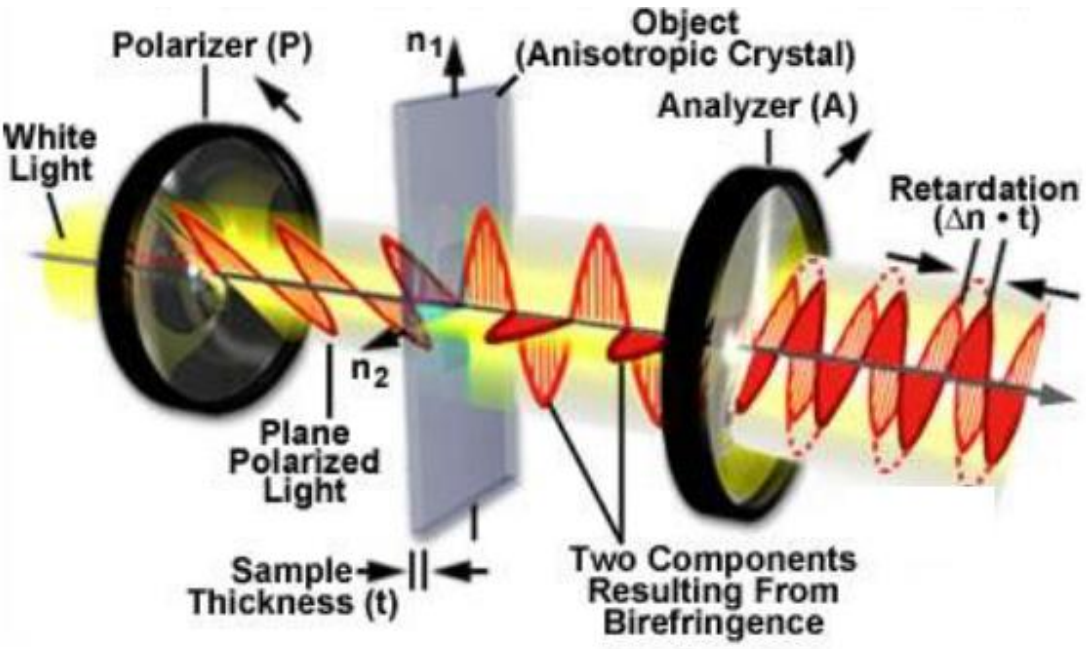

Figure 2.3: Schematic diagram of polarized optical microscopy. Figure reprinted from Reference 8 with permission.

In **Figure 2.3**,[8] a linear polarizer converts randomly polarized light from an incandescent source to a plane-polarized light with the electric field vector of the light restricted to a single direction. Then, the plane-polarized light passes through a birefringent specimen and the polarization direction is rotated by the sample. The polarization rotation is represented by the two components resulting from birefringence (see **Figure 2.3**). The light with rotated polarization passes through an analyzer. The analyzer only passes light in one plane so the image contrast relies on this rotation of plane polarized light. Birefringent specimens are usually anisotropic and this birefringence relies upon the refractive indexes of the specimen.[7] Therefore, if different areas of a specimen have different refractive indexes (like in a *n*-alkane single crystal), these different areas

will refract the plane-polarized light differently and, thus have different image intensities.[6] The image contrast due to refractive index also depends on the wavelength of light.[6]

2.4 NEXAFS Spectroscopy

X-rays are part of the electromagnetic spectrum, with a wavelength range of 10^{-8} - 10^{-11} meters, which corresponds to a photon energy range of 100 eV to 10^5 eV.[9] Wilhelm Konrad Röntgen discovered X-ray radiation in 1895 when they irradiated a metal surface with a beam of high energy electrons.[10] This process results in the ejection of core electrons from the anode metal atoms and the emission of X-ray radiation as metal core holes are refilled by upper level electrons. The energies of X-rays produced from this process depend on the anode material used, therefore, the wavelengths of radiation produced by this method varies from metal to metal. With few modifications, such X-ray tubes are still used in laboratories to generate X-rays today.[10] However, NEXAFS spectroscopy requires a tunable X-ray radiation source with a high photon flux and polarization control. Therefore, conventional X-ray sources are not sufficient for NEXAFS spectroscopy.

Bending Magnets (BM) and Insertion Devices (IDs) are two common sources used to generate synchrotron X-rays. These producing an intense and tunable X-rays with well-defined polarization properties. A general overview of synchrotron radiation is presented in §2.4.1, followed by an introduction to BMs and IDs in §2.4.1.1 and §2.4.1.2, respectively. Subsequent sections describe NEXAFS spectroscopy experimental procedures and present an overview of each beamline used in this work to obtain NEXAFS spectra.

2.4.1 Synchrotron Radiation

Synchrotron radiation is emitted when charged particles travelling at a relativistic speeds are accelerated radially.[11] A synchrotron radiation facility consists of four main sections: an electron gun, a linear accelerator (Linac), a booster ring, and a storage ring. A schematic diagram of a synchrotron facility and storage ring is shown in **Figure 2.4**.[11]

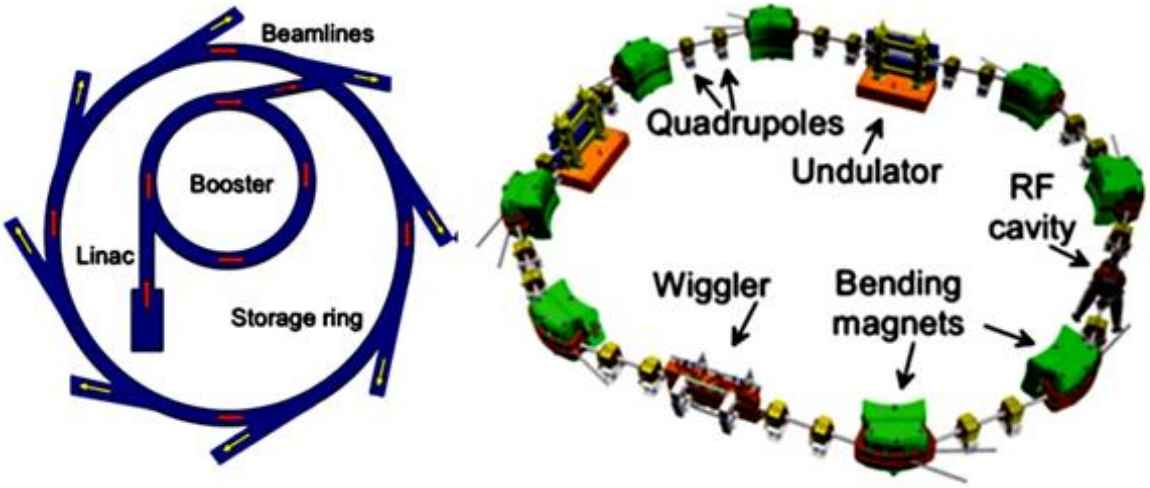

Figure 2.4: Schematic view of a synchrotron facility (left) and storage ring (right). Figure reprinted from Reference 11 with permission.

An electron gun injects bunches of electrons with energies of several tens of mega electron volts (MeV) into a Linac.[11] In a Linac, an electron beam is accelerated by a series of microwave radio frequency cavities and delivers it to the booster ring with an energy of several hundreds of MeV. In the booster ring, the electron beam is further accelerated until it reaches storage ring energy (a few GeV), at which time it is delivered to the storage ring.[11] The storage ring consists of a series of magnets in order to focus and bend the electron beam. Using BMs and straight linear sections of storage ring, the electron beam is forced to travel in a circular path. As the electron beam is forced to travel in a circular pathway, magnetic fields accelerate the relativistic charged particles in the storage ring and synchrotron light is produced (see right image in **Figure 2.4**). The energy of the electron beam decreases as radiation as emitted. Radio frequency (RF) cavities, installed in linear sections of the storage ring, are used to replenish the lost energy.[11]

First generation synchrotron facilities ran parasitically on high energy physics particle accelerators.[12-13] Second generation synchrotron facility were specifically built for producing synchrotron radiation using BMs.[12, 14] Third generation synchrotron facilities optimized the lattice structures of storage rings for insertion devices (undulators/wigglers).[12, 14] The NEXAFS experiments performed for this research were performed at the Canadian Light Source (CLS), a third generation synchrotron facility that uses wigglers, undulators, and bending magnets to generate synchrotron radiation.

The properties of the synchrotron X-ray radiation produced by each source (BMs, wigglers, or undulators) are characterized by their spectral distributions, flux, and brightness. Spectral distribution describes the photon energy range produced. Flux is the number of photons produced per unit of time per unit of bandwidth (0.1%) passing through a defined area.[11, 15-16] Using flux and spectral distribution, radiation brilliance can be determined using **Equation 2.2**. Brilliance describes how flux is distributed across a spatial and angular range (phase-space).

$$\textbf{Brilliance} = \frac{\textbf{(Flux)}}{\textbf{(solid angle of emission)(source area)}(I)\textbf{(spectral distribution)}} \qquad \textbf{Equation 2.2}$$

In addition to flux and spectral distribution, **Equation 2.2** also includes the variables solid angle of emission ($mrad^2$), source area, and electron current of the storage ring, *I*. The source area refers to the size of the electron beam used (mm^2). Brightness is similar to brilliance, but does not account for source area.

Although the beamlines used in this study did not use BMs to generate synchrotron light, it is important to introduce BMs in order to have a complete understanding of synchrotron radiation.[15-16] A schematic diagram of the radiation profiles, and spectral distribution/brightness curves of a BM and two insertion devices are shown in **Figure 2.5**.[15, 17]

2.4.1.1 Bending Magnet (BM) Sources

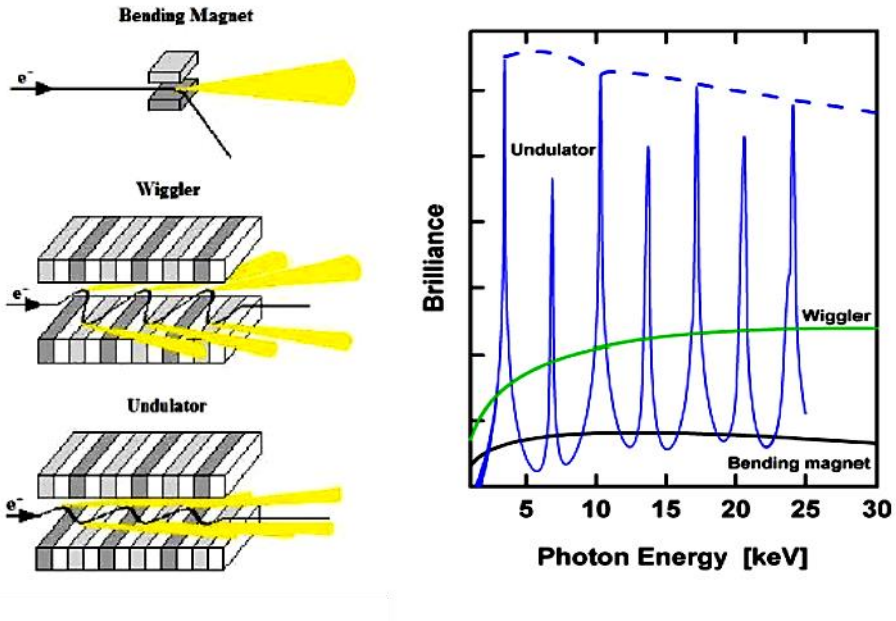

Figure 2.5: Schematic of the radiation profiles (left) and spectral distribution/brightness curves (right) of a bending magnet (BM) and the two types of insertion devices (IDs). Figure reprinted from References 15 and 17 with permission.

As shown in **Figure 2.5**, a BM is a single dipole magnet that causes a singularly curved electron trajectory and produces a cone of radiation emitted tangentially. BM emit linear and circular polarized radiation, and have a broad energy distribution.[11, 15] The linear polarized radiation is in plane of the ring, and circular polarized radiation is in above (left circular polarization) or below (right circular polarization) plane of the ring.[11, 15] However, the type of the polarization (left circular polarization vs right circular polarization) below/above the ring depends on the "handedness" of the synchrotron beam. For an example, in CLS, handedness is clockwise and left polarized radiation is in above plane of the ring.

2.4.1.2 Insertion Devices (IDs)

Insertion devices (IDs) are a series of magnets installed in the straight sections of a storage ring (see **Figure 2.4**). Wigglers and undulators are the two common IDs used in the synchrotron facility. These IDs are able to produce brighter synchrotron light than the BMs. The properties of

these IDs are characterized by the deflection parameter (K) which is given by **Equation 2.3** below.[11, 15-16]

$$K = {eB_{ID}\lambda_{ID}}/{2\pi m_e c} = 0.93\lambda_{ID}B_{ID} \qquad \textbf{Equation 2.3}$$

In **Equation 2.3**, e, m_e, and c are the charge of the electron, mass of the electron, and speed of light respectively. λ_{ID} (cm) is the period of the insertion device and B_{ID} is the peak magnetic field (T) of the insertion device.[11, 15] The value of K varies with the type of ID, and K affects the properties of the synchrotron light produced by the ID, including the maximum deflection angle of the particle beam, amplitude of the oscillation of particles in the beam, etc.

For IDs, the maximum deflection angle of the particle beam (θ_{max}) can be defined as:[11]

$$\theta_{max} = \left(\frac{K}{\gamma}\right) \qquad \textbf{Equation 2.4}$$

Where, $1/\gamma$ is the natural opening angle of the radiation and $\gamma = E/m_e c^2 = 1957\ E$ (GeV). E is the energy of the storage ring.[11]

Wigglers

Wigglers deflect electron beam periodically using strong magnetic fields and have larger deflection parameters (K>>1).[9, 11] The larger deflection parameters of wigglers result in larger oscillation amplitudes and produce larger cones of radiation ($\frac{K}{\gamma} >>> \frac{1}{\gamma}$) than BMs (see radiation profiles in **Figure 2.5**).[10-11, 15]

Undulators

Similar to the wigglers, undulators generate synchrotron radiation by deflecting the electron beam periodically using an array of magnets. However, unlike wigglers, undulators deflect the electron beam (K~1) using weak magnetic fields and generate smaller oscillation amplitudes ($\frac{K}{\gamma} \sim \frac{1}{\gamma}$) than wigglers.[9, 11] As a result, synchrotron radiation produced using an undulator has a narrower energy range (see undulator harmonics in **Figure 2.5**) than that of a wiggler. However, the useable X-ray energy range of an undulator can be tuned by varying the gap between the two rows of magnets and an undulator can produce harmonics. Linear undulators produce X-rays with linear polarization. To produce X-rays with different polarizations (circular, linear

inclined, linear horizontal, etc.), an elliptically polarized undulator (EPU) can be used.[18] A schematic diagram of an EPU is given in **Figure 2.6**.

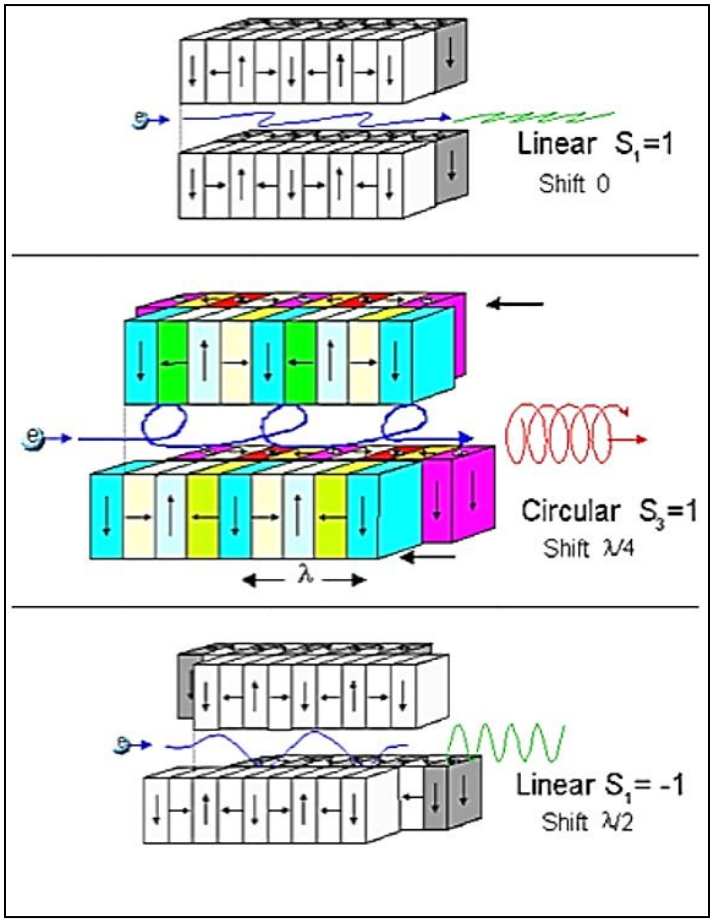

Figure 2.6: Schematic diagram of an elliptically polarized undulator (EPU). Figure reprinted from Reference 18 with permission.

An EPU consists of four quadrants of periodic magnets instead of the two rows in a linear undulator. A two quadrant row is placed above the electron path and a two quadrant row is placed below the electron path (see **Figure 2.6**). Within each row, one quadrant is fixed while the other can be moved longitudinally along the electron path. Consequently, the relative movements of the quadrants can be used to change the phases of the vertical and horizontal parts of the magnetic field and deliver X-rays with different degrees and characteristics of polarization. As shown in **Figure 2.6**, if there is no shift in the quadrants, the EPU produces horizontal linearly polarized light (top image of **Figure 2.6**). Circularly polarized light is produced using an equal amplitude shift in both the horizontal and vertical magnetic fields (middle image of **Figure 2.6**). If the two

rows are moved in an opposite directions, an EPU produces a linearly inclined polarized light (bottom image of **Figure 2.6**).[10, 18]

2.5 Measuring NEXAFS Spectra

2.5.1 X-ray Absorption and Subsequent Relaxation of a Core Excited Molecule

When incident X-ray radiation is absorbed by a molecule, short lived core excited states are formed. These core excited states can then undergo series of decay processes. The observable decay processes in the XAS are shown schematically in **Figure 2.7**.[19]

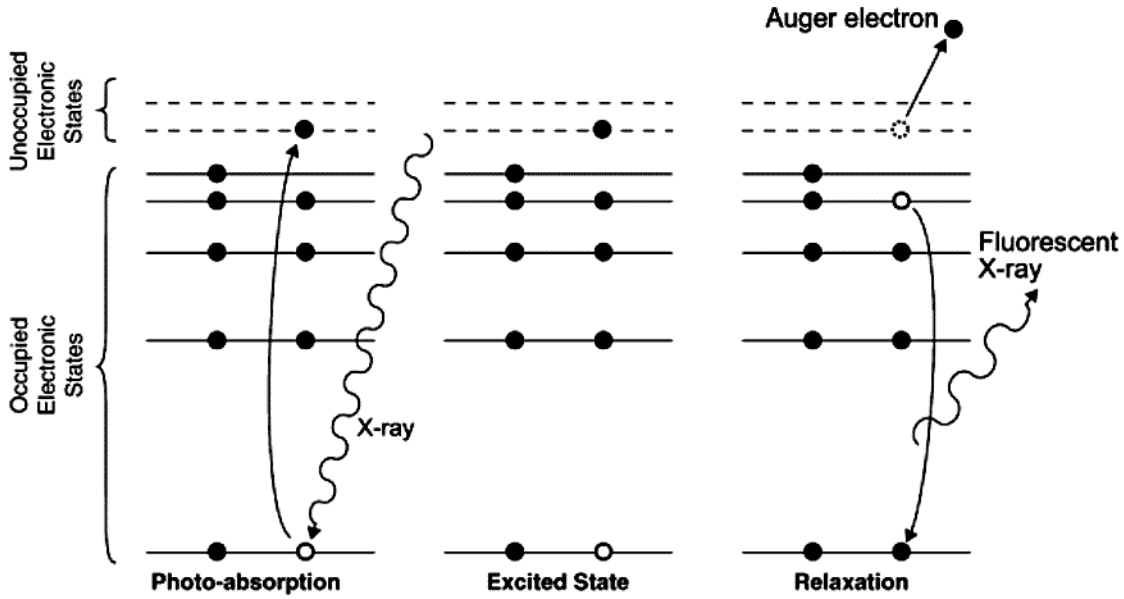

Figure 2.7: Schematic diagram of X-ray photon absorption and the subsequent relaxation of the excited molecule. Figure reprinted from Reference 19 with permission.

According to **Figure 2.7**, core excited states can decay by radiative mechanism such as fluorescence emission and non-radiative mechanism such as Auger emission. Florescence emission occurs when an electron refills a core hole and the excess energy is carried away as a photon. Auger emission occurs when a core hole is filled by an electron in an upper shell and the excess energy is carried away by the ejection of another electron, called an Auger electron.[13, 19]

2.5.2 Detection Techniques

NEXAFS spectra can be obtained either directly by measuring the transmitted X-ray photons through a sample, or indirectly by measuring the secondary processes that occur after the photo absorption, i.e. Auger electron emission, photoelectron emission, and fluorescence emission.[19] The most common detection modes of NEXAFS spectroscopy are shown in **Figure**

2.8. [19] However, discussion is limited to the transmission and total electron yield (TEY) detections, because those detection methods were the ones used in the experiments presented in this thesis.

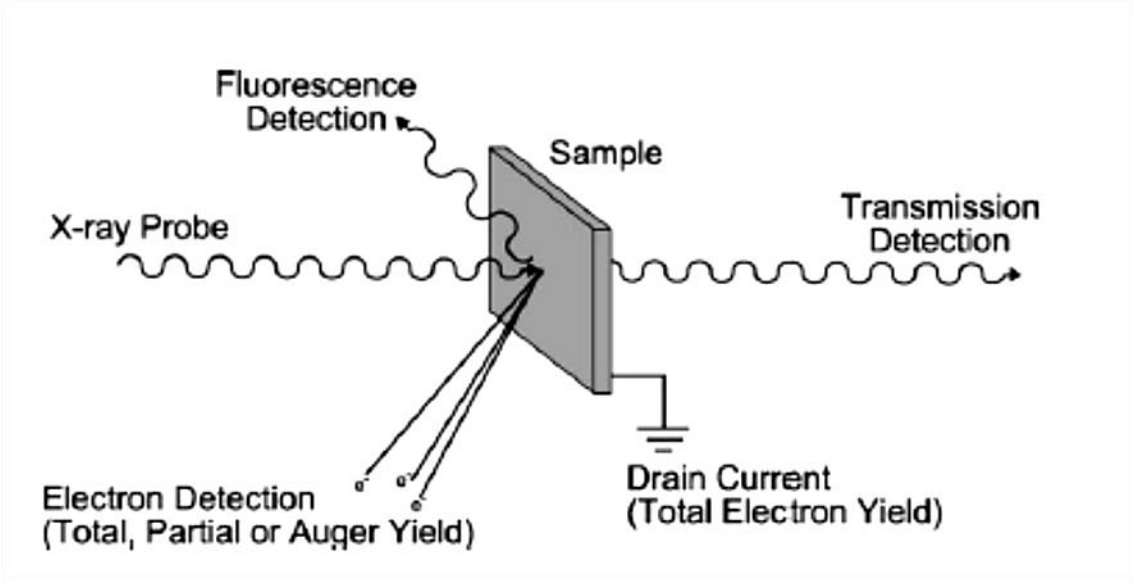

Figure 2.8: Schematic diagram of the most common measurement techniques used in NEXAFS spectroscopy. Figure reprinted from Reference 19 with permission.

2.5.2.1 Transmission Detection

In transmission detection mode, a thin sample is placed in between the X-ray source and a detector, and the transmitted photon flux passing through the sample is measured (see transmission detection mode in **Figure 2.8**). This detection mode is limited by the sample thickness; the sample must be thin enough for photons to penetrate and reach the detector. The transmitted signal is detected and plotted as a function of photon energy in the presence of a sample (I), and the incident signal is detected and plotted as a function of photon energy in the absence of the sample (I_0). The X-ray transmission spectrum is then obtained by calculating the optical density (OD) of the sample using Beer Lambert law.

$$OD = -ln\frac{I}{I_0} = \mu(E)\times\rho\times t \qquad \textbf{Equation 2.5}$$

In **Equation 2.5**, μ ($cm^2\ g^{-1}$) is the mass absorption coefficient, ρ ($g\ cm^{-3}$) is the density of the material, and t (cm) is the sample thickness. At a particular photon energy (E), μ and sample ρ depend on sample composition. The μ of a sample is related to its atomic absorption cross section as:[10]

$$\mu = \frac{N_A}{MW} \sum_i n_i \sigma_{xi}$$ **Equation 2.6**

Where N_A is the Avogadro number, σ_{xi} is the absorption cross section for the n_i atoms of each element i (see **Equation 1.1** for σ_{xi}), and MW is the molecular weight of the sample.[10]

2.5.2.2 Total Electron Yield (TEY) Mode

NEXAFS spectra can also be obtained indirectly by measuring the current of electrons emitted from a sample as a function of incident photon energy. This could be done in two ways. One is measuring the sample drain current generated from all the electrons that emerge from the sample surface by using a picoammeter (sample current).[19-21] The other method is directly measuring the electrons emitted from the sample surface by using an energy analyzer. [10, 20-21]

In this work, sample current Total Electron Yield (TEY) detection mode was used to obtain the XAS spectra of PCP in **Chapter 4**, therefore, this discussion is focused on the sample current TEY. TEY is a near surface/quasi-bulk sensitive detection mode. In TEY, the incident photon flux (I_0) can be detected by measuring the drain current from a gold mesh located upstream of the sample, and the sample drain current (I) is normalized with respect to the incident photon flux (I_0). The normalization equation for TEY is given below.

$$TEY = \frac{I}{I_0}$$ **Equation 2.7**

Since sample current TEY measures the drain current resulting from the emission of electrons from the sample, the reliability of the measurement depends on the conductivity of the sample. Therefore, non-conductive samples, like powdered PCPs must be mounted to a clean conductive substrate such as indium metal in order to facilitate sample current flow to the detector. Since this project focused on the carbon edge (280 - 320 eV), indium is a good conductive substrate to use as it is a soft metal that can support powders by imbedding.

2.5.3 Beam Lines Used to Obtain NEXAFS Spectroscopy

The Canadian Light Source (CLS) is located at the University of Saskatchewan in Saskatoon, Saskatchewan, Canada. NEXAFS spectra shown in this thesis were acquired from two different beamlines at the CLS: the SpectroMicroscopy (SM) beamline 10ID1[22] and the Spherical Grating Monochromator (SGM) beamline 11ID1[23]. Details of each beamline and their associated experimental techniques are reviewed in subsequent sections of this chapter.

2.5.3.1 SpectroMicroscopy (SM) Beamline

The X-ray source for the SM beam line is an Apple II Elliptically Polarized Undualtor (EPU). This EPU can deliver circular (left and right) and linear (horizontal, vertical, and inclined) polarizations by changing the relative positions of its four quadrants of periodic magnets (see §2.4.1.2 for EPU operation details). A schematic layout of the SM beamline is given in **Figure 2.9**.[22]

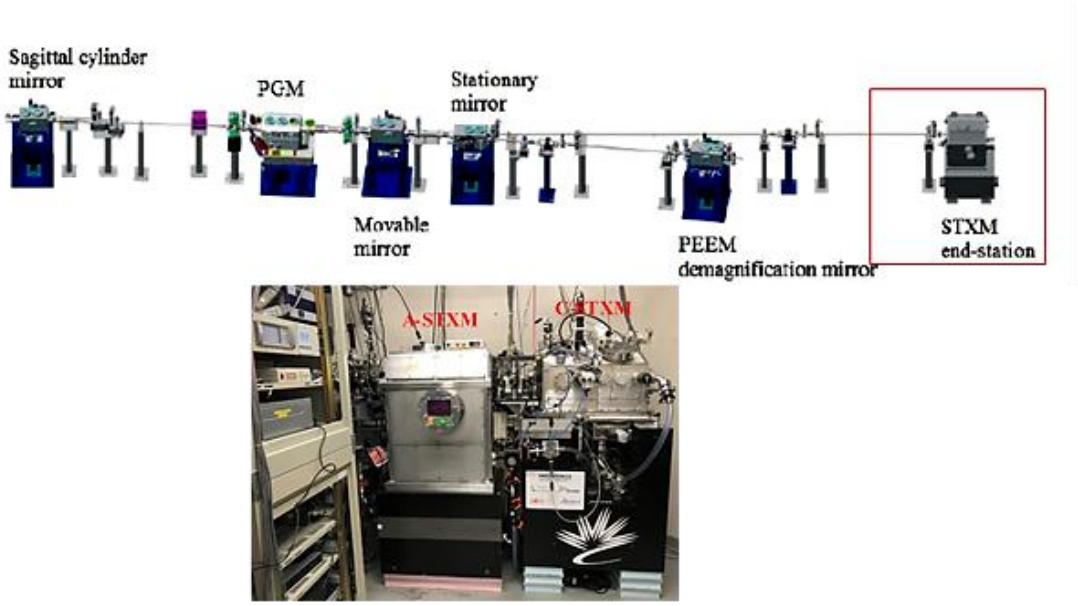

Figure 2.9: Layout of the SM beamline located at the CLS in Saskatchewan, Canada (top), and image of the two SM STXMs and the control cabinet, with the cryo-STXM in the right, beam downstream, side (bottom). Figure reprinted from Reference 22 with permission.

According to **Figure 2.9**, first, the X-ray beam produced by the EPU is horizontally deflected by a sagittal cylinder mirror and the beam is focused on the pre-mirrors of the Plane Grating Monochromator (PGM). The PGM of the SM beamline is equipped with three different gratings that covers an energy range of 100 - 2500 eV, making measurement of the carbon, nitrogen, and oxygen K-edge energies of a number of biological, environmental, and polymer samples accessible. Grating selection is based on the energy region required for an experiment. For instance, the 250 lines/mm grating is used to produce a monochromatic beam for low energy measurements (130 - 400 eV), such as carbon 1s NEXAFS measurements of organic materials.[22] After the PGM, the monochromatic X-ray beam is reflected using toroidal mirrors (see movable and stationary mirrors in **Figure 2.9**), and the beamline is split into two paths (see PEEM and

STXM in **Figure 2.9**). One of those paths directs the collimated light to the STXM chamber by focusing the X-ray beam through the exit slits.[22]

SM combines the chemical sensitivity of NEXAFS spectroscopy with the high spatial resolution (less than 30 nm) of X-ray imaging. **Chapters 5**, **6** and **7** of this work discusses the NEXAFS spectra of *n*-alkane single crystals and specifically **Chapter 5** relates them to the differences in crystalline environments (orthorhombic and monoclinic). In order to identify the crystal structures of the *n*-alkane single crystals, it was necessary to obtain high resolution images of alkane crystals as the internal angles of the *n*-alkane single crystals are different for the different crystal structures. For this reason, images and NEXAFS spectra were acquired from *n*-alkane single crystals using the Scanning Transmission X-ray microscopy (STXM) of the SM beamline at CLS.

2.5.3.1.1 Scanning Transmission X-ray Microscope (STXM)

STXM is a bulk sensitive photon transmission technique that can be used to examine wet or dry specimens. It is usually operated under a helium atmosphere or under vacuum (100 mtorr, or high vacuum). As mentioned in §2.5.2.1, spectroscopic output of the transmission detection technique is limited by sample thickness, and the transmission depends on photon energy. For instance, carbon edge measurements (280 - 320 eV) were typically done using sample thicknesses of approximately 100 nm.

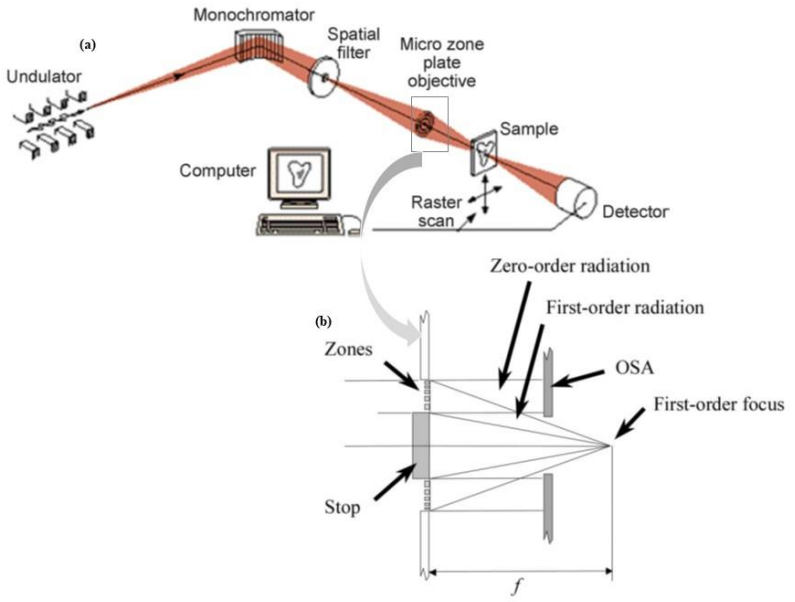

Figure 2.10: (a) Schematic Diagram of the instrumental setup of a zone-plate-based STXM, and (b) Schematic diagram of the first order X-ray beam focus used for STXM. Figures reprinted from References 24 and 25 with permission.

The instrumental setup of the zone-plate-based STXM is shown in **Figure 2.10**.[24-25]As shown in **Figure 2.10**, monochromatic X-rays produced by the PGM (monochromator in the top image in Figure **2.10**) pass through the spatial filter and a Fresnel zone plate (FZP) focused the beam. A magnified view of the FZP and focusing scheme of the STXM is shown in **Figure 2.10 (b)**. A FZP is a circular transmission diffraction grating with an alternatively transparent and opaque concentric rings. The FZP zone width decreases with increasing ring radius. The FZP outermost zone width determines the spatial resolution of a STXM image.

Moreover, in order to focus the X-ray beam onto the smallest possible spot on the sample, the FZP, Order Sorting Aperture (OSA), and sample stage must be aligned. Specifically, the OSA must be aligned with the FZP both transversely and longitudinally.[25] An interferometer controller is used to aid in the alignment of the FZP and the sample stage. The interferometer gives precise transverse position measurements of the FZP relative to the sample and helps to maintain long term FZP position stability. In addition to alignment, high quality STXM images require the removal of undiffracted and high order diffracted X-rays. Undiffracted light (zero order) and the high order diffracted X-rays (2^{nd} order and up) increase the background signal. Therefore, the central stop of the FZP excludes zero order light and the OSA blocks higher order diffracted X-rays.[24-25] This lets the first order X-rays to fall into the sample focus. The intensity of the

transmitted X-ray beam that passes through the sample is then measured as a function of photon energy and sample position using a detector mounted behind the sample.[24-25]

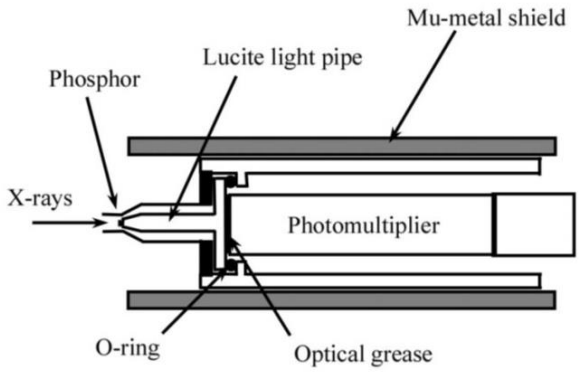

Figure 2.11: Schematic diagram of the soft X-ray STXM detector. Figure reprinted from Reference 25 with permission.

As shown in **Figure 2.11**, the detector consists of a phosphor, a Lucite light pipe, and a photomultiplier tube (PMT). The phosphorous screen converts transmitted X-ray photons into visible photons and the PMT measures the visible photons at a count rate of tens of megahertz (MH_Z). Photon counts are then used to generate transmission images and spectra for the sample.[24-25]

The cryo-STXM (c-STXM) at the CLS is operated similar to ambient STXM (a-STXM), but the sample in the c-STXM can be cooled to cryogenic temperatures. Moreover, the c-STXM is operated under high vacuum, whereas the ambient soft X-ray STXM is operated under helium or low vacuum conditions.[26]

2.5.3.1.2 Data Acquisition Modes of STXM

Spectromicroscopy can provide both X-ray transmission images and NEXAFS spectra. Transmission images are used to navigate to important areas of a sample. Areas of interest are then scanned by scanning the monochromator across the absorption edge to obtain NEXAFS spectra. Point scan, line scan, and image sequence scans are the three major STXM scanning modes used to obtain NEXAFS spectra.

Point scan

In a point scan, the X-ray beam is focused on a specific spot (x,y) on the sample and NEXAFS spectra are obtained by scanning the monochromator across the energy region of the absorption edge.[10] Point scans can generate NEXAFS spectra much faster than line or image sequence scans because they scan over a specific point rather than a whole area of the sample. Since point scans scan a single point, they do not tell anything about the nature of heterogeneous samples. However, point scans are an efficient means of acquiring the NEXAFS spectrum for homogeneous sample.

Line scan

In a line scan, the X-ray beam is focused on specific area of the sample and raster scanned over a line across the sample. As shown in **Figure 2.12**,[27] a line in the line scan can extend from the sample (I) to an open area (I_0) in the STXM image (red line in the **Figure 2.13a**). Then, this line is repeated as the monochromator setup over the energy region of the absorption edge. In the line scan, the transmission intensity of the I and I_0 has been integrated and converted to optical density (OD) using **Equation 2.5**. The OD spectrum generated by the line scan is shown in **Figure 2.12b**.

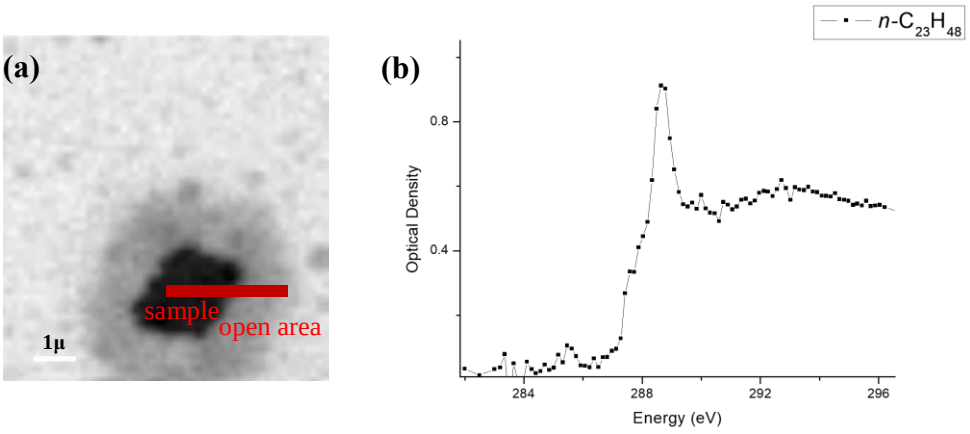

Figure 2.12: (a) STXM image obtained at 300 eV for *n*-tricosane (*n*-$C_{23}H_{48}$), (b) NEXAFS spectrum obtained from the line scan. Figure reprinted from Reference 27 with permission.

Image sequence scan

In this mode, a series of images are taken, scanning the absorption edge energy region, over a small area of interest. Once images have been collected over the entire X-ray energy region of interest, a NEXAFS spectrum is generated by integrating the transmitted X-ray photon signals

coming from different areas of images as a function of X-ray energy.[10, 22] Image sequence scans for *n*-octacosane (*n*-$C_{28}H_{58}$) alkane are shown in **Figure 2.13**.[27]

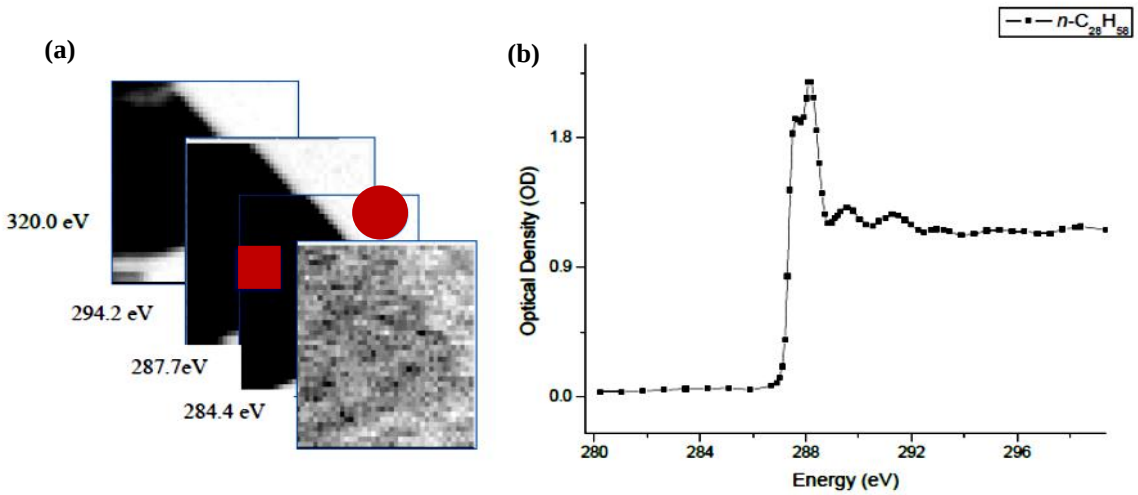

Figure 2.13: (a) A sequence of *n*-octacosane (*n*-$C_{28}H_{58}$) images obtained at different X-ray energies, and (b) carbon 1s NEXAFS spectra extracted from the image sequence of the *n*-octacosane (*n*-$C_{28}H_{58}$) sample. Figure reprinted from Reference 27 with permission.

In order to obtain a good NEXAFS spectrum, the scanning area of the image should include both sample and empty area of the sample. These provide a measure of both the I and I_0 signals simultaneously and across the X-ray entire energy region of interest. **Figure 2.13a** shows images recorded from different energy regions of the carbon edge, representing the pre edge region (~284. 4 eV), the carbon 1s → $\sigma^*_{C\text{-}H}$ transition (~287.7 eV) region, the carbon 1s → $\sigma^*_{C\text{-}C}$ transition (~294.2 eV) region, and the carbon 1s → continuum (~320.0 eV) region. The areas indicated by the circle and square in the STXM image of **Figure 2.13a** were used to obtain the incident (I_0) and transmission (I) spectra for the sample.[27] The transmission spectra were converted to optical density with Beer's law (**Equation 2.5**).

2.5.3.1.3 Radiation Sensitivity of the Carbon 1s NEXAFS Spectra of *n*-Alkanes

N-Alkanes are very sensitive to the X-ray radiation.[24, 28-30] Therefore, radiation damage is a significant issue in carbon 1s NEXAFS investigations of *n*-alkanes. Different scanning modes (i.e. point, line, and image sequence scans) have different radiation damage impacts on the samples.[24] Spectra are not trustworthy if taken from a sample that has been damaged by X-rays.

Therefore, experimental conditions are optimized in order to obtain a quality NEXAFS spectra of the *n*-alkanes, with minimum radiation damage.

Radiation damage can be seen in two ways. It can manifest in the form of additional peaks, which could be the result of the making or breaking of bonds within the molecule, facilitated by the X-ray radiation. For example, in carbon molecules such as *n*-alkanes, carbon-carbon double bonds can be formed from carbon single bonds.[28] In such situations, radiation damage can be identified by observing the peak around 285 eV for carbon 1s → $\pi^*_{C=C}$ transition to test for the formation of carbon-carbon double bond. Sample mass loss during the spectroscopic measurement also indicates radiation damage.[28] Mass loss can be identified by examining the optical density drop in the high energy (continuum) region of the spectrum.[28]

All of the *n*-alkane single crystals NEXAFS spectra presented in **Chapters 5**, **6** and **7** were obtained using the image sequence scan mode. Experimental conditions of this mode, such as energy point spacing and dwell time, were optimized to minimize the radiation exposure. Furthermore, each scan was obtained from a fresh area of the sample and the beam was defocused to a diameter of 150 nm to reduce the radiation dose.

2.5.3.1.4 Calibration of the Energy Scale for Carbon 1s NEXAFS Spectra of *n*-Alkanes

Good energy stability in the monochromator must be maintained to obtain reliable NEXAFS spectra. The energy scale of the *n*-alkane single crystal NEXAFS spectra presented in **Chapters 5** and **7** were calibrated by introducing CO_2 into the STXM chamber with sample in place. From this way, NEXAFS spectra of both the CO_2 gas and the sample were measured simultaneously in the STXM chamber and track down the exact energy shift experienced by the sample during the NEXAFS measurements. The following peaks of the CO_2 gas NEXAFS spectrum were used to calibrate the energy scale of the NEXAFS spectra of carbon samples (alkane). Carbon 1s → 3s (v=0) and carbon 1s → 3p (v=0) transitions were set to 292.74 eV and 294.96 eV, respectively, after Ma *et al*.[31]

2.5.3.2 Spherical Grating Monochromator (SGM) Beamline

SGM is a soft X-ray beamline located at the Canadian Light Source. For this work, XAS measurements of the PCP molecules described in **Chapter 4** were obtained under ultra-high vacuum using the SGM endstation and the TEY detection mode (see §2.5.2.2 for TEY**)**. A schematic diagram of the SGM beamline is given in **Figure 2.14**.[32]

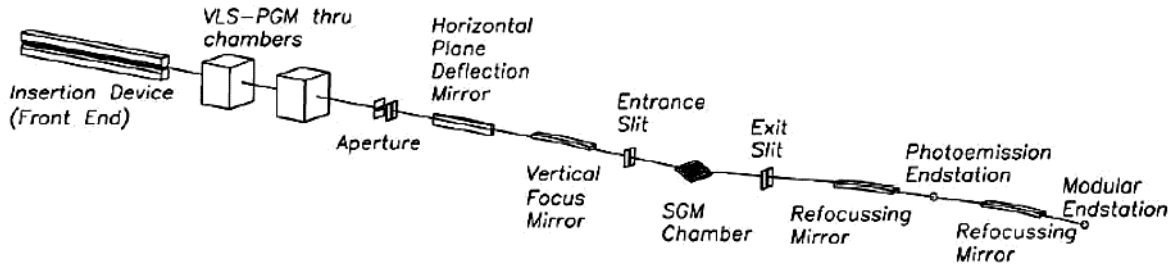

Figure 2.14: Schematic diagram of the layout of the Spherical Grating Monochromator (SGM) beamline at Canadian Light Source, Saskatchewan, Canada. Figure reprinted from Reference 32 with permission.

As shown in **Figure 2.14**, the X-ray beam produced from a linear undulator is deflected by two plane mirrors (see horizontal plane deflection mirror in **Figure 2.14**), and then a vertical focusing mirror focuses the X-ray beam through liquid cooled entrance slits and onto the selected grating in the monochromator (see SGM chamber in **Figure 2.14)**.[32] The X-ray beam then travels through movable exit slits, and monochromatic X-ray beam passing through the exit slits is refocused at the SGM endstations using a Au coated toroidal mirror and a pair of KB mirrors.[23] The SGM beamline is equipped with a monochromator with three different gratings and can deliver a bright monochromatic photon beam that covers an energy range of 250 to 2000 eV.[23, 32] Grating selection is based on the energy region required for an experiment. For instance, nickel coated 600 lines/mm grating is used to produce a monochromatic photon beam for low energy measurements, such as carbon 1s NEXAFS measurements of organic materials.

2.6 Raman Spectroscopy

Raman spectroscopy is a non-destructive technique (except when the laser melts the sample) that can be used to study vibrational and other low frequency modes of solid phase samples. The frequencies for the vibrational modes of different conformations of the same species can differ from one another because of their different order-disorder behaviours.[33-34] As such, Raman spectroscopy is a good technique for studying disorder in organic solids such as *n*-alkanes.[34-36]

In brief, this technique illuminates a sample surface with monochromatic light and examines the scattered light using a spectrometer. A schematic diagram of the Raman scattering process is shown in **Figure 2.15**.[37]

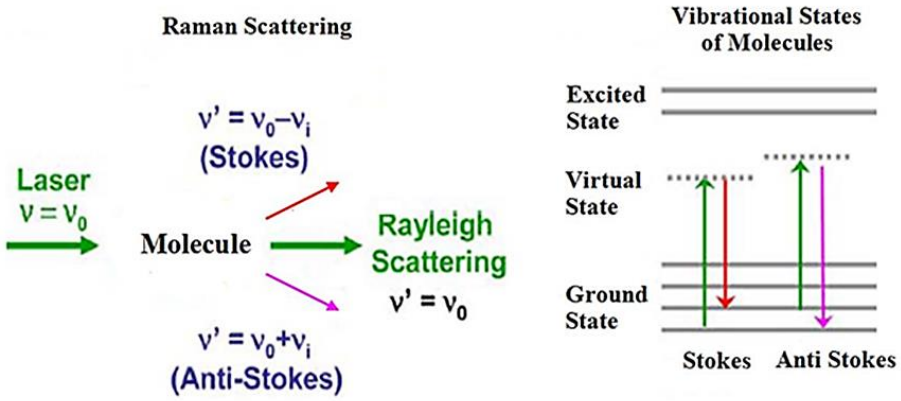

Figure 2.15: Schematic diagram of the Raman scattering process (left) and different vibrational states of a molecule (right). Figure reprinted from Reference 37 with permission.

Although most scattered photons return back to their initial states (e.g. with no energy or frequency change ($\upsilon = \nu_0$)), some photons return to other vibrational states, which are be more or less energetic than the initial states (see Stokes and Anti Stokes in **Figure 2.15**).[37] These are inelastic scattering events and Raman spectroscopy is based on the inelastic scattering of the monochromatic light. There are two types of inelastic scattering. Stokes scattering occurs when the final vibrational energy (v') is lower than the initial vibrational energy (ν_o). Anti-Stokes scattering occurs when the final vibrational energy (v') is greater than the initial vibrational energy (ν_o). In a Raman spectrum, these two modes are equally displaced with respect to the incident light but Stokes lines are generally more intense than anti-Stokes lines due to the Boltzmann distribution of vibrational populations at room temperature.[33, 37]

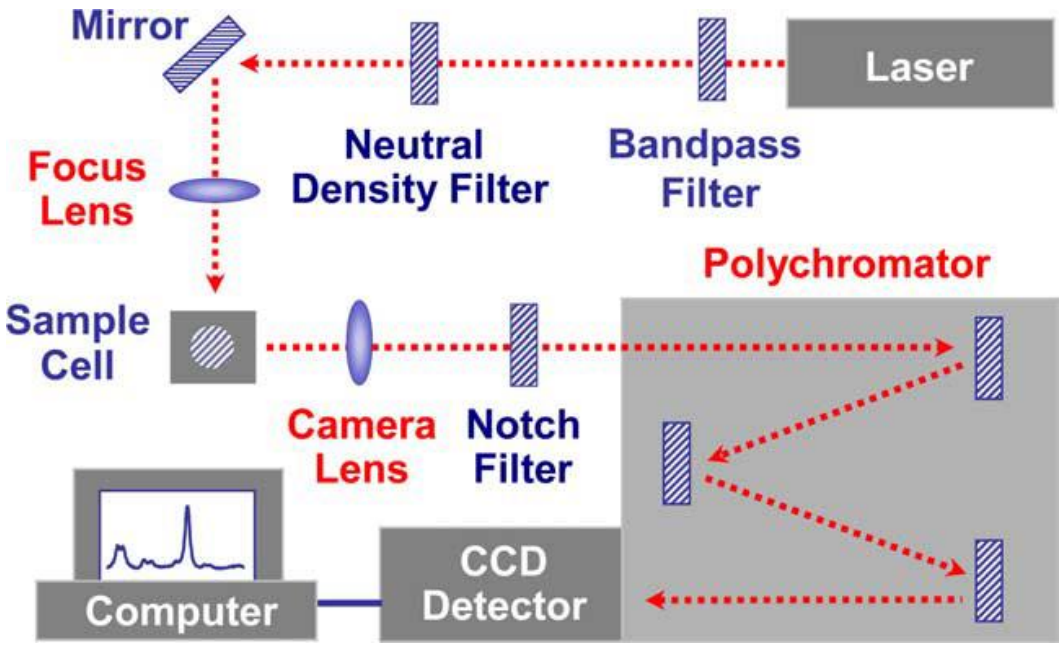

Figure 2.16: Schematic diagram of a Raman spectromicroscope. Figure reprinted with permission from Reference 37 with permission.

A schematic diagram of a Raman spectromicroscope is shown in **Figure 2.16**. [37] In **Figure 2.16**, a monochromatic beam is emitted from the laser source and focused onto the sample plate by the mirrors and focusing lens of the Raman microscope. Next, the camera lens focuses the resulting scattered light from the sample onto the entrance slits of the polychromator via a notch filter. The notch filter is placed between the camera lens and the polychromator to filter out the Rayleigh light (elastically scattered light). A polychromator is an optical device (crystal) that is used to dispersed light by wavelength.[37] The dispersed light outputs from the polychromator is then detected by the Charge Coupling Device (CCD) attached to the exit slit of the polychromator. Subsequently, data acquisition and curve fitting is done digitally by the computer attached to the CCD detector. A typical Raman spectrum plots the intensity of the scattered light as a function of the Raman shift (Δcm^{-1}). The Raman shift reflects the internal energy of the vibration modes present in the molecules. It scales with the energy difference between the scattered and incident photons.[33, 37]

Since structural deformations can alter the energies of the vibrational modes of molecules, Raman energy shifts can be used to study molecular disorder.[34] The intensity of a Raman line depends on many factors (i.e. polarizability, scattering cross section, concentration, and sample thickness).

The following strategies were used in order to optimize the intensity factors (see **C.1** for more details) constant throughout the measurements. In this thesis, Raman spectroscopy experiments were performed in scramble polarization mode. In this mode, the polarization controller varies the polarization of the light rapidly within to ensure that the average polarization over time is randomized throughout the experiment. This cancels out polarization effects to the Raman measurements. In addition, each measurement ensure that the *n*-alkane crystal is in focus of the Raman spectrometer, so that the optimally positioned crystal gives the strongest Raman signal at each time. The experimental challenges associated with Raman spectroscopy of *n*-alkane single crystals such as the effects of substrate thickness, laser power, and laser damage on the Raman spectra of *n*-alkane single crystals will be further discussed in **C.1**.

In this research work, Raman spectra of orthorhombic *n*-alkane single crystals were obtained using a Renishaw 2000 Raman microscope[38] at room temperature and ambient pressure. *n*-Alkane single crystals were deposited on a 500 nm thick gold-coated Si wafer by the solution casting method discussed in §2.2. The Si wafers were placed on glass slides for Raman measurements. The wavelength of the laser source was set to 785 nm. Light scattered from samples was dispersed with a 1200 lines/mm grating (polychromator) and collected using a Renishaw CCD camera.[38] All Raman microscopy images of *n*-alkane single crystals were obtained under a 50X objective lens. The Raman spectra of *n*-alkane single crystals were recorded over an energy range of 100 cm^{-1} to 3500 cm^{-1} using a laser exposure time of 10 seconds and laser power of 0.01 W.

2.7 References

1. Craig, S. R.; Hastie, G. P.; Roberts, K. J.; Sherwood, J. N. Investigation into the Structures of Some Normal Alkanes Within the Homologous Series $C_{13}H_{28}$ to $C_{60}H_{122}$ Using High-Resolution Synchrotron X-ray Powder Diffraction. *Journal of Materials Chemistry* **1994,** *4* (6), 977-981.

2. Brown, C.; Farthing, A. Preparation and Structure of di-p-Xylylene. *Nature* **1949,** *164*, 915-916.

3. Hope, H.; Bernstein, J.; Trueblood, K. The Crystal and Molecular Structure of 1, 1, 2, 2, 9, 9, 10, 10-Octafluoro-[2, 2] Paracyclophane and a Reinvestigation of the Structure of [2, 2] Paracyclophane. *Acta Crystallographica Section B: Structural Crystallography and Crystal Chemistry* **1972,** *28* (6), 1733-1743.

4. Gantzel, P.; Trueblood, K. The Crystal and Molecular Structure of [3,3] Paracyclophane. *Acta Crystallographica* **1965,** *18* (5), 958-968.

5. Introduction to Polarized Light Microscopy. http://bwoptics.com/newsend2.asp?id=7 (accessed 15th February **2018**).

6. Kino, G. S.; Corle, T. R. *Confocal Scanning Optical Microscopy and Related Imaging Systems*. Academic Press, **1996**.

7. Murphy, D. B.; Davidson, M. W. Phase Contrast microscopy and Darkfield Microscopy. *Fundamentals of Light Microscopy and Electronic Imaging, Second Edition* **2001**, 115-133.

8. Polarization Optical Microscopy. http://www.nikoninstruments.com/Information-Center/Polarizing2 (accesed 17th February **2018**).

9. Attwood, D.; Sakdinawat, A. *X-rays and Extreme Ultraviolet Radiation:Principles and Applications*. Cambridge University Press: Cambridege, UK, **2017**.

10. Otero, E. Soft X-ray Spectroscopy of Organic and Organometallic Molecules and Polymers. PhD Thesis, University of Saskatchewan, Ecommons, **2008**.

11. Mobilio, S.; Balerna, A. *Synchrotron Radiation*. 1 ed.; Springer-Verlag Berlin Heidelberg: New Delhi, India, **2015**.

12. Shenoy, G. Basic Characteristics of Synchrotron Radiation. *Structural Chemistry* **2003,** *14* (1), 3-14.

13. Hahner, G. Near Edge X-ray Absorption Fine Structure Spectroscopy As a Tool to Probe Electronic and Structural Properties of Thin Organic Films and Liquids. *Chemical Society Reviews* **2006,** *35* (12), 1244-1255.

14. Koningsberger, D.; Prins, R. *X-ray Absorption: Principles, Applications, Techniques of EXAFS, SEXAFS, and XANES*. John Wiley and Sons: New York, USA, **1988**.

15. Margaritondo, G. *Introduction to Synchrotron Radiation*. Oxford University Press: Oxford, UK, **1988**.

16. Lindau, I.; Spicer, W. *Beam Line and Associated Work: Operational Phase 1985-1987*. Stanford University Press: Stanford, California, USA, **1988.**

17. How Does a Synchrotron Radiation Source Works? http://photon-science.desy.de/research/students__teaching/primers/synchrotron_radiation/index_eng.html (accessed 02nd May **2018**).

18. Operation Modes of an APPLE II Type Undulator. https://www.helmholtz-berlin.de/forschung/oe/fg/undulatoren/arbeitsgebiete/operationsarten_en.html (accessed 17th February **2018**).

19. Watts, B.; Thomsen, L.; Dastoor, P. Methods in Carbon K-edge NEXAFS: Experiment and Analysis. *Journal of Electron Spectroscopy and Related Phenomena* **2006,** *151* (2), 105-120.

20. Stohr, J. *NEXAFS Spectroscopy*. Springer -Verlag: Berlin,Germany, **1992**.

21. Behyan, S. Development of Surface Sensitivity in Scanning X-ray Microscopy and NEXAFS Spectroscopy of Organosulphur Compounds. PhD Thesis, University of Saskatchewan, Ecommons, **2013**.

22. Kaznatcheev, K.; Karunakaran, C.; Lanke, U.; Urquhart, S.; Obst, M.; Hitchcock, A. Soft X-ray Spectromicroscopy Beamline at the CLS: Commissioning Results. *Nuclear Instruments and Methods in Physics Research Section A: Accelerators, Spectrometers, Detectors and Associated Equipment* **2007,** *582* (1), 96-99.

23. Regier, T.; Krochak, J.; Sham, T.; Hu, Y.; Thompson, J.; Blyth, R. Performance and Capabilities of the Canadian Dragon: The SGM Beamline at the Canadian Light Source. *Nuclear Instruments and Methods in Physics Research Section A: Accelerators, Spectrometers, Detectors and Associated Equipment* **2007,** *582* (1), 93-95.

24. Hitchcock, A. P.; Dynes, J. J.; Johansson, G.; Wang, J.; Botton, G. Comparison of NEXAFS Microscopy and TEM-EELS for Studies of Soft Matter. *Micron* **2008,** *39* (6), 741-748.

25. Kilcoyne, A.; Tyliszczak, T.; Steele, W.; Fakra, S.; Hitchcock, P.; Franck, K.; Anderson, E.; Harteneck, B.; Rightor, E.; Mitchell, G. Interferometer-Controlled Scanning Transmission X-ray Microscopes at the Advanced Light Source. *Journal of Synchrotron Radiation* **2003,** *10* (2), 125-136.

26. Leontowich, A. F.; Berg, R.; Regier, C. N.; Taylor, D. M.; Wang, J.; Beauregard, D.; Geilhufe, J.; Swirsky, J.; Wu, J.; Karunakaran, C. Cryo Scanning Transmission X-ray Microscope Optimized for Spectrotomography. *Review of Scientific Instruments* **2018,** *89* (9), 093704.

27. Perera, S. D. Effect of Intermolecular Interactions on the Carbon 1s Near Edge X-ray Absorption Fine Structure (NEXAFS) Spectroscopy of *n*-Alkanes. MSc Thesis, University of Saskatchewan, Ecommons, **2012**.

28. Coffey, T.; Urquhart, S.; Ade, H. Characterization of the Effects of Soft X-ray Irradiation on Polymers. *Journal of Electron Spectroscopy and Related Phenomena* **2002,** *122* (1), 65-78.

29. Tzvetkov, G.; Graf, B.; Wiegner, R.; Raabe, J.; Quitmann, C.; Fink, R. Soft X-ray Spectromicroscopy of phase-Change Microcapsules. *Micron* **2008,** *39* (3), 275-279.

30. Urquhart, S. G.; Hitchcock, A. P.; Smith, A. P.; Ade, H.; Rightor, E. G. Inner-Shell Excitation Spectroscopy of Polymer and Monomer Isomers of Dimethyl Phthalate. *The Journal of Physical Chemistry B* **1997,** *101* (13), 2267-2276.

31. Ma, Y.; Chen, C.; Meigs, G.; Randall, K.; Sette, F. High-Resolution K-Shell Photoabsorption Measurements of Simple Molecules. *Physical Review A* **1991,** *44* (3), 1848-1858.

32. Regier, T.; Paulsen, J.; Wright, G.; Coulthard, I.; Tan, K.; Sham, T. K.; Blyth, R. I. R. Commissioning of the Spherical Grating Monochromator Soft X-ray Spectroscopy Beamline at the Canadian Light Source. *AIP Conference Proceedings* **2007,** *879* (1), 473-476.

33. Ferraro, J.; Nakamoto, K.; Brown, C. *Introductory Raman Spectroscopy*. 2nd edn.; Academic Press: San Diego, Califonia, USA, **2003**.

34. Corsetti, S.; Rabl, T.; McGloin, D.; Kiefer, J. Intermediate Phases During Solid to Liquid Transitions in Long-Chain *n*-Alkanes. *Physical Chemistry Chemical Physics* **2017,** *19* (21), 13941-13950.

35. Wickramarachchi, P. S. R.; Spells, S. J.; de Silva, D. S. M. Study of Disorder in Different Phases of Tetratriacontane and a Binary Alkane Mixture, Using Vibrational Spectroscopy. *The Journal of Physical Chemistry B* **2007,** *111* (7), 1604-1609.

36. Barnes, J.; Fanconi, B. Raman Spectroscopy, Rotational Isomerism, and the "Rotator" Phase Transition in *n*-Alkanes. *The Journal of Chemical Physics* **1972,** *56* (10), 5190-5192.

37. Egawa, T.; Yeh, S.R. Structural and Functional Properties of Hemoglobins From Unicellular Organisms as Revealed by Resonance Raman Spectroscopy. *Journal of Inorganic Biochemistry* **2005,** *99* (1), 72-96.

38. Renishaw 2000 Raman Microscopy. http://www.renishaw.com/en/raman-spectroscopy--6150 (accessed 03rd March **2018**).

Chapter 3 Computational Methods

In **Chapter 4**, the carbon 1s TEY-XAS spectra of PCPs are interpreted with the aid of DFT calculations. This chapter will give a brief description on the quantum chemistry background behind the DFT calculations used to simulate the experimental NEXAFS spectra of PCPs.

3.1 Background

3.1.1 The N-body Problem

In this thesis, the electronic properties of the PCP molecules such as excitation energies were calculated in order to interpret experimental transition energies in their NEXAFS spectra. When determining the electronic properties (energies, dipole moments etc.) of a complex molecule (e.g. PCPs), calculations need to address the complex interactions between the electrons themselves, as well as between the electrons and the nuclei. The ground state energy of a material can be obtained through solutions to the Schrödinger equation (SE).[1-2]

$$\hat{H}\psi = E\psi \qquad \textbf{Equation 3.1}$$

In the **Equation 3.1**, $\hat{H}$ is the Hamiltonian of the system, ψ is the eigenfunction (ground state wave function), and E is the eigenvalue of the eigenfunction. For a many electron system, the Hamiltonian operator is expanded to address the complex interactions between the electrons and nuclei (see **Equation 3.2)**.[1-2] The equation is given in atomic units with $\hbar$ = e = $\frac{1}{4\pi\varepsilon_0}$ = 1.

$$\hat{H} = -\frac{1}{2}\sum_i \frac{\nabla^2}{M_i} - \frac{1}{2}\sum_i \frac{\nabla^2}{m_i} - \sum_{i,j} \frac{Z_i}{|\vec{R_i} - \vec{r_j}|} + \frac{1}{2}\sum_{i\neq j} \frac{1}{|\vec{r_i} - \vec{r_j}|} + \frac{1}{2}\sum_{i,j} \frac{Z_i Z_j}{\vec{R_i} - \vec{R_j}} \qquad \textbf{Equation 3.2}$$

Where M_i and m_i are the masses of nuclei and electrons of the system respectively. Z is the nuclear charge, and $\vec{R}$ and $\vec{r}$ are the position vectors of the nuclei and electrons. ∇^2 is the Laplace operator and in three dimension Cartesian coordinates (x, y, and z), it has the following form.

$$\nabla^2 = \frac{\partial^2}{\partial x^2} + \frac{\partial^2}{\partial y^2} + \frac{\partial^2}{\partial z^2} \qquad \textbf{Equation 3.3}$$

The kinetic ($\hat{T}$ and $\hat{T_n}$) and repulsive terms ($\hat{U_{ee}}$, $\hat{V_{nn}}$, $\hat{V_{ne}}$) of the electron and nucleus in **Equation 3.2** can be separated as below.

$$\hat{T} = -\frac{1}{2}\sum_i \frac{\nabla^2}{m_i} \qquad \hat{T_n} = -\frac{1}{2}\sum_i \frac{\nabla^2}{M_i} \qquad \hat{V_{nn}} = -\frac{1}{2}\sum_{i,j} \frac{Z_i Z_j}{|\vec{R_i} - \vec{R_j}|}$$

$$\hat{V_{ne}} = -\sum_{i,j} \frac{Z_i}{|\vec{R_i} - \vec{r_j}|} \qquad \hat{U_{ee}} = \frac{1}{2}\sum_{i\neq j} \frac{1}{|\vec{r_i} - \vec{r_j}|}$$

By using kinetic and repulsive terms, the total Hamiltonian expression in **Equation 3.2** can be simplified as:

$$\hat{H} = \hat{T} + \hat{T_n} + \hat{V_{nn}} + \hat{V_{ne}} + \hat{U_{ee}} \qquad \textbf{Equation 3.4}$$

In the **Equation 3.4**, the first and second terms represent the kinetic energies of the electrons and nuclei of the system, respectively. The third and fifth terms represent the nuclei-nuclei and electron-electron repulsion energies of the system, respectively. The fourth term represents the Coulombic attractions between the electrons and nuclei of the system.

As shown in **Equation 3.4**, the SE can include all of the electron-nuclei, electron-electron, and nuclei-nuclei interactions of a system. Unfortunately, exact solutions for such complex interactions in many-electron system are not achievable.[1-2] Therefore, approximations are required for many-electron molecules. Hence, the Born-Oppenheimer (BO) approximation and the Linear Combination of Atomic Orbital (LCAO) approximations are used. The Density Functional Theory (DFT) method is used to solve the complex nature of the many-electron system.

The Born-Oppenheimer (BO) Approximation

The BO approximation assumes that nuclei remain static on the time scale of electron motion due to the greater mass of nuclei.[3] Therefore, the BO approximation neglects the kinetic energy of the nuclei ($\hat{T_n}$ in **Equation 3.4**) and treats the nuclei-nuclei repulsion potential (V_{ne} in **Equation 3.4**) as a parameter.[3] This approximation redefines the nucleus – electron attraction term as V_{ext} in the presence of static nucleus, and condenses **Equation 3.4** to:

$$\hat{H} = \hat{T} + \hat{U_{ee}} + \hat{V_{ext}} \qquad \textbf{Equation 3.5}$$

The LCAO approximation is needed to approximate the molecular orbitals of many-electron molecules. LCAO is given in **Equation 3.6**.[4]

$$\psi_j = \sum_{i=1}^{N} a_{ij}\,\psi_i \qquad \textbf{Equation 3.6}$$

In the LCAO approximation, each MO is constructed by the quantum superposition of the atomic orbitals (AOs) of the atoms in the molecule, and knowing atomic coefficients (a_{ij}) of each AO will approximate the MOs of the many-electron molecule.[4]

3.2 Density Functional Theory (DFT)

As name implies, DFT measures the properties of the system such as energy, dipole moment and electronic structure as a functional of the electron density (ρ_0).[5-6] This method describes the ground state of the solid material from its ground state electron density, and describes the excited state of the system by considering the electron density of the excited state.[5-6] A detailed description of DFT will be given below.

DFT treats a many-electron molecule as a system in which electrons move under a static external potential (V_{ext}).[7] For a solid material, usually this static external potential (V_{ext}) is caused by its nuclei. This method is based on two theorems.[6]

1. For any system, the V_{ext} that affects the electron movements of the system (electrons) is unique, and the total energy of the system is a unique functional of the ρ_0.[6]
2. The ground state energy of the system can be determined variationally from ρ_0. In that case, the ρ_0 which minimizes the total energy is the exact ground state electron density.[6]

If two systems have different electronic structures, the first theorem says that each system should have a different V_{ext} and different ρ_0. The second theorem then explains how to identify the ρ_0 responsible for the V_{ext} identified in the first theorem. To do so, the ρ_0 of the system must be optimized. The correct ρ_0 must have an energy greater than the system's ground state energy whenever it is not in the ground state.[6-7]

Therefore, it is important to solve for the appropriate ρ_0 for the system since it holds as much information as the wave function. Kohn and Sham (K-S) developed a method that can be used to find the ground state electron density for many-electron systems.[5-6] The end goal is to determine the suitable form of the density function, and analyze it to extract the electronic properties (energies, dipole moments etc.) of the system. In this work, we are interested in the electronic properties of PCP molecules.

3.2.1 Kohn-Sham Equations

In K-S method, a many-electron material is defined as a system of non-interacting particles,[5-6] and the behaviour of each non-interacting electron in the system is described by the K-S equation. The K-S equation is similar to the single particle Schrödinger equation, and is given by **Equation 3.7**.[5]

$$\left(-\frac{1}{2m}\nabla^2+V_{eff}(r)\right)\psi_i(r)=\varepsilon_i^{KS}\,\psi_i(r),\quad \varepsilon_1^{KS}\leq\varepsilon_2^{KS}\leq\ldots, \qquad \textbf{Equation 3.7}$$

$$V_{eff}(r)=V_{ext}(r)+V_H(r)+V_{XC}(r) \qquad \textbf{Equation 3.8}$$

In **Equation 3.7**, the kinetic and effective potential experienced by each non-interacting electron in the system is given by $-\frac{1}{2m}\nabla^2$ and $V_{eff}(r)$. Moreover, ψ_i and ε_i^{KS} represent the K-S eigenstates and K-S energies of each non-interacting electrons in the system.[5]

According to the **Equation 3.8**, the $V_{eff}(r)$ of the system has three contributions. One is external potential [$V_{ext}(r)$] which is contributed by the nuclear potential term and any other applied electric field in the system. The other two factors are the Hartree potential [$V_H(r)$] and the exchange-correlation potential [$V_{xc}(r)$] of the system.

The $V_H(r)$ is contributed by the electrostatic potential produced from the electronic charge density $\rho(r)$.[5-6] The Poisson equation is used to describe potential field caused by a given charge and $\rho(r)$ can be derived from the Poisson equation as:

$$-\nabla^2 V_H(r)=\rho(r) \qquad \textbf{Equation 3.9}$$

With the known $\rho(r)$ in **Equation 3.9,** $V_H(r)$ can be solved by using **Equation 3.10**.

$$V_H(r)=\int\frac{\rho(r')}{|r-r'|}dr' \qquad \textbf{Equation 3.10}$$

The $V_{xc}(r)$ contribution of the $V_{eff}(r)$ of the system can be obtained by the functional derivatives of the exchange-correlation energy (E_{XC}) as: [5-7]

$$V_{XC}(r)=\frac{\delta E_{XC}[\rho(r)]}{\delta\rho(r)} \qquad \textbf{Equation 3.11}$$

In here, the approximations used to calculate the exact form of the E_{XC} is given in §3.2.2 and $\rho(r)$ can be expressed as:

$$\rho(r)=\sum_{i\ occupied}|\psi_i(r)|^2 \qquad \textbf{Equation 3.12}$$

With the normalized wave function ψ_i, where [$\langle\psi_i|\psi_i\rangle = 1$].

Since all three contributors of the $V_{eff}(r)$ are depend on the $\rho(r)$ (see **Equations 3.9 - 3.12**), the $V_{eff}(r)$ is a function of the $\rho(r)$.[5-6] Therefore, finding an exact $\rho(r)$ is important in order to extract electronic properties (such as molecular orbital energies of the ground state and excited states) from the K-S equation. The $\rho(r)$ can be found using the self-consistent calculation method.[5]

In the self-consistent calculation method, an $V_{eff}(r)$ is first constructed from an initial guess of $\rho(r)$.[5] Then, the $V_{eff}(r)$ in the first step is used to solve the K-S equations, and a K-S orbital for each non-interacting electron in the system is constructed. After that, the K-S orbitals are used to calculate a new $\rho(r)$ for the system using **Equation 3.12**. If the new $\rho(r)$ is different from the initial guess by more than a given tolerance limit, the initial guess $\rho(r)$ is replaced by the new $\rho(r)$ and the same calculation is repeated.[5] This procedure is repeated until it converges within the defined tolerance limit. Once it converges, the true $\rho(r)$ can be identified and used to extract the property of interest, i.e. the total energy of a system can be obtained by minimising the energy functional. For instance, the ground state energy can be obtained by solving the following reorganized K-S equation.[5]

$$E_0 = \sum_{i=1}^{N} \varepsilon_i + \frac{1}{2} \int \frac{\rho(r)\rho}{|r - r'|} dr dr' + E_{XC}[\rho(r)] - \int \rho(r) V_{XC}(r) dr \qquad \textbf{Equation 3.13}$$

In addition to the $\rho(r)$, E_{XC} is also important to determine $V_{eff}(r)$ of the system. Hence, the strength of DFT calculations is dependent on how well the calculation approximates the exact form of the E_{XC} in the K-S equations. For that approximation, DFT calculation software needs an input file to mimic the actual density function of the system. The input file in the DFT calculation software must identify two important things. One is the basis set selection to approximate the orbital behaviours of the elements present in the many-electron system. The other is a proper approximation to calculate the exact form of the E_{XC} of the system. The most popular approximations used for DFT calculations are the Local Density Approximation (LDA)[6] and the Generalized Gradient Approximation (GGA).[8-11] Basis sets and exchange correlation functions will be explained in §3.2.2 and 3.3.3 respectively.

3.2.2 Exchange Correlation Functional

LDA and GGA

The Local Density Approximation (LDA) treats the electrons in a system as a uniform electron gas.[6] Therefore, the LDA assumes that the exchange-correlation energy per electron of a non-uniform system at any point in space is equal to the exchange-correlation energy per electron in a uniform electron gas having the same density at this point. From this approximation, the exchange-correlation energy of a system can be expressed as:[6]

$$E_{XC}^{LDA}[\rho(r)] \approx \int \varepsilon_{XC}[\rho(r)]\rho(r) dr \qquad \textbf{Equation 3.14}$$

Where ε_{XC} is:

$$\varepsilon_{XC}[\rho(r)] \approx \frac{3e^2}{2\pi}\,[3\pi^2\rho(r)]^{\frac{1}{3}}\,\rho(r) \qquad \textbf{Equation 3.15}$$

According to **Equation 3.14** and **3.15**, the exchange-correlation energy of an electron ($\varepsilon_{XC}[\rho(r)]$) depends on the local $\rho(r)$ of the system. However, regardless of the electron position, the LDA method treats the local $\rho(r)$ of the electrons in the system the same throughout the entire area due to the uniform electron gas assumption.[6] Therefore, the LDA oversimplifies the $\rho(r)$ of a system since it does not account for the $\rho(r)$ variations that occur across a system.[6] While not perfect, this is a good approximation for systems that do not have significant $\rho(r)$ variations in different areas. In molecular solids like *n*-alkanes and paracyclophanes, $\rho(r)$ is not homogeneous or uniform. Therefore, the exchange – correlation function is needed to address $\rho(r)$ variation within the different areas of the sample.

In the Generalized Gradient Approximation (GGA), the exchange - correlation energy of an electron at a given point depends on the local $\rho(r)$ and a density gradient that occurs as a result of the position of the electron. The GGA can be expressed as: [8-11]

$$E_{XC}^{GGA} = \int f[\rho(r), \nabla\rho(r)]dr \qquad \textbf{Equation 3.16}$$

According to **Equation 3.16**, *f* is the universal function or enhancement factor of $\rho(r)$ and density gradients.[8-10] This factor can be parametrized differently in order to calculate the E_{XC} of a system. Therefore, the type of GGA varies according to the type of universal function used. However, the most common, widely used, and successful GGA is the Perdew-Burke-Ernzerhof (PBE) functional GGA.[12] This function has been successful at calculating vibrational energies, geometries, transition energies, and lattice parameters for many system.[9, 12-13]

3.2.3 Basis Sets

Basis sets are a set of functions which are used to approximate the behaviors of electrons in the system. Basis sets use *s*, *p*, *d*, *f* functions to mimic the actual behaviour of the *s*, *p*, *d*, *f* AOs, and MOs built from AOs using the LCAO approximation. In the beginning, Slater Type Orbitals (STO) are used as basis functions and general form of STO can be expressed in **Equation 3.17**.[14-16]

$$\phi^{STO}_{n,l,m}(r,\theta,\phi) = \frac{(2\zeta)^{n+1/2}}{[(2n)!]^{1/2}} r^{n-1} e^{-\zeta r} Y_l^m(\theta,\phi) \qquad \textbf{Equation 3.17}$$

Where ζ (zeta) is the radial dependence and it controls the size of the AOs. $Y_l^m(\theta,\phi)$ are spherical harmonics and *n,l,m* are the quantum numbers. STO have direct physical interpretation and they are usually a good basis function for MOs. However, STO has a disadvantage in point of computational cost (computational speed) since most of the required integrals in STO needed in to process the SCF procedure must be calculated numerically and that significantly decreases the computational speed. As a result, new numerical methods has been developed in order to have efficient SCF calculations using STOs. One way could be approximated STOs as linear combination of Gaussian type orbital (LCGTO), which can be expressed as: [14-16]

$$\psi_i = \sum_{j=1}^{N} a_j \phi_j^{GTO} \qquad \textbf{Equation 3.18}$$

Where N defines the size of the basis set and a_j are the coefficients of the GTO basis functions ϕ_j^{GTO}.The coefficients a_j are the terms which change during the DFT calculations. In here, ϕ_j^{GTO} is shown in **Equation 3.19**.[14-16]

$$\phi^{GTO}_{n,l,m}(r,\theta,\phi) = N_n r^{n-1} e^{-\alpha r^2} Y_l^m(\theta,\phi) \qquad \textbf{Equation 3.19}$$

Where N is a normalization factor, (*n, l, m*) are the quantum numbers and $Y_l^m(\theta,\phi)$ are the spherical harmonics. The variable α controls the radial size and *i, j, k* controls the shape of the AOs. This type of basis set is generally called an orbital basis set and smallest possible basis set is known as the minimal basis set.[14] Minimal basis set contain one orbital (one basis function) for each orbital on the free atom. For example, hydrogen has one orbital (1s) and carbon has five orbitals (1s, 2s, $2p_x$, $2p_y$, $2p_z$). The minimal basis set is usually defined as STO-nG where *n* is the integer that its value represent the number of GTOs used to approximate STO for both core and valence orbitals. STO-3G and STO-6G are some of the commonly used minimal basis sets. Minimal basis sets are usually gave rough estimation and are not sufficiently flexible for accurate representation of orbitals.[14-15]

Therefore, multiple basis functions are needed to be included to represent each orbital (inner shell and valence orbitals) in the atom/molecule. Such basis sets are known as extended basis sets. Split valence basis sets (which include different GTOs for inner shell and valence shell orbitals), polarized basis sets (include additional functions such as p, d, or f types to orbital basis

set based on the type of atom), diffuse basis sets (include additional s or p functions with a very diffuse radial distribution to the orbital basis set) are some of the different kinds of extended basis sets used in DFT calculations. Extended basis sets are generally expressed as *n-ijG*++* or *n-ijkG*+*. For an example, in *6-31G*+*, *6* is the number of Gaussian functions summed to describe the inner shell orbitals and *31* is the number of Gaussian functions summed to describe the valence shell orbitals. In this regard, *3* is the number of Gaussian functions that comprise the first STO of the double zeta (or inner valence shell) and *1* is the number of Gaussian functions summed in the second STO of the double zeta (or outer valence shell). The asterisk (*) sign in the notation represent polarization function and plus (+) sign represent the diffuse function in the extended basis set.

The type of extended basis set used for each atom depends on the application and the significance of that atom to the application. For instance, when simulating the X-ray absorption spectra of a molecule, a more diffuse basis set (IGLO - III)[17] is used for the core excited atom and relatively less diffuse, and smaller, basis sets, like triple-ξ valence plus polarization (TZVP), are used for the rest of the atoms in the molecule. Triple-ξ valence plus polarization (TZVP) diffuses the orbital basis set by using three radial functions. An orbital basis set can be further diffused by adding more radial functions to the basis set (e.g. quadruple-ξ valence plus polarization). In general, large diffuse basis sets efficiently approximate the electronic relaxations of core excited molecules (see §3.2.4 for electronic relaxation effect).

Other than the orbital basis sets, two more types of basis sets are involved in DFT calculations.

1. Auxiliary basis sets
2. Augmented basis sets

Auxiliary basis sets are similar to orbital basis sets, but used to match electron density and exchange-correlation functions in K-S equations.[18] Augmented basis sets contain large diffuse basis sets, i.e. hundreds of s, p, and, d type functions.[18] Therefore, augmented basis sets increase the flexibilities of the orbital basis sets and improve calculation accuracy for NEXAFS simulations[18]

3.2.4 Core-Excited Calculations

3.2.4.1 Core-Hole Relaxation

When a core-hole is formed, the excited electron and the other electrons in the system are affected by the potential created by the core hole, which affects the nature of the unoccupied

orbitals (MOs energies, electron densities etc.) in the core excited molecule.[19] Therefore, it is important to approximate the electronic relaxation caused by the core-hole.

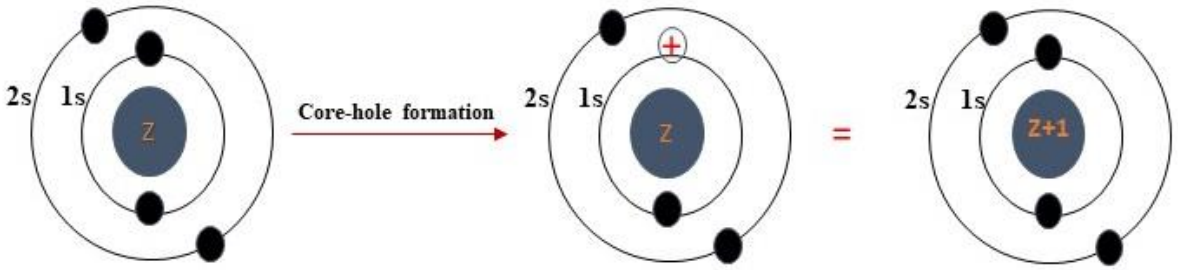

Figure 3.1: Schematic representation of the Z+1 approximation.

Core-hole formation can affect the system in many ways. According to **Figure 3.1**, removal of a core electron enhances the nuclear charge of the system by +1 with respect to the ground state (see first and third images of the **Figure 3.1**). One way of simulating the core-hole effect is the Equivalent Ionic Core Virtual Orbital Model (EICVOM) or Z+1 approximation.[20] This EICVOM approximation treats the atomic core charge (nuclear and core electron) of the core excited atom (Z) is same as the atomic core charge of the ground state atom with one greater nuclear charge (see Z+1 in the **Figure 3.1**). For instance, the atomic core charge of a core excited carbon (Z=6, core charge = 5) is similar as the atomic core charge of the ground state nitrogen atom (Z=7, core charge = 5).[21] This approach assumes that the effect caused by ionization of core electron to an outer orbital is the same as the effect caused by the change in the nuclear charge by one atomic unit.[22] When using this approximation, two changes are included in the calculation input file: the core excited atom of the calculation is replaced by its Z+1 counterpart; and the charge of the molecule is set to +1, in order to maintain the correct valence electron count.[21] The molecular geometry is kept the same during core excited state calculations. The EICVOM approximation provides a rough estimation for the core-hole effect and electronic relaxation in a core excited molecule. Core-hole relaxation is better approximated by explicitly simulating the core-hole potential of the system.

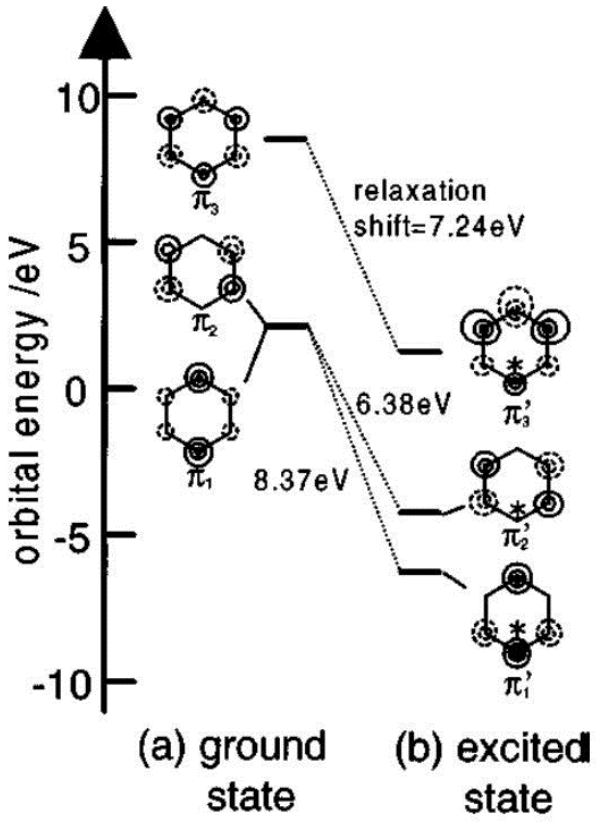

Figure 3.2: Energy diagram of the (a) ground state and (b) core-excited states of unoccupied π MOs of benzene. The origin of the orbital energy is the vacuum level, and asterisk symbol represents the core excited carbon atom. Figure reprinted from Reference 19 with permission.

Figure 3.2 represent the energy diagram of the ground and excited states of unoccupied π MOs of benzene, calculated with the Improved Virtual Orbital (IVO) approximation.[19,23] This example highlights the effect of a core-hole on the energy positions of core excited states. In this, IVO is an approximation used in Hartree – Fock (HF) calculations to simulate the core-hole effect, where the core hole contribution to the molecular potential is explicitly considered in the Hamiltonian equation.[21-23] According to **Figure 3.2**, the unoccupied π MOs of the benzene in the excited state show a downward energy shift with respect to the ground state.[19] In addition, each unoccupied π MO in the benzene excited state experiences a different relaxation effect, the largest effect being experienced by the Lowest Unoccupied Molecular Orbital (LUMO).[19] This example shows the importance of accounting core-hole effects when calculating the MOs energies of excited states.[19] Although changes in core-occupation (core-hole effect) cause the main relaxation effects in the core excited molecule, repulsion of the excited electron can also affect the system by decreasing the relative energy of the optical orbital.[24] This will be discussed further below.

The energies calculated using the IVO approximation are slightly higher than experimental values due to causes such as lack of exchange correlations and neglecting the shielding effect caused by the excited electron. However, if the molecular potential (N-1 electron system) is recalculated with the core hole vacancy and an optical orbital occupancy, the repulsion effect of the excited electron can be corrected.[25]

3.2.4.2 The Approximation Used to Account for Core-Hole Relaxation in DFT Calculations

In DFT calculations, the relaxation effect of the core-hole in the core excitation process can be accounted by using the Full Core Hole (FCH) and Half Core Hole (HCH) approaches.[24, 26-27] In FCH approach, relaxation of the core-hole state is included through a fully relaxed core-hole state.[24, 26-27]

Theoreticians also use the Half Core Hole (HCH) approach to determine the excited states of the core excited molecule.[24, 26] In the HCH approach, relaxation of the core-hole state is included through fully relaxed, half - occupied core-hole state.[24] Although half an electron (0.5) in an orbital does not represent a real physical spin or occupancy, theoreticians have found the HCH approach provides a better balance between the initial and final state effects of the core excitation process.[24, 28]

Transition-Potential Density Functional Theory (TP-DFT)

In this work, calculations performed to simulate the NEXAFS spectra of [n,n]paracyclophanes in **Chapter 4** were based on TP-DFT method. The TP-DFT[29] approach is an approximation of the Slater transition-state DFT method.[24, 28, 30] In the Slater transition-state DFT method, the core-hole is simulated with half an electron, and the excited states are formed explicitly by adding the excited half electron to various states, i.e. state-by-state calculations.[24] TP-DFT considers the relaxation of core-hole states through fully relaxed, half-occupied core-hole states, with oscillator strengths determined from transition dipole moments.[28] Moreover, TP - DFT avoids state-by-state calculations, and obtains excited states from a single matrix diagonalization (SMD) method.[24] SMD is similar to the IVO approximation.[31-32] That approximation includes all interactions between the excited electron and the molecular ion core and constrains the molecular ion core density to remain frozen and not relax when interacting with the excited electron.[24]

However, with the SMD approximation, the TP-DFT approach neglects the relaxation of the remaining molecular ion core in the presence of the excited electron. Additional energy corrections are needed in order to obtain a correct absolute energy scale.[24]

3.2.4.3 The Approximation Used to Account for Both Core-Hole Relaxation and Shielding Effect of the Excited Electron in DFT Calculations

Both approaches FCH and HCH ignore the excited electron and thus the shielding effect of the excited electron in the molecular ion core.[24, 33] However, this missing contribution can be accounted with a self-consistent inclusion of the excited electron. This is called the Excited Core Hole (XCH) approach.[27] The XCH method involved in determining the total energy of the first fully relaxed core-excited state in the delta Kohn-Sham (ΔK-S) method. Hence, XCH is the ΔK-S method. In this project, ΔK-S method used as an energy correction for the lowest-energy [C $1s^{-1}$; π*] core excited state in TP-DFT approach.

Energy Calibration: ΔK-S Method

In the ΔK-S method, the absolute energy scale is determined by calculating the total energy difference between the ground state and first fully relaxed core-excited state.[24] This can be further explained as below.

In general, the electronic structure of a core-excited molecule is made up of two parts.[25]

1. Active part, i.e. core hole and excited electron.
2. Passive part, i.e. rest of the molecule (N-1 part where N is the total electrons in the molecule)

When using ΔK-S method for XAS, the passive (N-1) part is recalculated with the core hole vacancy and the optical orbital occupancy by putting an electron to the lowest unoccupied molecular orbital. This accounts for the shielding effect of the excited electron and gives the absolute energy of the lowest unoccupied molecular orbital (LUMO). The ΔK-S method provides more accurate energies than the TP approach for excitation energies. For example, the experimental energy of the core → π* transition in CO_2 gas is 290.74 eV,[34] and the ΔK-S method reproduces the energy for the same transition more accurately (290.4 eV) than the TP-DFT calculation (291.7 eV). Sample ΔK-S calculations (both transition energy for LUMO and ionization potential) for the [n,n]PCP molecule are shown in **A.2**.

This research used the deMon2k calculations software to simulate NEXAFS spectra for the PCPs shown in **Chapter 4**. The theory of the demon2k and the calculation details will be given in §3.2.5.

3.2.5 deMon2k

The name deMon stands for density of Montreal, and it is a computational program developed for the DFT calculations of atom, molecules, and clusters.[35] The deMon2k code uses a LCGTO approach to achieve self-consistent solutions to the K-S DFT equations for orbital energies.[5-6] In addition, demon2k uses auxiliary functional sets to avoid the size limitation associated with electron density calculations, and provides better results for orbital energies when calculating excitation energies.[35]

3.2.5.1 Calculation Details

The molecular geometries of [n,n]PCP used in TP-DFT calculations were lowest energy conformations, determined by ω B97X-D DFT calculations at the 6-31G* level, performed with the program Spartan-14.[36]

All TP-DFT calculations were performed using the demon2k code[35] and the absolute energy for the LUMO was obtained using the ΔK-S method. For all DFT calculations, PBE GGA exchange-correlation fucntional[12, 37-38] was used with optimized DFT basis sets.

In this work, DFT calculations used both auxiliary and normal orbital basis sets to approximate the behaviours of the orbitals in each atom in the molecule. In addition, our calculations uses an augmented basis set for core excited carbon atom to enhance the flexibility of the basis function and increase the accuracy of the core excitation calculation (**Table 3.1**). The type of basis set/sets used for each atom depends on the importance of that particular atom for the calculation. For instance, the core excited atom is the most important atom in the molecule for core-excitation calculations. Therefore, the most advanced orbital basis set, i.e. IGLO III,[17] was used for the core excited atom, in combination with the advance auxiliary basis function GEN-A4* and the augmented diffuse basis function (XAS-I).

Table 3.1: Types of basis sets used for DFT calculations in [n,n]PCP molecules

Type of atom in PCP molecule	Basis Sets		
	Orbital	Auxiliary	Augmented
Core-excited carbon	IGLO-III	GEN-A4	XAS-I
Other carbons	ECP	GEN-A2	-
Hydrogens	TZVP	GEN-A2	-

For other carbon atoms in the molecule, Effective Core-Potential (ECP) or pseudopotentials were used as orbital basis set.[39] In an ECP, the nuclear charge of the atom (Z) is replaced with an effective charge (Z_{eff}) as below.[39]

$$Z_{eff} = Z - Z_{core} \qquad \textbf{Equation 3.20}$$

Where Z_{core} is the charge associated with the core electrons. The use of ECP on all heavy atoms but and ensure that a single core (1s) orbital is localized on the specific atom. The use of ECP avoids the convergence issues associated in the process of determining correct energy values for the carbon atoms in the PCP molecule.[39] The intensities of spectral lines were obtained from computed dipole transition matrix elements for excitations of core orbitals (1s).[29] Only core excitation carbon 1s $\rightarrow \pi^*$ transitions are considered for the PCP spectra shown in Chapter 4. The simulated spectra were obtained from the DFT calculations of each non-equivalent site by broadening the lower carbon 1s $\rightarrow \pi^*$ feature to a Gaussian line.[39] The spectra were then summed according to stoichiometric proportions to form simulated spectra for [n,n] PCP. The energy of the LUMO is then corrected by the ΔK-S method.[24] The calculated π^*excitation energies, ionization potentials, and term values for carbon 1s (C-H) $\rightarrow \pi^*_{C=C}$ and carbon 1s (C-R) $\rightarrow \pi^*_{C=C}$ transitions are shown in **Chapter 4**. The sample input file used for PCP calculations is given in **A.2**.

3.3 References

1. Duan, F.; Guojun, J. *Introduction To Condensed Matter Physics: Volume 1*. World Scientific: Singapore, **2005**.

2. Kohanoff, J. *Electronic Structure Calculations for Solids and Molecules: Theory and Computational Methods*. Cambridge University Press: Cambrideg, UK, **2006**.

3. Sutton, A. P. *Electronic Structure of Materials*. Oxford University Press: Oxford, UK, **1993**.

4. Engel, T. *Quantum Chemistry and Spectroscopy*. Pearson Education: India, **2006**.

5. Kohn, W.; Sham, L. J. Self-Consistent Equations Including Exchange and Correlation Effects. *Physical Review* **1965,** *140* (4A), A1133-A1138.

6. Hohenberg, P.; Kohn, W. Inhomogeneous Electron Gas. *Physical Review* **1964,** *136* (3B), B864-B871.

7. Forrest, J. Application Of X-ray Spectroscopy and Density Functional Theory to Toxicology of Polychlorinated Biphenyl. MSc Thesis, University of Saskatchewan, Ecommons, **2012**.

8. Perdew, J. P. Accurate Density Functional for the Energy: Real-Space Cutoff of the Gradient Expansion for the Exchange Hole. *Physical Review Letters* **1985,** *55* (16), 1665-1668.

9. Perdew, J. P.; Chevary, J. A.; Vosko, S. H.; Jackson, K. A.; Pederson, M. R.; Singh, D. J.; Fiolhais, C. Atoms, Molecules, Solids, and Surfaces: Applications of the Generalized Gradient Approximation for Exchange and Correlation. *Physical Review B* **1992,** *46* (11), 6671-6687.

10. Perdew, J. P.; Wang, Y. Accurate and Simple Anlytic Representation of the Electron-Gas Correlation Energy. *Physical Review B* **1992,** *45*, 13244-13249.

11. Levy, M.; Perdew, J. P. Hellmann-Feynman, Virial, and Scaling Requisites for the Exact Universal Density Functionals. Shape of the Correlation Potential and Diamagnetic Susceptibility for Atoms. *Physical Review A* **1985,** *32* (4), 2010-2021.

12. Perdew, J. P.; Burke, K.; Ernzerhof, M. Generalized Gradient Approximation Made Simple. *Physical Review Letters* **1996,** *77* (18), 3865-3868.

13. Wang, C.; Klein, B.; Krakauer, H. Theory of Magnetic and Structural Ordering in Iron. *Physical Review Letters* **1985,** *54* (16), 1852-1855.

14. Hehre, W. J.; Stewart, R. F.; Pople, J. A. Self-Consistent Molecular-Orbital Methods. I. Use of Gaussian Expansions of Slater-Type Atomic Orbitals. *The Journal of Chemical Physics* **1969,** *51* (6), 2657-2664.

15. Hehre, W. J.; Stewart, R. F.; Pople, J. A. Self-Consistent Molecular-Orbital Methods. IV. Use of Gaussian Expansions of Slater-Type Orbitals. Extension to Second-Row Molecules. *The Journal of Chemical Physics* **1970,** *52* (5), 2769-2773.

16. Ditchfield, R.; Hehre, W. J.; Pople, J. A. Self-Consistent Molecular-Orbital Methods. IX. An Extended Gaussian-Type Basis for Molecular-Orbital Studies of Organic Molecules. *The Journal of Chemical Physics* **1971,** *54* (2), 724-728.

17. Kutzelnigg, W.; Fleischer, U.; Schindler, M. The IGLO-Method: *ab-initio* Calculation and Interpretation of NMR Chemical Shifts and Magnetic Susceptibilities. In *Deuterium and Shift Calculation*, pp. 165-262. Springer-Verlag: Berlin, Germany, **1990**.

18. Godbout, N.; Salahub, D. R.; Andzelm, J.; Wimmer, E. Optimization of Gaussian-Type Basis Sets for Local Spin Density Functional Calculations. Part I. Boron through Neon, Technique and Validation. *Canadian Journal of Chemistry* **1992,** *70* (2), 560-571.

19. Oji, H.; Mitsumoto, R.; Ito, E.; Ishii, H.; Ouchi, Y.; Seki, K.; Yokoyama, T.; Ohta, T.; Kosugi, N. Core Hole Effect in NEXAFS Spectroscopy of Polycyclic Aromatic Hydrocarbons: Benzene, Chrysene, Perylene, and Coronene. *The Journal of Chemical Physics* **1998,** *109* (23), 10409-10418.

20. Schwarz, W. Interpretation of the Core Electron Excitation Spectra of Hydride Molecules and the Properties of Hydride Radicals. *Chemical Physics* **1975,** *11* (2), 217-228.

21. Urquhart, S. G. Delocalization and Functional Group Fingerprinting in the Core Excitation Spectroscopy of Molecules and Polymers. PhD Thesis, McMaster University, **1997**.

22. Stohr, J. *NEXAFS Spectroscopy*. Springer-Verlag: Berlin, Germany, **1992**.

23. Goddard III, W. A. Excited States of H_2O using Improved Virtual Orbitals. *Chemical Physics Letters* **1969,** *3* (6), 414-418.

24. Leetmaa, M.; Ljungberg, M.; Lyubartsev, A.; Nilsson, A.; Pettersson, L. G. Theoretical Approximations to X-ray Absorption Spectroscopy of Liquid Water and Ice. *Journal of Electron Spectroscopy and Related Phenomena* **2010,** *177* (2-3), 135-157.

25. Kosugi, N. *Advanced Course in Application of GSCF3 to Inner Shell Excitation*. Institute for Molecular Science: Okazaki, Japan, **2000** (Private Communication).

26. Zhang, Y.; Biggs, J. D.; Healion, D.; Govind, N.; Mukamel, S. Core and Valence Excitations in Resonant X-ray Spectroscopy Using Restricted Excitation Window Time-

Dependent Density Functional Theory. *The Journal of Chemical Physics* **2012,** *137* (19), 194306.

27. Prendergast, D.; Galli, G. X-ray Absorption Spectra of Water from First Principles Calculations. *Physical Review Letters* **2006,** *96* (21), 215502.

28. Fransson, T.; Zhovtobriukh, I.; Coriani, S.; Wikfeldt, K. T.; Norman, P.; Pettersson, L. G. Requirements of First-Principles Calculations of X-ray Absorption Spectra of Liquid Water. *Physical Chemistry Chemical Physics* **2016,** *18* (1), 566-583.

29. Triguero, L.; Pettersson, L.; Ågren, H. Calculations of Near-Edge X-ray-Absorption Spectra of Gas-Phase and Condense-Phase Molecules by Means of Density-Functional and Transition-Potential Theory. *Physical Review B* **1998,** *58* (12), 8097

.

30. Slater, J. C. Statistical Exchange-Correlation in the Self-Consistent Field. In *Advances in Quantum Chemistry*, pp. 1-92. Elsevier: **1972**.

31. Ågren, H.; Carravetta, V.; Vahtras, O.; Pettersson, L. G. Direct, Atomic Orbital, Static Exchange Calculations of Photoabsorption Spectra of Large Molecules and Clusters. *Chemical Physics Letters* **1994,** *222* (1-2), 75-81.

32. Ågren, H.; Carravetta, V.; Vahtras, O.; Pettersson, L. G. Direct SCF Direct Static-Exchange Calculations of Electronic Spectra. *Theoretical Chemistry Accounts* **1997,** *97* (1-4), 14-40.

33. Luo, Y.; Ågren, H.; Keil, M.; Friedlein, R.; Salaneck, W. R. A Theoretical Investigation of the Near-Edge X-Ray Absorption Spectrum of Hexa-Peri-Hexabenzocoronene. *Chemical Physics Letters* **2001,** *337* (1-3), 176-180.

34. Ma, Y.; Chen, C.; Meigs, G.; Randall, K.; Sette, F. High-Resolution K-Shell Photoabsorption Measurements of Simple Molecules. *Physical Review A* **1991,** *44* (3), 1848-1858.

35. Geudtner, G.; Calaminici, P.; Carmona-Espíndola, J.; del Campo, J. M.; Domínguez-Soria, V. D.; Moreno, R. F.; Gamboa, G. U.; Goursot, A.; Köster, A. M.; Reveles, J. U. deMon2k. *Wiley Interdisciplinary Reviews: Computational Molecular Science* **2012,** *2* (4), 548-555.

36. *Spartan 14'*, Wavefunction, Inc: Irvine, Califonia, USA, **2014**.

37. Zhang, Y.; Yang, W. Comment on "Generalized Gradient Approximation Made Simple". *Physical Review Letters* **1998,** *80* (4), 890-890.

38. Hammer, B.; Hansen, L. B.; Nørskov, J. K. Improved Adsorption Energetics Within Density-Functional Theory Using Revised Perdew-Burke-Ernzerhof Functionals. *Physical Review B* **1999,** *59* (11), 7413-7421.

39. Pettersson, L. G.; Wahlgren, U.; Gropen, O. Effective Core Potential Parameters for First- and Second-Row Atoms. *The Journal of Chemical Physics* **1987,** *86* (4), 2176-2184.

Chapter 4 Effect of π-π Interactions on NEXAFS Spectroscopy

4.1 Description

Chapter 4 investigates how π-π interactions between adjacent aromatic groups affect NEXAFS spectra. The effects between the cofacial benzene rings were examined using paracyclophane (PCP) molecules as a model system. Paracyclophane is an aromatic compound which contains two benzene rings connected by a bridging aliphatic group with variable lengths. The variable alkyl length separates the benzene rings of the PCP molecule and control the benzene-benzene separation of the molecule. Therefore, PCP molecule with different aliphatic bridging groups systematically control the π-π interactions between the cofacial benzene rings. Furthermore, single crystal diffraction studies of PCP showed that phenyl rings on different PCP molecules are not facially aligned with each other as the rings are within a PCP molecule. Therefore, PCP is a good intramolecular proxy to identify the role of intermolecular interactions in NEXAFS spectroscopy.

The experimental trends in the XAS spectra of PCP molecules were initially reproduced and rationalized with the *ab initio* based GSCF3 calculation package which uses the improved virtual orbital (IVO) approximation (not shown in this thesis). However, we moved to DFT calculations since DFT calculations are better in studying larger systems like PCPs molecules. In these calculations, the TP-DFT method was used to simulate the NEXAFS spectra. The energy of the lowest energy (C $1s^{-1}$, π*) core excited states and carbon 1s ionization potentials (IPs) were calculated using the ΔK-S method. The ΔK-S method was more accurate than the transitional potential method (for excitation energies) and Koopmans's theorem (for IPs). The nature of the interactions between the cofacial benzene rings were examined by using molecular orbital plots of the LUMO in ground state and C-H/C-R core excited states of the PCP molecules. This study confirmed that both core binding and π* orbital energy variations were caused the π-π interactions. Those π-π interactions were higher in PCP molecules with shorter bridging units.

The experimental and theoretical work in this study was published in the Journal of Physical Chemistry A [Reproduced with permission from Journal of Chemistry A, 121, 4907-4913, Sahan D. Perera and Stephen G. Urquhart, Systematic Investigation of π–π Interactions in Near-Edge X-ray Fine Structure (NEXAFS) Spectroscopy of Paracyclophanes, Copyright 2017, American Chemical Society]. This chapter is a literal copy of a paper published in the Journal of

Physical Chemistry A with changes to make figures and table numbers consistent throughout the thesis.

4.2 Description of Candidate Contribution

The author of this thesis was the primary investigator for this research work. He prepared the samples, justified the sample identity, acquired the experimental data (experimental NEXAFS spectra of [n,n]PCP), simulated the NEXAFS spectra of [n,n]PCP by TP-DFT calculations, interpreted the results, and wrote the manuscript. T. Regier helped with the experimental set-up for XAS measurements of PCP molecules. S. G Urquhart provided guidance throughout the experiments, the process of data analysis and actively involved in the editing process of this manuscript. Dr. S. G. Urquhart kindly gave me his permission to include this manuscript in this dissertation, and agreed to my description of my contribution in this document.

4.3 Relation of Contribution to Research Objectives

π-π interactions are the dominant intermolecular interactions in the unsaturated systems. Therefore, investigating the effect of π-π interactions between the cofacial benzene rings will contribute to the broader goal of building general understanding of the role of intermolecular interactions in NEXAFS spectroscopy. The detail descriptions of the experimental methodology and calculation methods used in this manuscript can be found in **Chapter 2** and **3**. A comprehensive discussion of the results in this chapter as a part of the whole study, i.e. study of systematic investigation of the intermolecular interactions in NEXAFS spectroscopy is provided in **Chapter 8**.

4.4 Systematic Investigation of π-π Interactions in Near Edge X-ray Absorption Fine Structure (NEXAFS) Spectroscopy of Paracyclophanes

Sahan D. Perera, Stephen G. Urquhart*

Department of Chemistry, University of Saskatchewan, Treaty Six Territory, Saskatoon, SK, Canada S7N 5C9

Abstract

NEXAFS spectroscopy has potential for study of packing and order in organic materials, but only if intermolecular effects are understood. This work studies how π-π interactions between adjacent unsaturated groups affect their NEXAFS spectra, with a broader goal of building a general understanding of the role of intermolecular effects in NEXAFS spectroscopy. These effects are examined using paracyclophane (PCP) molecules, in which the benzene-benzene separation distance is controlled by varying the length of the alkyl groups separating the benzene rings. NEXAFS spectroscopy and density functional theory (DFT) simulations are used to examine spectroscopic changes related to the strength of these π-π interactions. A characteristic red shift is observed as adjacent benzene rings get closer together. This shift is attributed to Coulombic and orbital interactions between the adjacent benzene rings, mediated through overlapping π / π* orbitals.

4.4.1 Introduction

The near edge X-ray absorption fine structure (NEXAFS) spectra of organic molecules are sensitive to molecular bonding and orientation. As a consequence, many NEXAFS studies of organic materials focus on chemical analysis, such as the presence of specific functional groups[1-4] or the chemical composition in blends, alloys and composites,[3, 5-10] or orientation through linear dichroism measurements.[11-19]

In contrast to these *intra*-molecular effects (bonding, etc.), *inter*molecular effects are not as extensively explored. These effects could be used to study molecular packing, order and disorder in molecular materials. Broadly, intermolecular effects in NEXAFS spectra of organic molecules are expected to arise from conformation and bonding changes in the condensed state, and perturbations due to electronic interactions between adjacent molecules, such as quenching of Rydberg character in condensed phases.

Rydberg quenching has been observed in the NEXAFS spectra of simple alkanes. The spectra of small gas phase alkanes (methane, ethane, etc.) are dominated by a Rydberg series (carbon 1s → 3s, 3p, 3d, etc.),[20] but their spectra is broadened and blue-shifted in the condensed phase.[21] The origin of these differences has been controversial, but is now attributed to quenching of Rydberg character in the solid state and the emergence of carbon 1s → σ*(C-H) character.[21] Quenching effects were observed in the NEXAFS spectra of saturated polymers such as polyethylene. Schöll *et al*.[22] demonstrated that the NEXAFS spectra of polyethylene copolymers vary with the degree of crystallinity and with disorder induced by melting, where NEXAFS features were broader in molten / less crystalline polymers. Recently, Schmidt *et al*[23] observed Rydberg quenching in naphthalene through gas / solid phase NEXAFS comparisons and high-level DFT calculations. Hydrogen bonding can also have a role in the NEXAFS spectra of condensed species, demonstrated in NEXAFS spectra of water [24-29] and recently for molecular solids.[30-31]

In studying the NEXAFS spectra of aromatic clusters, Rühl *et al*. [32] observed a small red shift (50-70 meV) in solid clusters relative to their gas phase spectra. The magnitude of this shift was found to depend on the size and the homogeneity of the cluster.[33-34] This effect was attributed to dynamic stabilization, in which the core excited cluster deforms to trap the core-excited molecule in a modified geometry, with a carbon 1s → π* transition red-shifted relative to its gas phase spectrum.[34] As dynamic stabilization is proposed for clusters relative to their gas phase

spectra,[32] this effect should be constant within a series of solid phase materials, such as the PCP studies described below.

Face to face π-π interactions occur and are important for the structure and electronic property of organic electronic materials such as poly(3-hexyl thiophene) (P3HT).[35-36] on the basis of the potential of NEXAFS spectroscopy to be sensitive to weak intermolecular interactions, this work explores π-π interactions between cofacial benzene rings, using paracyclophane (PCP) as a model system. PCP compounds consist of two benzene rings connected by a bridging unit of variable length (see **Figure 4.3**).[37-39] The length of the bridging unit determines the separation between the benzene rings; shorter bridges such as in these in [2,2] PCP bring the benzene rings to a distance that is lower than the limit of van der Waals interactions. This separation increases for longer bridging groups, such as in [3,3] PCP.[40-44] Analysis of the single-crystal diffraction structures of [2,2] PCP,[40, 45] [3,3]PCP,[42] and [4,4] PCP[46] shows that the phenyl rings in *different* PCP molecules are not facially aligned with each other. The only facial π-π interactions between phenyl rings are therefore *within* the PCP molecules. Therefore, PCP molecules are a good model system to identify the role of intermolecular interactions in NEXAFS spectroscopy.

Studies on direct information on π-π interactions and π orbital overlap in these materials by using NEXAFS spectroscopy are limited in literature.[39] Batra *et al.*[39] examined the carbon 1s NEXAFS spectra of monolayer and multilayers of the [2,2] PCP and [4,4] PCP as part of a multi-technique study to examine electron transfer processes. They observed an energy shift between the two species but did not account for this shift in terms of π-π interactions.[39]

In this work, π-π interactions will be examined through high-resolution carbon 1s NEXAFS spectra of PCP structures with different bridge lengths separating the co-facial benzene rings. These spectroscopic studies will be coupled with high quality DFT simulations of the NEXAFS spectra of these PCP models. This work will be used to examine the origin and magnitude of π-π interactions as a function of benzene-benzene separation. The knowledge of this work could be also applied to the spectroscopy of industrially important organic electronic polymers, such as P3HT, and could provide unique information on structure and order.[35-36]

4.4.2 Experimental Section

Samples and Sample Preparation

Samples: The paracyclophane (PCP) molecules used in this study were [2,2] PCP (Sigma-Aldrich 97%) and [3,3] PCP (> 95%) where [n, n] refers to the length of the alkane bridge between

the benzene rings (see **Figure 4.3**). [3,3]PCP was obtained from Prof. Henning Höpf (Technische Universität Braunschweig, Germany). The structures of [2,2] PCP and [3,3] PCP were verified by NMR, and used without further purification. Commercially available [5,5] PCP was found by NMR spectroscopy to not be compound claimed, and was not used in this study.

Sample Preparation: Samples were prepared by pressing the powder form onto clean indium foil (5 x 5 mm squares), and loading into a vacuum of the endstation on the SGM beamline.

NEXAFS Spectroscopy

NEXAFS spectra of the [n,n] paracyclophane compounds were recorded on the SGM beamline (11ID-1) at the Canadian Light Source.[47] Spectra were recorded in Total Electron Yield (TEY) detection mode. TEY carbon 1s NEXAFS spectra were normalized by taking the ratio of sample current (I) and gold reference current (I_R), where the gold reference spectrum was acquired by a separate scan. To remove the normalization artifacts in the carbon 1s spectra, the intensity of the gold reference spectrum was modified so that the intensity in the pre-edge region was superimposed with the sample spectrum (I), as previously described by Otero *et al*.[48] Spectral analysis was performed using aXis 2000,[49] and spectra were plotted for presentation using Origin 7.5. The entrance and exit slit for these measurements were 5 and 3µm, corresponding to a resolving power greater than 5000.

The SGM monochromator energy scale was calibrated to the first CH peak in the carbon 1s NEXAFS spectra of *n*-tetracontane (*n*-$C_{40}H_{82}$), calibrated previously in measurements in the Scanning Transmission X-ray Microscope on the SM beamline.[50] The calibrated energy scale was determined by measuring the spectrum of CO_2 (g) along with that of *n*-tetracontane. The carbon 1s → 3s (v=0) and carbon 1s → 3p (v=0) transitions in CO_2 (g) were set to 292.74 eV and 294.96 eV, respectively, after the measurements of Ma *et al*. [51] On this basis, the first peak in the carbon 1s NEXAFS spectrum of *n*-tetracontane (*n*-$C_{40}H_{82}$) was calibrated to 287.48(5) eV. Measurements of *n*-tetracontane on the SGM beamline, recorded at the same time as the PCP spectra, were used to calibrate the energy scale for these spectra.

4.4.3 Computational Section

Methodology

To aid spectral assignments, DFT[52-53] calculations were carried out using deMon2k package.[54-55] NEXAFS simulations were initially performed using the transition potential (TP-

DFT) method,[56-57] which uses the half core hole approximation. Subsequently, carbon 1s ionization potentials (IPs) and the energy required to create the lowest energy [C $1s^{-1}$; π*] core excited state were calculated with the ΔK-S method.[56] This method provides more accurate energies than the Koopmans' theorem (for IPs) and transition potential (for excitation energies) approaches. Spectra obtained from TP-DFT simulations were recalibrated by setting the energy of the first transition to that calculated for the [C $1s^{-1}$; π*] core excited state by the ΔK-S method.

Molecular geometries of benzene and [n, n] PCP (n = 2, 3, and 4) species were lowest energy structures, determined by ω B97X-D DFT calculations at the 6-31G* level, performed with the program Spartan' 14.[58] No imaginary frequencies were observed. For studies of benzene-benzene separation, two benzene molecules were manually placed in a cofacial structure, at different fixed benzene – benzene separation distances.

For all DFT calculations, the PBE GGA exchange and correlation functional[59-60] was used, with the GEN-A4* auxiliary basis set for the core excited carbon atom, and the GEN-A2* basis set for all other atoms.[61-62] The orbital basis sets used are IGLO-III[63] for the excited carbon atom, TZVP for hydrogen atoms, and effective core potentials (ECP)[64] for all other carbon atoms. The augmented diffuse basis set (XAS-I) was used for the core exited atom.[56] The intensity of the spectral lines is obtained from the computed dipole transition matrix elements for excitations from the core (carbon 1s) orbitals. Only the core excitation carbon 1s → π* transitions were considered, and simulated spectra were obtained from the DFT calculations of each nonequivalent site by broadening the lower carbon 1s → π* feature as a Gaussian line. These spectra were then summed according to their stoichiometric proportions to form a simulated NEXAFS spectrum of the π* band.

4.4.4 Results

4.4.4.1 Carbon 1s NEXAFS Spectra of [n,n] Paracyclophanes

Figure 4.1 presents the experimental carbon 1s NEXAFS spectra for [2,2] and [3,3] paracyclophanes, recorded using TEY detection. Transition energies and assignments for the carbon 1s → π* band are presented in **Table 4.1**.

Table 4.2: Experimental carbon 1s → π* transition energies from the NEXAFS spectra of [2,2] and [3,3] PCP.

[n, n]PCP	Carbon 1s → π* Transition Energy (eV)	
	C-H site	C-R site
[2,2]PCP	284.8	284.9
[3,3]PCP	285.0	285.3

The energy in the carbon 1s → π* region shows a red shift in the spectrum of [2,2] PCP relative to that of [3,3] PCP. At the same time, the shape of the π* band changes. The decreased alkane tether length brings the benzene rings closer together, which is correlated to the decreased carbon 1s → π* transition energy.

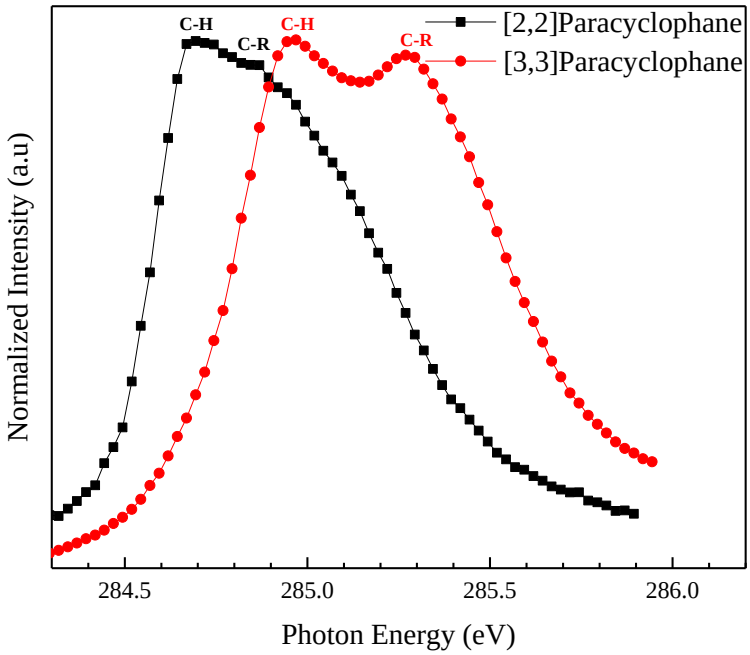

Figure 4.1: Carbon 1s NEXAFS spectra of [2,2] and [3,3] paracyclophane, recorded with total electron yield (TEY) detection.

4.4.4.2 DFT Simulations of the NEXAFS Spectra of [n,n] Paracyclophanes

NEXAFS simulations were obtained from ΔK-S-DFT calculations of [2,2], [3,3], and [4,4] PCP, in order to interpret features observed in their experimental spectra. These simulated carbon 1s NEXAFS simulations are presented in **Figure 4.2**. Calculated carbon 1s IPs, transition energies, and orbital term values (TV) for the lowest-energy carbon 1s → π* transition, based on ΔK-S-DFT calculations, are presented in **Table 4.2**.

The ΔK-S-DFT simulations reproduce the trend as observed in experiment, where the carbon 1s → π* transition moves to lower energy as the benzene ring separation decreases, from [4,4] PCP to [2,2] PCP. The carbon 1s → π* transition energy shifts are larger between [4,4] PCP and [3,3] PCP than those between [3,3] PCP and [2,2] PCP. The magnitude of the energy shift between [3,3] PCP and [2,2] PCP is underestimated by the ΔK-S-DFT calculations (ΔK-S-DFT: 0.045 eV versus 0.2 eV in experiment), but the direction of the energy shift is consistent.

The calculated carbon 1s IPs and the π* orbital TVs help interpret the experimental observations. The π* orbital TVs increase as the bridging group length decreases, from [4,4] PCP to [2,2] PCP. A larger TV indicates that the π* orbital occurs at lower energy, relative to the IP, and appear at lower energy overall.

Table 4.3: The Calculated IPs, transition energies, and TVs of [2,2], [3,3] and [4,4] PCP from the ΔK-S method.

[n, n]PCP	Ionization Potential (eV)		Carbon 1s → π* Transition Energy (eV)		π* Orbital Term value (eV)	
	C-H site (eV)	C-R site (eV)	C-H site (eV)	C-R site (eV)	C-H site (eV)	C-R site (eV)
[2,2] PCP	288.772	288.891	284.087	284.328	4.685	4.563
[3,3] PCP	288.644	288.798	284.132	284.390	4.512	4.408
[4,4] PCP	288.732	288.847	284.382	284.532	4.350	4.315

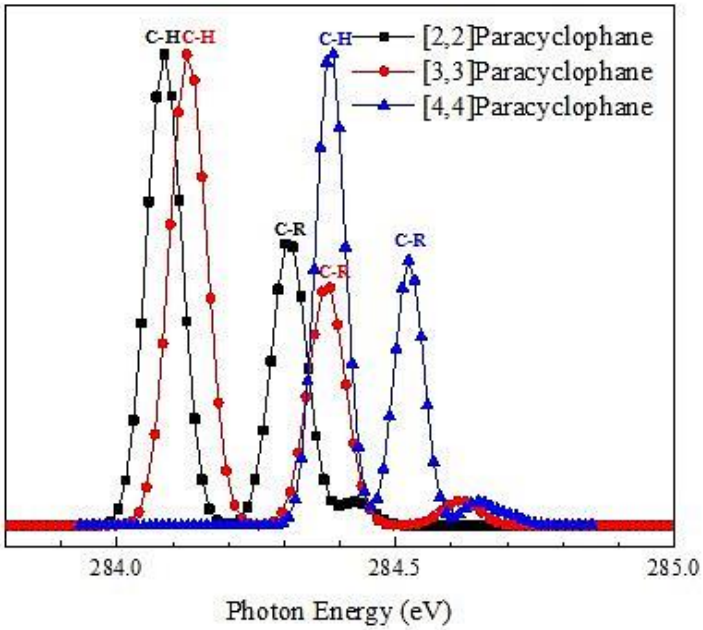

Figure 4.2: ΔK-S DFT simulations of the NEXAFS spectra of [2,2], [3,3] and [4,4] paracyclophane. These traces were calculated from TP-DFT calculations, and the first transition was calibrated to the results of ΔK-S calculations for the lowest-energy [C $1s^{-1}$; π*] core excited state.

In a simple molecular orbital picture, stronger bonds will have their highest occupied molecular orbital (HOMO; π) occurring at lower energy and their higher lowest unoccupied molecular orbital (LUMO; π*) occurring at higher energy (e.g. an increased HOMO/LUMO splitting). As the NEXAFS transitions probe the π* LUMO, a decrease in the LUMO energy can be attributed to weakening of the benzene ring π-bonding as the rings come closer together. In the case of PCP molecules, the TV for the π* LUMO increases as the bridging group length decreases, from [4, 4] PCP to [2, 2] PCP, indicating weaker ring bonding.

The carbon 1s IPs has an opposite effect on the core → π* transition energy, increasing between [3,3] PCP and [2,2] PCP, and shifting the core → π* transition to higher energy. These TV / bonding and IP shifts will partially cancel, but the overall trend remains; core → π* transition shift to lower energy as the benzene rings move closer together.

A carbon 1s (C-R) → π* transition occurs at higher energy than the carbon 1s (C-H) → π*, on account of the weak inductive effect of the alkyl spacer (e.g. the "C-R" site). This inductive effect increases the IP of the C-R site relative to that of the C-H site.[65] The energy difference between the C-H and C-R carbon 1s → π* transition is similar (0.24 – 0.25 eV) for [2,2] PCP and

[3,3] PCP, but smaller (0.15 eV) for [4,4] PCP. This suggests that the orbital environment in [4,4] PCP is different from that of the two species with the rings closer together.

4.4.5 Discussion

The tether or bridging group [n,n] attached to the two benzene rings of the PCP molecule creates two non-equivalent carbon atom sites in the PCP molecule (C-H and C-R, see **Figure 4.3**).

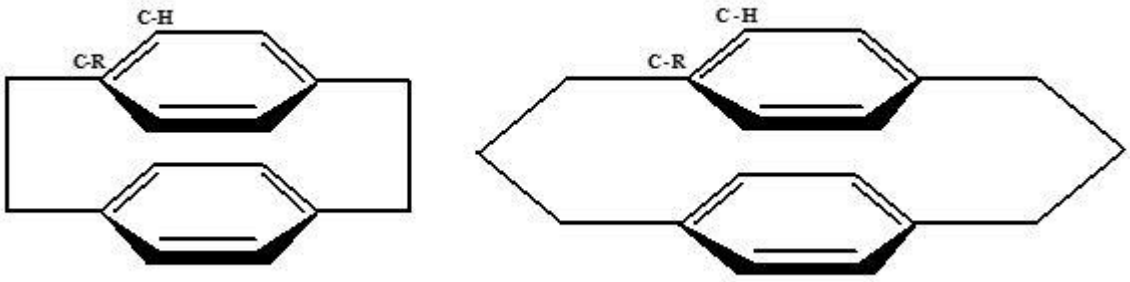

Figure 4.3: Chemical structures of [2,2] paracyclophane and [3,3] paracyclophane.

A doublet structure (see **Figure 4.1** and **4.2**) arises in the carbon 1s $\rightarrow \pi^*$ region from this C-H/C-R splitting. The shape of the simulation and experimental spectra differ, as the experiment spectrum is convoluted by unresolved vibronic features.[66] This π^* band shape was observed in previous NEXAFS measurements by Batra *et al.*[39] Our ΔK-S calculations reproduce the experimentally observed energy shift, albeit with a different magnitude, and attribute this shift largely from changes to the energy of the π^* orbital term value with ring separation.

The benzene rings in [2,2] PCP are 3.09 Å apart,[40-41, 44] which is significantly smaller than the van der Waals separation for the benzene rings (e.g. two times the van der Waals radii of carbon, or 3.40 Å). The benzene-benzene separation in [3,3] PCP is 3.30 Å,[42] which is only slightly smaller than the van der Waals separation. Only in [4,4] PCP are the benzene rings further apart than the van der Waals separation (3.99 Å).[46]

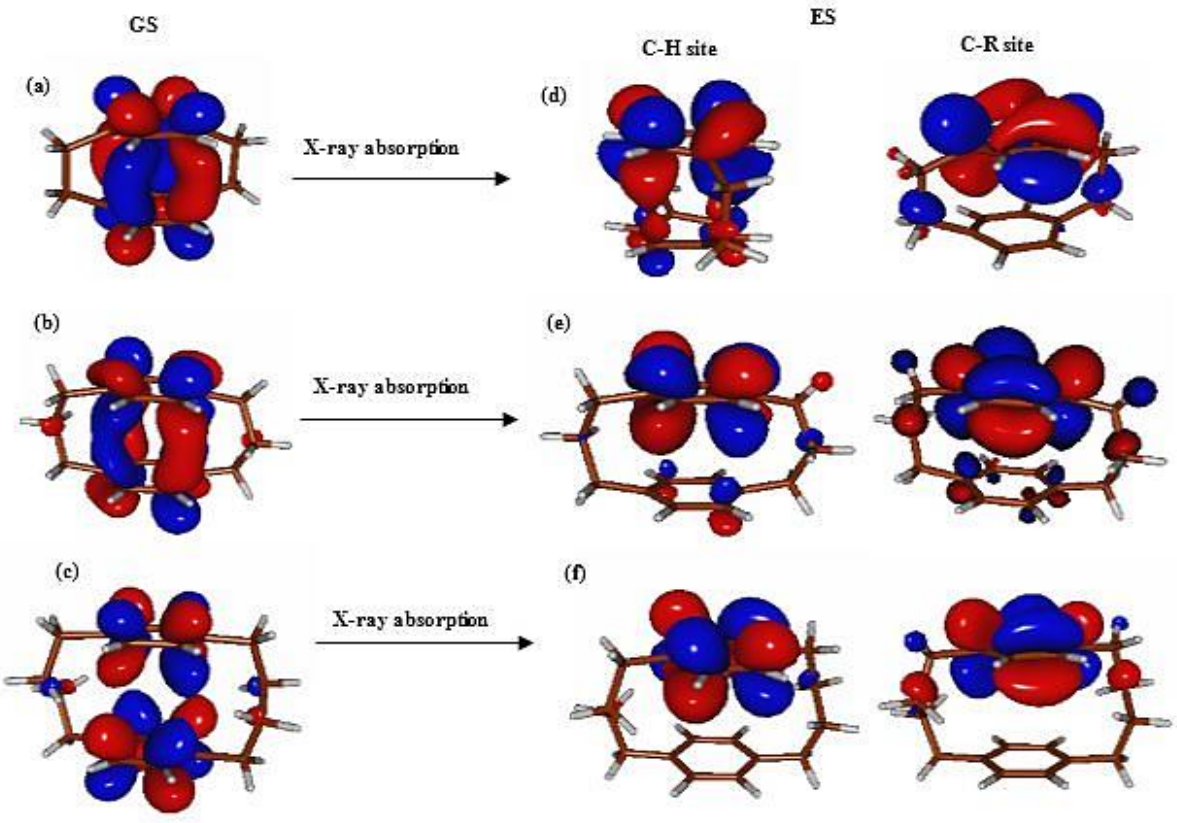

Figure 4.4: (a-c) Iso-surface plots of the LUMOs for [2,2] PCP, [3,3] PCP and [4,4] PCP, respectively, from ground state DFT calculations. (d-f) Iso-surface plots of the core excited state LUMOs for [2,2]PCP, [3,3]PCP and [4,4]PCP, respectively, from DFT calculations. The isosurface value for all of the plots is set to 0.03.

The nature of the interaction between adjacent benzene rings in the PCP molecules can be examined by using molecular orbital plots of the LUMO, as presented in **Figure 4.4** for the ground state and C-H / C-R core excited state LUMO in the three PCP molecules. While benzene has degenerated LUMO/LUMO+1 π^* molecular orbitals, only the LUMO is shown here. Our previous work[67] demonstrated that the carbon 1s → LUMO+1 transition is silent in benzene due to the location of an orbital node at the site of the core hole. When benzene rings are functionalized, the carbon 1s → LUMO+1 transition is very weak as functionalization can "lock in" the LUMO+1 molecular orbital so that it does not necessarily have an orbital node at the site of the core hole. **Figure 4.2** shows that the carbon 1s → LUMO+1 transition is a very weak transition (at ~284.65 eV) and not significant overall. As only the carbon 1s → LUMO transition is significant, only that transition is discussed further.

In **Figure 4.3**, the ground state π* LUMOs for all PCP molecules are delocalized between the top and bottom benzene rings, with an in-phase overlap of the orbitals in the space between the two benzene rings. A similar result can be seen for the LUMO of dibenzene, which is included in the Supporting Information. In the molecular orbital plots for the C−H/C−R core excited states, the LUMO becomes localized onto the ring with the core hole.

An orbital interaction is observed in the space between the benzene rings in [2,2] PCP, is less in [3,3] PCP, and nonexistent in [4,4] PCP. The observed orbital overlap is a function of the magnitude of the isosurface density used for the plot, but the interaction is clearly greater in [2,2] PCP. The MO plots indicate that the carbon 1s → π* transition in PCP is sensitive to orbital interactions between the adjacent benzene rings, with a greater shift as the rings get closer together. The orbital interaction is a bonding (in phase) orbital interaction between the rings and an antibonding (π*) interaction within each ring. This interaction will scale with the closeness of the benzene rings.

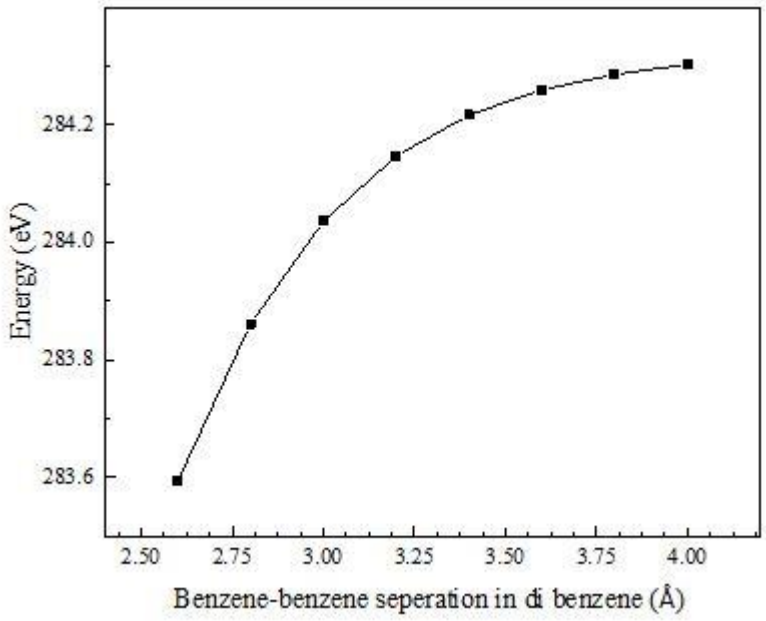

Figure 4.5: Variation in the calculated carbon 1s → π* transition energy in dibenzene molecule as a function of inter-ring distance. Energies were calculated by the ΔK-S DFT method.

Another way to investigate the shift in carbon 1s → π* transition energy with benzene-benzene separation is to use a dibenzene model with different separation distances. **Figure 4.5** presents a plot of the lowest energy carbon 1s → π* transition energy (ΔK-S DFT) for this dibenzene species as a function of inter-ring distance, from 2.6 Å - 4.0 Å. This plot shows a clear

red shift as the rings get closer together, with a larger slope below the van der Waals separation distance (3.4 Å). As the separation increases, the carbon 1s → π* transition energy increases and tends to an asymptote. This indicates a relatively long range effect on the carbon 1s → π* transition energy, with a larger shift below near the van der Waals separation distance.

4.4.6 Conclusions

The carbon 1s NEXAFS spectroscopy of [2,2] PCP and [3,3] PCP have been recorded and interpreted with the aid of DFT calculations. PCP compounds are used to provide a careful examination of π-π interactions as they provide an experiment model-defined benzene-benzene separation distances. The systematic spectral trend in the carbon 1s → π* transition energies was explored as a function of benzene-benzene separation distances. These observed trends were interpreted with ΔK-S-DFT calculations. Variations in both core binding and π^* orbital energies arose from the magnitude of π-π interactions, which increased for PCP molecules with a smaller bridging unit.

The knowledge of this work can be used to simply and understand the spectroscopy of complex organic electronic polymers, and could provide unique information on structure and order. These results are now informing studies of packing, order, and intermolecular interactions in P3HT.[68]

4.4.7 References

1. Dhez, O.; Ade, H.; Urquhart, S. G. Calibrated NEXAFS Spectra of Some Common Polymers. *Journal of Electron Spectroscopy and Related Phenomena* **2003,** *128* (1), 85-96.

2. Ade, H.; Urquhart, S. NEXAFS Spectroscopy and Microscopy of Natural and Synthetic Polymers. In *Chemical Applications of Synchrotron Radiation: Part I: Dynamics and VUV Spectroscopy Part II: X-Ray Applications*, pp. 285-355. World Scientific: Singapore, **2002**.

3. Rightor, E. G.; Urquhart, S. G.; Hitchcock, A. P.; Ade, H.; Smith, A. P.; Mitchell, G. E.; Priester, R. D.; Aneja, A.; Appel, G.; Wilkes, G.; Lidy, W. E. Identification and Quantitation of Urea Precipitates in Flexible Polyurethane Foam Formulations by X-ray Spectromicroscopy. *Macromolecules* **2002,** *35* (15), 5873-5882.

4. Gainar, A.; Stevens, J. S.; Jaye, C.; Fischer, D. A.; Schroeder, S. L. M. NEXAFS Sensitivity to Bond Lengths in Complex Molecular Materials: A Study of Crystalline Saccharides. *The Journal of Physical Chemistry B* **2015,** *119* (45), 14373-14381.

5. Lipton-Duffin, J.; Miwa, J. A.; Urquhart, S. G.; Contini, G.; Cossaro, A.; Casalis, L.; Barth, J. V.; Floreano, L.; Morgante, A.; Rosei, F. Binding Geometry of Hydrogen-Bonded Chain Motif in Self-Assembled Gratings and Layers on Ag(111). *Langmuir* **2012,** *28* (40), 14291-14300.

6. Qaqish, S. E.; Urquhart, S. G.; Lanke, U.; Brunet, S. M. K.; Paige, M. F. Phase Separation of Palmitic Acid and Perfluorooctadecanoic Acid in Mixed Langmuir−Blodgett Monolayer Films. *Langmuir* **2009,** *25* (13), 7401-7409.

7. Iyer, G. R. S.; Wang, J.; Wells, G.; Bradley, M. P.; Borondics, F. Nanoscale Imaging of Freestanding Nitrogen Doped Single Layer Graphene. *Nanoscale* **2015,** *7* (6), 2289-2294.

8. Hitchcock, A. P.; Berejnov, V.; Lee, V.; West, M.; Colbow, V.; Dutta, M.; Wessel, S. Carbon Corrosion of Proton Exchange Membrane Fuel Cell Catalyst Layers Studied by Scanning Transmission X-ray Microscopy. *Journal of Power Sources* **2014,** *266*, 66-78.

9. Meier, R.; Schindler, M.; Müller-Buschbaum, P.; Watts, B. Residual Solvent Content in Conducting Polymer-Blend Films Mapped With Scanning Transmission X-ray Microscopy. *Physical Review B* **2011,** *84* (17), 174205.

10. Zhong, J.; Zhang, H.; Sun, X.; Lee, S. T. Synchrotron Soft X-ray Absorption Spectroscopy Study of Carbon and Silicon Nanostructures for Energy Applications. *Advanced Materials* **2014,** *26* (46), 7786-7806.

11. Ney, A.; Ney, V.; Ollefs, K.; Schauries, D.; Wilhelm, F.; Rogalev, A. X-Ray Linear Dichroism: An Element-Selective Spectroscopic Probe for Local Structural Properties and Valence. *Journal of Surfaces and Interfaces of Materials* **2014,** *2* (1), 14-23.

12. Rossi, G.; d'Acapito, F.; Amidani, L.; Boscherini, F.; Pedio, M. Local Environment of Metal ions in Phthalocyanines: K-Edge X-ray Absorption Spectra. *Physical Chemistry Chemical Physics* **2016,** *18* (34), 23686-23694.

13. Marchetto, H.; Schmidt, T.; Groh, U.; Maier, F. C.; Levesque, P. L.; Fink, R. H.; Freund, H. J.; Umbach, E. Direct Observation of Epitaxial Organic Film Growth: Temperature-Dependent Growth Mechanisms and Metastability. *Physical Chemistry Chemical Physics* **2015,** *17* (43), 29150-29160.

14. Baio, J. E.; Jaye, C.; Fischer, D. A.; Weidner, T. High-Throughput Analysis of Molecular Orientation on Surfaces by NEXAFS Imaging of Curved Sample Arrays. *ACS Combinatorial Science* **2014,** *16* (9), 449-453.

15. Patel, S. N.; Su, G. M.; Luo, C.; Wang, M.; Perez, L. A.; Fischer, D. A.; Prendergast, D.; Bazan, G. C.; Heeger, A. J.; Chabinyc, M. L. NEXAFS Spectroscopy Reveals the Molecular Orientation in Blade-Coated Pyridal [2, 1, 3] Thiadiazole-Containing Conjugated Polymer Thin films. *Macromolecules* **2015,** *48* (18), 6606-6616.

16. Masnadi, M.; Urquhart, S. G. Indirect Molecular Epitaxy: Deposition of *n*-Alkane Thin Films on Au Coated NaCl (001) and HOPG (0001) Surfaces. *Langmuir* **2013,** *29* (21), 6302-6307.

17. Urquhart, S. G.; Lanke, U. D.; Fu, J. Characterisation of Molecular Orientation in Organic Nanomaterials by X-ray Linear Dichroism Microscopy. *International Journal of Nanotechnology* **2008,** *5* (9-12), 1138-1170.

18. Fu, J.; Urquhart, S. G. Linear Dichroism in the X-ray Absorption Spectra of Linear *n*-Alkanes. *The Journal of Physical Chemistry A* **2005,** *109* (51), 11724-11732.

19. Ade, H. NEXAFS and X-Ray Linear Dichroism Microscopy and Applications to Polymer Science. In *X-Ray Microscopy and Spectromicroscopy: Status Report from the Fifth International Conference, Würzburg, August 19–23, 1996*, Thieme, J.; Schmahl, G.; Rudolph, D.; Umbach, E., Eds. Springer Berlin Heidelberg: Berlin, Heidelberg, Germany, **1998**.

20. Urquhart, S. G.; Gillies, R. Rydberg-Valence Mixing in the Carbon 1s Near-Edge X-ray Absorption Fine Structure Spectra of Gaseous Alkanes. *The Journal of Physical Chemistry A* **2005,** *109* (10), 2151-2159.

21. Urquhart, S. G.; Gillies, R. Matrix Effects in the Carbon 1s Near Edge X-ray Absorption Fine Structure Spectra of Condensed alkanes. *The Journal of Chemical Physics* **2006,** *124* (23), 234704.

22. Scholl, A.; Fink, R.; Umbach, E.; Mitchell, G. E.; Urquhart, S. G.; Ade, H. Towards a Detailed Understanding of the NEXAFS Spectra of Bulk Polyethylene Copolymers and Related Alkanes. *Chemical Physics Letters* **2003,** *370* (5), 834-841.

23. Schmidt, N.; Wenzel, J.; Dreuw, A.; Fink, R. H.; Hieringer, W. Matrix Effects in the Carbon 1s Photoabsorption Spectra of Condensed Naphthalene. *The Journal of Chemical Physics* **2016,** *145* (23), 234307.

24. Nilsson, A.; Pettersson, L. G. M. The Structural Origin of Anomalous Properties of Liquid Water. *Nature Communications* **2015,** *6*, 8998.

25. Fransson, T.; Zhovtobriukh, I.; Coriani, S.; Wikfeldt, K. T.; Norman, P.; Pettersson, L. G. M. Requirements of First-Principles Calculations of X-ray Absorption Spectra of Liquid Water. *Physical Chemistry Chemical Physics* **2016,** *18* (1), 566-583.

26. Wernet, P.; Nordlund, D.; Bergmann, U.; Cavalleri, M.; Odelius, M.; Ogasawara, H.; Näslund, L.; Hirsch, T. K.; Ojamäe, L.; Glatzel, P. The Structure of the First Coordination Shell in Liquid Water. *Science* **2004,** *304* (5673), 995-999.

27. Prendergast, D.; Galli, G. X-ray Absorption Spectra of Water from First Principles Calculations. *Physical Review Letters* **2006,** *96* (21), 215502.

28. Cai, Y. Q.; Mao, H. K.; Chow, P. C.; Tse, J. S.; Ma, Y.; Patchkovskii, S.; Shu, J. F.; Struzhkin, V.; Hemley, R. J.; Ishii, H. Ordering of Hydrogen Bonds in High-Pressure Low-Temperature H_2O. *Physical Review Letters* **2005,** *94* (2), 025502.

29. Leetmaa, M.; Ljungberg, M. P.; Lyubartsev, A.; Nilsson, A.; Pettersson, L. G. M. Theoretical Approximations to X-ray Absorption Spectroscopy of Liquid Water and Ice. *Journal of Electron Spectroscopy and Related Phenomena* **2010,** *177* (2), 135-157.

30. Stevens, J. S.; Seabourne, C. R.; Jaye, C.; Fischer, D. A.; Scott, A. J.; Schroeder, S. L. M. Incisive Probing of Intermolecular Interactions in Molecular Crystals: Core Level Spectroscopy Combined with Density Functional Theory. *The Journal of Physical Chemistry B* **2014,** *118* (42), 12121-12129.

31. Stevens, J. S; Gainar, A.; Jaye, C.; Fischer, D. A; Schroeder, S. L. M. NEXAFS and XPS of P-Aminobenzoic Acid Polymorphs: The Influence of Local Environment. *Journal of Physics: Conference Series* **2016,** *712*, 012133.

32. Bradeanu, I. L.; Flesch, R.; Kosugi, N.; Pavlychev, A. A.; Ruhl, E. Carbon 1s $\rightarrow \pi^*$ Excitation in Variable Size Benzene Clusters. *Physical Chemistry Chemical Physics* **2006,** *8* (16), 1906-1913.

33. Flesch, R.; Pavlychev, A. A.; Neville, J. J.; Blumberg, J.; Kuhlmann, M.; Tappe, W.; Senf, F.; Schwarzkopf, O.; Hitchcock, A. P.; Ruhl, E. Dynamic Stabilization in Excited Nitrogen Clusters. *Physical Review Letters* **2001,** *86* (17), 3767-3770.

34. Pavlychev, A. A.; Flesch, R.; Ruhl, E. Line Shapes of Excited Molecular Clusters. *Physical Review A* **2004,** *70* (1), 015201.

35. Kim, D. H.; Park, Y. D.; Jang, Y.; Yang, H.; Kim, Y. H.; Han, J. I.; Moon, D. G.; Park, S.; Chang, T.; Chang, C. Enhancement of Field Effect Mobility Due to Surface Mediated Molecular Ordering in Regioregular Polythiophene Thin Film Transistors. *Advanced Functional Materials* **2005,** *15* (1), 77-82.

36. Obata, S.; Shimoi, Y. Control of Molecular Orientations of Poly(3-hexylthiophene) on Self-Aassembled Monolayers: Molecular Dynamics Simulations. *Physical Chemistry Chemical Physics* **2013,** *15* (23), 9265-9270.

37. Hu, W.; Gompf, B.; Pflaum, J.; Schweitzer, D.; Dressel, M. Transport Properties of [2,2]-Paracyclophane Thin Films. *Applied Physics Letters* **2004,** *84* (23), 4720-4722.

38. Bachrach, S. M. DFT Study of [2,2], [3,3], and [4,4] Paracyclophanes: Strain Energy, Conformations, and Rotational Barriers. *The Journal of Physical Chemistry A* **2011,** *115* (11), 2396-2401.

39. Batra, A.; Kladnik, G.; Vazquez, H.; Meisner, J. S.; Floreano, L.; Nuckolls, C.; Cvetko, D.; Morgante, A.; Venkataraman, L. Quantifying Through-Space Charge Transfer Dynamics in π-Coupled Molecular Systems. *Nature Communications* **2012,** *3*, 1086.

40. Hope, H.; Bernstein, J.; Trueblood, K. The Crystal and Molecular Structure of 1, 1, 2, 2, 9, 9, 10, 10-Octafluoro-[2, 2] Paracyclophane and a Reinvestigation of the Structure of [2, 2] Paracyclophane. *Acta Crystallographica Section B: Structural Crystallography and Crystal Chemistry* **1972,** *28* (6), 1733-1743.

41. Lonsdale, D. K.; Milledge, H. J.; Rao, K. V. K. Studies of the Structure, Thermal Expansion and Molecular Vibrations of di-p-Xylylene $C_{16}H_{16}$ at 93K and 291K. *Proceedings of the Royal Society of London A: Mathematical, Physical and Engineering Sciences* **1960,** 82-100.

42. Gantzel, P.; Trueblood, K. The Crystal and Molecular Structure of [3,3] Paracyclophane. *Acta Crystallographica* **1965,** *18* (5), 958-968.

43. Lyssenko, K. A.; Korlyukov, A. A.; Antipin, M. Y. The Role of Intermolecular H-H and C-H Interactions in the Ordering of [2,2] Paracyclophane at 100 K: Estimation of the Sublimation Energy from the Experimental Electron Density Function. *Mendeleev Communications* **2005,** *15* (3), 90-92.

44. Brown, C.; Farthing, A. Preparation and Structure of di-p-Xylylene. *Nature* **1949,** *164* (4178), 915-916.

45. Dodziuk, H.; Szymański, S.; Jaźwiński, J.; Ostrowski, M.; Demissie, T. B.; Ruud, K.; Kuś, P.; Hopf, H.; Lin, S. T. Structure and NMR Spectra of Some [2,2] Paracyclophanes. The Dilemma of [2.2] Paracyclophane Symmetry. *The Journal of Physical Chemistry A* **2011,** *115* (38), 10638-10649.

46. Jones, P.; Hopf, H.; Pechlivanidis, Z.; Boese, R. Structure of [4,4] Paracyclophane and Three [mn] Paracyclophane Derivatives. *Zeitschrift fur Kristallographie* **1994,** *209*, 673-676.

47. Regier, T.; Krochak, J.; Sham, T. K.; Hu, Y. F.; Thompson, J.; Blyth, R. I. R. Performance and Capabilities of the Canadian Dragon: The SGM Beamline at the Canadian Light Source. *Nuclear Instruments and Methods in Physics Research Section A: Accelerators, Spectrometers, Detectors and Associated Equipment* **2007,** *582* (1), 93-95.

48. Otero, E.; Wilks, R. G.; Regier, T.; Blyth, R. I. R.; Moewes, A.; Urquhart, S. G. Substituent Effects in the Iron 2p and Carbon 1s Edge Near-Edge X-ray Absorption Fine Structure (NEXAFS) Spectroscopy of Ferrocene Compounds. *The Journal of Physical Chemistry A* **2008,** *112* (4), 624-634.

49. *aXis; Software for Analysis of X-ray Microscopy Images and Spectra*, McMaster University: Ontario, Canada, **2000**.

50. Kaznatcheev, K. V.; Karunakaran, C.; Lanke, U. D.; Urquhart, S. G.; Obst, M.; Hitchcock, A. P. Soft X-ray Spectromicroscopy Beamline at the CLS: Commissioning Results. *Nuclear Instruments and Methods in Physics Research Section A: Accelerators, Spectrometers, Detectors and Associated Equipment* **2007,** *582* (1), 96-99.

51. Ma, Y.; Chen, C. T.; Meigs, G.; Randall, K.; Sette, F. High-Resolution K-Shell Photoabsorption Measurements of Simple Molecules. *Physical Review A* **1991,** *44* (3), 1848-1858.

52. Kohn, W.; Sham, L. J. Self-Consistent Equations Including Exchange and Correlation Effects. *Physical Review* **1965,** *140* (4A), A1133-A1138.

53. Hohenberg, P.; Kohn, W. Inhomogeneous Electron Gas. *Physical Review* **1964,** *136* (3B), B864-B871.

54. Geudtner, G.; Calaminici, P.; Carmona-Espíndola, J.; del Campo, J. M. N.; Domiínguez-Soria, V. C.; Moreno, R. F.; Gamboa, G. U.; Goursot, A.; Köster, A. M.; Reveles, J. U.; Mineva, T.; Vásquez-Pérez, J. M.; Vela, A.; Zuniga-Gutierrez, B.; Salahub, D. R. DeMon2k. *Wiley Interdisciplinary Reviews: Computational Molecular Science* **2012,** *2* (4), 548-555.

55. Koster, A. M.; Geudtner, G.; Calaminici, P.; Casida, M. E.; Dominguez, V. D.; Flores-Moreno, R.; Gamboa, G. U.; Goursot, A.; Heine, T.; Ipatov, A. *deMon2k, Version 3* Cinvestav: Mexico City, **2011**.

56. Triguero, L.; Pettersson, L. G. M.; Ågren, H. Calculations of Near-Edge X-ray-Absorption Spectra of Gas-Phase and Chemisorbed Molecules by Means of Density-Functional and Transition-Potential Theory. *Physical Review B* **1998,** *58* (12), 8097-8110

57. Leetmaa, M.; Ljungberg, M.; Nilsson, A.; Pettersson, L. G. M. *X-Ray Spectroscopy Calculations within Kohn–Sham DFT: Theory and Applications*. Wiley-VCH Verlag GmbH & Co. : Weinheim, Germany, **2009**.

58. *Spartan 14'*, Wavefunction, Inc: Irvine, Califonia, USA, **2014**.

59. Perdew, J. P.; Burke, K.; Ernzerhof, M. Generalized Gradient Approximation Made Simple. *Physical Review Letters* **1996,** *77* (18), 3865-3868.

60. Hammer, B.; Hansen, L. B.; Narskov, J. K. Improved Adsorption Energetics Within Density-Functional Theory Using Revised Perdew-Burke-Ernzerhof Functionals. *Physical Review B* **1999,** *59* (11), 7413-7421.

61. Calaminici, P.; Janetzko, F.; Kaster, A. M.; Mejia-Olvera, R.; Zuniga-Gutierrez, B. Density Functional Theory Optimized Basis Sets for Gradient Corrected Functionals: 3d Transition Metal Systems. *The Journal of Chemical Physics* **2007,** *126* (4), 044108.

62. Calaminici, P.; Flores-Moreno, R.; Koester, A. M. A Density Functional Study of Structures and Vibrations of Ta_3O and Ta_3O. *Computing Letters* **2005,** *1* (4), 164-171.

63. Kutzelnigg, W.; Fleischer, U.; Schindler, M. The IGLO-Method: *ab-initio* Calculation and Interpretation of NMR Chemical Shifts and Magnetic Susceptibilities. In *Deuterium and Shift Calculation*, pp. 165-262. Springer-Verlag: Berlin, Germany, **1990**.

64. Pettersson, L. G. M.; Wahlgren, U.; Gropen, O. Effective Core Potential Parameters for First and Second Row Atoms. *The Journal of Chemical Physics* **1987,** *86* (4), 2176-2184.

65. Cooney, R. R.; Urquhart, S. G. Chemical Trends in the Near-Edge X-ray Absorption Fine Structure of Monosubstituted and Para-Bisubstituted Benzenes. *The Journal of Physical Chemistry B* **2004,** *108* (47), 18185-18191.

66. Urquhart, S. G.; Ade, H.; Rafailovich, M.; Sokolov, J. S.; Zhang, Y. Chemical and Vibronic Effects in the High-Resolution Near-Edge X-ray Absorption Fine Structure Spectra of Polystyrene Isotopomers. *Chemical Physics Letters* **2000,** *322* (5), 412-418.

67. Urquhart, S. G.; Hitchcock, A. P.; Smith, A. P.; Ade, H.; Rightor, E. G. Inner-Shell Excitation Spectroscopy of Polymer and Monomer Isomers of Dimethyl Phthalate. *The Journal of Physical Chemistry B* **1997,** *101* (13), 2267-2276.

68. Urquhart, S. G.; Martinson, M.; Eger, S.; Murcia, V.; Ade, H.; Collins, B. A. Connecting Molecular Conformation to Aggregation in P3HT Using Near Edge X-ray Absorption Fine Structure Spectroscopy. *The Journal of Physical Chemistry C* **2017,** *121* (39), 21720-21728.

Chapter 5 Linear Dichroism in the NEXAFS Spectra of *n*-Alkanes

5.1 Description

Chapter 5 investigates the linear dichroism effect in *n*-alkanes by examining the variation in the C-H band (287 − 288 eV) of the carbon 1s NEXAFS spectra of *n*-alkanes with different chain lengths (*n*-$C_{28}H_{58}$, *n*-$C_{32}H_{66}$ and *n*-$C_{40}H_{82}$) and with different crystalline polymorphs (monoclinic and orthorhombic). Each *n*-alkane in this work is either orthorhombic (acute interior angle 68 ±1 °) or monoclinic (acute interior angle 74 ±1 °) when it cast at room temperature (25 ±1 °C) and at a lower temperature inside the refrigerator (8 ±1 °C). Thinner orthorhombic crystals are favoured at a lower casting temperature whereas thinner monoclinic crystals are favoured at room temperature (25 ±1 °C).

The data presentation focuses on the C-H band, in order to highlight features that are expected to vary with crystal structure and chain length. In these experiments, the X-ray polarization ($\bar{E}$) was directed along the principal crystal axes, X and Y, of the well-defined single crystals. When the polarization ($\bar{E}$) is directed along the short (Y) axis, the first C-H peak ($\sigma^*_{C\text{-}H}$ / $R_{\parallel}$) is stronger and the second C-H peak ($\sigma^*_{C\text{-}H}$ / $R_{\perp}$) is weaker (see **Figure 5.5**). The relative intensity is inverted when the polarization ($\bar{E}$) is directed along the long (X) axis of each single crystal (see **Figure 5.4**). The shape of the "C-H" band with different *n*-alkane chain lengths (*n*-$C_{28}H_{58}$, *n*-$C_{32}H_{66}$ and *n*-$C_{40}H_{82}$) is similar when the X-ray linear polarization ($\bar{E}$) is directed along either the X or the Y principle axes, but different *n*-alkane polymorphs (orthorhombic and monoclinic) exhibit different linear dichroism in their NEXAFS spectra. Especially, a backbone-oriented transition contributing to the low-energy "C-H" band in the monoclinic polymorph.

The experimental work in this study was published in the Journal of Electron Spectroscopy and Related Phenomena [Reproduced with permission from the Journal of Electron Spectroscopy and Related Phenomena, 232, 5-10, Sahan D. Perera and Stephen G. Urquhart, Linear Dichroism in the NEXAFS Spectra of *n*-Alkane Crystalline Polymorphs, Copyright 2018, Elsevier]. This chapter is a literal copy of a paper published in the Journal of Electron Spectroscopy and Related Phenomena with changes to make references, figures, and table numbers consistent throughout the thesis.

5.2 Description of Candidate Contribution

The author of this thesis was the primary investigator for this research work. He prepared the samples, acquired the experimental data, interpreted the experimental results, and wrote the manuscript. J.Wang helped with the experimental set-up for the NEXAFS measurements of *n*-alkane molecules. S. G Urquhart provided guidance throughout the experiments, the process of data analysis and actively involved in the editing process of this manuscript. Dr. S. G. Urquhart and Dr. Jian Wang kindly gave me their permissions to include this manuscript in this dissertation, and agreed to my description of my contribution in this document.

5.3 Relation of Contribution to Research Objectives

The orthorhombic and monoclinic crystal structures of *n*-alkanes differ from each other from their orientation of the paraffin chains with respect to their end group (CH_3) planes. In the monoclinic structure, paraffin chains are inclined to the end group (CH_3) planes whereas paraffin chains are perpendicular to the end group planes in orthorhombic structure. The initial goal of this research work is to examine the effects of Rydberg quenching on the degree of Rydberg-valence mixing in saturated molecules to the NEXAFS spectroscopy caused by different crystalline environments of the saturated molecules (*n*-alkanes) with a broader goal of building a general understanding of the role of intermolecular interactions in NEXAFS spectroscopy. However, at end of this study it was found that these two structures have similar crystalline behaviors due to their nearly similar molecular arrangements of the sub cell (the unit cell). This work did not exhibit differences due to variations in the Rydberg–valence mixing to the low-energy C-H band in the NEXAFS spectra of *n*-alkanes, but this work demonstrated a specific contribution caused by the LD resulted from the different crystalline environment of *n*-alkanes along their principal crystal axes (X and Y). That is orthorhombic and monoclinic polymorphs exhibit different LD in their NEXAFS spectra, in particular a backbone-oriented transition contributing to the low-energy "C-H" band in the monoclinic polymorph.

5.4 Linear Dichroism in the NEXAFS Spectra of *n*-Alkane Crystalline Polymorphs

Sahan D. Perera[1], Jian Wang[2], Stephen G. Urquhart[1]*

1. Department of Chemistry, University of Saskatchewan, Saskatoon, SK, Treaty Six Territory, Canada S7N 5C9
2. Canadian Light Source, University of Saskatchewan, Saskatoon, SK, Canada S7N 0X4

Abstract

Linear Dichroism (LD) in Near Edge X-ray Absorption Fine Structure (NEXAFS) spectroscopy is a useful tool for studying molecular orientation and for clarifying spectroscopic assignments. *n*-Alkane molecules can form single crystals with different polymorphs; orthorhombic and monoclinic in the case of even chain lengths between *n*-$C_{28}H_{58}$ and *n*-$C_{40}H_{82}$. These polymorphs exhibit different LD in their NEXAFS spectra, in particular a backbone-oriented transition contributing to the low-energy "C-H" band in the monoclinic polymorph.

5.4.1 Introduction

n-Alkanes ($C_n H_{2n+2}$) are simple building blocks of complex molecules that include oils, liquid crystals, and polymers. Although *n*-alkanes have a simple structure built upon methyl and methylene groups, the Near Edge X-ray Absorption Fine Structure (NEXAFS) spectra of *n*-alkanes have significant complexity. These spectra vary with the crystalline polymorph, chain length and degree of disorder.

NEXAFS spectroscopy is often used to study the chemical composition[1-7] and bonding[1, 8-10] in organic molecules. In NEXAFS spectroscopy, spectral features are often described as one electron transitions from core electron (e.g. carbon 1s) to an unoccupied valence molecular orbital (e.g. a carbon 1s → σ* or a carbon 1s → π* transition), to Rydberg orbitals (e.g. a carbon 1s → 3p transition), or to transitions with mixed Rydberg / valence character.[11-13] The intensities of these resonances depend on the angle (θ) between the electric field vector of the X-rays ($\overline{E}$) and the transition dipole moment (TDM) for a particular transition. The angle dependence of these resonances follow the below equations.

$$I \propto \left|\overline{E} \cdot \mu_{if}\right|^2 \propto \cos^2\theta \qquad (1)$$

Where μ_{if} is the TDM for the one electron transition from the initial state ψ_i to the final state ψ_f:

$$\mu_{if} = \langle \psi_f | \mu | \psi_i \rangle, \qquad (2)$$

where μ is electric dipole operator. The maximum absorption intensity occurs when the TDM of a NEXAFS transition is parallel to the electric field vector ($\overline{E}$). This linear dichroism (LD) can be used to study molecular orientation for *n*-alkanes and other molecular species and can help clarify spectroscopic assignments.[14-23]

The morphology of an *n*-alkane sample and the orientation of *n*-alkane chains within this sample is affected by conditions that include *n*-alkane chain length,[24] substrate temperature during growth, and the sample preparation method (solution casting versus epitaxial growth by physical vapour deposition).[21, 23-26] Semi-ordered films can be grown by the casting of dilute *n*-alkane solutions onto a surface; these generally have their *n*-alkane chains oriented normal to the surface or at some tilt angle, with rotational disorder about the surface normal. In-plane oriented *n*-alkane thin films can be prepared by epitaxial growth on high symmetry substrates. For example, *n*-alkane films deposited on NaCl(001) or HOPG(0001) surfaces grow with an in-plane orientation that

depends on the surface symmetry, with crystalline morphologies that depend on chain length and substrate temperature.[19, 24, 26-27] Endo *et al.*[28] have used angle dependent NEXAFS spectroscopy to characterize the geometries of in-plane oriented *n*-$C_{12}H_{26}$ on HOPG (0001) as a function of deposition thicknesses. As the film thickness increased, the *n*-alkane chain orientation changed from a geometry with the *n*-alkane C-C-C plane parallel to the HOPG (0001) surface at monolayer coverage, to a geometry with the *n*-alkane C-C-C plane perpendicular to the substrate plane at multilayer thicknesses.[28]

n-Alkane molecules can be crystalized in a regular diamond or parallelogram shape with straight edges, where the *n*-alkane chains within the crystal are directed ~perpendicular to the lamella surface.[23, 29] At room temperature, higher even *n*-alkanes (n > 26) exhibit two different crystalline polymorphs: orthorhombic (o-rh) and monoclinic (mon).[29] For a given alkane chain length, both polymorphs can be formed. Plomp *et al*.[30] found that the metastable orthorhombic polymorph is formed instead of the stable monoclinic form when impurities consisting of *n*-alkanes with shorter chain lengths were present.[30] Solvent selection can also affect the formation of polymorphic structures for given alkane chain length.[31]

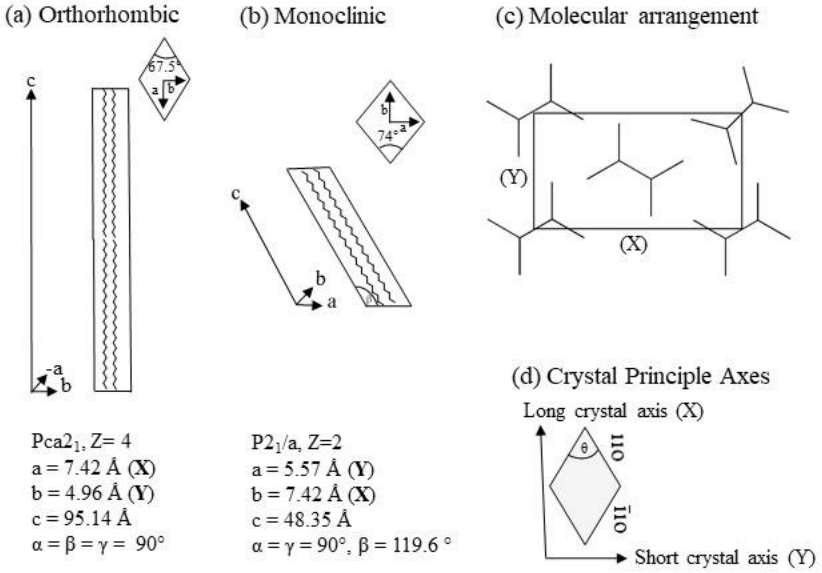

Figure 5.1: Schematic diagram for the chain length orientation, published unit cell parameters and internal angles for (a) orthorhombic and (b) monoclinic structure of *n*-$C_{40}H_{82}$ [30, 34, 50] (c) the molecular arrangement in the orthorhombic and monoclinic polymorph, viewed within the (a,b) plane (vertices are carbon; terminal positions are hydrogen) and (d) principle crystal axes for the *n*-alkane single crystals used in NEXAFS measurements.

The structural difference between monoclinic and orthorhombic polymorphs of a given *n*-alkane is the way that *n*-alkane molecules stack within a layer.[30, 32-33] In the orthorhombic polymorph ($Pca2_1$),[34] *n*-alkane chains are oriented normal to the substrate (a,b) plane, while in the monoclinic polymorph ($P2_1/a$),[35] *n*-alkane chains are tilted with an angle of about 61-65° with respect to the substrate (a,b) plane (**Figure 5.1**).[30, 32, 35-36] A third possible orthorhombic polymorph (polytypic; Pcab,[30] not shown in **Figure 5.1**) consists of two alternating tilted layers – each layer individually like the monoclinic polymorph, but together forming an orthorhombic structure.[30, 37-38] The orthorhombic and monoclinic polymorphs can be resolved by optical microscopy, and therefore provide excellent structural models for single-crystal resolved NEXAFS spectroscopy studies.

Broadly, the NEXAFS spectra of *n*-alkanes consists of a low energy "C-H" band (287-288 eV) and higher energy carbon 1s → σ^*_{C-C} transitions (295-305 eV).[21] The LD of the higher energy carbon 1s → σ^*_{C-C} band is the subject of a long-standing controversy between a "building block" model that treats the molecule's electronic structure as an assembly of bond-specific σ^*_{C-C} orbitals[37] and a molecular-orbital (MO) model[38] that recognizes that MOs are not localized to atom pairs, but are delocalized along the *n*-alkane backbone. When LD is used for orientation measurements, these contrasting models provide different descriptions of the molecular orientation; the $\cos^2\theta$ dependence means that there is no angle where the carbon 1s → σ^*_{C-C} transition intensity would go to zero in the "building block" model, while the intensity of this transition goes to zero in the molecular orbital model.[21] Molecular disorder could be misinterpreted as evidence for the "building block" model, as it would have the same effect on the experimental data. Fu *et al*[21] examined the angle resolved NEXAFS spectra of laterally oriented *n*-alkane single crystals, and found that their LD results corresponded to the molecular orbital model, explicitly excluding the "building block" model.[21]

This work is focused on the low energy "C-H" band (287-288 eV) in the NEXAFS spectra of *n*-alkanes. This band is also a rich source of LD effects. The TDM for the primary "C-H" band spectroscopic features is directed in the CH_2 plane of the methylene group, normal to the chain axis.[21] The polarization dependence of these "C-H" band transitions has been explored by several groups.[28, 39-40] We will use the notion of Endo *et al*.,[39] as illustrated in **Figure 5.2**. The first resonance is assigned as the carbon 1s → σ^*_{C-H} / $R_{\parallel}$ transition, with its TDM within the C-C-C

plane but perpendicular to the *n*-alkane long axis (e.g. parallel to the C-C-C plane).[28] The second resonance is assigned as the carbon 1s → $\sigma^*_{C\text{-}H}$ / $R_\perp$ transition, with its TDM is perpendicular to both the C-C-C plane and to the *n*-alkane long axis (e.g. ⊥ to the C-C-C plane).[28]

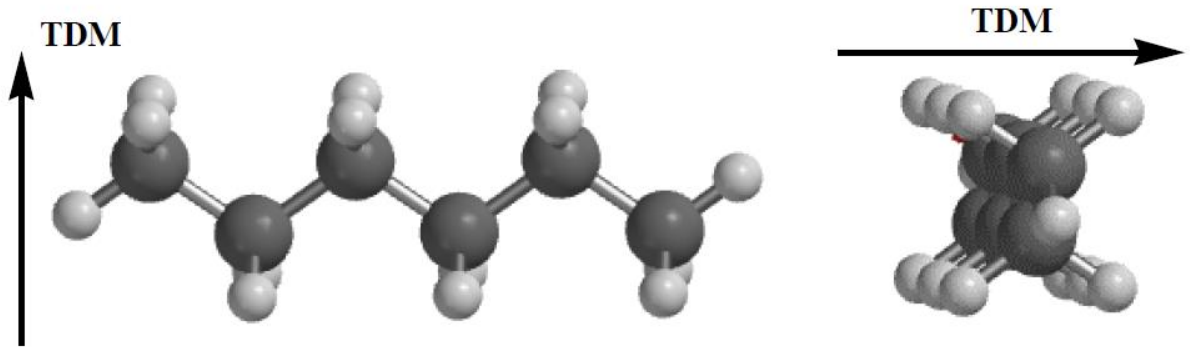

Figure 5.2: Schematic diagram of the TDM for the a) first "C-H" band transition (carbon 1s → $\sigma^*_{C\text{-}H}$ / $R_\parallel$ transition) and the b) second "C-H" band transition (carbon 1s → $\sigma^*_{C\text{-}H}$ / $R_\perp$ transition), relative to a representative *n*-alkane chain (*n*-C_5H_{12}). Parallel and perpendicular are directions relative to the C-C-C plane; both perpendicular to the *n*-alkane backbone.

These assignments are based on the geometry of the individual molecule. In contrast to this molecular view, Zou *et al.*[25] proposed that the LD in these "C-H" band transitions reflects the symmetry of the crystalline sample rather than of a collection of individual molecules.[25] The origin of their proposed breakdown of the individual molecule model has not yet been clarified by theory.

Swaraj *et al.*[26] examined the variation in the carbon 1s NEXAFS spectra as a function of *n*-alkane chain length and the parity of the carbon back bone (e.g. odd and even chain lengths). They proposed that the pre-edge "C-H" band features are affected by the parity (e.g. odd and even chain lengths) of the carbon backbone, but not the *n*-alkane chain length. This work did not account the crystal polymorphism in the *n*-alkane single crystals. As NEXAFS is sensitive to orientation, order, density[41] and crystal symmetry,[25] the crystal polymorph should also be important in determining the NEXAFS spectra and angle dependence, for *n*-alkane single crystals.[25]

In their study on laterally oriented *n*-alkane single crystals, Fu and Urquhart observed a backbone oriented transition ~30 meV above the second peak in the "C-H" band, above the carbon 1s → $\sigma^*_{C\text{-}H}$ / $R_\perp$transition, at 288.51 eV in *n*-hexatriacontane, *n*-$C_{60}H_{122}$).[21] This low-energy

backbone oriented transition was observed in addition to the traditionally assigned carbon 1s → $\sigma^*_{C\text{-}C}$ backbone oriented transition at higher energy (295-305 eV).[21] This observation goes against the common conception of the LD NEXAFS spectra of *n*-alkanes, where the low energy "C-H" band was seen only as having a polarization normal to the chain axis, in the CH_2 plane.

Scanning Transmission X-ray Microscopy (STXM)[9, 42] is useful for these NEXAFS spectroscopy studies, as individual *n*-alkane single crystals can be individually identified and examined. The typical experimental geometry in a STXM is normal incidence to planar substrate. For orthorhombic crystals, the X-ray electric field vector ($\vec{E}$) will be projected in the crystal (a,b) plane, whereas for monoclinic crystals, the electric field vector ($\vec{E}$) will also have a weak projection along the c axis of the crystal, or along the *n*-alkane molecular backbone.

To better understand the NEXAFS spectra of *n*-alkane single crystals and to clarify assignments, we have examined the LD in the carbon 1s NEXAFS spectroscopy of several linear *n*-alkanes (*n*-$C_{28}H_{58}$, *n*-$C_{32}H_{66}$ and *n*-$C_{40}H_{82}$), for different well-resolved crystal structures (orthorhombic and monoclinic). Systematic differences with chain length and crystal structure are characterized and interpreted.

5.4.2 Experimental Section

Samples and Sample Preparation

Samples: Linear alkanes used in this study are *n*-tetracontane (*n*-$C_{40}H_{82}$, 97+ %), *n*-dotriacontane (*n*-$C_{32}H_{66}$, 98%) and *n*-octacosane (*n*-$C_{28}H_{58}$, 99%). These were purchased from Alfa Aesar and used without further purification. All the solvents (toluene, 99.9% and isopropyl alcohol, 99.9%) used in this work were ACS grade and purchased from Fisher Scientific.

For optical microscopy experiments, *n*-alkane samples were prepared on 500 µm thick phosphorus doped silicon (110) wafers (University Wafer). For X-ray spectroscopy and microscope experiments, samples were prepared on 100 nm thick, 0.5 × 0.5 mm low stress silicon nitride (Si_3N_4) windows (Norcada Inc.).

Sample Preparation: Thin crystals of *n*-tetracontane (*n*-$C_{40}H_{82}$), *n*-dotriacontane (*n*-$C_{32}H_{66}$) and *n*-octacosane (*n*-$C_{28}H_{58}$) were prepared by solution casting.[25-26] *n*-Alkane molecules were dissolved in a suitable solvent with a mass/volume ratio of 1.0 mg/2.00 ml and stirred at 50 °C. A drop of a solution was placed on the substrate and solvent evaporation occurred. The substrate temperature

during evaporation, the solvent and substrate were optimized in order to isolate orthorhombic monoclinic polymorphs for a given *n*-alkane chain length (see **Table 2.1** in **Chapter 2**).

Optical and X-ray microscopy shows that these crystals are diamond or rectangular in shape; this indicates that the (a,b) unit cell axes of the crystals are oriented in the substrate plane. Single crystals with straight facet edges and well-defined facet angles could be found for all *n*-alkane samples. As discussed below (see §5.4.3.1), crystals were assigned to monoclinic or orthorhombic crystal structures based on measurement of interior angles. As the convention for defining the a and b axes differs between the orthorhombic and monoclinic polymorphs (see **Figure 5.1a** and **1b**), the principle axis of the crystal shapes (long axis, X; short axis, Y) are used to describe the LD-NEXAFS experimental geometry.

Optical Microscopy and X-ray Spectromicroscopy Characterization

The morphology of the *n*-alkane single crystals was characterized by optical microscopy (Nikon Eclipse ME600, with a Q-Imaging CCD camera) under bright field mode. Representative images are presented in the **Figure 5.3**.

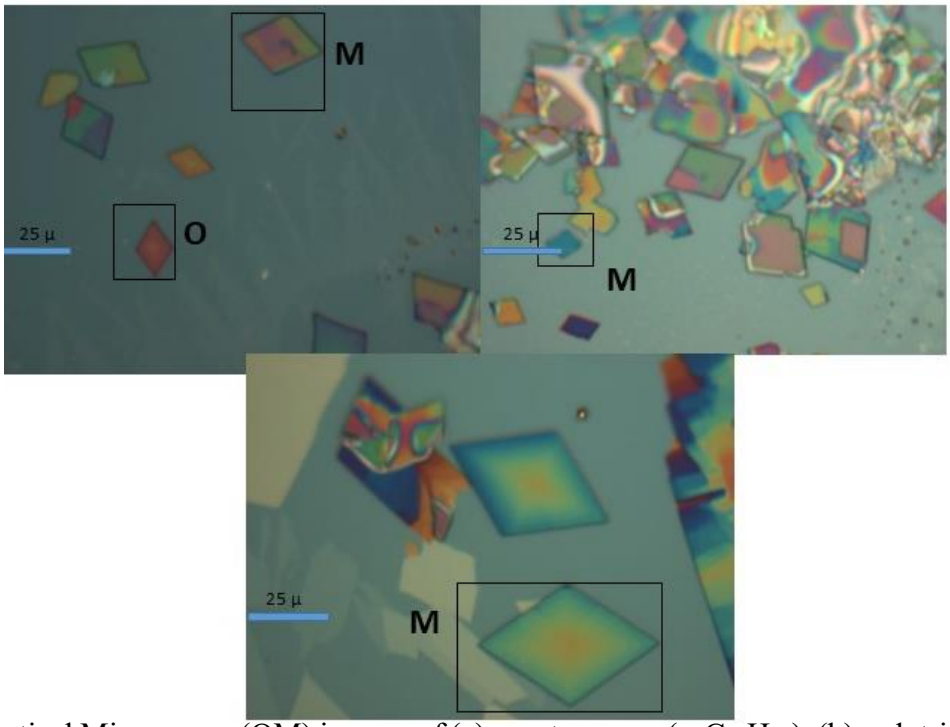

Figure 5.3: Optical Microscopy (OM) images of (a) *n*-octacosane (*n*-$C_{28}H_{58}$), (b) *n*-dotriacontane (*n*-$C_{32}H_{68}$) and (c) *n*-tetracontane (*n*-$C_{40}H_{82}$) under bright field illumination. M and O are monoclinic (mon) and orthorhombic (o-rh) crystal structure. Objective is 50 X with 4*4 binning.

NEXAFS imaging and spectroscopy were obtained at the Spectromicroscopy (SM) beamline (10ID-1, Apple II Elliptically Polarized Undulator) at the Canadian Light Source (CLS), using the ambient Scanning Transmission X-ray Microscope (a-STXM).[42] Spectra and images were acquired in a transmission mode. This presentation focuses on carbon 1s → σ^*_{C-H} transitions (the "C-H" band; 287 − 288 eV), in order to highlight LD features that are expected to vary with crystal structure and chain length. STXM images used for quantitative measurement of the *n*-alkane internal angles were recorded in "point by point" mode, as this mode produced images with less distortion than "rapid scan" imaging mode.

Angle dependent NEXAFS spectra were measured by rotating the sample azimuthally, that is, around the photon propagation direction, while using a fixed electric field polarization vector. The SM beamline's elliptically polarized undulator (EPU) can produce arbitrarily inclined linear polarization. However, small variations in the degree of linear polarization have been observed in the proximity of the carbon dip for horizontal and vertically polarized radiation (see **B.2.1**). To control for this variable, a fixed horizontal polarization was used so that the degree of polarization would be constant for all measurements. Crystals were selected with their principle axes (X or Y) directed horizontally. Small misalignments of the crystal principle axes (see **B.2.3**) with respect to the horizontal linear polarization also has a small effect on the relative intensity of features in the "C-H" band.

The relatively high radiation sensitivity of *n*-alkane molecules[43] limits the permissible dose that can be used for NEXAFS measurements. Experimental conditions (energy point spacing, dwell time, etc.) were optimized to minimize radiation exposure. Image sequence[44] acquisition was used, so that the radiation was distributed over a larger sample volume, and so that the I and I_0 spectra could be acquired simultaneously. The STXM beam was defocused to 150 nm diameter during image sequence data acquisition. Fresh sample areas were used for each spectrum. The threshold for radiation damage was determined by examining the NEXAFS spectra in the carbon 1s continuum (300 eV) to test for mass loss and at the energy of the carbon 1s → $\pi^*_{C=C}$ transition (285 eV) to test for the formation of C=C double bonds.[43, 45] In the experimental conditions used, radiation damage was found to be minimal.

The calibration of the energy scale in the spectra at carbon 1s edge was performed by introducing CO_2 into the microscope chamber with the sample in place, allowing the NEXAFS

spectrum of the alkane sample and CO_2 gas to be recorded simultaneously. The monochromator energy scale was calibrated based on the two vibronic peaks of gaseous CO_2: carbon 1s →3s (v=0) and carbon 1s → 3p (v=0) transitions, which were set to the value of 292.74 eV and 294.96 eV respectively, after Ma *et al*.[8, 46] As all spectra were recorded with *in situ* CO_2 calibration, the spectra are distorted by the strong carbon 1s → π* transition centred at 290.74 eV.

Transmission spectra were converted to optical density with Beer's law (OD = -ln (I/I_0). Data analysis were performed using aXis 2000[47] and spectra are presented using Origin 7.5 software package.[48]

5.4.3 Results

5.4.3.1 Crystal Characterization of *n*-Alkanes

Optical microscopy (OM) was used to identify the shape (diamond or parallelogram) of the well-defined *n*-alkane crystals. Acute interior angles of each *n*-alkane crystal were calculated from high resolution point-by-point STXM images of *n*-alkane crystal. With the aid of literature,[29-30, 34-35, 49-53] acute interior angles were used to determine the crystal structure of each *n*-alkane single crystal.

Figure 5.1 presents the literature unit cell parameters, acute interior angles of the crystal polymorphs, schematics of the unit cells and the chain orientation within these cells, the molecular arrangement within the orthorhombic and monoclinic crystal, and the principle axes (long axis, X and short axis, Y) of the *n*-alkane single crystals used to obtain the NEXAFS spectra.[25-26, 29-31, 34-36, 49-56] Our measured acute internal angles agree with the values derived from literature orthorhombic and monoclinic crystal structures. Each *n*-alkane crystal examined in this work shows either an orthorhombic (acute interior angle 68 ±1 °) or a monoclinic structure (acute interior angle 74 ±1 °) when cast at room temperature (25 ±1 °C) or at lower temperature inside a refrigerator (8 ±1 °C). Thinner orthorhombic crystals are favoured at lower casting temperature whereas thinner monoclinic crystals are favoured at room temperature (25 ±1 °C). Polarized optical microscopy images of *n*-tetracontane ($C_{40}H_{82}$), *n*-dotriacontane ($C_{32}H_{66}$), *n*-octacosane ($C_{28}H_{58}$) crystals obtained from solution casting method were shown in **Figure 5.3**.

5.4.3.2 NEXAFS Measurements of *n*-Alkanes

Figures 5.4 and **5.5** presents the variation in the "C-H" band of the carbon 1s NEXAFS spectra of *n*-alkanes with different chain lengths (*n*-$C_{28}H_{58}$, *n*-$C_{32}H_{66}$ and *n*-$C_{40}H_{82}$) and with

different crystal structures (orthorhombic and monoclinic) with the X-ray polarization directed along the principal crystal axes X (**Figure 5.4**) and Y (**Figure 5.5**), respectively. Spectra are normalized by matching the minimum and maximum intensity feature within the "C-H" band.

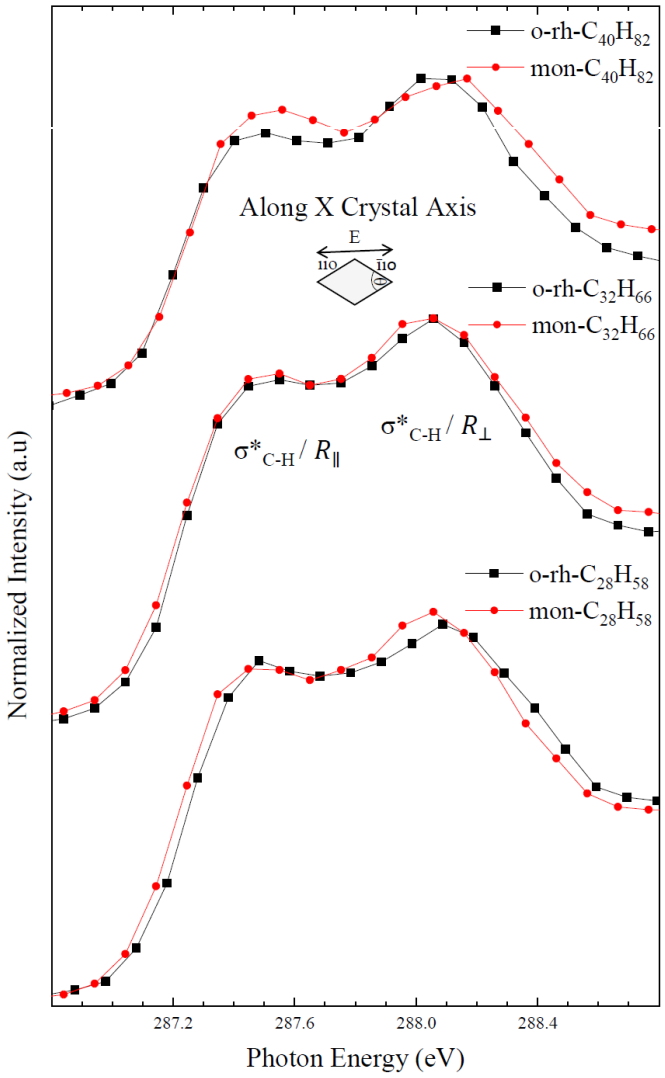

Figure 5.4: Carbon 1s NEXAFS spectra of the "C-H" band for *n*-alkanes (*n*-$C_{40}H_{82}$, *n*-$C_{32}H_{66}$, and *n*-$C_{28}H_{58}$) with orthorhombic (black) monoclinic (red) crystal structure with X-ray linear horizontal polarization directed along long (X) crystal axis.

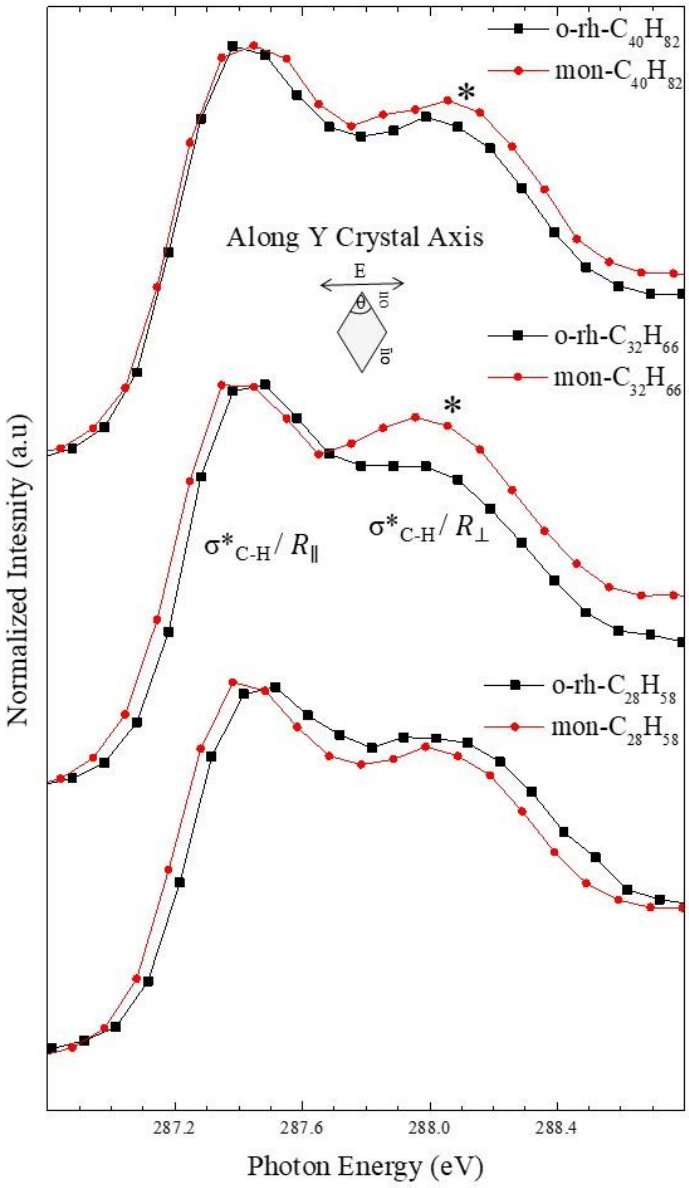

Figure 5.5: Carbon 1s NEXAFS spectra of the "C-H" band for *n*-alkanes (*n*-$C_{40}H_{82}$, *n*-$C_{32}H_{66}$, and *n*-$C_{28}H_{58}$) with orthorhombic (black) monoclinic (red) crystal structure with X-ray linear horizontal polarization directed along short (Y) crystal axis. An asterisk indicates the backbone oriented transition in the NEXAFS spectrum of *n*-$C_{40}H_{82}$ and *n*-$C_{32}H_{66}$.

The shape of the "C-H" band is similar when the X-ray linear polarization ($\overline{E}$) is directed along either the X or the Y principle axes, with only small differences between the different crystalline polymorphs. When the polarization ($\overline{E}$) is directed along the long (X) axis, the first peak ($\sigma^*_{C\text{-}H} / R_{\parallel}$) is weaker and the second peak ($\sigma^*_{C\text{-}H} / R_{\perp}$) is stronger (see **Figure 5.4**). The relative intensity is inverted when the polarization ($\overline{E}$) is directed along the short (Y) axis of each single crystal (see **Figure 5.5**). Detailed differences between these spectra will be discussed below.

5.4.4 Discussion

Each *n*-alkane (*n*-$C_{40}H_{82}$, *n*-$C_{32}H_{66}$ and *n*-$C_{28}H_{58}$) examined in this study forms crystals with monoclinic and orthorhombic forms. The carbon 1s NEXAFS spectra of *n*-alkanes with these two crystal forms are similar to each other in shape. The greatest difference is between monoclinic and orthorhombic spectra, for the spectra recorded when the polarization was directed along the Y crystal axis (**Figure 5.5**).

The local structure (next neighbor, or chain to chain packing) in the monoclinic form is very similar to that in the orthorhombic form. The monoclinic crystal can be described by an orthorhombic sub-cell oriented along the *n*-alkane backbone; this sub-cell has nearly the same local arrangement and geometry as in the orthorhombic structure ($\beta = 91.67°$ in the orthorhombic subshell in the monoclinic polymorph; $\beta = 90°$ in the orthorhombic polymorph).[30, 35] Differences in density, order and packing are known to affect the carbon 1s NEXAFS of polyethyene,[41] which we attribute to variations in Rydberg quenching and Rydberg – valence mixing with the degree of chain packing and density. As the local packing environment of both polymorphs is so similar, differences in Rydberg quenching / Rydberg – valence mixing are not expected. A similar spectroscopic interpretation can be used for both crystalline polymorphs.

It is intuitive to interpret the LD of the "C-H" band in terms of the sum of contributions from *n*-alkane molecules at the center and corner positions of the unit cell, as shown in **Figure 5.1c**. The center and corner sites show a different inclination of their C-C-C backbone plane (setting angle) relative to the unit cell (a, b) vectors. Kawaguchi *et al.*[57] measured a setting angle of 47° between the C-C-C plane and the a axis for *n*-$C_{32}H_{66;}$ Zou *et al.*[25] estimated an angle of ~48° for *n*-$C_{40}H_{82}$[25] from the crystallography data of Teare *et al.*[34] In the Pca2 and $P2_1/a$ space groups, the centre site is related to the corner site by a glide symmetry element, so the C-C-C setting angles are not necessarily orthogonal (although they would be orthogonal for a setting angle of 45°). Analysis of the LD in the NEXAFS spectra of orthorhombic crystals of *n*-tetracontane (*n*-$C_{40}H_{82}$) and *n*-nonadecane (*n*-$C_{19}H_{40}$) by Zou *et al.*[25] showed that a simple molecular-geometry linear dichroism model does not work.[25] When Zou *et al.*[25] examined dichroic ratios for the two "C-H band peaks, they found that these dichroic ratios differed from that expected from molecular geometry considerations. Zou *et al.* proposed that solid-state effects that reflect the symmetry of the crystal modify the LD, and postulated that a band structure interpretation is more appropriate

to interpret the LD of these NEXAFS spectra.[25] An analysis of dichroic ratios was not performed in this work, as our use of *in situ* CO_2 calibration prevents the spectroscopic continuum normalization needed for accurate difference calculations. As well, in the monoclinic species, the second C-H band peak (the carbon 1s → $\sigma^*_{C\text{-}H}$ / $R_\perp$ transition) will overlap with a backbone-oriented transition discussed below; this transition is present in only one polarization. These facts, and unresolved vibronic[12] and nuclear motion[58] contributions obscure any simple analysis of these intensities and the calculation of linear dichroism differences.

The onset of the first peak (carbon 1s → $\sigma^*_{C\text{-}H}$ / $R_\parallel$ transition) appears at slightly lower energy in the spectra of the lower molecular weight monoclinic polymorphs (*n*-$C_{28}H_{58}$ and *n*-$C_{32}H_{66}$; not for *n*-$C_{40}H_{82}$). The origin of this low energy onset is not immediately obvious. From modeling of defect structures, we expect the "C-H" band transitions to appear at lower energy for *n*-alkanes with thermally populated vibrational modes or with gauche defects.[58] However, and particularly for these shorter *n*-alkanes, the monoclinic polymorph is the thermodynamically stable form. Given the *in situ* calibration of the energy scale, we have a high confidence in the fidelity of this energy shift observation. Reflecting the band-structure postulate of Zou *et al*.[25] in modifying the LD of the carbon 1s → $\sigma^*_{C\text{-}H}$ / $R_\parallel$ and the carbon 1s → $\sigma^*_{C\text{-}H}$ / $R_\perp$ transitions, a further modification of the $\sigma^*_{C\text{-}H}$ / $R_\parallel$ core excited state unique to the monoclinic polymorph could be possible. However, as DFT simulations of NEXAFS spectra with periodic boundary conditions are non-trivial for non-orthorhombic unit cells, resolution of this question must be left to future work.

In the monoclinic polymorph, the *n*-alkane chain is inclined towards the short crystal axis (Y in **Figure 5.1**; $\beta = 119.6°$ instead of $\beta = 90°$ in the orthorhombic polymorph). As a result, NEXAFS spectra with the polarization component directed along the long axis (X in **Figure 5.1b**) will only have only have $\sigma^*_{C\text{-}H}$ / $R_\parallel$ and $\sigma^*_{C\text{-}H}$ / $R_\perp$ character, while the component along the short axis (Y in **Figure 5.1b**) will have some backbone TDM component. Fu and Urquhart demonstrated that a backbone-oriented transition is found ~30 meV above the second "C-H" band ($\sigma^*_{C\text{-}H}$ / $R_\perp$; at 288.51 eV in *n*-hexatriacontane, *n*-$C_{60}H_{122}$.[21] Based on Fu's results, we expect a backbone-oriented transition to be observed in the monoclinic polymorph, but only when the polarization is directed along the short crystal axis, Y. Further, as the optical orbital for this transition is largely within the molecule itself, it should not be affected by the band structure / intermolecular effects

proposed by Zou *et al.*[25] for the carbon 1s → $\sigma^*_{C\text{-}H}$ / $R_{\parallel}$ and carbon 1s → $\sigma^*_{C\text{-}H}$ / $R_{\perp}$ transitions.[25] The intensity of this transition will be ~24% of that when the polarization is completely directed along the *n*-alkane backbone (applying equation 1, β = 119.6° gives a backbone angle of 60.4° from the polarization vector). This higher energy backbone-oriented component will be only visible in the "C-H" band for the Y-axis polarized spectra of the monoclinic polymorph. This is precisely the difference observed as a higher energy shoulder in **Figure 5.5** (Y-axis polarized) for the monoclinic spectra (~288 eV) and absent in **Figure 5.4** (X-axis polarized). We note that the comparison of the spectra of the orthorhombic and monoclinic *n*-$C_{28}H_{58}$ is not consistent with this trend; an exploration of the role of a thermally accessible defect mode uniquely present in the orthorhombic species is the subject of temperature dependent NEXAFS studies now underway.[58, 59]

5.4.5 Conclusions

This work presents the linear dichroism (LD) in the carbon 1s NEXAFS spectra of a series of *n*-alkanes (*n*-$C_{28}H_{58}$ *n*-$C_{32}H_{66}$ and *n*-$C_{40}H_{82}$), with orthorhombic and monoclinic structures. The key structural difference between the monoclinic and orthorhombic polymorphs is the inclination of the monoclinic unit cell (β = 119.6° versus 90° in the orthorhombic structure), towards the short axis of the monoclinic single crystals. This inclination leads to a contribution from a backbone-oriented transition in the "C-H" band, as observed by Fu *et al.*[21] This contribution appears as a high energy shoulder in the "C-H" band, but only for spectra with the polarization directed along the short axis (Y) of the monoclinic crystal. These results show the importance of detailed crystal structure considerations when interpreting the NEXAFS spectra of single crystals.

5.4.6 References

1. Rightor, E. G.; Urquhart, S. G.; Hitchcock, A. P.; Ade, H.; Smith, A. P.; Mitchell, G. E.; Priester, R. D.; Aneja, A.; Appel, G.; Wilkes, G.; Lidy, W. E. Identification and Quantitation of Urea Precipitates in Flexible Polyurethane Foam Formulations by X-ray Spectromicroscopy. *Macromolecules* **2002,** *35* (15), 5873-5882.

2. Lipton-Duffin, J.; Miwa, J. A.; Urquhart, S. G.; Contini, G.; Cossaro, A.; Casalis, L.; Barth, J. V.; Floreano, L.; Morgante, A.; Rosei, F. Binding Geometry of Hydrogen-Bonded Chain Motif in Self-Assembled Gratings and Layers on Ag(111). *Langmuir* **2012,** *28* (40), 14291-14300.

3. Qaqish, S. E.; Urquhart, S. G.; Lanke, U.; Brunet, S. M. K.; Paige, M. F. Phase Separation of Palmitic Acid and Perfluorooctadecanoic Acid in Mixed Langmuir−Blodgett Monolayer Films. *Langmuir* **2009,** *25* (13), 7401-7409.

4. Iyer, G. R. S.; Wang, J.; Wells, G.; Bradley, M. P.; Borondics, F. Nanoscale Imaging of Freestanding Nitrogen Doped Single Layer Graphene. *Nanoscale* **2015,** *7* (6), 2289-2294.

5. Hitchcock, A. P.; Berejnov, V.; Lee, V.; West, M.; Colbow, V.; Dutta, M.; Wessel, S. Carbon Corrosion of Proton Exchange Membrane Fuel Cell Catalyst Layers Studied by Scanning Transmission X-ray Microscopy. *Journal of Power Sources* **2014,** *266*, 66-78.

6. Meier, R.; Schindler, M.; Müller-Buschbaum, P.; Watts, B. Residual Solvent Content in Conducting Polymer-Blend Films Mapped With Scanning Transmission X-ray Microscopy. *Physical Review B* **2011,** *84* (17), 174205.

7. Zhong, J.; Zhang, H.; Sun, X.; Lee, S. T. Synchrotron Soft X-ray Absorption Spectroscopy Study of Carbon and Silicon Nanostructures for Energy Applications. *Advanced Materials* **2014,** *26* (46), 7786-7806.

8. Dhez, O.; Ade, H.; Urquhart, S. G. Calibrated NEXAFS Spectra of Some Common Polymers. *Journal of Electron Spectroscopy and Related Phenomena* **2003,** *128* (1), 85-96.

9. Ade, H.; Urquhart, S. G. NEXAFS Spectroscopy and Microscopy of Natural and Synthetic Polymers. In *Chemical Applications Of Synchrotron Radiation: Part I: Dynamics and VUV SpectroscopyPart II: X-Ray Applications*, pp. 285-355. World Scientific: Singapore, **2002**.

10. Gainar, A.; Stevens, J. S.; Jaye, C.; Fischer, D. A.; Schroeder, S. L. M. NEXAFS Sensitivity to Bond Lengths in Complex Molecular Materials: A Study of Crystalline Saccharides. *The Journal of Physical Chemistry B* **2015,** *119* (45), 14373-14381.

11. Stohr, J. *NEXAFS Spectroscopy*. Springer-Verlag: Berlin, Germany, **1992**.

12. Urquhart, S. G.; Gillies, R. Rydberg-Valence Mixing in the Carbon 1s Near-Edge X-ray Absorption Fine Structure Spectra of Gaseous Alkanes. *The Journal of Physical Chemistry A* **2005,** *109* (10), 2151-2159.

13. Urquhart, S. G.; Gillies, R. Matrix Effects in the Carbon 1s Near Edge X-ray Absorption Fine Structure Spectra of Condensed Alkanes. *The Journal of Chemical Physics* **2006,** *124* (23), 234704.

14. Ney, A.; Ney, V.; Ollefs, K.; Schauries, D.; Wilhelm, F.; Rogalev, A. X-Ray Linear Dichroism: An Element-Selective Spectroscopic Probe for Local Structural Properties and Valence. *Journal of Surfaces and Interfaces of Materials* **2014,** *2* (1), 14-23.

15. Rossi, G.; d'Acapito, F.; Amidani, L.; Boscherini, F.; Pedio, M. Local Environment of Metal ions in Phthalocyanines: K-Edge X-ray Absorption Spectra. *Physical Chemistry Chemical Physics* **2016,** *18* (34), 23686-23694.

16. Marchetto, H.; Schmidt, T.; Groh, U.; Maier, F. C.; Levesque, P. L.; Fink, R. H.; Freund, H. J.; Umbach, E. Direct Observation of Epitaxial Organic Film Growth: Temperature-Dependent Growth Mechanisms and Metastability. *Physical Chemistry Chemical Physics* **2015,** *17* (43), 29150-29160.

17. Baio, J. E.; Jaye, C.; Fischer, D. A.; Weidner, T. High-Throughput Analysis of Molecular Orientation on Surfaces by NEXAFS Imaging of Curved Sample Arrays. *ACS Combinatorial Science* **2014,** *16* (9), 449-453.

18. Patel, S. N.; Su, G. M.; Luo, C.; Wang, M.; Perez, L. A.; Fischer, D. A.; Prendergast, D.; Bazan, G. C.; Heeger, A. J.; Chabinyc, M. L.; Kramer, E. J. NEXAFS Spectroscopy Reveals the Molecular Orientation in Blade-Coated Pyridal[2,1,3]Thiadiazole-Containing Conjugated Polymer Thin Films. *Macromolecules* **2015,** *48* (18), 6606-6616.

19. Masnadi, M.; Urquhart, S. G. Indirect Molecular Epitaxy: Deposition of *n*-Alkane Thin Films on Au Coated NaCl(001) and HOPG(0001) Surfaces. *Langmuir* **2013,** *29* (21), 6302-6307.

20. Urquhart, S. G.; Lanke, U. D.; Fu, J. Characterisation of Molecular Orientation in Organic Nanomaterials by X-ray Linear Dichroism Microscopy. *International Journal of Nanotechnology* **2008,** *5* (9-12), 1138-1170.

21. Fu, J.; Urquhart, S. G. Linear Dichroism in the X-ray Absorption Spectra of Linear *n*-Alkanes. *The Journal of Physical Chemistry A* **2005,** *109* (51), 11724-11732.

22. Thieme, J.; Schmahl, G.; Rudolph, D.; Umbach, E. *X-Ray Microscopy and Spectromicroscopy: Status Report from the Fifth International Conference, Würzburg, August 19–23, 1996*. Springer Science & Business Media, **2013**.

23. Hastie, G. P.; Johnstone, J.; Roberts, K. J.; Fischer, D. Examination of the Structure and Melting Behaviour of Thin film *n*-Alkanes Using Ultra-Soft Polarised Near-Edge X-ray Absorption Spectroscopy. *Journal of the Chemical Society, Faraday Transactions* **1996,** *92* (5), 783-789.

24. Fu, J.; Urquhart, S. G. Effect of Chain Length and Substrate Temperature on the Growth and Morphology of *n*-Alkane Thin Films. *Langmuir* **2007,** *23* (5), 2615-2622.

25. Zou, Y.; Araki, T.; Appel, G.; Kilcoyne, A. L. D.; Ade, H. Solid State Effects in the NEXAFS Spectra of Alkane-Based van der Waals Crystals: Breakdown of Molecular Model. *Chemical Physics Letters* **2006,** *430* (4), 287-292.

26. Swaraj, S.; Ade, H. Differences in NEXAFS of Odd/Even Long Chain *n*-Alkane Crystals. *Journal of Electron Spectroscopy and Related Phenomena* **2013,** *191*, 60-64.

27. Masnadi, M.; Urquhart, S. G. Effect of Substrate Temperature on the Epitaxial Growth of Oriented *n*-Alkane Thin Films on Graphite. *Langmuir* **2012,** *28* (34), 12493-12501.

28. Endo, O.; Horikoshi, T.; Katsumata, N.; Otani, K.; Fujishima, T.; Goto, H.; Minami, K.; Akaike, K.; Ozaki, H.; Sumii, R. Incommensurate Crystalline Phase of *n*-Alkane Monolayers on Graphite (0001). *The Journal of Physical Chemistry C* **2011,** *115* (13), 5720-5725.

29. Broadhurst, M. G. An Analysis of the Solid Phase Behavior of the Normal Paraffins. *Journal of Research of the National Bureau of Standards* **1962,** *66*, 241-249.

30. Plomp, M.; Van Enckevort, W.; Van Hoof, P.; Van De Streek, C. Morphology of and Dislocation Movement in *n*-$C_{40}H_{82}$ Paraffin Crystals Grown From Solution. *Journal of Crystal Growth* **2003,** *249* (3), 600-613.

31. Boistelle, R.; Simon, B.; Pepe, G. Polytypic Structures of *n*-$C_{28}H_{58}$ (*n*-Octacosane) and *n*-$C_{36}H_{74}$ (*n*-Hexatriacontane). *Acta Crystallographica Section B* **1976,** *32* (4), 1240-1243.

32. Kubota, H.; Kaneko, F.; Kawaguchi, T.; Kawasaki, M. Polytypic Transition of *n*-Hexatriacontane During Solution Crystallization. *Crystal Growth & Design* **2004,** *4* (2), 369-375.

33. Kubota, H.; Kaneko, F.; Kawaguchi, T.; Kawasaki, M. Polytypic Transformation During Crystal Growth Monitored By Newly Developed Micro-FTIR System for Three-Dimensional Structural Studies. *Journal of Crystal Growth* **2002,** *237*, 373-378.

34. Teare, P. The Crystal Structure of Orthorhombic *n*-Hexatriacontane, *n*-$C_{36}H_{74}$. *Acta Crystallographica* **1959,** *12* (4), 294-300.

35. Shearer, H.; Vand, V. The Crystal Structure of the Monoclinic Form of *n*-Hexatriacontane. *Acta Crystallographica* **1956,** *9* (4), 379-384.

36. Turner, W. R. Normal Alkanes. *Industrial & Engineering Chemistry Product Research and Development* **1971,** *10* (3), 238-260.

37. Outka, D.; Stöhr, J.; Rabe, J.; Swalen, J.; Rotermund, H. Orientation of Arachidate Chains in Langmuir-Blodgett Monolayers on Si (111). *Physical Review Letters* **1987,** *59* (12), 1321-1324.

38. Hähner, G.; Kinzler, M.; Wöll, C.; Grunze, M.; Scheller, M.; Cederbaum, L. Near Edge X-Ray-Absorption Fine-Structure Determination of Alkyl-Chain Orientation: Breakdown of the ''Building-Block''Scheme. *Physical Review Letters* **1991,** *67* (7), 851-854.

39. Endo, O.; Ozaki, H.; Sumii, R.; Amemiya, K.; Nakamura, M.; Kosugi, N. Orientation of *n*-Alkane in Thin Films on Graphite (0 0 0 1) Studied Using Carbon K-NEXAFS. *Journal of Electron Spectroscopy and Related Phenomena* **2011,** *184* (3-6), 257-260.

40. Weiss, K.; Öström, H.; Triguero, L.; Ogasawara, H.; Garnier, M.; Pettersson, L.; Nilsson, A. XPS and XAS Investigation of Condensed and Adsorbed *n*-Octane on a Cu (110) Surface. *Journal of Electron Spectroscopy and Related Phenomena* **2003,** *128* (2-3), 179-191.

41. Schöll, A.; Fink, R.; Umbach, E.; Mitchell, G.; Urquhart, S.; Ade, H. Towards a Detailed Understanding of the NEXAFS Spectra of Bulk Polyethylene Copolymers and Related Alkanes. *Chemical Physics Letters* **2003,** *370* (5-6), 834-841.

42. Kaznatcheev, K.; Karunakaran, C.; Lanke, U.; Urquhart, S.; Obst, M.; Hitchcock, A. Soft X-ray Spectromicroscopy Beamline at the CLS: Commissioning Results. *Nuclear Instruments and Methods in Physics Research Section A: Accelerators, Spectrometers, Detectors and Associated Equipment* **2007,** *582* (1), 96-99.

43. Coffey, T.; Urquhart, S.; Ade, H. Characterization of the Effects of Soft X-ray Irradiation on Polymers. *Journal of Electron Spectroscopy and Related Phenomena* **2002,** *122* (1), 65-78.

44. Jacobsen, C.; Wirick, S.; Flynn, G.; Zimba, C. Soft X-Ray Spectroscopy from Image Sequences with Sub-100 nm Spatial Resolution. *Journal of Microscopy* **2000,** *197* (2), 173-184.

45. Rightor, E.; Hitchcock, A.; Ade, H.; Leapman, R.; Urquhart, S.; Smith, A.; Mitchell, G.; Fischer, D.; Shin, H.; Warwick, T. Spectromicroscopy of Poly (Ethylene Terephthalate): Comparison of Spectra and Radiation Damage Rates in X-ray Absorption and Electron Energy Loss. *The Journal of Physical Chemistry B* **1997,** *101* (11), 1950-1960.

46. Ma, Y.; Chen, C.; Meigs, G.; Randall, K.; Sette, F. High-Resolution K-Shell Photoabsorption Measurements of Simple Molecules. *Physical Review A* **1991,** *44* (3), 1848-1858.

47. *aXis; Software for Analysis of X-ray Microscopy Images and Spectra*, McMaster University: Ontario, Canada, **2000**.

48. *Origin; Software For Data Analysis and Graphing*, Version 7.5; Origin Lab: Northampton State, USA, **1991**.

49. Liu, X. Y.; Bennema, P. On the Morphology of Normal Alkane Crystals with Monoclinic Structures: Theory and Observations. *Journal of Applied Crystallography* **1993,** *26* (2), 229-242.

50. Craig, S. R.; Hastie, G. P.; Roberts, K. J.; Sherwood, J. N. Investigation into the Structures of Some Normal Alkanes Within the Homologous Series $C_{13}H_{28}$ to $C_{60}H_{122}$ Using High-Resolution Synchrotron X-ray Powder Diffraction. *Journal of Materials Chemistry* **1994,** *4* (6), 977-981.

51. Dorset, D. L. Crystal Structure of an *n*-Paraffin Binary Eutectic Solid. An Electron Diffraction Determination. *The Journal of Physical Chemistry B* **1997,** *101* (25), 4870-4874.

52. Nyburg, S.; Potworowski, J. Prediction of unit Cells and Atomic Coordinates for the *n*-Alkanes. *Acta Crystallographica Section B: Structural Crystallography and Crystal Chemistry* **1973,** *29* (2), 347-352.

53. Chevallier, V.; Petitjean, D.; Ruffier-Meray, V.; Dirand, M. Correlations Between the Crystalline Long c-Parameter and The Number of Carbon Atoms of Pure *n*-Alkanes. *Polymer* **1999,** *40* (21), 5953-5956.

54. Hubbard, B. Some Observations on the Optical Properties of Long Chain Normal Paraffins. *American Mineralogist: Journal of Earth and Planetary Materials* **1945,** *30* (11-12), 645-672.

55. Streek, J. V. D.; Verwer, P.; Bennema, P.; Vlieg, E. On the Influence of Thermal Motion on the Crystal Structures and Polymorphism of Even *n*-Alkanes. *Acta Crystallographica Section B: Structural Science* **2002,** *58* (4), 677-683.

56. Kawaguchi, A.; Isoda, S.; Ohara, M.; Katayama, K. I. Radiation-Induced Phase Transition of Paraffins. *Bulletin of the Institute for Chemical Research, Kyoto University* **1981,** *59* (4), 284-292.

57. Kawaguchi, A.; Ohara, M.; Kobayashi, K. Setting Angle of Molecular Chains in Polyethylene Crystals. *Journal of Macromolecular Science, Part B: Physics* **1979,** *16* (2), 193-212.

58. Perera, S. D.; Shokatian, S.; Wang, J.; Urquhart, S. G. Temperature Dependence in the NEXAFS Spectra of *n*-Alkanes. *The Journal of Physical Chemistry A* **2018,** *122* (49), 9512-9517.

59. Perera, S. D.; Wang, J.; Urquhart, S.G. Contribution of Molecular Disorder Effect to the Carbon 1s NEXAFS Spectra of *n*-Alkanes, **2019** (Chapter 7).

Chapter 6 Contribution of Nuclear Motion Effect to the Carbon 1s NEXAFS Spectra of *n*-Alkanes

6.1 Description

Chapters 6 and **7** investigate the contribution of nuclear motion to the carbon 1s NEXAFS spectroscopy of *n*-alkanes. In this chapter, the origin for the spectral broadening observed for short chain o-rh *n*-$C_{28}H_{58}$ in **Chapter 5** is discussed in terms of nuclear motion attributed to thermally populated vibrational and defect modes. The o-rh *n*-$C_{28}H_{58}$ crystals were prepared by using solution casting method and their crystal structure confirmed by measuring the interior angles of each *n*-alkane crystal with high resolution point-by-point STXM images, recorded at 287.5 eV.

In this work, the nuclear motion contribution to the spectral broadening in NEXAFS spectroscopy was examined by a spectral comparison of o-rh *n*-$C_{28}H_{58}$ at room temperature and at cryogenic temperatures, where nuclear motion (save zero-point motion) contribution should be minimal. The result shows the C-H band (287-288 eV) in the NEXAFS spectrum of o-rh *n*-$C_{28}H_{58}$ is broader and appears at a lower energy (~ 200 meV lower) in the room temperature (298 K) spectrum than in its NEXAFS spectrum recorded at cryogenic temperature (93 K). This suggests that nuclear motion effect plays an important role in the spectral broadening and lower energy onset in the NEXAFS spectroscopy. A broader C-H band at room temperature is expected since nuclear motion will be more significant at higher temperature (298 K vs 93 K). However, the lower energy onset of the C-H band in the room temperature spectrum is unexpected. With the aid of DFT calculations, it was found that gauche defects and populated vibrational modes at room temperature cause the lower energy onset. The experimental and theoretical work in this study was published in the Journal of Physical Chemistry A [Reproduced with permission from Journal of Chemistry A, 122 (49), 9512-9517, Sahan D. Perera, Sadegh Shokatian, Jian Wang and Stephen G. Urquhart, Temperature Dependence in the NEXAFS Spectra of *n*-Alkanes, Copyright 2018, American Chemical Society]. This chapter is a literal copy of a paper published in the Journal of Physical Chemistry A with changes to make references, figures, and table numbers consistent throughout the thesis.

6.2 Description of Candidate Contribution

The author of this thesis was the primary investigator for this research work. He prepared the samples, acquired the experimental data (experimental NEXAFS spectra of *n*-alkanes), interpreted the experimental results, and wrote the manuscript. Sadegh Shokatian was the second author of this work and he simulated the DFT calculations and assisted with interpretation of the spectral trends with the DFT calculations. J.Wang helped with the experimental set-up for the NEXAFS measurements of *n*-alkane molecules. S. G Urquhart provided guidance throughout the experiments, the process of data analysis and actively involved in the editing process of this manuscript. Dr. S. G. Urquhart, Sadegh Shokatian and Dr. Jian Wang kindly gave me their permissions to include this manuscript in this dissertation, and agreed to my description of my contribution in this document.

6.3 Relation of Contribution to Research Objectives

This work attempts to examine the origin behind the spectral broadening in the NEXAFS spectra of short chain o-rh *n*-alkanes, in particular for the short chain o-rh *n*-$C_{28}H_{58}$. This work supported the fact that contribution of the nuclear motion effect is significant in the spectral broadening in NEXAFS spectroscopy. The research work in this chapter contributed to the one of the research objectives in this thesis: effects of nuclear motion contributions to the molecular NEXAFS spectroscopy.

6.4 Temperature Dependence in the NEXAFS Spectra of *n*-Alkanes

Sahan D. Perera,† Sadegh Shokatian,† Jian Wang,‡ Stephen G. Urquhart†*

† Department of Chemistry, University of Saskatchewan, Saskatoon, SK, Treaty Six Territory, Canada S7N 5C9. ‡ Canadian Light Source, University of Saskatchewan, Saskatoon, SK, Canada S7N 0X4

Abstract

The Near Edge X-ray Absorption Fine Structure (NEXAFS) spectra of orthorhombic single crystals of *n*-$C_{28}H_{58}$, recorded at room temperature (298 K) and at cryogenic temperatures (93 K), show distinct differences. The characteristic carbon 1s → $\sigma^*_{C\text{-}H}$ band in the NEXAFS spectrum of o-rh *n*-$C_{28}H_{58}$ is broader and appears at lower energy in the room temperature spectrum than in its NEXAFS spectrum recorded at cryogenic temperatures. Density functional theory simulations show that nuclear motion and molecular disorder contribute to the observed spectral broadness and are the origin of the low-energy onset of the C-H band in the room temperature spectrum.

6.4.1 Introduction

The variation of molecular spectra (NMR, IR, etc.) with temperature can be used to probe molecular dynamics. Sensitivity to molecular dynamics and motion is also expected in Near Edge X-ray Absorption Fine Structure (NEXAFS) spectroscopy. As an example, NEXAFS spectra of gas, liquid, supercooled liquid, and solid water show a sensitivity to local hydrogen bonding and changes in this bonding with temperature and phase.[1] To date, experimental studies of the temperature variation of the NEXAFS spectra of molecules are limited.

This study examines the temperature dependence in the NEXAFS spectra of *n*-alkanes. *n*-Alkanes, $CH_3(CH)_nCH_3$ are a family of simple organic molecules consisting of methyl (CH_3) and methylene (CH_2) moieties. Despite their relative simplicity, the NEXAFS spectra of *n*-alkanes show significant complexity, with characteristic differences with phase (gas versus condensed), chain length, degree of order, and with temperature.[2-10] Chemical analysis of these materials would be strengthened if fundamental understandings of their NEXAFS spectroscopy (including the role of order and dynamics) were improved, and if stronger structure / spectra relationships were established.

The carbon 1s NEXAFS spectra of simple gas phase alkanes (methane, ethane, propane, etc.) are dominated by series of narrow and well-resolved carbon 1s $\rightarrow$ Rydberg transitions, with a rich array of vibronic features.[2, 10-11] These gas phase spectra are well modeled by calculations that consider the lowest-energy geometry but neglect vibronic transitions,[2, 10] as core-excited potential energy surfaces are difficult to model. When neopentane was examined in the gas and condensed phases, characteristic Rydberg transitions observed in the gas phase spectra were shifted to higher energy and were broadened in the condensed phase spectra.[3] This effect was attributed to Rydberg quenching in the solid state, and the emergence of valence (σ^*_{C-H}) character.[3] In the carbon 1s NEXAFS spectra of *n*-alkane solids such as paraffin and polyethylene, two low-energy transitions of nearly equal strength (the "C-H band", at 287.6 and 288.2 eV in paraffin) dominate the spectra.[7, 12] Schöll *et al.*[7] examined how this C-H band changed with elevated temperature and the degree of crystallinity in polyethylene copolymers. They found that NEXAFS features were broader in the more disordered polymer as well as in molten polyethylene. The origin of these changes was not well-understood, but the following observation can be made: increased disorder leads to a broader "C-H" band.

Nuclear motion is predicted to play a role in the variation of NEXAFS spectra with temperature.[13-15] Pettersson and Nilsson have extensively studied the NEXAFS spectra of water (liquid, supercooled liquid, and solid phases) and have shown that its oxygen 1s NEXAFS spectrum is sensitive to the local hydrogen-bonded network, and its change with temperature and phase.[1, 16] The Pendergast group[13-14] has examined how 'nuclear motion' effects leads to spectral broadening in NEXAFS spectra of amino acids and related molecules. Their work compared DFT spectral simulations based on the lowest energy molecular geometry to simulations that model the nuclear degrees of freedom by averaging 'snapshots' from molecular dynamics simulations. Their work predicted that zero-point motion and thermally excited vibrational modes contribute to the shape of NEXAFS spectra. In molecular solids such as glycine, these MD-DFT simulations predict that solid-phase vibrational modes are the origin of temperature dependent broadening.[14-15]

Gauche defects (e.g. rotation about individual C-C bonds, distorting an *n*-alkane from the lowest energy, all trans geometry) are another possible contributor to disorder in the NEXAFS spectra of *n*-alkanes, including single crystal *n*-alkanes. In the examination of the spin-lattice relaxation time ($T_{1\rho}$) for *n*-alkanes of various lengths, Basson *et al.*[17] observed a thermally populated defect below the melting point for solid *n*-alkanes of length 28 (*n*-$C_{28}H_{58}$) or shorter. This dynamic process was identified as a thermally populated trans-*gauche* defect motion near the end of the *n*-alkane chains[17] (later classified as an end-*gauche* defects[18]). These defects were seen well below the characteristic pre-melting point solid / solid phase transition to the pseudohexagonal rotator phase,[19] in which an increased population of gauche defects near chain ends was also observed.[20] We therefore expect that some fraction of thermally populated gauche defects will be present in solid *n*-alkanes, particular for shorter *n*-alkane chains.

There is little experimental temperature dependent NEXAFS spectra of organic molecules, and none that we are aware of at cryogenic temperatures. In this work, we examine the carbon 1s NEXAFS spectra of orthorhombic (o-rh) single crystals of *n*-$C_{28}H_{58}$ recorded at room temperature (298 K) and cryogenic temperature (93 K). Regular diamond or parallelogram shaped *n*-$C_{28}H_{58}$ crystallites with straight edges and well-defined angles[21-23] were identified by optical microscopy (OM). These spectroscopic studies are accompanied by DFT simulations that model the effect of defects and vibrational modes on the NEXAFS spectra.

6.4.2 Experimental Section

Samples and Sample Preparation

Sample: *n*-Octacosane (*n*-$C_{28}H_{58}$, 99%) was purchased from Alfa Aesar and used without purification. Isopropyl alcohol (99.9%) was ACS grade and purchased from Fisher Scientific.

Sample Preparation: Samples were prepared on 100 nm, 0.5 × 0.5 mm low stress silicon nitride (Si_3N_4) windows (Norcada Inc.). Thin single crystals of *n*-octacosane (*n*-$C_{28}H_{58}$) were prepared by solution casting[5, 9] from an isopropyl alcohol solution with a mass/volume ratio of 1.0 mg/2.00 ml. The substrate temperature during solvent evaporation was optimized in order to isolate the orthorhombic structure over its monoclinic polymorph. Thin orthorhombic single crystals were obtained when the samples were cast at a lower solvent evaporation temperature (~ 8 °C).

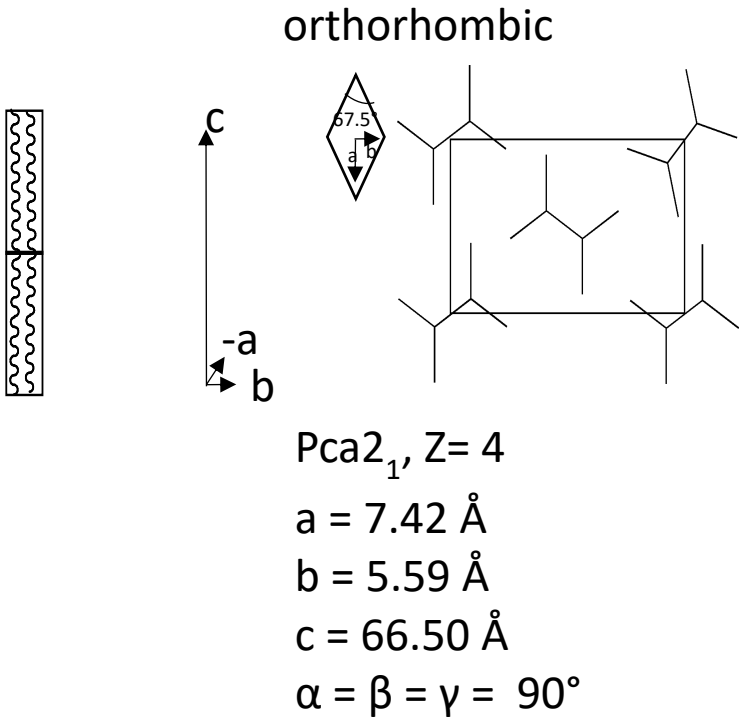

Figure 6.1: Schematic diagram for chain length orientation, published unit cell parameters of orthorhombic structure of *n*-$C_{28}H_{58}$.[21-23]

The morphology of the *n*-$C_{28}H_{58}$ single crystals was characterized by optical microscopy (Nikon Eclipse ME600, with a Q-Imaging CCD camera). *n*-$C_{28}H_{58}$ crystals were found to be rectangular or diamond in shape in optical and X-ray microscopy examination. This indicates that

the (*a,b*) unit cell axes of the crystals are oriented in the plane of the substrate (see **Figure 6.1**). Regular diamond or parallelogram shaped *n*-alkane crystallites with straight edges and well-defined angles were identified by optical microscopy (OM). *n*-Alkane crystals with acute interior angles of 68° ±1 ° are orthorhombic, with those with acute interior angles of 74° ±1 ° are monoclinic.[21-23] Only orthorhombic single crystals of *n*-$C_{28}H_{58}$ were examined in this work.

X-ray Spectromicroscopy Characterization

X-ray microscope images and variable temperature NEXAFS spectra were obtained at the spectromicroscopy (SM) beamline[24] at the Canadian Light Source (CLS), using the cryogenic Scanning Transmission X-ray Microscope (c-STXM)[25] and the ambient STXM microscope (a-STXM).[24] STXM microscopy allows one to acquire the transmission (I) spectra from individual single crystals, and to measure the incident flux (I_0) from areas adjacent to these crystals. NEXAFS spectra were acquired at cryogenic (93 K) and ambient temperatures (~ 298 K) with the c-STXM microscope.[25] All NEXAFS spectra were acquired using left circular X-ray polarization to eliminate potential linear dichroism from oriented crystals. Transmission spectra were converted to optical density with Beer's law ($OD = -\ln(I/I_0)$).

Data analysis were performed using aXis 2000[26] and spectra are presented using the Origin Lab Pro software package[27] The data presentation focuses on the carbon 1s → σ^*_{C-H} band (287 − 288 eV), in order to highlight features that vary with nuclear motion contributions.

Care was taken to exclude experimental artefacts such as radiation damage and thickness effects. In order to avoid thickness effects associated with the small fraction of higher order photons, only spectra from thinner crystals (OD < 1.5) were considered. The relatively high radiation sensitivity of *n*-alkane molecules[28] limits the permissible dose that can be used for NEXAFS measurements. Experimental conditions (energy point spacing, dwell time, etc.) were optimized to minimize radiation exposure, and the STXM was defocused to 150 nm diameter during image sequence data acquisition. Fresh sample areas were used for each spectrum. Radiation damage was monitored by examining the NEXAFS spectra in the carbon 1s continuum (300 eV) to test for mass loss and at the energy of the carbon 1s → $\pi^*_{C=C}$ transition (285 eV) to test for the formation of C=C double bonds.[28-29] Radiation damage was found to be minimal in the experimental conditions used.

The energy scale of the ambient temperature NEXAFS spectrum was confirmed through *in situ* calibration to the Rydberg transitions (carbon 1s →3s (v=0) transition at 292.74 eV

and carbon 1s → 3p (v=0) transition at 294.96 eV; after Ma *et al.*)[11] in the NEXAFS spectrum of CO_2, performed in the a-STXM. These data were used to calibrate the ambient temperature NEXAFS spectrum recorded in the c-STXM. The same shift was applied to calibrate the energy scale of the cryogenic measurements.

6.4.3 Computational Section
Density Functional Theory Calculations

n-Decane (*n*-$C_{10}H_{22}$) was used as a computational model for this study. The lowest-energy geometry (all trans) of *n*-decane was determined by ωB97X-D DFT calculations at the 6-31+G(d,p) level, performed with the program Gaussian 16.[30] There were no imaginary frequencies in the vibrational analysis calculation. Several variations of the all-trans *n*-decane structure were examined in order to study the effect of disorder and nuclear motion effects. The effect of these gauche defects on the NEXAFS spectra are studied by rotating bond dihedrals in *n*-decane individually. The population of gauche defects at room temperature was obtained from the molecular dynamic simulation study of *n*-decane by Thomas *et al.*[31] NEXAFS spectra were averaged according to the weights of these calculated gauche defect configurations. This method provides an estimate of the effect of gauche defects in *n*-decane, as an approximation for the effect of gauche defects in longer *n*-alkane crystals. In the solid phase, such defects could be static, but Basson *et al.*[17] have noted that end-gauche defects can be thermally populated at room temperature in octacosane (*n*-$C_{28}H_{58}$).[17-18]

Many forms of motion can contribute to 'nuclear motion effects' in an *n*-alkane solid, including zero-point motion and thermally populated vibrational modes. Zero-point motions should be expected to contribute at all temperatures, while the Boltzmann distribution of thermally populated vibrational modes will increase with sample temperature.

To examine the spectroscopic effect of a thermally populated modes, we have constructed a simple model based on the *n*-$C_{10}H_{22}$ molecule, which has 90 (3N-6) vibrational modes. We have constructed geometries for the turning points of all of these vibrational modes, on the principle that the molecule's geometry will spend most of its time at these turning points. DFT spectroscopic simulations were performed for these turning-point geometries, and were averaged according to the expected Boltzmann population of these vibrational modes at 298 K. All vibrations are considered, as weighted by their Boltzmann population. This simple approach neglects the effects

of zero-point motion, as well as the population of vibrational modes above υ = 1, which will be significant for low-energy vibration modes.

Carbon 1s NEXAFS simulations of *n*-decane structures were obtained from DFT calculations[32-33] using the deMon2k package.[34-35] All NEXAFS simulations were performed using Transition Potential (TP-DFT) method with the half-core hole (HCH) approximation.[36] Spectral lines were simulated using 0.2 eV wide Gaussian line shapes. The molecular spectrum is generated by averaging the DFT simulation from each carbon atom. The IGLO-III basis set[37] was used for the core excited carbon atom, effective core potential (ECPs) for all other carbon atoms,[38] and the triple-zeta (TZVP) basis set for hydrogen atoms.[38] XAS-I augmentation orbitals were used on the core excited carbon atom.[36] The GEN-A4* auxiliary basis and the PBE GGA exchange-correlation functional were used.[39-40]

6.4.4 Results

Figure 6.2 presents the variation in the C-H band of the carbon 1s NEXAFS spectra of o-rh *n*-$C_{28}H_{58}$ with temperature, comparing the room temperature (298 K) spectrum with that recorded at cryogenic temperatures (93 K). The shape of the C-H band is significantly broader at room temperature, and the C-H band has a lower energy onset (~200 meV lower) relative to that recorded at cryogenic temperatures. A broader C-H band is expected at higher temperature, as nuclear motion will be more significant. However, the lower-energy offset for the room temperature spectra is unexpected and requires further discussion. The observed spectroscopic trends (width and onset) were also observed for *n*-$C_{40}H_{82}$ powders, recorded in TEY mode on the CLS SGM beamline (11 ID-1).[41]

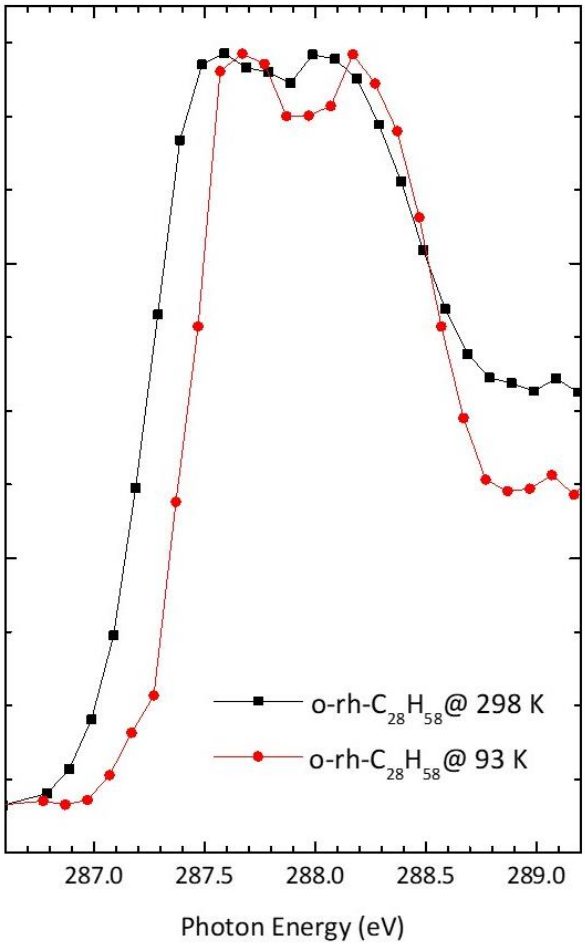

Figure 6.2: Carbon 1s NEXAFS spectra of orthorhombic *n*-$C_{28}H_{58}$ at cryogenic (93 K) and ambient (298 K) temperatures, recorded with circular left polarization. Optical density spectra are rescaled for comparison.

Figure 6.3 compares the TP-DFT simulations of the carbon 1s NEXAFS spectra of *n*-$C_{10}H_{22}$ with an all-trans minimum energy geometry, to simulations of gauche defects and thermally populated vibrational models. The shape of the TP-DFT simulation of the carbon 1s spectrum of *n*-$C_{10}H_{22}$ (in the all trans geometry) differs from the experimental carbon 1s spectrum of *n*-$C_{28}H_{58}$ on account of the length of the model. The methyl group and the first methylene in from the end of the chain contribute to the third band observed in **Figure 6.3**, at ~289.2 eV. For *n*-$C_{10}H_{22}$, these sites correspond to 40% of the atomic sites in the *n*-alkane chain; therefore, this third band is exaggerated in this short *n*-alkane model. A full examination of the chain length dependence in the NEXAFS spectra of *n*-alkanes is in preparation.[42]

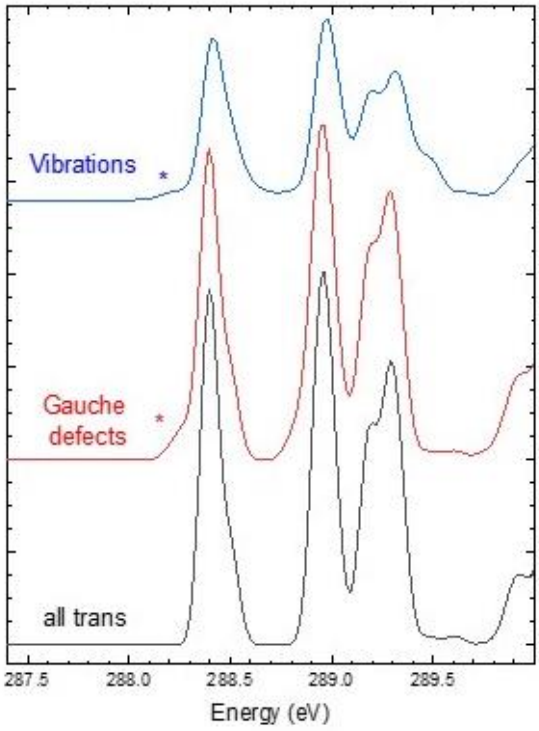

Figure 6.3: TP-DFT simulations of the effect of thermally populated gauche defects and thermally populated vibrations (υ = 1) on the NEXAFS spectra of the isolated *n*-$C_{10}H_{22}$ molecule.

The splitting between the first two peaks in the TP-DFT simulation (~0.6 eV) roughly matches the observed splitting in the experimental carbon 1s spectrum of *n*-$C_{28}H_{58}$ recorded at cryogenic temperatures.

When gauche defects and populated vibrational modes are considered, new contributions are observed at lower energy; these are indicated by an asterisk in **Figure 6.3**. This trend is consistent with the lower energy onset of the C-H band observed in the room temperature NEXAFS spectrum of o-rh *n*-$C_{28}H_{58}$ relative to the spectrum recorded at cryogenic temperatures.

6.4.5 Discussion

Spectral broadening in the carbon 1s NEXAFS spectra of molecular solids is expected to have several origins. Beyond the intrinsic broadening from the core-hole lifetime (~80 meV), vibronic contributions, disorder, and nuclear motion are expected to contribute to the shape of the NEXAFS transtions.[13-14, 43] Vibronic contributions[2, 11] should be similar for spectra recorded at ambient and at cryogenic temperatures; as the additional energy required for vibronic excitation (e.g. C 1s (υ = 0) → $\sigma^*_{C\text{-}H}$ (υ = 1) transition) comes from the absorbed photon. Vibronic

contributions will therefore appear at higher energy. Vibronic contributions therefore cannot responsible for the low-energy onset observed in the room temperature NEXAFS spectrum of *n*-$C_{28}H_{58}$.

Nuclear motion effects, via population of vibrational modes and thermally populated molecular defects, are expected to differ with temperature. The effect of the thermal population of vibrational modes and defects on the NEXAFS spectrum of *n*-alkanes was examined using TP-DFT simulations. This distortion from the lowest-energy, all trans geometry results in lower energy transitions appearing at lower-energy side of the C-H band. This is a reasonable observation; as geometries are distorted from the lowest energy geometry, the HOMO-LUMO gap in a molecule is expected to decrease, and with it, the energy of the core → LUMO transition will also decrease. This trend is observed for thermally populated gauche defects as well as vibrations.

We note that the TP-DFT simulations of thermally populated vibrations and gauche defects do not reproduce the intensity of the low energy onset observed in the room temperature NEXAFS spectrum. This is not completely unexpected, as our computational model is limited. We examined a shorter chain (10 carbon atoms long instead of 28) in order to be computationally more accessible (90 versus 252 normal modes). We have also only examined the turning points for the lowest -energy thermally populated vibration ($\upsilon = 1$), and not higher quantum number vibrational states ($\upsilon > 1$), expected to be populated for low energy normal modes.

Our vibrational model is that of an isolated *n*-alkane molecule, and not a solid structure. This model does not capture changes to vibrations due to intermolecular interactions in the condensed phase, or the low-energy shifts expected from dynamic stabilization.[44] A full approach to examine the temperature dependent spectroscopy will require molecular dynamics simulations, which, with appropriate size, will be able to capture the effect of the solid-phase on nuclear motion contributions to the NEXAFS spectra, as well as thermally populated gauche defects. This requires considerable development, and will be the subject of future work.

In this work, the carbon 1s NEXAFS spectrum of a condensed *n*-alkane (o-rh *n*-$C_{28}H_{58}$) recorded at cryogenic temperatures (93 K), is compared to its NEXAFS spectrum recorded at room temperature. Characteristic differences are observed with temperature. Specifically, the distinctive "C-H band" in the NEXAFS spectrum is narrower in the spectrum recorded at cryogenic temperatures, and the onset of this band appears at higher energy. DFT simulations show that distortions from the lowest-energy all trans geometry, from thermally populated vibrational modes

and gauche defects, result in new features appearing at lower energy in the NEXAFS spectrum. Cryogenic temperatures restrict thermal motion in the sample, from a lower population of vibrational modes and thermally accessible defects. This results in a narrower C-H band in the spectrum recorded at cryogenic temperatures. At ambient temperatures, gauche defects will be more common, and nuclear motion effects will be enhanced.

6.4.6 Conclusions

This work reports remarkable differences in the NEXAFS spectra of an organic molecule with temperature, and attributes these spectroscopic differences to molecular vibrations and defects populated at ambient temperatures, relative to that at cryogenic temperatures. Future work will include the acquisition of NEXAFS spectra at a broader range of temperatures and a more rigorous exploration of the temperature dependence of the observed nuclear motion effects.

6.4.7 References

1. Fransson, T.; Harada, Y.; Kosugi, N.; Besley, N. A.; Winter, B.; Rehr, J. J.; Pettersson, L. G. M.; Nilsson, A. X-ray and Electron Spectroscopy of Water. *Chemical Reviews* **2016,** *116* (13), 7551-7569.

2. Urquhart, S. G.; Gillies, R. Rydberg-Valence Mixing in the Carbon 1s Near-Edge X-ray Absorption Fine Structure Spectra of Gaseous Alkanes. *The Journal of Physical Chemistry A* **2005,** *109* (10), 2151-2159.

3. Urquhart, S. G.; Gillies, R. Matrix Effects in the Carbon 1s Near Edge X-ray Absorption Fine Structure Spectra of Condensed Alkanes. *The Journal of Chemical Physics* **2006,** *124* (23), 234704.

4. Weiss, K.; Bagus, P.; Wöll, C. Rydberg Transitions in X-ray Absorption Spectroscopy of Alkanes: The Importance of Matrix Effects. *The Journal of Chemical Physics* **1999,** *111* (15), 6834-6845.

5. Zou, Y.; Araki, T.; Appel, G.; Kilcoyne, A. L. D.; Ade, H. Solid State Effects in the NEXAFS Spectra of Alkane-Based van der Waals Crystals: Breakdown of Molecular Model. *Chemical Physics Letters* **2006,** *430* (4), 287-292.

6. Bagus, P.; Weiss, K.; Schertel, A.; Wöll, C.; Braun, W.; Hellwig, C.; Jung, C. Identification of Transitions into Rydberg States in the X-ray Absorption Spectra of Condensed Long-Chain Alkanes. *Chemical Physics Letters* **1996,** *248* (3-4), 129-135.

7. Schöll, A.; Fink, R.; Umbach, E.; Mitchell, G.; Urquhart, S.; Ade, H. Towards a Detailed Understanding of the NEXAFS Spectra of Bulk Polyethylene Copolymers and Related Alkanes. *Chemical Physics Letters* **2003,** *370* (5-6), 834-841.

8. Stöhr, J.; Outka, D.; Baberschke, K.; Arvanitis, D.; Horsley, J. Identification of C-H Resonances in the K-Shell Excitation Spectra of Gas-Phase, Chemisorbed, and Polymeric Hydrocarbons. *Physical Review B* **1987,** *36* (5), 2976-2979.

9. Swaraj, S.; Ade, H. Differences in NEXAFS of Odd/Even Long Chain *n*-Alkane Crystals. *Journal of Electron Spectroscopy and Related Phenomena* **2013,** *191*, 60-64.

10. Ueda, K.; Okunishi, M.; Chiba, H.; Shimizu, Y.; Ohmori, K.; Sato, Y.; Shigemasa, E.; Kosugi, N. Rydberg-Valence Mixing in the C 1s Excited States of CH_4 Probed by Electron Spectroscopy. *Chemical Physics Letters* **1995,** *236* (3), 311-317.

11. Ma, Y.; Chen, C.; Meigs, G.; Randall, K.; Sette, F. High-Resolution K-Shell Photoabsorption Measurements of Simple Molecules. *Physical Review A* **1991,** *44* (3), 1848-1858.

12. Fu, J.; Urquhart, S. G. Linear Dichroism in the X-ray Absorption Spectra of Linear *n*-Alkanes. *The Journal of Physical Chemistry A* **2005,** *109* (51), 11724-11732.

13. Uejio, J. S.; Schwartz, C. P.; Saykally, R. J.; Prendergast, D. Effects of Vibrational Motion on Core-Level Spectra of Prototype Organic Molecules. *Chemical Physics Letters* **2008,** *467* (1-3), 195-199.

14. Schwartz, C. P.; Uejio, J. S.; Saykally, R. J.; Prendergast, D. On the Importance of Nuclear Quantum Motions in Near Edge X-ray Absorption Fine Structure Spectroscopy of Molecules. *The Journal of Chemical Physics* **2009,** *130* (18), 184109.

15. Schwartz, C. P.; Saykally, R. J.; Prendergast, D. An Analysis of the NEXAFS Spectra of a Molecular Crystal: α-Glycine. *The Journal of Chemical Physics* **2010,** *133* (4), 044507.

16. Sellberg, J. A.; Kaya, S.; Segtnan, V. H.; Chen, C.; Tyliszczak, T.; Ogasawara, H.; Nordlund, D.; Pettersson, L. G.; Nilsson, A. Comparison of X-Ray Absorption Spectra Between Water and Ice: New Ice Data with Low Pre-Edge Absorption Cross-Section. *The Journal of Chemical Physics* **2014,** *141* (3), 034507.

17. Basson, I.; Reynhardt, E. C. Identification of a Defect Chain Motion in *n*-Alkanes by Means of Nuclear Magnetic Resonance Spin–Lattice Relaxation Time Measurements. *The Journal of Chemical Physics* **1990,** *93* (5), 3604-3609.

18. Basson, I.; Reynhardt, E. C. Identification of Defect Chain Motions in the Low Temperature Orthorhombic Phase of Binary Mixtures of *n*-Alkanes by Means of Nuclear Magnetic Resonance Spin-Lattice Relaxation Time Measurements. *The Journal of Chemical Physics* **1991,** *95* (2), 1215-1222.

19. Mukherjee, P. K. Phase Transitions Among the Rotator Phases of the Normal Alkanes: A Review. *Physics Reports* **2015,** *588*, 1-54.

20. Maroncelli, M.; Strauss, H.; Snyder, R. The Distribution of Conformational Disorder in the High-Temperature Phases of the Crystalline *n*-Alkanes. *The Journal of Chemical Physics* **1985,** *82* (6), 2811-2824.

21. Craig, S. R.; Hastie, G. P.; Roberts, K. J.; Sherwood, J. N. Investigation into the Structures of Some Normal Alkanes Within the Homologous Series $C_{13}H_{28}$ to $C_{60}H_{122}$ Using High-Resolution Synchrotron X-ray Powder Diffraction. *Journal of Materials Chemistry* **1994,** *4* (6), 977-981.

22. Plomp, M.; Van Enckevort, W.; Van Hoof, P.; Van De Streek, C. Morphology of and Dislocation Movement in *n*-$C_{40}H_{82}$ Paraffin Crystals Grown From Solution. *Journal of Crystal Growth* **2003,** *249* (3), 600-613.

23. Teare, P. The Crystal Structure of Orthorhombic Hexatriacontane, $C_{36}H_{74}$. *Acta Crystallographica* **1959,** *12* (4), 294-300.

24. Kaznatcheev, K.; Karunakaran, C.; Lanke, U.; Urquhart, S.; Obst, M.; Hitchcock, A. Soft X-ray Spectromicroscopy Beamline at the CLS: Commissioning Results. *Nuclear*

Instruments and Methods in Physics Research Section A: Accelerators, Spectrometers, Detectors and Associated Equipment **2007,** *582* (1), 96-99.

25. Leontowich, A. F.; Berg, R.; Regier, C. N.; Taylor, D. M.; Wang, J.; Beauregard, D.; Geilhufe, J.; Swirsky, J.; Wu, J.; Karunakaran, C. Cryo Scanning Transmission X-ray Microscope Optimized for Spectrotomography. *Review of Scientific Instruments* **2018,** *89* (9), 093704.

26. *aXis; Software for Analysis of X-ray Microscopy Images and Spectra*, McMaster University: Ontario, Canada, **2000**.

27. *Origin; Software For Data Analysis and Graphing*, Version 7.5; Origin Lab: Northampton State, USA, **1991**.

28. Coffey, T.; Urquhart, S.; Ade, H. Characterization of the Effects of Soft X-ray Irradiation on Polymers. *Journal of Electron Spectroscopy and Related Phenomena* **2002,** *122* (1), 65-78.

29. Rightor, E.; Hitchcock, A.; Ade, H.; Leapman, R.; Urquhart, S.; Smith, A.; Mitchell, G.; Fischer, D.; Shin, H.; Warwick, T. Spectromicroscopy of Poly (ethylene terephthalate): Comparison of Spectra and Radiation Damage Rates in X-ray Absorption and Electron Energy Loss. *The Journal of Physical Chemistry B* **1997,** *101* (11), 1950-1960.

30. Frisch, M. J.; Trucks, G. W.; Schlegel, H. B.; Scuseria, G. E.; Robb, M. A.; Cheeseman, J. R.; Scalmani, G.; Barone, V.; Petersson, G. A.; Nakatsuji, H.; Li, X.; Caricato, M.; Marenich, A. V.; Bloino, J.; Janesko, B. G.; Gomperts, R.; Mennucci, B.; Hratchian, H. P.; Ortiz, J. V.; Izmaylov, A. F.; Sonnenberg, J. L.; Williams; Ding, F.; Lipparini, F.; Egidi, F.; Goings, J.; Peng, B.; Petrone, A.; Henderson, T.; Ranasinghe, D.; Zakrzewski, V. G.; Gao, J.; Rega, N.; Zheng, G.; Liang, W.; Hada, M.; Ehara, M.; Toyota, K.; Fukuda, R.; Hasegawa, J.; Ishida, M.; Nakajima, T.; Honda, Y.; Kitao, O.; Nakai, H.; Vreven, T.; Throssell, K.; Montgomery Jr., J. A.; Peralta, J. E.; Ogliaro, F.; Bearpark, M. J.; Heyd, J. J.; Brothers, E. N.; Kudin, K. N.; Staroverov, V. N.; Keith, T. A.; Kobayashi, R.; Normand, J.; Raghavachari, K.; Rendell, A. P.; Burant, J. C.; Iyengar, S. S.; Tomasi, J.; Cossi, M.; Millam, J. M.; Klene, M.; Adamo, C.; Cammi, R.; Ochterski, J. W.; Martin, R. L.; Morokuma, K.; Farkas, O.; Foresman, J. B.; Fox, D. J. *Gaussian 16 Rev. B.01*, Wallingford, CT, **2016**.

31. Thomas, L. L.; Christakis, T. J.; Jorgensen, W. L. Conformation of Alkanes in the Gas Phase and Pure Liquids. *The Journal of Physical Chemistry B* **2006,** *110* (42), 21198-21204.

32. Kohn, W.; Sham, L. J. Self-Consistent Equations Including Exchange and Correlation Effects. *Physical Review* **1965,** *140* (4A), A1133-A1138.

33. Hohenberg, P.; Kohn, W. Inhomogeneous Electron Gas. *Physical Review* **1964,** *136* (3B), B864-B871.

34. Geudtner, G.; Calaminici, P.; Carmona-Espíndola, J.; del Campo, J. M.; Domínguez-Soria, V. D.; Moreno, R. F.; Gamboa, G. U.; Goursot, A.; Köster, A. M.; Reveles, J. U. DeMon2k. *Wiley Interdisciplinary Reviews: Computational Molecular Science* **2012,** *2* (4), 548-555.

35. Koster, A.; Geudtner, G.; Calaminici, P.; Casida, M.; Dominguez, V.; Flores-Moreno, R.; Gamboa, G.; Goursot, A.; Heine, T.; Ipatov, A. DeMon2k, Version 3. *The deMon Developers, Cinvestav: Mexico City, Mexico* **2011**.

36. Triguero, L.; Pettersson, L.; Ågren, H. Calculations of Near-Edge X-ray-Absorption Spectra of Gas-Phase and Condense- Phase Molecules by Means of Density-Functional and Transition-Potential Theory. *Physical Review B* **1998,** *58* (12), 8097-8110.

37. Kutzelnigg, W.; Fleischer, U.; Schindler, M. The IGLO-Method: *ab-initio* Calculation and Interpretation of NMR Chemical Shifts and Magnetic Susceptibilities. In *Deuterium and Shift Calculation*, Springer-Verlag:Berlin, Germany, **1990**.

38. Certain, P. R.; Moiseyev, N. Highly Excited Vibrational States by Adiabatic Vs Self-Consistent-Field Methods. *The Journal of Chemical Physics* **1987,** *86* (4), 2146-2151.

39. Calaminici, P.; Flores–Moreno, R.; Köster, A. M. Density Functional Study of Structures and Vibrations of Ta_3O and Ta_3O^-. *Computing Letters* **2005,** *1* (4), 164-171.

40. Calaminici, P.; Janetzko, F.; Köster, A. M.; Mejia-Olvera, R.; Zuniga-Gutierrez, B. Density Functional Theory Optimized Basis Sets for Gradient Corrected Functionals: 3d Transition Metal Systems. *The Journal of Chemical Physics* **2007,** *126* (4), 044108.

41. Regier, T.; Paulsen, J.; Wright, G.; Coulthard, I.; Tan, K.; Sham, T. K.; Blyth, R. I. R. Commissioning of the Spherical Grating Monochromator Soft X-ray Spectroscopy Beamline at the Canadian Light Source. *AIP Conference Proceedings* **2007,** *879* (1), 473-476.

42. Shokatian, S.; Urquhart, S. G. Near Edge X-ray Absorption Fine Structure Spectra of Linear *n*-Alkanes: Variation with Chain Length. **2019** (In preparation).

43. Patel, S. N.; Su, G. M.; Luo, C.; Wang, M.; Perez, L. A.; Fischer, D. A.; Prendergast, D.; Bazan, G. C.; Heeger, A. J.; Chabinyc, M. L.; Kramer, E. J. NEXAFS Spectroscopy Reveals the Molecular Orientation in Blade-Coated Pyridal[2,1,3]Thiadiazole-Containing Conjugated Polymer Thin Films. *Macromolecules* **2015,** *48* (18), 6606-6616.

44. Flesch, R.; Pavlychev, A.; Neville, J.; Blumberg, J.; Kuhlmann, M.; Tappe, W.; Senf, F.; Schwarzkopf, O.; Hitchcock, A.; Rühl, E. Dynamic Stabilization in $1\sigma_u \rightarrow 1\pi_g$ Excited Nitrogen Clusters. *Physical Review Letters* **2001,** *86* (17), 3767-3770.

Chapter 7 Contribution of Molecular Disorder Effect to the Carbon 1s NEXAFS Spectra of *n*-Alkanes

7.1 Description

In **Chapter 5**, the characteristic C-H band (carbon 1s → $\sigma^*_{C\text{-}H}$) of *n*-$C_{28}H_{58}$ is observed to be unusual and spectral broadening is observed in particular for the short chain o-rh *n*-$C_{28}H_{58}$. Hence, in this chapter, the contribution of molecular disorder effect to the carbon 1s NEXAFS spectra of short chain o-rh *n*-alkanes was studied with a broader goal of identifying the origin for the unusual spectral behavior of the short chain o-rh *n*-$C_{28}H_{58}$. The experimental procedure used in **Chapter 5** was used to prepare orthorhombic *n*-alkane single crystals (see **Chapter 5** for details) for this work, and their crystal structures were confirmed by measuring the interior angles of each *n*-alkane crystal with high resolution point-by-point STXM images, recorded at 287.5 eV.

The molecular disorder in orthorhombic *n*-alkane crystals was examined by Raman spectroscopy (785 nm laser). Raman spectra (C-H stretching and bending regions) of orthorhombic *n*-alkanes (*n*-$C_{28}H_{58}$, *n*-$C_{32}H_{66}$ and *n*-$C_{40}H_{82}$) show that shorter alkane chain lengths (*n*-$C_{28}H_{58}$) are more disordered. However, Raman measurements did not determine the specific type of molecular disorder that exists in the *n*-alkane molecule (o-rh *n*-$C_{28}H_{58}$), but future suggestions (see **Chapter 9**) could help to track down the type of molecular disorder in the short chain *n*-alkanes. According to literature, this molecular disorder could be due to the presence of a dynamic end-*gauche* defect mode present exclusively in o-rh *n*-$C_{28}H_{58}$ at room temperature.[1] The results are presented in the format of a journal manuscript.

7.2 Description of Candidate Contribution

The author of this thesis was the primary investigator for this research work. He prepared the samples, acquired the experimental data, interpreted the experimental results, and wrote the manuscript. J.Wang helped with the experimental set-up for the NEXAFS measurements of *n*-alkane molecules. S. G Urquhart provided guidance throughout the experiments, the process of data analysis and actively involved in the editing process of this manuscript. Dr. S. G. Urquhart and Dr. Jian Wang kindly gave me their permissions to include this manuscript in this dissertation, and agreed to my description of my contribution in this document.

7.3 Relation of Contribution to Research Objectives

This work focused on studying the unusual characteristic C-H band (carbon 1s → $\sigma^*_{C\text{-}H}$) observed in the shorter *n*-alkane crystal, *n*-$C_{28}H_{58}$. The study showed that shorter *n*-alkane crystal, *n*-$C_{28}H_{58}$ is more disordered. The research work in this chapter contributed to the one of the research objectives in this thesis: effects of nuclear motion contributions to the molecular NEXAFS spectroscopy.

7.4 Contributions of Molecular Disorder to the Carbon 1s Near Edge X-ray Absorption Fine Structure (NEXAFS) Spectra of Short Chain *n*-Alkanes

Sahan D. Perera[1], Jian Wang[2], Stephen G. Urquhart[1]*

3. Department of Chemistry, University of Saskatchewan, Saskatoon, SK, Treaty Six Territory, Canada S7N 5C9
4. Canadian Light Source, University of Saskatchewan, Saskatoon, SK, Canada S7N 0X4

Abstract

The origin for the spectral broadening and line shapes in the Near Edge X-ray Absorption Fine Structure (NEXAFS) spectra of organic solids like *n*-alkanes is not fully understood. In particularly, the shape of the low-energy carbon 1s → $\sigma^*_{C\text{-}H}$ band in the NEXAFS spectra of *n*-alkanes has contributions other than intrinsic lifetime broadening, such as vibrionic coupling, nuclear motion effects, and molecular disorder associated with the alkane chain length. This paper explores the NEXAFS spectra of orthorhombic *n*-alkane single crystals with different chain lengths (*n*-$C_{40}H_{82}$, *n*-$C_{32}H_{66}$, and *n*-$C_{28}H_{58}$). The unusual broadness of carbon 1s → σ^*_{CH} band in the shorter *n*-alkane crystal, *n*-$C_{28}H_{58,}$ is attributed to the molecular disorder in this shorter chain length crystal.

7.4.1 Introduction

n-Alkanes, $CH_3(CH)_nCH_3$ are some of the simplest organic molecules. They form the basic units of more complex molecules such as liquid crystals, oils and surfactants. These have been continuously used as models for understanding solid-state effects on the Near Edge X-ray Absorption Fine Structure (NEXAFS) spectroscopy of complex organic materials due to their characteristic differences with degree of disorder, phase (gaseous versus solid) and chain length.[2-10] Even though analysis of molecular NEXAFS spectra is well famous for finding intramolecular effects such as how electronic structure, molecular orientation, and different bonding environment alter the spectra,[7, 11-21] NEXAFS coupled with high spatial resolution X-ray microscopy also a powerful technique to characterize the intermolecular interactions and order-disorder effects of organic molecules. The strong fundamental understanding of these effect to their NXAFS spectroscopy will strengthen the chemical analysis of organic solids such as *n*-alkanes.

Spectral broadening in molecular NEXAFS spectra, beyond that from intrinsic lifetime broadening, can arise from factors including chemical shifts, intermolecular perturbations such as Rydberg quenching[3] and hydrogen bond formation,[22] vibronic transitions,[2, 23] and nuclear motion contributions.[22, 24-27] Nuclear motion effects refer to spectroscopic contributions from the energetically accessible vibrations (including zero point motion) and conformations present at experimental temperatures.[24, 26]

At the outset, it is useful to categorize nuclear motion effects and effects of molecular disorder in the alkane chains on NEXAFS spectroscopy, and to differentiate these effects from vibronic contributions. Vibronic features occur when core excitation is accompanied by vibrational excitation, such as the carbon 1s ($\nu = 0$) $\rightarrow \pi^*(\nu = 1)$ transition that appears above the lowest energy carbon 1s ($\nu = 0$) $\rightarrow \pi^*(\nu = 0)$ transition in unsaturated molecules. Vibronic series can be resolved in the high resolution NEXAFS spectra of small molecules,[2, 23] providing vibrational energies that reflect bonding in the core excited molecule. Unresolved vibronic transitions lead to asymmetric broadening of NEXAFS lineshapes.

In contrast to vibronic transitions, 'nuclear motion effects' refer to the spectroscopic sampling of the distribution of geometries found in the electronic ground state. These geometry distributions occur because zero-point motion ($\nu = 0$), thermally populated vibrational modes ($\nu = 1, 2 \ldots$), and thermally populated molecular conformations with their own vibrational manifolds.

The NEXAFS spectrum will reflect the contributions of these geometries. DFT simulations of structural averages obtained from molecular dynamics simulations differ from simulation based on the lowest energy geometry. These NEXAFS averages also show a temperature dependence.[24, 26, 28] To address the range of molecular structures present, Gordon *et al.*[29] used improved virtual orbital simulations of several thermally accessible conformations to reproduce the NEXAFS spectra of glycene.[29] Pettersson's group[22, 25, 27]made extensive studies of the liquid and solid water, combining molecular dynamics (MD) with density functional theory (DFT) simulations. Their work showed that a range of structures, including high and low density forms associated with the anomalous properties of liquid water, contribute to the shape of the NEXAFS spectrum of water. The Pendergast group[24, 26] examined how nuclear motion leads to spectral broadening in NEXAFS spectra of amino acids and related molecules. This work compared spectral simulations in the fixed nuclei model (single lowest energy geometry) to simulations that model nuclear degrees of freedom, by averaging spectral simulations of structural snapshots from a molecular dynamics simulation. Their work showed that zero point motion contributes to the shape of the NEXAFS spectra, in addition to excited vibrational modes. In molecular solids such as glycine, MD-DFT simulations predict that solid-phase vibrational modes are the origin of temperature dependent broadening effects.[24, 28] This work showed the importance quantum dynamics over classical dynamics in simulating these nuclear motion contributions.[24]

In this work, we examine how molecular disorder contribute to the NEXAFS spectra of *n*-alkanes. An increase in molecular disorder is expected for shorter *n*-alkane chains, even at temperatures below the melting point and well below the transition to the pre-melting point rotator phases.[30] Suggestive evidence for the prediction regarding molecular disorder can be found in the stability of *n*-alkane single crystals made from short *n*-alkane chains. Crystals formed from *n*-$C_{28}H_{58}$ (and shorter chains) are unstable at room temperature and lose the sharpness of their facet edges within a day. As the melting point of *n*-$C_{28}H_{58}$ is 62° C, this physical instability implies some form of molecular motion, well below the melting point. However, the relationship between this molecular motion and the 'nuclear motion effect' contributions to NEXAFS spectra is initially unclear.

There is evidence to suggest a role for nuclear motion and disorder contributions to the NEXAFS spectra of condensed alkanes. In the carbon 1s NEXAFS spectra of condensed phase *n*-

alkanes such as paraffin and polyethylene, two low energy transitions of nearly equal strength (the "C-H band", at 287.6 and 288.2 eV in paraffin) dominate the spectra.[7, 15] Schöll *et al.*[7] examined how the NEXAFS spectra of polyethylene copolymers varied with temperature and the degree of crystallinity. They found that NEXAFS features (C-H band) were broader in more disordered polymer as well as in molten polyethylene. This disorder is likely trapped in the solid polymer, but dynamic in the form of chain reptation in the molten polymer. These results indicate that NEXAFS spectroscopy is sensitive to molecular order-disorder for alkanes. Moreover, **Chapter 6** results in this thesis provide evidence for role of nuclear motion contributions in the *n*-alkane molecules. According to **Chapter 6**, characteristic carbon 1s → $\sigma^*_{C\text{-}H}$ band in the NEXAFS spectrum of *n*-alkane is broader and appears at lower energy when the spectrum was recorded at room temperature (298 K) relative to the cryogenic temperature (93 K). The density functional theory simulations in **Chapter 6** showed that nuclear motion and molecular disorder contribute to the observed spectral broadness and are the origin of the low-energy onset of the C-H band in the room temperature spectrum.

In this work, we have examined the crystal-symmetry resolved NEXAFS spectra of orthorhombic *n*-alkane single crystals as a function of chain length (o-rh *n*-$C_{28}H_{58}$, o-rh *n*-$C_{32}H_{66}$ and o-rh *n*-$C_{40}H_{82}$). We initially hypothesized that shorter chains would exhibit greater molecular disorder at ambient temperature. Systematic differences with the chain length were characterized in carbon 1s NEXAFS spectroscopy. Specific observations in the NEXAFS spectra of o-rh *n*-$C_{28}H_{58}$ are attributed to dynamic motion to defects and disorder accessible at room temperature.

7.4.2 Experimental Section

Samples and Sample Preparation

Samples: Linear alkanes used in this study are *n*-tetracontane (*n*-$C_{40}H_{82}$, 97+ %), *n*-dotriacontane (*n*-$C_{32}H_{66}$, 98%) and *n*-octacosane (*n*-$C_{28}H_{58}$, 99%). These were purchased from Alfa Aesar and used without purification. The solvents toluene (99.9%) and isopropyl alcohol (99.9%) were ACS grade and purchased from Fisher Scientific.

For optical microscopy experiments, *n*-alkane samples were prepared on 500 μm thick phosphorus doped silicon (110) wafers (University Wafer). For X-ray spectroscopy and microscopy experiments, samples were prepared on 100 nm thick, 0.5 × 0.5 mm low stress silicon

nitride (Si_3N_4) windows (Norcada Inc.). For Raman spectroscopy and microscopy experiments, *n*-alkane samples were prepared on 500 μm Au coated silicon (110) wafers (University Wafer).

Sample Preparation: Thin crystals of *n*-tetracontane (*n*-$C_{40}H_{82}$), *n*-dotriacontane (*n*-$C_{32}H_{66}$) and *n*-octacosane (*n*-$C_{28}H_{58}$) were prepared by solution casting[5, 9] as described in the experimental section of **Chapter 5**.

Optical and X-ray microscopy of orthorhombic crystals found them to be rectangular or diamond in shape, indicating that the (*a*,*b*) unit cell axes of the crystals are oriented in the plane of the substrate, and that the *c* axis was perpendicular to the substrate (see **Figure 6.1** in **Chapter 6**). Numerous well-defined single crystals could be found for all *n*-alkane samples. As discussed below (experimental results), crystals were selected and assigned to the orthorhombic crystal structure, based on X-ray or optical microscopy measurements. The long axis (X) and short axis (Y) of the *n*-alkane single crystals are used as the two principal axes when obtaining angle resolved NEXAFS spectra (see **Figure 7.1**) at room temperature.

Optical Microscopy and X-ray Spectromicroscopy Characterization

The morphology of the *n*-alkane single crystals was characterized by optical microscopy (Nikon Eclipse ME600, with a Q-Imaging CCD camera). Images were acquired in bright field.

NEXAFS imaging and spectroscopy were obtained at the spectromicroscopy (SM) beamline (10ID-1, Apple II Elliptically Polarized Undulator) at the Canadian Light Source (CLS), using the ambient Scanning Transmission X-ray Microscope (a-STXM).[31] All NEXAFS spectra and images were acquired in a transmission mode. The data presentation focuses on the carbon 1s $\rightarrow \sigma^*_{C-H}$ band (287 − 288 eV), in order to highlight features that are expected to vary with chain length and molecular disorder associated with the chain length. STXM images used for quantitative measurement of the *n*-alkane single crystal morphology (internal angles) were recorded in "point by point" mode. This mode produces images with less image distortion than "rapid scan" or "fly scan" imaging mode. A great deal of effort was expended in order to exclude the experimental artefacts (including crystal thickness effect, radiation damage, and the possibility of energy scale instability), as described in the experimental section of **Chapter 5**.

Raman Microscopy and Spectroscopy Characterization

Raman spectra of orthorhombic *n*-alkanes were measured using a Renishaw Invia Reflex Raman microscope at room temperature and atmospheric pressure. A 785 nm laser source was used as an excitation source. This laser was focused onto the *n*-alkane sample with a 50X microscope objective. The laser exposure time and power were set to 10 seconds and 0.01 W respectively. The scattered light from the sample was dispersed with a 1200 line/mm grating, and counted with a high sensitivity ultra - low noise CCD camera. The data presentation focus on the CH_2 stretching (2800 cm^{-1} - 2950 cm^{-1}) and CH_2 bending (1450 cm^{-1} – 1480 cm^{-1}) bands in order to highlight features that are expected to vary with the molecular disorder in *n*-alkanes.[32-33] A polarization scrambler was used before the entrance slit in order to eliminate the effect of polarization effects on the measured peak intensities. A depth scan was performed on each crystal in order to find the optimum position that gives the highest Raman signals.

7.4.3 Experimental Results

7.4.3.1 Crystal Characterization of *n*-Alkanes

Regular diamond or parallelogram shaped *n*-alkane crystallites with straight edges and well-defined angles were initially identified by optical microscopy (OM). *n*-Alkanes with chain lengths between 28 and 40 typically crystalize in a monoclinic crystal structure, but can form orthorhombic crystals when impurities are present.[34-36] In this work, we focus on orthorhombic crystals due to their simpler linear dichroism (only the a,b plane are probed in spectra recorded at normal incidence).

To determine the crystal structure of observed *n*-alkane single crystals, the acute interior angles of each *n*-alkane crystal were calculated from high resolution point-by-point STXM images. With the aid of literature lattice parameters,[36-39] these angles were used to confirm the crystal structure of each *n*-alkane single crystal. **Figure 6.1a** in **Chapter 6** presents the literature unit cell parameters, acute interior angle of the crystal, a schematic of the chain orientation within the orthorhombic unit cell, and, the top view of the orthorhombic unit cell.[36-39] Measured acute internal angles for individual *n*-alkane single crystals agree with the values derived from literature orthorhombic crystal structures. Each *n*-alkane in this work shows either an orthorhombic (acute interior angle 68 ±1 °) or a monoclinic structure (acute interior angle 74 ±1 °) when it cast at room temperature (25 ±1 °C) and lower temperature inside a refrigerator (8 ±1 °C). Thinner

orthorhombic crystals are favoured at lower casting temperature. Polarized optical microscopy images of *n*-tetracontane (o-rh *n*-$C_{40}H_{82}$), *n*-dotriacontane (o-rh *n*-$C_{32}H_{66}$), *n*-octacosane (o-rh *n*-$C_{28}H_{58}$) crystals obtained from solution casting method are shown in **Chapter 5** (**Figure 5.3**).

7.4.3.2 NEXAFS Measurements of *n*-Alkanes

Figure 7.1 presents the variation in the C-H band of the carbon 1s NEXAFS spectra of orthorhombic *n*-alkanes with different chain lengths (o-rh *n*-$C_{28}H_{58}$, o-rh *n*-$C_{32}H_{66}$ and o-rh *n*-$C_{40}H_{82}$) with the X-ray polarization directed along the principal crystal axes, X and Y. The spectra are normalized by matching the minimum and maximum intensity feature within the C-H band.

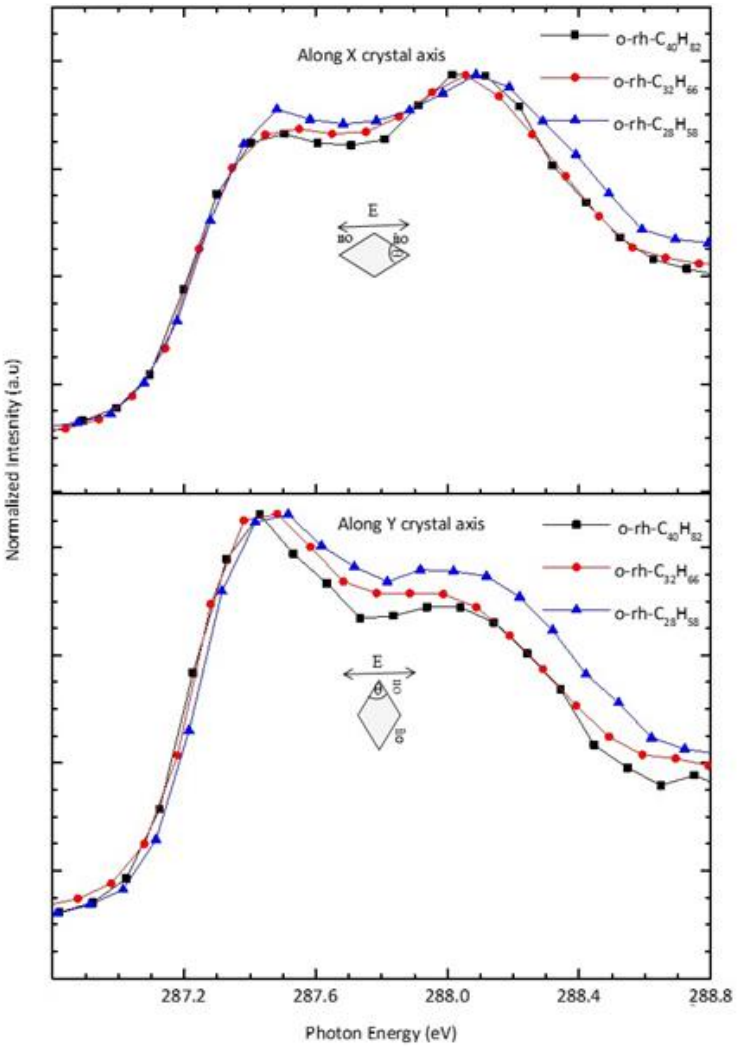

Figure 7.1: Carbon 1s NEXAFS spectra of *n*-alkanes (*n*-$C_{40}C_{82}$, *n*-$C_{32}H_{66}$ and *n*-$C_{28}H_{58}$) with an orthorhombic crystal structure (a) with X-ray linear horizontal polarization directed along long (X) crystal axis and (b) with X-ray linear horizontal polarization directed along short (Y) crystal axis.

The use of *in situ* CO_2 calibration limits the energy range of these NEXAFS spectra to before the onset of the strong carbon 1s → π^* band for CO_2 (g). Broadly, these spectra are similar to previously examined angle resolved NEXAFS spectra from individual *n*-alkane single crystals, from studies where *n*-alkane crystalline polymorphism was not explicitly examined.[5, 9]

The shape and the peak position (energy) of the C-H band is similar when the X-ray linear polarization is directed along either the X or the Y principal axes of the *n*-alkane single crystals with different chain length. However, the C-H band for the orthorhombic *n*-alkane crystals narrows between o-rh *n*-$C_{28}H_{58}$ and the longer chains, o-rh *n*-$C_{32}H_{66}$ and o-rh *n*-$C_{40}H_{82}$. This observation was initially a source of consternation; a trend with chain length was expected, but this discontinuity between o-rh *n*-$C_{28}H_{58}$ and the longer chains was unexpected.

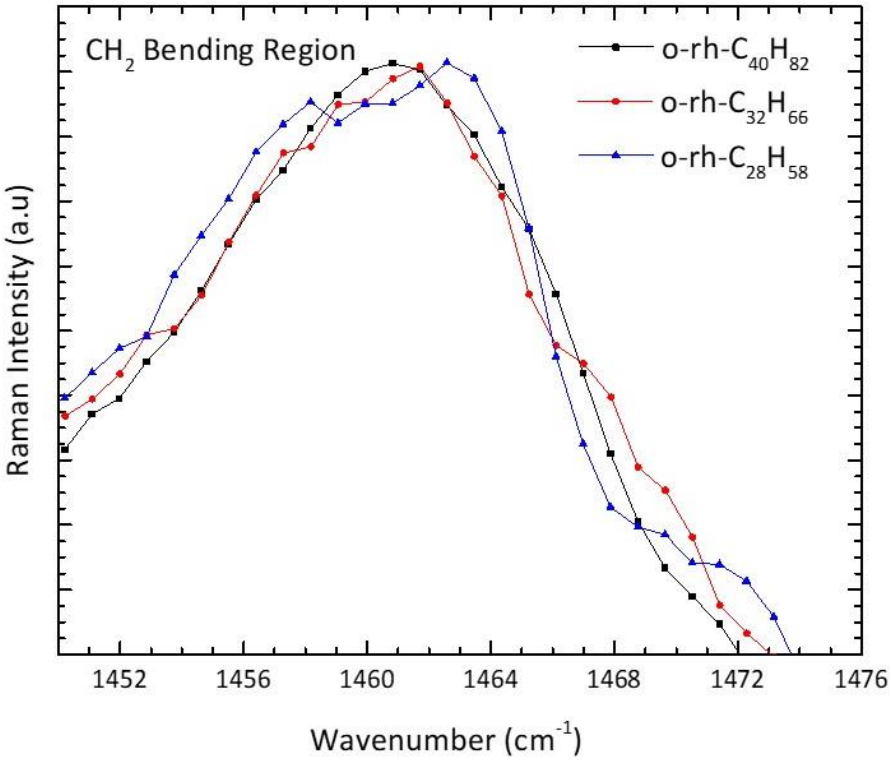

Figure 7.2: Raman measurements of *n*-alkanes (*n*-$C_{40}C_{82}$, *n*-$C_{32}H_{66}$ and *n*-$C_{28}H_{58}$) with an orthorhombic crystal structure at CH_2 bending region.

Figure 7.2 presents the variation in the CH_2 bending bands of the Raman spectra of orthorhombic *n*-alkanes with different chain lengths (o-rh *n*-$C_{28}H_{58}$, o-rh *n*-$C_{32}H_{66}$ and o-rh *n*-$C_{40}H_{82}$) with the unpolarized 785 nm laser source. Relative to the longer o-rh *n*-$C_{40}H_{82}$ alkane, the CH_2 bending peak at 1460 cm^{-1} is asymmetrically split for shorter o-rh *n*-$C_{28}H_{58}$ and two

distinguished peaks were observed at 1457 cm^{-1} and 1463 cm^{-1}. The asymmetric peak split at 1460 cm^{-1} is an evidence for molecular disorder [32, 40] in o-rh *n*-$C_{28}H_{58}$ alkane crystal. This is explained further in below.

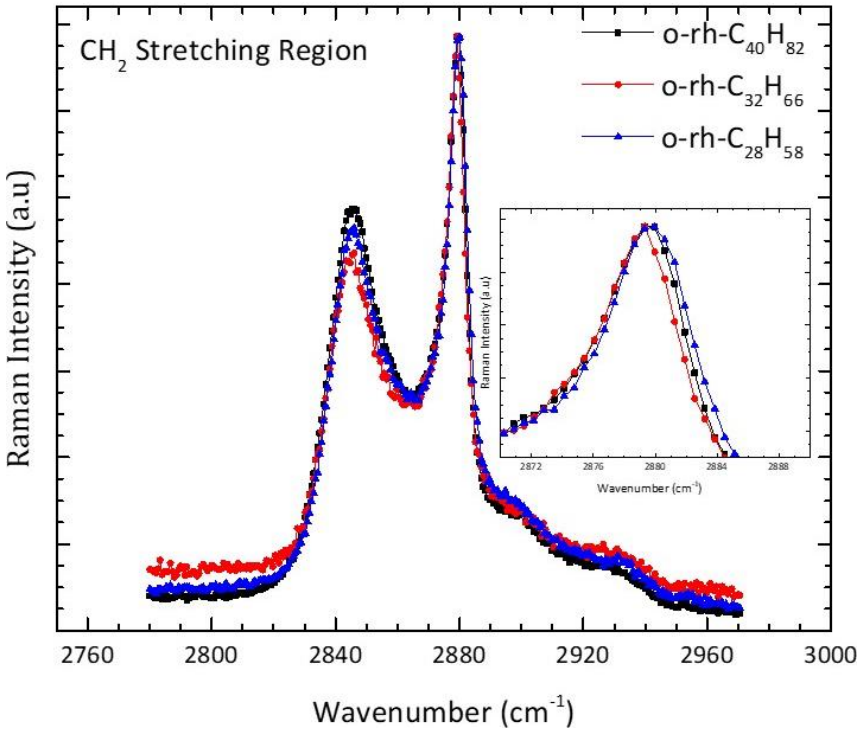

Figure 7.3: Raman measurements of *n*-alkanes (*n*-$C_{40}C_{82}$, *n*-$C_{32}H_{66}$ and *n*-$C_{28}H_{58}$) with an orthorhombic crystal structure at CH_2 stretching region.

Figure 7.3 presents the variation in the CH_2 stretching bands in the Raman spectra of orthorhombic *n*-alkanes with different chain lengths (o-rh *n*-$C_{28}H_{58}$, o-rh *n*-$C_{32}H_{66}$ and o-rh *n*-$C_{40}H_{82}$) with the unpolarized 785 nm laser source. In the stretching region (2800 – 2960 cm^{-1}), the 2880 cm^{-1} stretching peak exhibits a small blue energy shift for the shorter alkane chain length (o-rh *n*-$C_{28}H_{58}$) with relative to the longer chains (*n*-$C_{32}H_{66}$; not for *n*-$C_{40}H_{82}$). Although the observed energy shift is small, the blue energy shift in this particular peak (2880 cm^{-1}) is supported by the literature for greater molecular disorder.[33] This is explained further below.

7.4.4 Discussion

Individual orthorhombic crystals were selected by X-ray microscopy, and examined spectroscopically. **Figure 7.1** presents the NEXAFS spectra of orthorhombic single crystal *n*-alkanes o-rh *n*-$C_{40}C_{82}$, o-rh *n*-$C_{32}H_{66}$ and o-rh *n*-$C_{28}H_{58}$ with the X-ray linear horizontal polarization directed along long (X) crystal axis and the short (Y) crystal axis. The carbon 1s

NEXAFS spectra of orthorhombic *n*-alkanes show a small variation with chain length, where the width of the C-H band is broader for o-rh *n*-$C_{28}H_{58}$ than for the longer chains, o-rh *n*-$C_{32}H_{66}$ and o-rh *n*-$C_{40}H_{82}$. The characteristic C-H band of o-rh *n*-$C_{28}H_{58}$ is unusual and the study was continued to examine the origin behind the unusual spectral behaviour of o-rh *n*-$C_{28}H_{58}$.

Spectral broadening in the carbon 1s NEXAFS spectra of molecular solids is expected to have several origins. Beyond the intrinsic broadening from the core-hole lifetime (~80 meV), vibronic contributions, molecular disorder, and nuclear motion effects are expected to contribute to the shape of the NEXAFS transitions.[11, 24, 26]

In starting this project, we hypothesized that shorter chains (*n*-$C_{28}H_{58}$; MP = 62 ± 1°C) would have greater molecular disorder than longer chains (*n*-$C_{40}H_{82}$; MP = 81 ±1°C), and that these effects might be visible in NEXAFS spectra recorded at room temperature. Evidence for molecular disorder in the solid phase comes from the room temperature stability of *n*-alkane single crystals: crystals of short *n*-alkanes chains deform at room temperature, while crystals of longer *n*-alkanes chains are stable with time. Therefore, stability of the crystal morphology at room temperature supported the fact that short chain o-rh *n*-$C_{28}H_{58}$ alkane could have greater molecular disorder than the long chain o-rh *n*-alkanes (o-rh *n*-$C_{40}C_{82}$, o-rh *n*-$C_{32}H_{66}$). The molecular disorder in each *n*-alkane chain length further studied by Raman spectroscopy. The Raman measurements of this study are focused on the CH_2 bending and stretching bands of *n*-alkanes because, shapes of the bending peak at 1460 cm^{-1}, and position of the stretching peak at 2880 cm^{-1} are expected to vary with the alkane molecular disorder.[32-33, 40]

The study of molecular disorder in different phases (crystal → rotator (disorder phases close to its melt) → melt) of *n*-tetratriacontane (*n*-$C_{34}H_{70}$; M.P = 76 ± 1°C) by Spell *et al*.[32] found that spectral features in the CH_2 bending region of Raman spectra are varied with the molecular disorder in each phase. When *n*-$C_{34}H_{70}$ alkane was heated up to its melting point, they observed a split peak around 1460 cm^{-1} at temperatures close to its melting point (temperatures between 60 - 76 °C). They assigned these spectral variations (split peak) to chain length disorder associated with the temperature.

In our room temperature Raman measurements, a split peak was observed at 1460 cm^{-1} (1457 cm^{-1} and 1463 cm^{-1}) for o-rh *n*-$C_{28}H_{58}$. This observation is consistent with the spectral observation of Spell *et al*.[32] The split peak behaviour could suggest the existence of two different

structures for o-rh *n*-$C_{28}H_{58}$ alkane. Hence, our short chain o-rh *n*-$C_{28}H_{58}$ alkane could be more disordered than the long chain o-rh *n*-alkanes in our system.

In addition to the CH_2 bending peaks, the CH_2 stretching peak (2880 cm^{-1}) also varies with molecular disorder. Corsetti *et al.*[33] studied the intermediate phases during the solid to liquid transitions in *n*-pentadecane (*n*-$C_{15}H_{32}$) as a function of temperature (-4.2 °C to 9.8 °C). In their work, the CH_2 stretching peak exhibited a small blue energy shift when the spectra goes from -4.2 °C to 9.8 °C. During their temperature dependent study, they confirmed that *n*-$C_{15}H_{32}$ showed its rotator phase at -3.6 °C and then it melts at 9.8 °C. Since rotator and melt phases are more disordered than the crystalline phase, the blue shift observed with increased temperature in the CH_2 stretching peak (2880 cm^{-1}) supports greater molecular disorder in *n*-$C_{15}H_{32}$ at higher temperatures. In our Raman study, the CH_2 stretching peak at 2880 cm^{-1} is shifted to a higher energy (higher wavenumber) when spectra goes from o-rh *n*-$C_{32}H_{66}$ to o-rh *n*-$C_{28}H_{58}$. This again supported the fact that short chain o-rh *n*-$C_{28}H_{58}$ alkane is relatively more disordered than the long chain o-rh *n*-alkanes at room temperature.

However, our Raman measurements were unable to provide specific information regarding the type of molecular disorder that exists for o-rh *n*-$C_{28}H_{58}$ at room temperature. Published NMR studies can provide specific information on the nature of nuclear motion and dynamics in *n*-alkanes. Basson *et al.*[1] examined the spin-lattice relaxation time ($T_{1\rho}$) for *n*-alkanes of various lengths. For chains o-rh *n*-$C_{28}H_{58}$ and shorter, they observed a dynamic process in solid *n*-alkanes below the melting point, and well below the characteristic pre-melting point solid / solid phase transition to the rotator phase.[30] This dynamic process was assigned by Basson *et al.*[1] as a thermally populated trans-*gauche* defect motion near the end of the *n*-alkane chains[1](later known as an end-*gauche* defects[41]). An increased population of gauche defects near chain ends was also seen in the Snyder`s studies of rotator phases in *n*-alkanes.[42]

The trans-*gauche* defect has a population of ~1% at ambient temperatures (~285 K for o-rh *n*-$C_{28}H_{58}$).[1] This small population should not make a substantial contribution to the NEXAFS spectrum of a single crystal. In a subsequent work on binary *n*-alkane mixtures (*n*-tetracosane : *n*-octacosane, and others), Basson and Reynhardt found that the concentration of end-*gauche* defects is higher in these binary mixtures, as voids created at chain-ends from the presence of shorter chains provide room for defects in the longer chains. The population of defects increases to ~5%.[41]

The orthorhombic crystal form of *n*-$C_{28}H_{58}$ is not the most stable polymorph, but is found when the sample has impurities, usually of shorter chains. These impurities can lead to an increase in the end-*gauche* defect density in the o-rh *n*-$C_{28}H_{58}$ single crystals. The similarity of the NEXAFS spectra of the longer species (o-rh *n*-$C_{32}H_{66}$ and o-rh *n*-$C_{40}H_{82}$) to each other is consistent with the expected lack of end-*gauche* defects in these samples.

The temperature at which this end-*gauche* defect occurs increases with *n*-alkane chain length. In NMR, this defect is difficult to observe for chains longer than *n*-$C_{31}H_{64}$, as the end-*gauche* transition temperature is shifted close to the temperature of the solid/solid phase transition to the rotator phase.

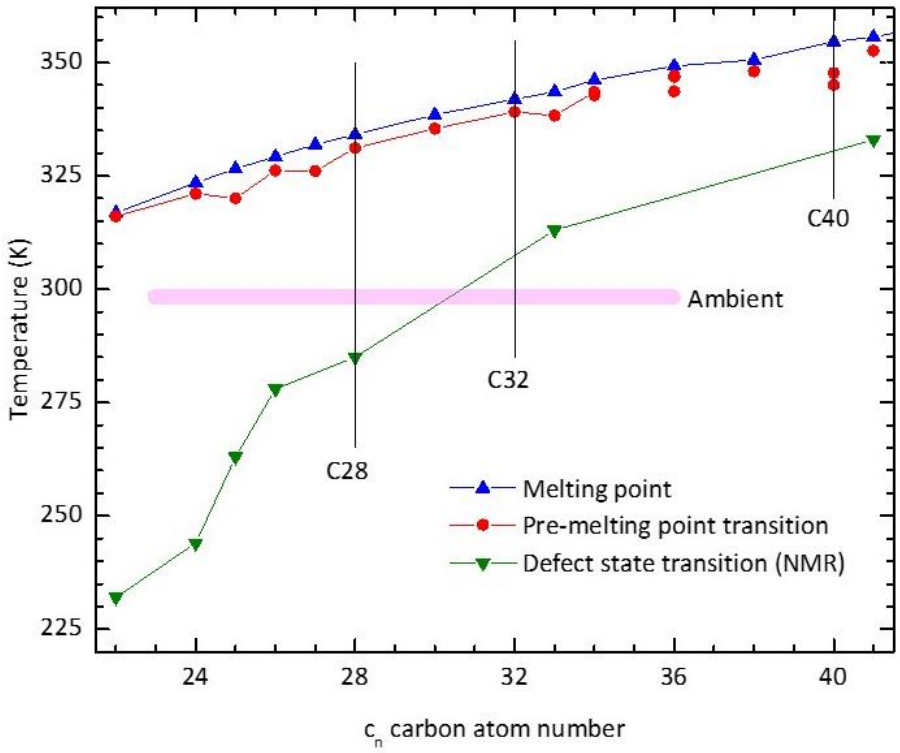

Figure 7.4: Temperature of the melting point transition, pre-melting point solid → solid transition [43-46] and the temperature for the onset of the end-gauche defect state[1], as a function of chain length.

Figure 7.4 presents a plot of the melting point transition temperature, the pre-melting point solid → solid transition (usually to the rotatory phase) and the temperature for the onset of the end-*gauche* defect state, as a function of the *n*-alkane chain length. The temperatures of the melting point and the pre-melting point phase transition are assembled from literature sources,[43-46] and the temperature for the onset of the end-*gauche* defect is estimated from the minima in the spin relaxation times, from Basson and Reynhardt.[1] The end-*gauche* defect state is only accessible at

ambient temperatures for o-rh *n*-$C_{28}H_{58}$; the transition to this state is likely above room temperature for o-rh *n*-$C_{32}H_{66}$.

An accessible local minimum corresponding to the end-*gauche* defect is expected for o-rh *n*-$C_{28}H_{58}$. This will exist in addition to common global minimum for the all trans *n*-alkane configuration for o-rh *n*-$C_{28}H_{58}$, o-rh *n*-$C_{32}H_{66}$, and o-rh *n*-$C_{40}H_{82}$ single crystals. This end-*gauche* defect, observed by NMR and exclusively present in *n*-$C_{28}H_{58}$ at ambient temperature, is proposed as the origin of the greater molecular disorder in *n*-$C_{28}H_{58}$.

This argument can be confirmed by either heating o-rh *n*-$C_{32}H_{66}$ alkane above the end-*gauche* defect state transition temperature (311K or higher) or cooling the o-rh *n*-$C_{28}H_{58}$ alkane below the end-*gauche* defect state transition temperature (280 K or lower). If the end-*gauche* defect is responsible for molecular disorder in the *n*-alkane chain length, C-H band of the carbon 1s NEXAFS spectrum of o-rh *n*-$C_{32}H_{66}$ should be relatively broader at 311K with respect to its room temperature spectrum. On the other hand, C-H band of the carbon 1s NEXAFS spectrum of o-rh *n*-$C_{28}H_{58}$ should be narrow at 280 K relative to its room temperature spectrum.

However, the higher energy band/shift for both the long and short axis of the o-rh *n*-$C_{28}H_{58}$ is likely not due to defect modes in the shortest orthorhombic *n*-alkane (see discussion of the **Chapter 6**). In **Chapter 6**, DFT simulations (*n*-decane) that model the effect of defects and vibrational modes on the NEXAFS spectra shown that defects and vibrational modes caused new contributions to appear at lower energy side of the C-H band instead of higher energy. This observation is reasonable since the HOMO-LUMO gap will decrease as the geometries are distorted from the lowest energy geometry (all trans geometry) and with it, the energy of the core → LUMO transition will also decrease. A plausible reason for the higher energy onset in the C-H band of the o-rh *n*-$C_{28}H_{58}$ is a backbone contribution along the crystal axes X and Y. The backbone peak appears at slightly higher energy.[15] According to **Chapter 5**, if the unit cell of the crystal structure is inclined, the inclination will lead to a contribution from a backbone-oriented transition in the C-H band. This contribution then appear as high energy shoulder in the C-H band of the NEXAFS spectra.[15, 47]

7.4.5 Conclusions

We report crystal symmetry resolved carbon 1s NEXAFS spectra for orthorhombic *n*-alkanes as a function of different chain lengths, from o-rh *n*-$C_{28}H_{58}$ to o-rh *n*-$C_{40}H_{82}$, recorded at room temperature. The C-H band in the carbon 1s NEXAFS spectrum of the shortest *n*-alkane, o-rh *n*-$C_{28}H_{58,}$ is broader than that of the longer *n*-alkane chains. This broadness could be an effect of molecular disorder that exists in the o-rh *n*-$C_{28}H_{58}$ alkane chain length, but the higher energy onset of the C-H band observed in the carbon 1s NEXAFS spectrum of o-rh *n*-$C_{28}H_{58}$ alkane is not most likely due to molecular disorder in the alkane chain length. The higher energy onset of the C-H band observed in the carbon 1s NEXAFS spectrum of o-rh *n*-$C_{28}H_{58}$ alkane along the crystal axes could be due to backbone contribution along the crystal axes X and Y.

7.4.6 References

1. Basson, I.; Reynhardt, E. C. Identification of a Defect Chain Motion in *n*-Alkanes by Means of Nuclear Magnetic Resonance Spin–Lattice Relaxation Time Measurements. *The Journal of Chemical Physics* **1990,** *93* (5), 3604-3609.

2. Urquhart, S. G.; Gillies, R. Rydberg-Valence Mixing in the Carbon 1s Near-Edge X-ray Absorption Fine Structure Spectra of Gaseous Alkanes. *The Journal of Physical Chemistry A* **2005,** *109* (10), 2151-2159.

3. Urquhart, S. G.; Gillies, R. Matrix Effects in the Carbon 1s Near Edge X-ray Absorption Fine Structure Spectra of Condensed Alkanes. *The Journal of Chemical Physics* **2006,** *124* (23), 234704.

4. Weiss, K.; Bagus, P.; Wöll, C. Rydberg Transitions in X-ray Absorption Spectroscopy of Alkanes: The Importance of Matrix Effects. *The Journal of Chemical Physics* **1999,** *111* (15), 6834-6845.

5. Zou, Y.; Araki, T.; Appel, G.; Kilcoyne, A. L. D.; Ade, H. Solid State Effects in the NEXAFS Spectra of Alkane-Based van der Waals Crystals: Breakdown of Molecular Model. *Chemical Physics Letters* **2006,** *430* (4), 287-292.

6. Bagus, P.; Weiss, K.; Schertel, A.; Wöll, C.; Braun, W.; Hellwig, C.; Jung, C. Identification of Transitions into Rydberg States in the X-ray Absorption Spectra of Condensed Long-Chain Alkanes. *Chemical Physics Letters* **1996,** *248* (3-4), 129-135.

7. Schöll, A.; Fink, R.; Umbach, E.; Mitchell, G.; Urquhart, S.; Ade, H. Towards a Detailed Understanding of the NEXAFS Spectra of Bulk Polyethylene Copolymers and Related Alkanes. *Chemical Physics Letters* **2003,** *370* (5-6), 834-841.

8. Stöhr, J.; Outka, D.; Baberschke, K.; Arvanitis, D.; Horsley, J. Identification of C-H Resonances in the K-Shell Excitation Spectra of Gas-Phase, Chemisorbed, and Polymeric Hydrocarbons. *Physical Review B* **1987,** *36* (5), 2976-2979.

9. Swaraj, S.; Ade, H. Differences in NEXAFS of Odd/Even Long Chain *n*-Alkane Crystals. *Journal of Electron Spectroscopy and Related Phenomena* **2013,** *191*, 60-64.

10. Ueda, K.; Okunishi, M.; Chiba, H.; Shimizu, Y.; Ohmori, K.; Sato, Y.; Shigemasa, E.; Kosugi, N. Rydberg-Valence Mixing in the Carbon 1s Excited States of CH_4 Probed by Electron Spectroscopy. *Chemical Physics Letters* **1995,** *236* (3), 311-317.

11. Patel, S. N.; Su, G. M.; Luo, C.; Wang, M.; Perez, L. A.; Fischer, D. A.; Prendergast, D.; Bazan, G. C.; Heeger, A. J.; Chabinyc, M. L.; Kramer, E. J. NEXAFS Spectroscopy Reveals the Molecular Orientation in Blade-Coated Pyridal[2,1,3]Thiadiazole-Containing Conjugated Polymer Thin Films. *Macromolecules* **2015,** *48* (18), 6606-6616.

12. Urquhart, S. G.; Hitchcock, A. P.; Smith, A. P.; Ade, H. W.; Lidy, W.; Rightor, E. G.; Mitchell, G. E. NEXAFS Spectromicroscopy of Polymers: Overview and Quantitative Analysis of Polyurethane Polymers. *Journal of Electron Spectroscopy and Related Phenomena* **1999,** *100* (1-3), 119-135.

13. Ade, H.; Stoll, H. Near-Edge X-ray Absorption Fine-Structure Microscopy of Organic and Magnetic Materials. *Nature Materials* **2009,** *8* (4), 281-290.

14. Hitchcock, A. P.; Stöver, H. D.; Croll, L. M.; Childs, R. F. Chemical Mapping of Polymer Microstructure Using Soft X-ray Spectromicroscopy. *Australian Journal of Chemistry* **2005,** *58* (6), 423-432.

15. Fu, J.; Urquhart, S. G. Linear Dichroism in the X-ray Absorption Spectra of Linear *n*-Alkanes. *The Journal of Physical Chemistry A* **2005,** *109* (51), 11724-11732.

16. Hahner, G. Near Edge X-ray Absorption Fine Structure Spectroscopy As a Tool to Probe Electronic and Structural Properties of Thin Organic Films and Liquids. *Chemical Society Reviews* **2006,** *35* (12), 1244-1255.

17. Ade, H.; Hitchcock, A. P. NEXAFS Microscopy and Resonant Scattering: Composition and Orientation Probed in Real and Reciprocal Space. *Polymer* **2008,** *49* (3), 643-675.

18. Lehmann, J.; Solomon, D.; Brandes, J.; Fleckenstein, H.; Jacobson, C.; Thieme, J.; Senesi, N.; Xing, B.; Huang, P. Synchrotron-Based Near-Edge X-ray Spectroscopy of Natural Organic Matter in Soils and Sediments. *Biophysico-Chemical Processes Involving Natural Nonliving Organic Matter in Environmental Systems* **2009**, 729-781.

19. Fu, J.; Urquhart, S. G. Effect of Chain Length and Substrate Temperature on the Growth and Morphology of *n*-Alkane Thin Films. *Langmuir* **2007,** *23* (5), 2615-2622.

20. Masnadi, M.; Urquhart, S. G. Effect of Substrate Temperature on the Epitaxial Growth of Oriented *n*-Alkane Thin Films on Graphite. *Langmuir* **2012,** *28* (34), 12493-12501.

21. Masnadi, M.; Urquhart, S. G. Indirect Molecular Epitaxy: Deposition of *n*-Alkane Thin Films on Au Coated NaCl(001) and HOPG(0001) Surfaces. *Langmuir* **2013,** *29* (21), 6302-6307.

22. Leetmaa, M.; Ljungberg, M.; Lyubartsev, A.; Nilsson, A.; Pettersson, L. G. Theoretical Approximations to X-ray Absorption Spectroscopy of Liquid Water and Ice. *Journal of Electron Spectroscopy and Related Phenomena* **2010,** *177* (2-3), 135-157.

23. Ma, Y.; Chen, C.; Meigs, G.; Randall, K.; Sette, F. High-Resolution K-Shell Photoabsorption Measurements of Simple Molecules. *Physical Review A* **1991,** *44* (3), 1848-1858.

24. Schwartz, C. P.; Uejio, J. S.; Saykally, R. J.; Prendergast, D. On the Importance of Nuclear Quantum Motions in Near Edge X-ray Absorption Fine Structure Spectroscopy of Molecules. *The Journal of Chemical Physics* **2009,** *130* (18), 184109.

25. Nilsson, A.; Pettersson, L. G. The Structural Origin of Anomalous Properties of Liquid Water. *Nature Communications* **2015,** *6*, 8998.

26. Uejio, J. S.; Schwartz, C. P.; Saykally, R. J.; Prendergast, D. Effects of Vibrational Motion on Core-Level Spectra of Prototype Organic Molecules. *Chemical Physics Letters* **2008,** *467* (1-3), 195-199.

27. Fransson, T.; Zhovtobriukh, I.; Coriani, S.; Wikfeldt, K. T.; Norman, P.; Pettersson, L. G. Requirements of First-Principles Calculations of X-ray Absorption Spectra of Liquid Water. *Physical Chemistry Chemical Physics* **2016,** *18* (1), 566-583.

28. Schwartz, C. P.; Saykally, R. J.; Prendergast, D. An Analysis of the NEXAFS Spectra of a Molecular Crystal: α-Glycine. *The Journal of Chemical Physics* **2010,** *133* (4), 044507.

29. Gordon, M. L.; Cooper, G.; Morin, C.; Araki, T.; Turci, C. C.; Kaznatcheev, K.; Hitchcock, A. P. Inner-Shell Excitation Spectroscopy of the Peptide Bond: Comparison of the C 1s, N 1s, and O 1s Spectra of Glycine, Glycyl-Glycine, and Glycyl-Glycyl-Glycine. *The Journal of Physical Chemistry A* **2003,** *107* (32), 6144-6159.

30. Mukherjee, P. K. Phase Transitions Among the Rotator Phases of the Normal Alkanes: A Review. *Physics Reports* **2015,** *588*, 1-54.

31. Kaznatcheev, K.; Karunakaran, C.; Lanke, U.; Urquhart, S.; Obst, M.; Hitchcock, A. Soft X-ray Spectromicroscopy Beamline at the CLS: Commissioning Results. *Nuclear Instruments and Methods in Physics Research Section A: Accelerators, Spectrometers, Detectors and Associated Equipment* **2007,** *582* (1), 96-99.

32. Wickramarachchi, P. S. R.; Spells, S. J.; de Silva, D. S. M. Study of Disorder in Different Phases of Tetratriacontane and a Binary Alkane Mixture, Using Vibrational Spectroscopy. *The Journal of Physical Chemistry B* **2007,** *111* (7), 1604-1609.

33. Corsetti, S.; Rabl, T.; McGloin, D.; Kiefer, J. Intermediate Phases During Solid to Liquid Transitions in Long-Chain *n*-Alkanes. *Physical Chemistry Chemical Physics* **2017,** *19* (21), 13941-13950.

34. Broadhurst, M. G. An Analysis of the Solid Phase Behavior of the Normal Paraffins. *Journal of Research of the National Bureau of Standards* **1962,** *66*, 241-249.

35. Nyburg, S.; Potworowski, J. Prediction of unit Cells and Atomic Coordinates for the *n*-Alkanes. *Acta Crystallographica Section B: Structural Crystallography and Crystal Chemistry* **1973,** *29* (2), 347-352.

36. Boistelle, R.; Simon, B.; Pepe, G. Polytypic Structures of *n*-$C_{28}H_{58}$ (*n*-octacosane) and *n*-$C_{36}H_{74}$ (*n*-Hexatriacontane). *Acta Crystallographica Section B* **1976,** *32* (4), 1240-1243.

37. Craig, S. R.; Hastie, G. P.; Roberts, K. J.; Sherwood, J. N. Investigation into the Structures of Some Normal Alkanes Within the Homologous Series $C_{13}H_{28}$ to $C_{60}H_{122}$ Using High-Resolution Synchrotron X-ray Powder Diffraction. *Journal of Materials Chemistry* **1994,** *4* (6), 977-981.

38. Plomp, M.; Van Enckevort, W.; Van Hoof, P.; Van De Streek, C. Morphology of and Dislocation Movement in *n*-$C_{40}H_{82}$ Paraffin Crystals Grown From Solution. *Journal of Crystal Growth* **2003,** *249* (3), 600-613.

39. Teare, P. The Crystal Structure of Orthorhombic *n*-Hexatriacontane, *n*-$C_{36}H_{74}$. *Acta Crystallographica* **1959,** *12* (4), 294-300.

40. Barnes, J.; Fanconi, B. Raman Spectroscopy, Rotational Isomerism, and the``Rotator" Phase Transition in *n*-Alkanes. *The Journal of Chemical Physics* **1972,** *56* (10), 5190-5192.

41. Basson, I.; Reynhardt, E. C. Identification of Defect Chain Motions in the Low Temperature Orthorhombic Phase of Binary Mixtures of *n*-Alkanes by Means of Nuclear Magnetic Resonance Spin-Lattice Relaxation Time Measurements. *The Journal of Chemical Physics* **1991,** *95* (2), 1215-1222.

42. Maroncelli, M.; Strauss, H.; Snyder, R. The Distribution of Conformational Disorder in the High-Temperature Phases of the Crystalline *n*-Alkanes. *The Journal of Chemical Physics* **1985,** *82* (6), 2811-2824.

43. Sirota, E.; Singer, D. Phase Transitions Among the Rotator Phases of the Normal Alkanes. *The Journal of Chemical Physics* **1994,** *101* (12), 10873-10882.

44. Briard, A. J.; Bouroukba, M.; Petitjean, D.; Hubert, N.; Dirand, M. Experimental Enthalpy Increments from the Solid Phases to the Liquid Phase of Homologous *n*-Alkane Series (C18 to C38 and C41, C44, C46, C50, C54, and C60). *Journal of Chemical & Engineering Data* **2003,** *48* (3), 497-513.

45. Wang, S.; Tozaki, K. I.; Hayashi, H.; Inaba, H.; Yamamoto, H. Observation of Multiple Phase Transitions in Some Even *n*-Alkanes Using a High Resolution and Super-Sensitive DSC. *Thermochimica Acta* **2006,** *448* (2), 73-81.

46. Tozaki, K. I.; Inaba, H.; Hayashi, H.; Quan, C.; Nemoto, N.; Kimura, T. Phase Transitions of *n*-$C_{32}H_{66}$ Measured by Means of High Resolution and Super-Sensitive DSC. *Thermochimica Acta* **2003,** *397* (1–2), 155-161.

47. Perera, S. D., ; Wang, J.; Urquhart, S.G. Linear Dichroism (LD) in the NEXAFS Spectra of *n*-Alkanes with Different Crystalline Polymorphs. *Journal of Electron Spectroscopy and Related Phenomena* **2019,** *232*, 5-10.

Chapter 8 Discussion and Conclusions

The goal of this research work is to build a general understanding on how different intermolecular interactions affect the carbon 1s NEXAFS spectroscopy of molecules. In order to achieve our goal, the study focused on two types of interactions: π-π interactions for unsaturated molecules (first research objective) and effects of Rydberg quenching on the degree of Rydberg-valence mixing for saturated molecules (second research objective). However, in pursuing the second research objective, NEXAFS spectroscopy of orthorhombic *n*-alkanes exhibited a spectral broadening with the shorter chain o-rh *n*-$C_{28}H_{58}$ (see **Chapter 5**). Therefore, spectral broadening in the orthorhombic *n*-alkane spectra was studied in terms of nuclear motion contribution (see **Chapter 6**) and molecular disorder in the short chain orthorhombic *n*-alkanes (see **Chapter 7**).

8.1 Effects of π-π Interactions to the Carbon 1s NEXAFS Spectroscopy

In this research work, [n,n] paracyclophane (PCP) molecules are used as a model system to study the effects of π-π interactions on the NEXAFS spectra. [n,n]PCP molecule consists of two benzene rings connected by an aliphatic bridging unit of variable length.

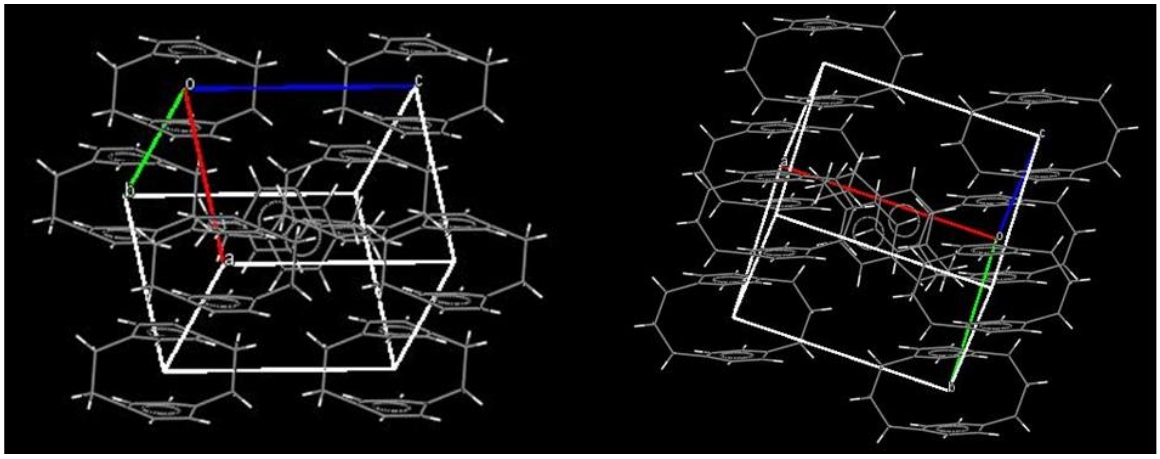

Figure 8.1: Crystal structure of [2,2]PCP (left)[1,2] and [3,3]PCP (right).[1,3]

Although more than one PCP molecules occupies in a unit cell, crystallographic data of the PCP molecules ([2,2], [3,3]) used in this work confirms that π-π interactions of the PCP molecules are controlled by the distance between the two rings *within the PCP molecule*.[1-3] The crystal structure of the [2,2]PCP and [3,3]PCP is given in **Figure 8.1**. According to **Figure 8.1**, both [2,2] and [3,3]PCPs have two molecules per unit cell.[1] Moreover, PCP molecule at the center of the unit cell have a different phenyl ring orientation than the PCP molecules at the corners.[1-3] The most

important observation is phenyl rings in the different PCPs are not facially aligned to each other. Only the phenyl rings within the molecule are facially aligned.[1-3] This confirms that π-π interactions of the PCP molecules originate from the benzene-benzene separation within the molecule, not from the benzene-benzene interactions between different PCP molecules. Therefore, PCP molecules with different inter-ring distances, systematically vary the π-π interactions between the two benzene rings, and PCP molecules are good experimental model to study the π-π interactions. Hence, spectroscopic changes in the experimental carbon 1s NEXAFS spectra of PCPs highlight the effects of π-π interactions in the NEXAFS spectroscopy.

The experimental results of this work showed that carbon 1s → π* transition energy of the PCP molecules shifts to the lower energy as the PCP benzene rings are closer together ([3,3]PCP → [2,2]PCP). This experimental trend was reproduced and rationalized by the high quality Transition Potential Density Functional Theory (TP-DFT) calculations (see **Chapter 4**). The magnitude of the experimental energy shift (0.2 eV) observed between the PCPs with different benzene/benzene separation in this research work was justified by using TP-DFT calculations of dibenzene model with different ring separation distances. According to the TP-DFT calculations of dibenzene model, the magnitude of the energy shift is larger when the benzene-benzene separation is below the van der Waals separation distance (3.4 Å). Since our PCP molecules (both [2,2] and [3,3]) have a benzene-benzene ring distance less than van der Waals separation distance (3.4 Å), a larger magnitude of the experimental energy shift is expected and theoretical predictions of the dibenzene model were matched with our experimental trend. However, the di benzene model also showed that once the benzene-benzene ring distance is greater than the van der Waals separation distance (3.4 Å), the magnitude of the energy shift is decreased and effects of π-π interactions to the NEXAFS spectroscopy will be weak. This prediction was confirmed by the recent NEXAFS study of P3HT to understand the sensitivity of the NEXAFS spectroscopy to molecular conformation and aggregation.[4] The P3HT molecules used in their work have a chain separation distance of 3.9 Å which is greater than the van der Waals separation distance.[4] For this reason, effects of π-π interactions in the P3HT molecules to the NEXAFS spectroscopy should be minimum. The small spectral energy shift (~ 10 meV) observed in their work is confirmed our theoretical prediction. However, chain separation distance of the P3HT molecules can be decreased by preparing P3HT samples with different sample preparation techniques such as epitaxial growth.[5] In such cases, significant effect might be observed from the π-π interactions of

P3HT molecules. Therefore, our research work not only highlight the effects of π-π interactions in the NEXAFS spectroscopy, it also helpful to comment the significance of the effects of π-π interactions to the NEXAFS spectroscopy as a function of separation distance.

8.2 Effects of Rydberg Quenching on the Degree of Rydberg-Valence Mixing to the Carbon 1s NEXAFS Spectra of Saturated Molecules (*n*-Alkanes)

In the second part of this research, the effects of Rydberg quenching on the degree of Rydberg-valence mixing to the carbon 1s NEXAFS spectra of saturated molecules were studied by using *n*-alkane molecules as a model system. The initial goal was to explore the contribution of the differences in the Rydberg-valence mixing to the NEXAFS spectroscopy as a function of chain lengths (*n*-$C_{28}H_{58}$, *n*-$C_{32}H_{66}$ and *n*-$C_{40}H_{82}$) and for well-defined crystal structures, orthorhombic (o-rh) and monoclinic (mon). During the study, experimental challenges in single crystal *n*-alkane spectroscopy such as crystal thickness, crystal misalignment, radiation damage, and the purity of the X-ray polarization were carefully addressed and separated in order to isolate the spectroscopic contribution of the Rydberg valance mixing to the NEXAFS spectra (see **B.2**). However, a comparison of the NEXAFS spectra of orthorhombic and monoclinic *n*-alkanes did not exhibit differences in Rydberg-valence mixing. The effect of Rydberg quenching on the degree of Rydberg-valence mixing to the NEXAFS spectroscopy caused by different crystal structures of *n*-alkanes were not significant. Orthorhombic and monoclinic crystal structures of *n*-alkanes had similar crystalline behaviour in their molecular arrangements of the sub-cell. The local geometry (named as a sub-cell oriented along the *n*-alkane backbone) of monoclinic structure is similar to the orthorhombic structure. Since local geometries (sub-cells) are identical in both orthorhombic and monoclinic structures, the degree of Rydberg quenching should be the same for each crystalline polymorph (orthorhombic and monoclinic). Therefore, the effect of next-neighbour interactions should be same for both crystal structures, and it justified the similar spectral behaviour between the two crystal structures in our work.

The arrangement of the *n*-alkane chains within the layer, and stacking of the layers are different between the orthorhombic and monoclinic structures (**Figure 5.1**). This is the reason for having a distinct linear dichroism effect along the principle crystal axes (X and Y in **Figure 5.1**) of the orthorhombic and monoclinic *n*-alkane single crystals. According to **Figure 5.1**, chain axis of the orthorhombic and monoclinic crystals are oriented differently with respect to their end group

plane. In orthorhombic crystals, the chain axis is normal to the end group plane whereas the chain axis of the monoclinic crystals is tilted. [6-8]

In the monoclinic structure, the chains are inclined (tilted) by 27° towards the short crystal axis (Y), by rotation about long crystal axis (X). This makes the angle between c crystal axis and long crystal axis (b or X axis) of the monoclinic crystal (see β angle in **Figure 5.1** in **Chapter 5**) higher than 90°.[9-10] Furthermore, in monoclinic structure, the component along long crystal axis (b or X) will be all C-H, while the component along the short crystal axis (a or Y) will have some c axis component. Hence, the contributions of TDMs directed along the a and c lattice vectors varies with the polymorph and that causes a distinct linear dichroism effect along the principle crystal axes (X and Y) of the orthorhombic and monoclinic *n*-alkane single crystals. As a result, a macromolecular backbone contribution should be visible in the C-H band along the Y crystal axis for monoclinic chains. As mentioned in the discussion of **Chapter 5**, such backbone sensitivity should be visible through the weak C-H feature at 288.5 eV that have a TDM oriented along the c axis, orthogonal to the CH_2 plane, but this weak third resonance was not resolved in the experimental NEXAFS spectra of both orthorhombic and monoclinic alkanes (**Figures 5.4** and **5.5** in **Chapter 5**). However, an unresolved higher energy shoulder for monoclinic structure along the Y crystal axis was observed in this work (see $\sigma^*_{C\text{-}H} / R_\perp$ peak in **Figure 5.5**). This observation is assigned as a contribution from the chain backbone in the monoclinic structure since monoclinic chains are tilt in one direction (along the Y crystal axis).

Though the observed linear dichroism effect did not contribute to the broader goal of building a general understanding of the role of intermolecular interactions in NEXAFS spectroscopy, the knowledge acquired from this work will be useful and contributed to the literature. In addition to the linear dichroism effect, spectral broadening was observed for shorter chains of orthorhombic *n*-alkanes (o-rh *n*-$C_{28}H_{58}$). Therefore, study was continued to address the scientific reasons behind the unusual spectral broadening in NEXAFS spectroscopy with the shorter o-rh *n*-$C_{28}H_{58}$ alkane chain length.

8.3 Effects of Nuclear Motion on the Carbon 1s NEXAFS Spectroscopy of *n*-Alkanes

Typically, the shape of the core-level spectra of molecular solids, such as *n*-alkanes, is interpreted without considering the nuclear motion contribution. However, unresolved nuclear motion effects contribute to the shape of the core-level spectra and lead to asymmetric broadening

of NEXAFS lineshapes. The spectroscopic sampling of the distribution of geometries found in the electronic ground state is usually called as "nuclear motion effects". In general, such geometric distributions occur due to zero-point motion (υ = 0), thermally populated vibration modes (υ = 1,2,3…), and thermally populated molecular conformations with their own vibrational manifolds. Since NEXAFS spectrum reflects the average contribution of all these geometries, sampling the contributions of each geometries are important for complete understanding of the spectrum.

In this research, nuclear motion contributions and molecular disorder associated with the orthorhombic *n*-alkane chains were studied in order to address the origin behind the spectral broadening in the orthorhombic *n*-alkane spectra. The shortest orthorhombic *n*-alkane (o-rh *n*-$C_{28}H_{58}$) in our system was examined by comparing the NEXAFS spectra of o-rh *n*-$C_{28}H_{58}$ alkane at room temperature (~ 298 K) and at cryogenic temperatures (~ 93 K). Nuclear motion contributions to the spectra should be minimal at cryogenic temperature, but not completely disappeared since zero-point motion will still exist at cryogenic temperature. However, the spectral difference between these two temperatures (~ 298 K vs ~ 93 K) will allow us to isolate the spectroscopic contribution arise from the nuclear motions of o-rh *n*-$C_{28}H_{58}$ since this comparison will be able to see the spectral contribution of the thermally excited vibrational modes, as Boltzmann distribution of thermally populated vibrational modes will increase with sample temperature. The shape of the carbon 1s NEXAFS spectrum (C-H band) of o-rh *n*-$C_{28}H_{58}$ at room temperature is relatively broader than the spectrum obtained at cryogenic temperature and C-H band has a lower energy onset. A broader C-H band is expected at higher temperature, as nuclear motion will be more significant. However, an onset energy difference in the C-H band between the temperatures is unexpected, and the TP-DFT simulations of the carbon 1s NEXAFS spectra of *n*-decane (*n*-$C_{10}H_{22}$) with an all trans minimum energy geometry, to simulations of gauche defects and thermally populated vibrational models used as a model system to explained this unexpected onset energy difference. By rotating bond dihedrals in *n*-decane (*n*-$C_{10}H_{22}$) individually, the effects of gauche defects on the NEXAFS spectra were studied. The populations of gauche defects at room temperature was obtained from the molecular dynamic study of Thomas *et al*.[11] The simulations showed that, gauche defects and thermally populated vibration modes in the *n*-alkane chain (*n*-$C_{10}H_{22}$) caused new spectral contributions at lower energy side of the spectra relative to lowest energy all trans geometry. In general, gauche defects and thermally populated vibrational modes caused structural distortions from all trans geometry. This helps in explaining the lower energy

onset of the C-H band in the room temperature spectrum. As geometries are distorted from all trans geometry, HOMO-LUMO gap will decrease and with it, the energy of the core → LUMO transition will decrease. The shape variation between the two temperatures can be explained by considering the restricted thermal motion at cryogenic temperature. At cryogenic temperature, thermal motion in the sample is restricted and leads to lower thermal populations of vibrational modes and defects. This results a narrower band and a higher energy onset at cryogenic temperature (~ 93 K) relative to the room temperature (~ 298 K). The study confirmed the active role of nuclear motion in the spectral broadening of carbon 1s NEXAFS spectroscopy.

8.4 Effects of Molecular Disorder on the Carbon 1s NEXAFS Spectroscopy of *n*-Alkanes

Raman spectroscopy used to study the molecular disorder in *n*-alkane chain lengths. Room temperature Raman measurements of orthorhombic *n*-alkanes (*n*-$C_{28}H_{58}$, *n*-$C_{32}H_{66}$ and *n*-$C_{40}H_{82}$) supported the greater molecular disorder behaviour in the o-rh *n*-$C_{28}H_{58}$ (see the discussion in **Chapter 7**). Our Raman measurements of the o-rh *n*-$C_{28}H_{58}$ did not determine the specific type of molecular disorder exist in the *n*-alkane molecule, it only proved the fact that short chain o-rh *n*-$C_{28}H_{58}$ alkane is more disordered than the other two orthorhombic-*n*-alkanes (o-rh *n*-$C_{32}H_{66}$ and o-rh *n*-$C_{40}H_{82}$). However, there was an evidence in literature[12-13] that provides specific information on the nature of nuclear motion and dynamics in *n*-alkanes, particular for the short chain o-rh *n*-$C_{28}H_{58}$. According to the literature NMR dynamic studies,[12-13] molecular disorder in o-rh *n*-$C_{28}H_{58}$ could originate from dynamic end-*gauche* defect mode present exclusively in orh *n*-$C_{28}H_{58}$ at room temperature.[12-13] For o-rh *n*-$C_{28}H_{58}$, this defect mode is active temperatures above 285 K, and this backbone oriented compound is predicted to be visible for o-rh *n*-$C_{32}H_{66}$ above 311 K.[12]

In the future, this type of spectral broadening in *n*-alkanes can be identified by performing temperature dependence NEXAFS measurements for o-rh *n*-$C_{28}H_{58}$ and o-rh *n*-$C_{32}H_{66}$ alkane chains (see **Chapter 9** for **Future work**). For an example, it was determined that the end-*gauche* defect mode is visible for o-rh *n*-$C_{32}H_{66}$ above 311 K.[12] Hence, if the NEXAFS spectra (C-H band) getting broader and the C-H band is observed a lower energy onset with the temperature greater than 311 K for o-rh *n*-$C_{32}H_{66}$ in our temperature dependence NEXAFS measurements, dynamic end-*gauche* could be the defect type responsible for the spectral broadening. However, the effects of the defects in the short chain orthorhombic *n*-alkanes does not explain the higher energy band observed in the carbon 1s NEXAFS spectra (C-H band) of o-rh *n*-$C_{28}H_{58}$ (see discussion of

Chapter 6). This higher energy band is most likely due to backbone contribution along the crystal axes X and Y since backbone peak appears at slightly higher energy (see discussion of **Chapter 5**). This could happened if the unit cell of the crystal structure is inclined towards the crystal axes X and Y and with it, a contribution from a backbone-oriented transition can appear as high energy shoulder in the C-H band of the NEXAFS spectra.

The knowledge of this research could be useful to understand the spectroscopy of complex organic electronic polymers and could provide information on structure and order. Therefore, research outcome of this work contributed to the broader goal of building a general understanding of the role of intermolecular interactions in NEXAFS spectroscopy.

8.5 Conclusions

Effects of π-π interactions to the carbon 1s NEXAFS spectra of unsaturated molecules

The carbon 1s NEXAFS spectra of [2,2]PCP and [3,3]PCP were carefully examined in order to identify the effects of π-π interactions between the unsaturated molecules to the carbon 1s NEXAFS spectroscopy. The effects of π-π interactions was studied as a function of benzene-benzene separation distance in the PCP molecules. The distinct spectroscopy changes observed between the two different benzene-benzene separation distances of the PCP molecules ([2,2]PCP and [3,3]PCP). The spectroscopic changes in the PCP molecules were reproduced and rationalized with the ΔK-S-DFT calculations. Both experimental and simulation spectra validate the active role of π-π interactions in the carbon 1s NEXAFS spectroscopy of unsaturated molecules. The differences in both core binding energies and π* orbital energies originated from the strength of the π-π interactions in each PCPs, and strength will be enhanced when the benzene rings are closed to each other (PCP with the smaller bridging group). Moreover, The effects of π-π interactions to the NEXAFS spectroscopy is significant when the distance between the unsaturated molecules is less than the van der Waals distance (3.4 Å), and the effects diminished when unsaturated molecules are further apart.

Effects of Rydberg quenching on the degree of Rydberg – valence mixing to the carbon 1s NEXAFS spectra of saturated molecules

The carbon 1s NEXAFS spectra of *n*-alkanes were carefully examined as a function of chain lengths (*n*-$C_{28}H_{58}$, *n*-$C_{32}H_{66}$, and *n*-$C_{40}H_{82}$) and the function of different crystalline polymorphs (orthorhombic and monoclinic) to identify the effects of Rydberg quenching on the degree of Rydberg – valence mixing present between the saturated molecules to the NEXAFS spectroscopy.

Well-ordered diamond shape *n*-alkane single crystals were obtained by using solution casting method. The experimental conditions of the solution casting method was optimized, and obtained both orthorhombic and monoclinic crystal structures for each alkanes. The shape of the short chain *n*-alkanes used in this work was highly unstable and crystals were destroyed during the data acquisition. The differences in the Rydberg-valence mixing arise from the different chain lengths and different crystalline polymorphs of the *n*-alkanes have a weak effect to the carbon 1s NEXAFS spectroscopy. Instead, distinct linear dichroism effect was observed with the angle

dependent carbon 1s NEXAFS spectra (C-H band) of *n*-alkanes. The linear dichroism effect is similar for orthorhombic and monoclinic crystal structures, but it is different for a given crystal structure (orthorhombic or monoclinic) along the principal crystal axes of the crystal (X and Y). Specifically, inclination towards the short crystal axis Y in the monoclinic unit cell leads to a backbone contribution in the C-H band, and it appeared as a high energy shoulder in the C-H band. This study shows the importance of considering crystal structure when interpreting the NEXAFS spectra of single crystals.

Effects of nuclear motion and molecular disorder to the carbon 1s NEXAFS spectra of saturated molecules

In addition to that, the characteristic of the C-H band of the short chain o-rh *n*-$C_{28}H_{58}$ is unusual and spectral broadening observed in particular for o-rh *n*-$C_{28}H_{58}$ was studied in terms of nuclear motion attributed to thermally populated defects and vibrational modes. From the temperature dependence (~ 298 K vs ~ 93 K) study of the NEXAFS spectra of *n*-alkanes, it was found that nuclear motion caused distinctive spectral change to the C-H band recorded at room temperature (~ 298 K). In that study, DFT simulations show that structural distortions arise from the gauche defects or thermally populated vibrational modes (nuclear motion) result in new features appearing at lower energy in the NEXAFS spectrum and are the origins for the lower energy onset of the C-H band observed in the room temperature NEXAFS spectrum. These thermal motions in the sample are higher at room temperature and leads to higher population of vibrational modes and thermally accessible defects relative to the cryogenic temperature. Hence, C-H band in the spectrum recorded at room temperature is broader than the spectrum reordered at cryogenic temperature. The room temperature Raman measurements of orthorhombic-*n*-alkanes (o-rh *n*-$C_{28}H_{58}$, o-rh *n*-$C_{32}H_{66}$, and o-rh *n*-$C_{40}H_{82}$) showed that molecular disorder is greater in the o-rh *n*-$C_{28}H_{58}$ alkane. Although Raman measurements unable to provide the specific information regarding the type of molecular disorder exist for o-rh *n*-$C_{28}H_{58}$ alkane at room temperature, published NMR studies in literature suggested that dynamic end-*gauche* defect mode present exclusively in o-rh *n*-$C_{28}H_{58}$ alkane at room temperature.[12-13] Both molecular disorder and nuclear motion contributed to the spectral broadening in the orthorhombic spectra.

8.6 References

1. Groom, C. R.; Bruno, I. J.; Lightfoot, M. P.; Ward, S. C. The Cambridge Structural Database. *Acta Crystallographica Section B* **2016,** *72* (2), 171-179.

2. Hope, H.; Bernstein, J.; Trueblood, K. The Crystal and Molecular Structure of 1, 1, 2, 2, 9, 9, 10, 10-Octafluoro-[2, 2] Paracyclophane and a Reinvestigation of the Structure of [2, 2] Paracyclophane. *Acta Crystallographica Section B: Structural Crystallography and Crystal Chemistry* **1972,** *28* (6), 1733-1743.

3. Gantzel, P.; Trueblood, K. The Crystal and Molecular Structure of [3,3] Paracyclophane. *Acta Crystallographica* **1965,** *18* (5), 958-968.

4. Urquhart, S. G.; Martinson, M.; Eger, S.; Murcia, V.; Ade, H.; Collins, B. A. Connecting Molecular Conformation to Aggregation in P3HT Using Near Edge X-ray Absorption Fine Structure Spectroscopy. *The Journal of Physical Chemistry C* **2017,** *121* (39), 21720-21728.

5. Dudenko, D.; Kiersnowski, A.; Shu, J.; Pisula, W.; Sebastiani, D.; Spiess, H. W.; Hansen, M. R. A Strategy for Revealing the Packing in Semicrystalline Π-Conjugated Polymers: Crystal Structure of Bulk Poly-3-Hexyl-Thiophene (P3HT). *Angewandte Chemie International Edition* **2012,** *51* (44), 11068-11072.

6. Turner, W. R. Normal Alkanes. *Industrial & Engineering Chemistry Product Research and Development* **1971,** *10* (3), 238-260.

7. Plomp, M.; Van Enckevort, W.; Van Hoof, P.; Van De Streek, C. Morphology of and Dislocation Movement in *n*-$C_{40}H_{82}$ Paraffin Crystals Grown From Solution. *Journal of Crystal Growth* **2003,** *249* (3), 600-613.

8. Broadhurst, M. G. An Analysis of the Solid Phase Behavior of the Normal Paraffins. *Journal of Research of the National Bureau of Standards* **1962,** *66*, 241-249.

9. Kubota, H.; Kaneko, F.; Kawaguchi, T.; Kawasaki, M. Polytypic Transition of *n*-Hexatriacontane During Solution Crystallization. *Crystal Growth & Design* **2004,** *4* (2), 369-375.

10. Kubota, H.; Kaneko, F.; Kawaguchi, T.; Kawasaki, M. Polytypic Transformation During Crystal Growth Monitored By Newly Developed Micro-FTIR System for Three-Dimensional Structural Studies. *Journal of Crystal Growth* **2002,** *237*, 373-378.

11. Thomas, L. L.; Christakis, T. J.; Jorgensen, W. L. Conformation of Alkanes in the Gas Phase and Pure Liquids. *The Journal of Physical Chemistry B* **2006,** *110* (42), 21198-21204.

12. Basson, I.; Reynhardt, E. C. Identification of a Defect Chain Motion in *n*-Alkanes by Means of Nuclear Magnetic Resonance Spin-Lattice Relaxation Time Measurements. *The Journal of Chemical Physics* **1990,** *93* (5), 3604-3609.

13. Basson, I.; Reynhardt, E. C. Identification of Defect Chain Motions in the Low Temperature Orthorhombic Phase of Binary Mixtures of *n*-Alkanes by Means of Nuclear Magnetic Resonance Spin-Lattice Relaxation Time Measurements. *The Journal of Chemical Physics* **1991,** *95* (2), 1215-1222.

Chapter 9 Future Work

9.1 Examination of the Type of Molecular Disorder Responsible for the Spectral Broadening in o-rh *n*-Alkane Spectra

In **Chapter 7**, it was found that greater molecular disorder in the short chain o-rh *n*-$C_{28}H_{58}$ alkane broaden its carbon 1s NEXAFS spectra at room temperature. In Basson *et al*[1-2] NMR studies, a dynamic process was observed in solid *n*-alkanes below their melting point, and well below the characteristic solid-solid phase transition (rotator phases) temperatures.[1-2] For chains o-rh *n*-$C_{28}H_{58}$ and shorter, this dynamic process started below room temperature and therefore, it could be present in our room temperature measurements. In Basson *et al*[1-2] work, they concluded that this dynamic process arises from the thermally populated trans-*gauche* defect motion or an end-*gauche* near the end of the *n*-alkane chains. They mentioned that end-*gauche* defect near the end of the *n*-alkane chains will be observed for shorter chain o-rh *n*-$C_{28}H_{58}$ at temperatures above 285 K, and this defect state transition temperature is gradually increased with the *n*-alkane chain length. For o-rh *n*-$C_{32}H_{66}$, this defect state transition occurs at the temperatures above 311 K. In our present work, Raman measurements of o-rh *n*-alkanes were able to support the fact that short chain o-rh *n*-$C_{28}H_{58}$ is relatively more disordered than the other two o-rh *n*-alkanes: *n*-$C_{32}H_{66}$ and *n*-$C_{40}H_{82}$. However, our Raman measurements did not determine the specific type of disorder responsible for the spectral broadening in the short chain o-rh *n*-$C_{28}H_{58}$.

By cooling to 98 K (see **Chapter 6**), we depopulate many thermally activated modes in the molecule in addition to the end-*gauche* defects modes. Our goal is to isolate the NEXAFS spectral contribution results from the end-*gauche* defects in the molecule. In the future, this study can continue to track down the type of disorder responsible for the spectral broadening of the o-rh *n*-$C_{28}H_{58}$ NEXAFS spectra as follows. Since o-rh *n*-$C_{32}H_{66}$ alkane supposed to show the end-*gauche* defect state transition at temperatures above 311 K, one way of identifying the end-*gauche* defect motion effect to the NEXAFS spectra is to compare the o-rh *n*-$C_{32}H_{66}$ spectrum at room temperature (~ 300 K) with the spectrum obtained at 311 K temperature. In this approach, if the end–*gauche* mode is actively participating in spectral broadening, o-rh *n*-$C_{32}H_{66}$ spectrum at 311 K should give a relatively broader spectrum than at 300 K.

According to the literature[1], o-rh *n*-$C_{28}H_{58}$ should show the end-*gauche* defect state transition at 280 K which is slightly below the room temperature. Hence, the role of end-*gauche*

defect mode to the spectra can also be identified by cooling the NEXAFS spectra of o-rh *n*-$C_{28}H_{58}$ alkane below 275 K as well. In this case, if the carbon 1s NEXAFS spectra of o-rh *n*-$C_{28}H_{58}$ at 280 K is relatively narrower than its room temperature spectrum, we could safely say that end-*gauche* defect could involve in the spectral broadening of the short chain o-rh *n*-$C_{28}H_{58}$. The c-STXM could be used to obtain the NEXAFS spectra of o-rh *n*-$C_{28}H_{58}$ at 280 K.

Initial Studies

The main challenge in this approach is to have a stable and accurate temperature for each spectral measurement. This is even harder when comparing two low temperatures slightly differ from one another (the temperature difference is 11 degrees), especially at near room temperature.

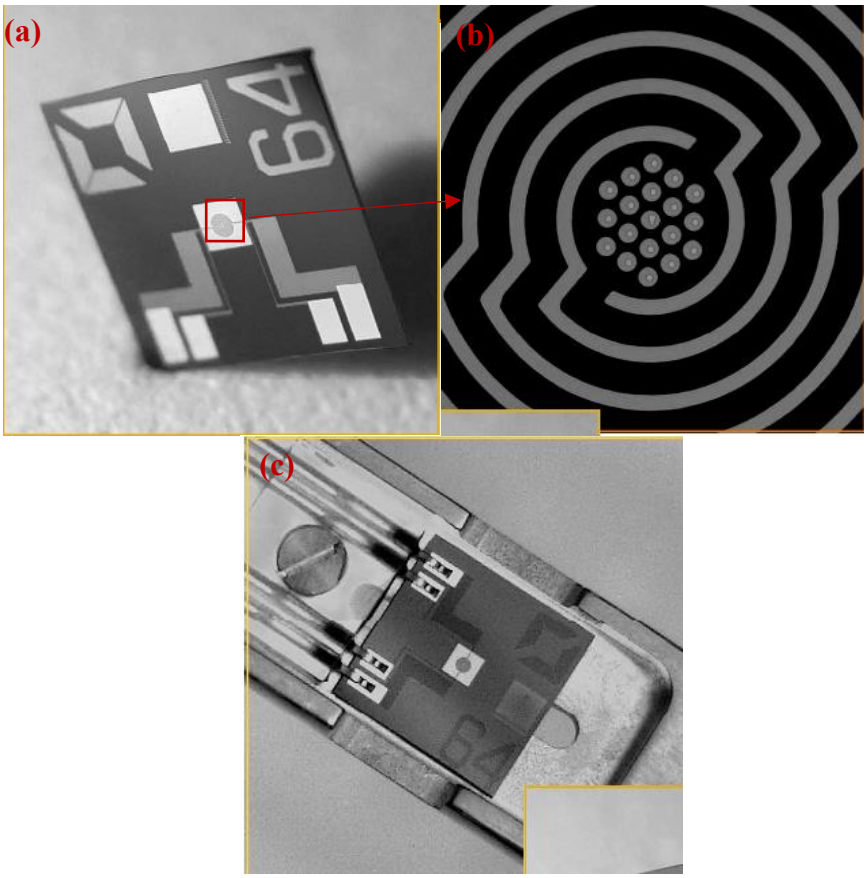

Figure 9.1: Norcada MEMS *in situ* heating device (a) fabricated Si_3N_4 chip, (b) A magnified view of the Si_3N_4 window, and (c) the software control heating device for the fabricated Si_3N_4 chip.

In order to overcome such problems, *in situ* heating cell like Norcada's Micro-Electro-Mechanical-Systems (MEMS) *in situ* device can be used for the temperature dependent NEXAFS measurements of *n*-alkanes. The device is shown in **Figure 9.1.**

This device is calibrated for the temperature range from 25 °C to 1100 °C and it provides excellent temperature uniformity in the sample area with ultra-small lateral drift and lateral displacement at each temperature measurement.[3] In addition, high temperature stability can be achieved at each temperature of the above temperature range, and temperature can be stabilized within a few seconds. Due to those features, this *in situ* heating cell could be used for the temperature dependent NEXAFS measurements of o-rh *n*-$C_{32}H_{66}$.

Although this device is ideal for our work, to have the optimum performance of the device, *n*-alkane single crystals needs to be deposited exactly at the middle of the Si_3N_4 window (small circle area in **Figure 9.1b**). This device is not useful if the crystals are deposited outside of the selected area, and those areas are too thick to penetrate X-rays for have good transmission measurements. Hence, *n*-alkane single crystals needs to be carefully deposited at the specific window area.

9.2 References

1. Basson, I.; Reynhardt, E. C. Identification of a Defect Chain Motion in *n*-Alkanes by Means of Nuclear Magnetic Resonance Spin–Lattice Relaxation Time Measurements. *The Journal of Chemical Physics* **1990,** *93* (5), 3604-3609.

2. Basson, I.; Reynhardt, E. C. Identification of Defect Chain Motions in the Low Temperature Orthorhombic Phase of Binary Mixtures of *n*-Alkanes by Means of Nuclear Magnetic Resonance Spin-Lattice Relaxation Time Measurements. *The Journal of Chemical Physics* **1991,** *95* (2), 1215-1222.

3. Norcada MEMS *in situ* Heating Device. https://www.norcada.com/products/in-situ-tem/ (accesed 08th November **2018**)

Appendix

Appendix A: Effects of π-π Interactions to the Carbon 1s NEXAFS Spectroscopy

A.1 Examination of the Purity of [n,n]PCP Molecules

Due to observed inconsistences in the NEXAFS spectra of the PCP molecules, their purity was examined. The purity and the structure of all [n,n]PCP molecules used in **Chapter 4** were confirmed using ^{1}H-NMR and ^{13}C-NMR spectroscopy. This section presents the NMR spectra of [2,2], [3,3], and [5,5]PCP molecules. All NMR spectra were obtained from the FBR1 Bruker Avance III HD 600 MHz NMR Spectrometer in the Saskatchewan Structural Science Center (SSSC) at the University of Saskatchewan. NMR spectra were integrated, calibrated with solvent peak $CDCl_3$ (7.27 δ H, 77.23 δ C) and with zero and first order phase corrections. Multiplicity is indicated by one or more of the following: s (singlet), m (multiplet), br (broad).

[2,2]PCP

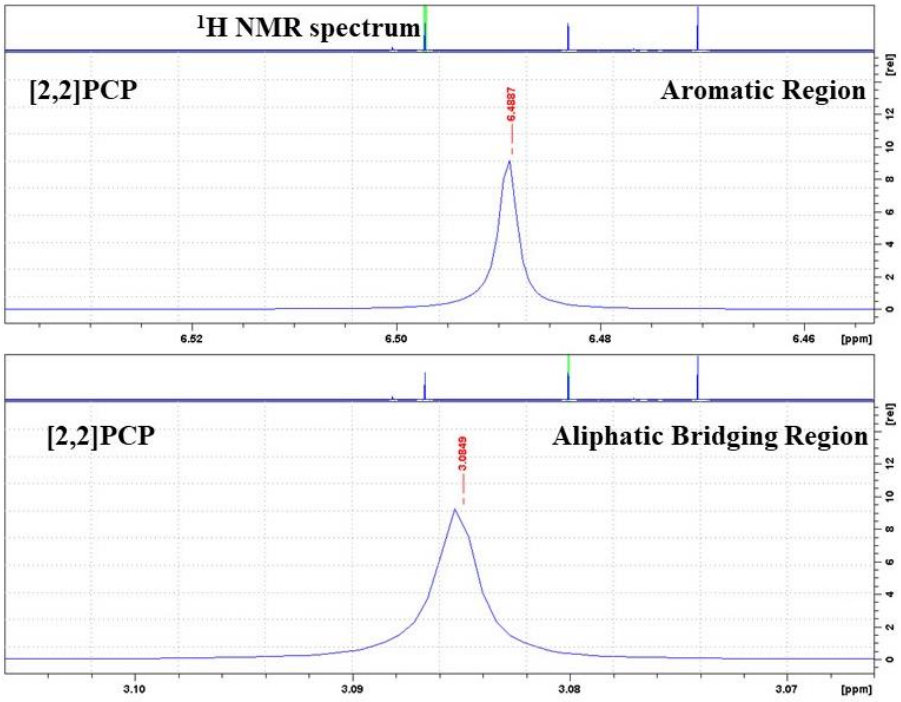

Figure A.1: Aromatic (top) and aliphatic (bottom) region in the ^{1}H-NMR spectra of [2,2]PCP.

According to the chemical structure of [2,2]PCP (**Figure 4.3**), the aliphatic region should have one chemically inequivalent hydrogen and carbon atom. In the aromatic region, it should have two chemically inequivalent carbon atoms and one chemically inequivalent hydrogen atom.

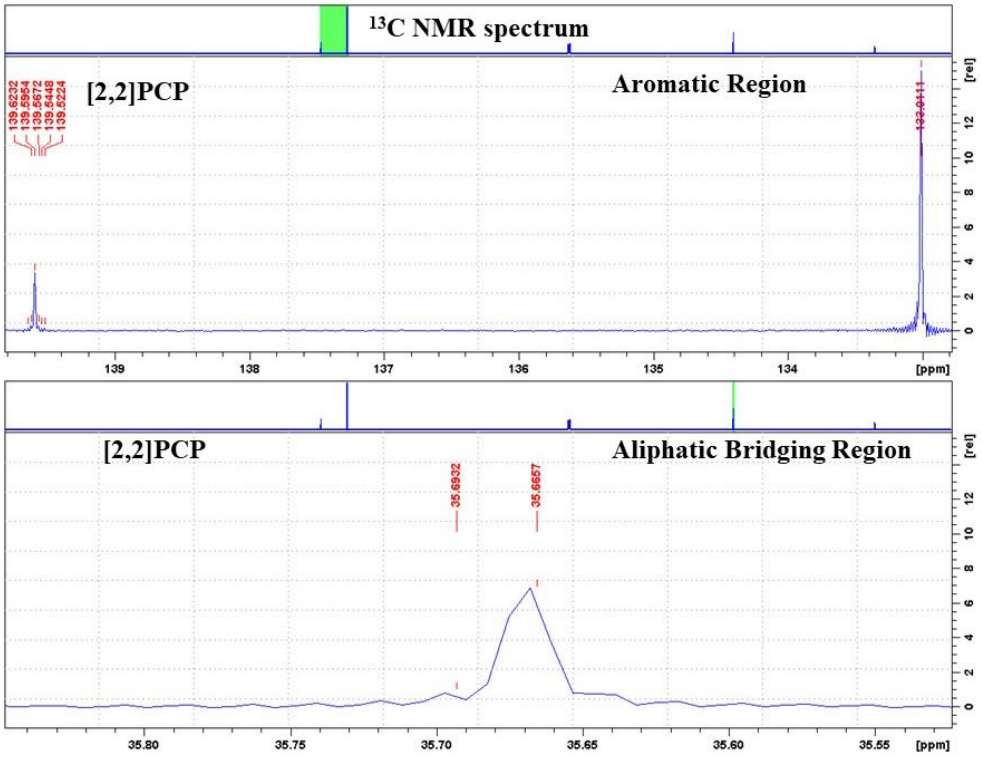

Figure A.2: Aromatic (top) and aliphatic (bottom) region in the ^{13}C-NMR spectra of [2,2] PCP molecule.

^{1}H-NMR: δ 3.08 (8H, br), 6.49 (8H, br) **^{13}C-NMR:** δ 35.67 (br), 133.01 (m), 139.52-139.62 (m).

According to the **Figure A.1**, the single peak in both aliphatic and aromatic region in the ^{1}H-NMR spectrum confirms that [2,2]PCP has one chemically inequivalent hydrogen atom in each region. Similarly, two carbon peaks in the aromatic region of the ^{13}C-NMR spectrum (**Figure A.2**) confirms that it has two chemically inequivalent carbon atoms in the benzene ring. The number of peaks and the position of [2,2]PCP ^{1}H-NMR and ^{13}C-NMR spectra in this work match with the published literature.[1] Therefore, the NMR spectra of [2,2]PCP in this work are consistent with its chemical structure.

[3,3]PCP and [5,5]PCP

According to the chemical structure of [3,3]PCP (**Figure 4.3**), this molecule should have two chemically inequivalent carbon atoms in both the aromatic and aliphatic bridging groups. In

addition, it should have one chemically inequivalent aromatic hydrogen and two chemically inequivalent aliphatic hydrogens in the structure. The ^{1}H-NMR and ^{13}C-NMR spectra of [3,3]PCP and [5,5]PCP in this work are shown in **Figures A.3 – A.6**. The NEXAFS spectrum of [5,5]PCP in this work was similar to the the NEXAFS spectrum of [3,3]PCP. Therefore, we hypothesiz that either [5,5]PCP or [3,3]PCP is not be the compound it claimed. To verify the correct PCP, each NMR region of [3,3]PCP is overplotted with [5,5]PCP.

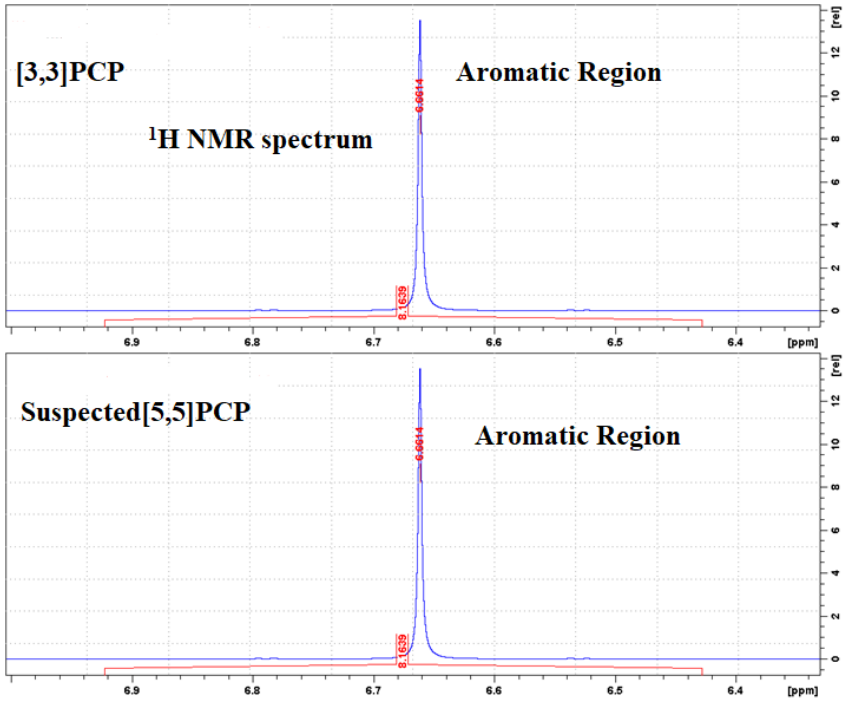

Figure A.3: Aromatic region in the ^{1}H-NMR spectra of [3,3] PCP (top) and [5,5]PCP (bottom).

^{1}H-NMR for [3,3]PCP: δ 2.69 (8H, br), 2.03-2.06 (4H, m), 6.67 (8H, s) **^{1}H-NMR for [5,5]PCP:** δ 2.74 (8H, br), 2.07-2.11 (4H, m), 6.67 (8H, s)

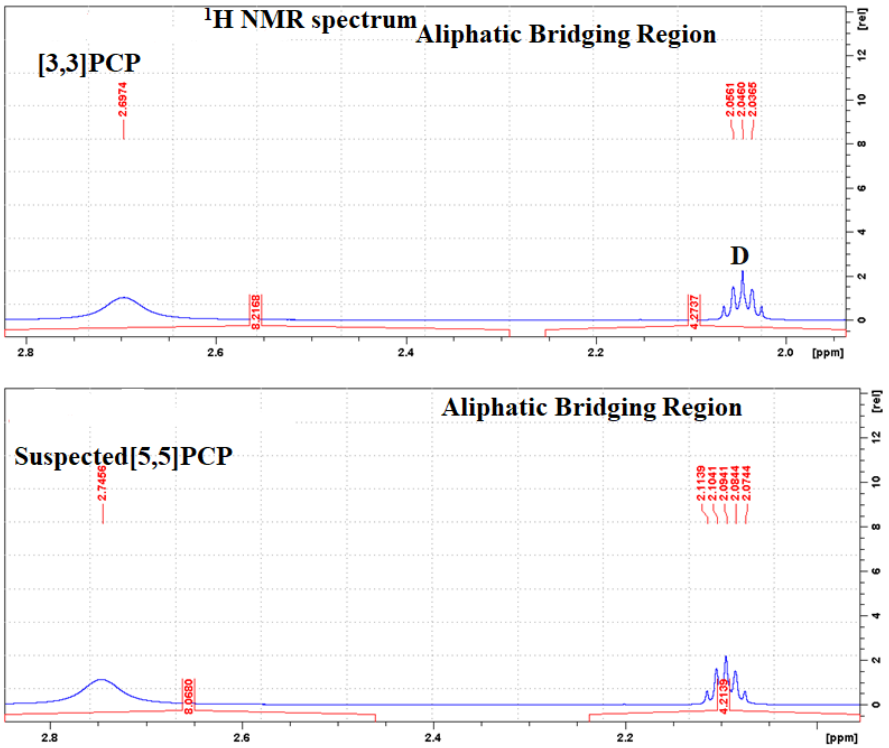

Figure A.4: Aliphatic region in the ^{1}H-NMR spectra of [3,3] PCP (top) and [5,5]PCP (bottom).

The number of peaks and peak position of [3,3]PCP in ^{1}H-NMR spectrum is matches with the published literature.[2] The ^{1}H-NMR spectrum of [5,5]PCP in this work is same to the [3,3]PCP spectrum. Even the multiplicity of each H peak in [5,5]PCP is matched with the [3,3]PCP. This suggested that [5,5]PCP is not be the compound it claimed and our [5,5]PCP is same to the [3,3]PCP. The identification of our [5,5]PCP further comfirmed from its ^{13}C-NMR spectra and it is shown in **Figures A.5 – A.6**.

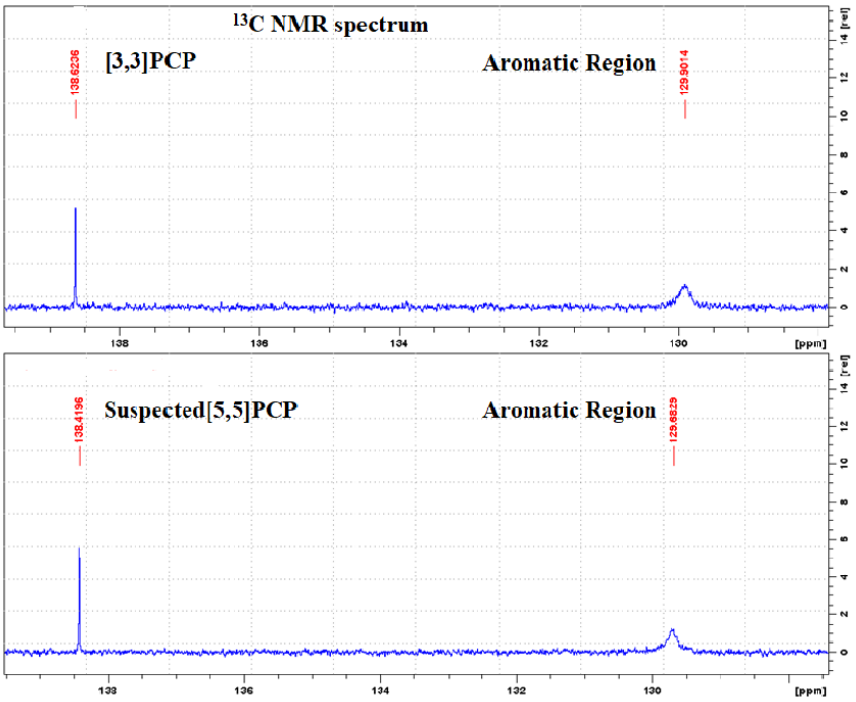

Figure A.5: Aromatic region in the ^{13}C-NMR spectra of [3,3] PCP (top) and [5,5]PCP (bottom).

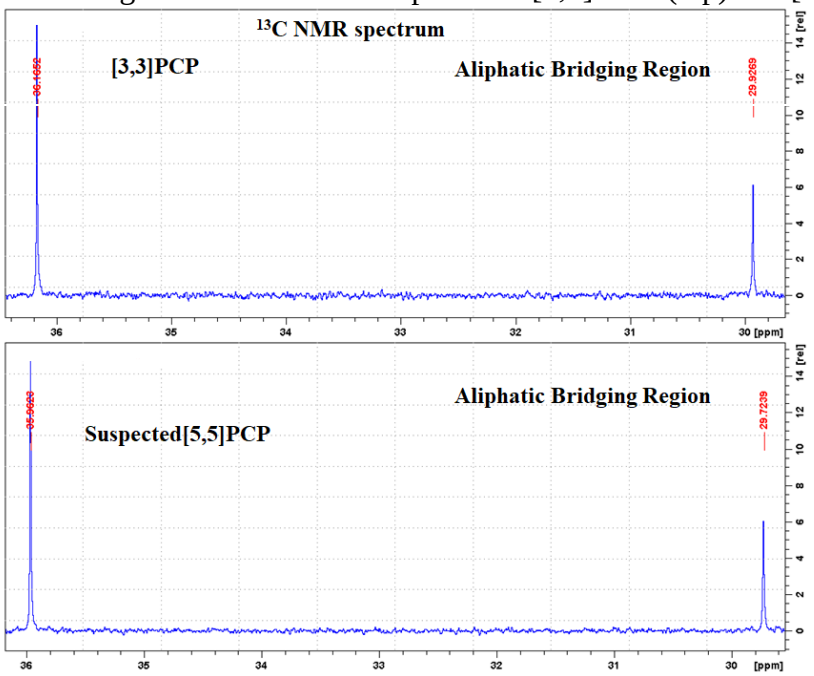

Figure A.6: Aliphatic region in the ^{13}C-NMR spectra of [3,3] PCP (top) and [5,5]PCP (bottom).

^{13}C-NMR for [3,3]PCP : δ 29.93 (s), 36.16 (s), 129.90 (s), 138.62 **^{13}C-NMR for [3,3]PCP :** δ 29.72 (s), 35.96 (s), 129.68 (s), 138.42(s)

Like ^{1}H-NMR spectra, the number of peaks and peak poistion of [5,5]PCP ^{13}C-NMR spectrum is matched with the [3,3]PCP spectrum and consistent with the chemical structure of [3,3]PCP. This confirmed that our [5,5]PCP is not be the compound it claimed to be and it was removed from our data set.

A.2 Input Files for the TP-DFT Simulations of the Carbon 1s NEXAFS Spectra of [n,n]PCP Molecules

An example input file ([3,3]PCP aromatic C-H position) used in this work for TP-DFT simulation is given below. The input file contains information on the xyz coordinates of each atom in the PCP molecule, the basis set selection for each atom, location of the core hole, definition of ECPs on all other heavy atoms, commands to plot molecular orbitals (MO), etc. The MO coefficients of the [3,3]PCP (NEXAFS simulations) molecule were obtained from a calculation using the input file given below (**Figure A.7**). In the example given below, an atom in the C-H position of the benzene ring was selected as the core excited atom for the calculation.

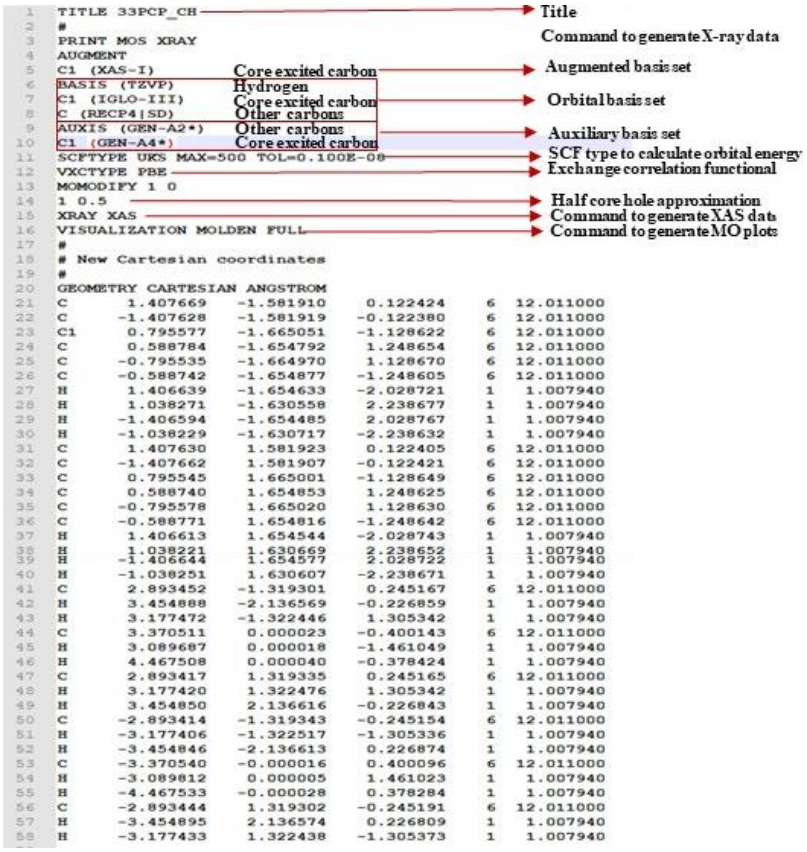

Figure A.7: Input file for the TP-DFT calculations of [3,3]PCP aromatic C-H position.

This TP-DFT calculation uses the half core hole approximation (see **Chapter 3** for theory of TP-DFT) to simulate NEXAFS spectra. This can be seen by the MOMODIFY for MO #1, which

is always the C1 atom because of the use of ECPs for all other heavy atoms. The transition energy (TE) can be calculated by using following equation.[3]

$$\Delta E_{TE} = \epsilon_f^T - \epsilon_{1s}^T \qquad \textbf{Equation A.1}$$

In **Equation A.1**, first term refers to the term value for 1s excitation to the final level (f), and the second term represent the term value for 1s ionization potential (IP).[3]

In deMon2k, this transition energy (delta) is calculated by using following equation, represented using the program variables.

DELTA = EIGVAL (IORB) - EIGVAL (IHOLE) **Equation A.2**

Where, EIGVAL (IORB) is the term value of the unoccupied MO without and electron in it, and EIGVAL (IHOLE) is the 1s IP. The "XAS MO COEFFICENTS" table in the output file (**Figure A.8**) contains the values needed for **Equation A.2**. In this output file, energy of the MO with an occupancy of 0.5 (-10.0421 a.u) is EIGVAL (IHOLE), or the 1s IP, and the energy of the first unoccupied MO with zero occupancy (0.0872 a.u) is the EIGVAL (IORM) for Lowest unoccupied Molecular Orbital (LUMO). The differences between EIGVAL (IORB) and EIGVAL (IHOLE) will give the transition energy. The sample TP-DFT calculation output file for carbon 1s $\rightarrow \pi^*_{(C\text{-}H)}$ transition of [3,3] PCP molecule is shown below.

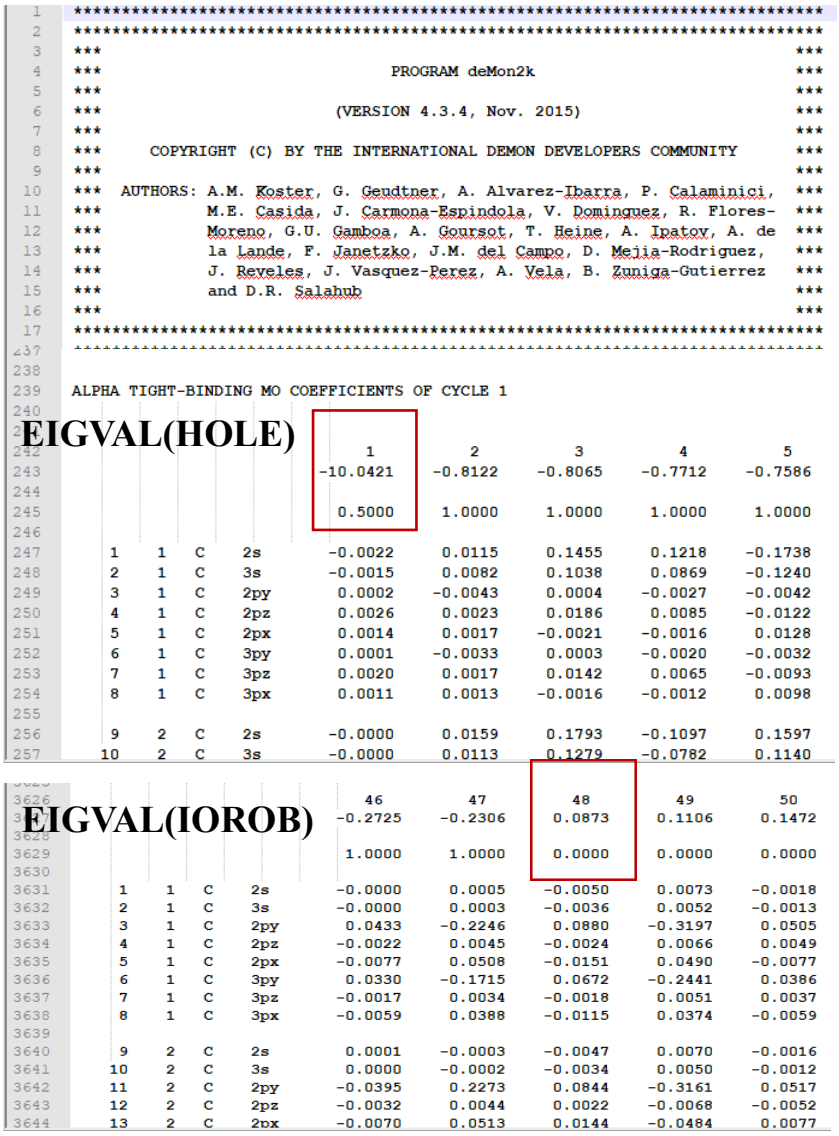

Figure A.8: Output file for the carbon 1s → π*(C-H) TP-DFT calculation of [3,3]PCP.

.

ΔK-S method

ΔK-S method used to correct the energy of the carbon 1s → LUMO transition by explicitly calculating the ($C1s^{-1}$, $LUMO^{+1}$) excited state. This research work used ΔK-S method to correct the energy of the simulated spectra obtained from TP-DFT calculation.

$$\Delta E = E(C1s^{-1};LUMO^{+1}) - E(\text{Ground state}) \qquad \textbf{Equation A.3}$$

To do this, we need to compare the ground state energy and the excited state ($C1s^{-1}$; $LUMO^{+1}$) energy. The ($C1s^{-1}$; $LUMO^{+1}$) calculation corrects for the screening of the electron in the $LUMO^{+1}$ orbital. The ΔK-S method involved three different calculations.

1. Ground state calculation: Basis set used for each atom should be same in both ground state and EHC (second step) calculations. The output file of the ground state calculation provides total ground state energy for a given molecule (**Figure A.10**).

```
TITLE 33PCP_GS                                  → Title
#
PRINT MOS XRAY                                  → Command to generate X-ray data
BASIS (TZVP)      Hydrogen
C1 (IGLO-III)     Core excited carbon
C (RECP4|SD)      Other carbons                 → Orbital basis set
AUXIS (GEN-A2*)   Other carbons                 → Auxiliary basis set
C1 (GEN-A4*)      Core excited carbon
SCFTYPE UKS MAX=500 TOL=0.100E-08               → SCF type to calculate orbital energy
VXCTYPE PBE                                     → Exchange correlation functional
VISUALIZATION MOLDEN FULL                       → Command to generate MO plots
#
# New Cartesian coordinates
#
GEOMETRY CARTESIAN ANGSTROM
C1      1.407669   -1.581910    0.122424    6  12.011000
C      -1.407628   -1.581919   -0.122380    6  12.011000
C       0.795577   -1.665051   -1.128622    6  12.011000
C       0.588784   -1.654792    1.248654    6  12.011000
C      -0.795535   -1.664970    1.128670    6  12.011000
C      -0.588742   -1.654877   -1.248605    6  12.011000
H       1.406639   -1.654633   -2.028721    1   1.007940
H       1.038271   -1.630558    2.238677    1   1.007940
H      -1.406594   -1.654485    2.028767    1   1.007940
H      -1.038229   -1.630717   -2.238632    1   1.007940
C       1.407630    1.581923    0.122405    6  12.011000
C      -1.407662    1.581907   -0.122421    6  12.011000
C       0.795545    1.665001   -1.128649    6  12.011000
C       0.588740    1.654853    1.248625    6  12.011000
C      -0.795578    1.665020    1.128630    6  12.011000
C      -0.588771    1.654816   -1.248642    6  12.011000
H       1.406613    1.654544   -2.028743    1   1.007940
H       1.038221    1.630669    2.238652    1   1.007940
H      -1.406644    1.654577    2.028722    1   1.007940
H      -1.038251    1.630607   -2.238671    1   1.007940
C       2.893452   -1.319301    0.245167    6  12.011000
H       3.454888   -2.136569   -0.226859    1   1.007940
H       3.177472   -1.322446    1.305342    1   1.007940
C       3.370511    0.000023   -0.400143    6  12.011000
H       3.089687    0.000018   -1.461049    1   1.007940
H       4.467508    0.000040   -0.378424    1   1.007940
C       2.893417    1.319335    0.245165    6  12.011000
H       3.177420    1.322476    1.305342    1   1.007940
H       3.454850    2.136616   -0.226843    1   1.007940
C      -2.893414   -1.319343   -0.245154    6  12.011000
H      -3.177406   -1.322517   -1.305336    1   1.007940
H      -3.454846   -2.136613    0.226874    1   1.007940
C      -3.370540   -0.000016    0.400096    6  12.011000
H      -3.089812    0.000005    1.461023    1   1.007940
H      -4.467533   -0.000028    0.378284    1   1.007940
C      -2.893444    1.319302   -0.245191    6  12.011000
H      -3.454895    2.136574    0.226809    1   1.007940
H      -3.177433    1.322438   -1.305373    1   1.007940
```

Figure A.9: Input file for the ground state energy calculation of [3,3]PCP.

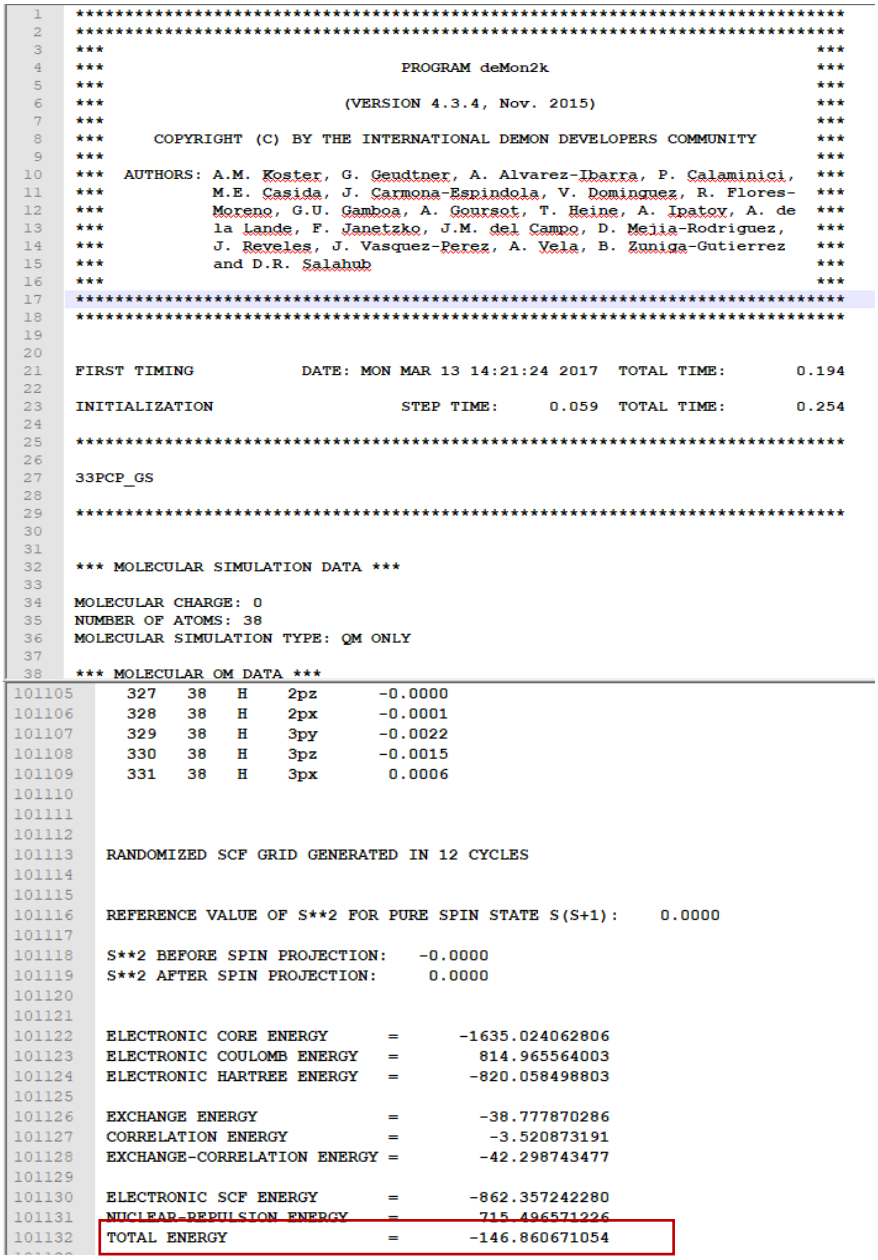

```
1  ********************************************************************************
2  ********************************************************************************
3  ***                                                                          ***
4  ***                              PROGRAM deMon2k                             ***
5  ***                                                                          ***
6  ***                         (VERSION 4.3.4, Nov. 2015)                       ***
7  ***                                                                          ***
8  ***     COPYRIGHT (C) BY THE INTERNATIONAL DEMON DEVELOPERS COMMUNITY        ***
9  ***                                                                          ***
10 ***  AUTHORS: A.M. Koster, G. Geudtner, A. Alvarez-Ibarra, P. Calaminici,    ***
11 ***           M.E. Casida, J. Carmona-Espindola, V. Dominguez, R. Flores-    ***
12 ***           Moreno, G.U. Gamboa, A. Goursot, T. Heine, A. Ipatov, A. de    ***
13 ***           la Lande, F. Janetzko, J.M. del Campo, D. Mejia-Rodriguez,     ***
14 ***           J. Reveles, J. Vasquez-Perez, A. Vela, B. Zuniga-Gutierrez     ***
15 ***           and D.R. Salahub                                               ***
16 ***                                                                          ***
17 ********************************************************************************
18 ********************************************************************************
19
20
21 FIRST TIMING           DATE: MON MAR 13 14:21:24 2017  TOTAL TIME:       0.194
22
23 INITIALIZATION                   STEP TIME:     0.059  TOTAL TIME:       0.254
24
25 ********************************************************************************
26
27 33PCP_GS
28
29 ********************************************************************************
30
31
32 *** MOLECULAR SIMULATION DATA ***
33
34 MOLECULAR CHARGE: 0
35 NUMBER OF ATOMS: 38
36 MOLECULAR SIMULATION TYPE: QM ONLY
37
38 *** MOLECULAR QM DATA ***
```

```
101105    327   38   H    2pz      -0.0000
101106    328   38   H    2px      -0.0001
101107    329   38   H    3py      -0.0022
101108    330   38   H    3pz      -0.0015
101109    331   38   H    3px       0.0006
101110
101111
101112
101113 RANDOMIZED SCF GRID GENERATED IN 12 CYCLES
101114
101115
101116 REFERENCE VALUE OF S**2 FOR PURE SPIN STATE S(S+1):    0.0000
101117
101118 S**2 BEFORE SPIN PROJECTION:   -0.0000
101119 S**2 AFTER SPIN PROJECTION:     0.0000
101120
101121
101122 ELECTRONIC CORE ENERGY      =      -1635.024062806
101123 ELECTRONIC COULOMB ENERGY   =        814.965564003
101124 ELECTRONIC HARTREE ENERGY   =       -820.058498803
101125
101126 EXCHANGE ENERGY             =        -38.777870286
101127 CORRELATION ENERGY          =         -3.520873191
101128 EXCHANGE-CORRELATION ENERGY =        -42.298743477
101129
101130 ELECTRONIC SCF ENERGY       =       -862.357242280
101131 NUCLEAR-REPULSION ENERGY    =        715.496571226
101132 TOTAL ENERGY                =       -146.860671054
```

Figure A.10: Output file for the total ground state energy calculations of [3,3]PCP molecule.

2. EHC calculation ($C1s^{-1}$; $LUMO^{+1}$): An extra electron will be added to the molecule to make the charge of the molecule -1 (see **Figure A.11**). In addition, molecular orbital modification (MOMODIFY) term in EHC calculation input file puts a full-core hole (0.0) on the lowest energy MO. This creates the configuration ($C1s^{-1}$; π^*). Therefore, unlike TP-DFT NEXAFS calculation, a full-core electron will be removed from the core level (see **Figure A.11**).

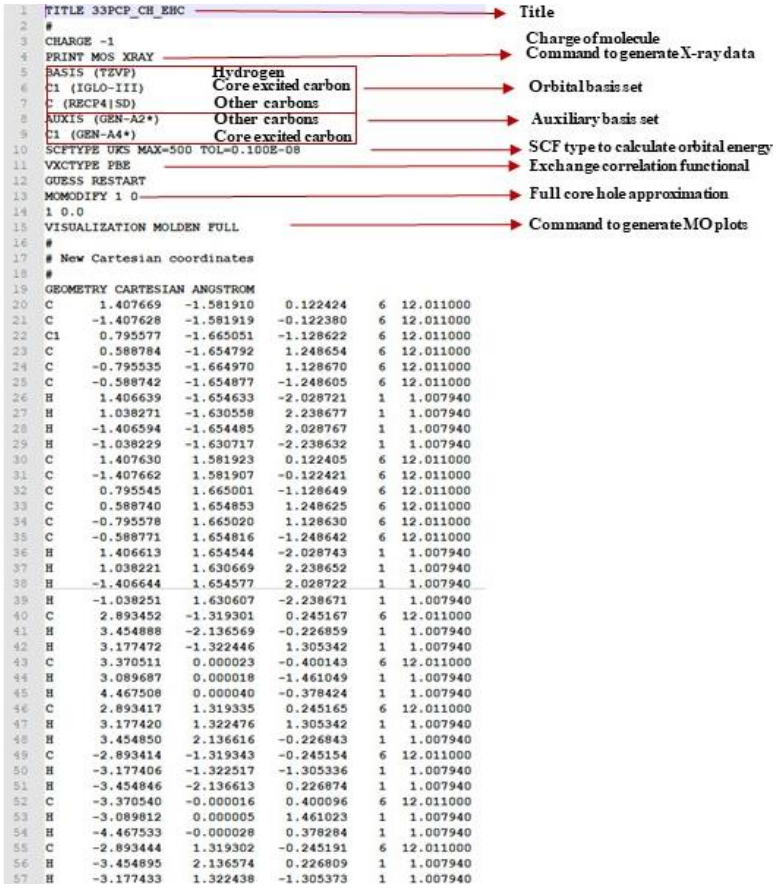

Figure A.11: Input file for the EHC calculation of [3,3]PCP aromatic C-H position.

From the first two calculations (total energy output from each calculation), the energy of the carbon 1s → LUMO transition can be obtained by using the **Equation A.3**. An example calculation is shown below. The resulted energy from the ΔK-S method can be then used to calibrate the energy of the first transition in TP-DFT XAS calculation.

```
 3  ***                                                                          ***
 4  ***                          PROGRAM deMon2k                                 ***
 5  ***                                                                          ***
 6  ***                      (VERSION 4.3.4, Nov. 2015)                          ***
 7  ***                                                                          ***
 8  ***     COPYRIGHT (C) BY THE INTERNATIONAL DEMON DEVELOPERS COMMUNITY        ***
 9  ***                                                                          ***
10  ***  AUTHORS: A.M. Koster, G. Geudtner, A. Alvarez-Ibarra, P. Calaminici,    ***
11  ***           M.E. Casida, J. Carmona-Espindola, V. Dominguez, R. Flores-    ***
12  ***           Moreno, G.U. Gamboa, A. Goursot, T. Heine, A. Ipatov, A. de    ***
13  ***           la Lande, F. Janetzko, J.M. del Campo, D. Mejia-Rodriguez,     ***
14  ***           J. Reveles, J. Vasquez-Perez, A. Vela, B. Zuniga-Gutierrez     ***
15  ***           and D.R. Salahub                                               ***
16  ***                                                                          ***
17  ******************************************************************************
18  ******************************************************************************
19
20
21  FIRST TIMING           DATE: TUE MAR 21 13:15:12 2017  TOTAL TIME:       0.908
22
23  INITIALIZATION                  STEP TIME:     0.047  TOTAL TIME:       0.955
24
25  ******************************************************************************
26
27  33PCP_CH_EHC
28
29  ******************************************************************************
101142    327   38   H    2pz       0.0002
101143    328   38   H    2px       0.0000
101144    329   38   H    3py       0.0053
101145    330   38   H    3pz       0.0044
101146    331   38   H    3px       0.0018
101147
101148
101149
101150  RANDOMIZED SCF GRID GENERATED IN 13 CYCLES
101151
101152
101153  REFERENCE VALUE OF S**2 FOR PURE SPIN STATE S(S+1):    0.7500
101154
101155  S**2 BEFORE SPIN PROJECTION:    1.7722
101156  S**2 AFTER SPIN PROJECTION:     0.8254
101157
101158
101159  ELECTRONIC CORE ENERGY      =      -1619.348976942
101160  ELECTRONIC COULOMB ENERGY   =        810.084497984
101161  ELECTRONIC HARTREE ENERGY   =       -809.264478959
101162
101163  EXCHANGE ENERGY             =        -37.807701322
101164  CORRELATION ENERGY          =         -3.523670954
101165  EXCHANGE-CORRELATION ENERGY =        -41.331372277
101166
101167  ELECTRONIC SCF ENERGY       =       -850.595851235
101168  NUCLEAR-REPULSION ENERGY    =        714.176980829
101169  TOTAL ENERGY                =       -136.418870407
101170
```

Figure A.12: Output file for total EHC calculations for the carbon 1s → $\pi^*_{(C\text{-}H)}$ transition of [3,3]PCP molecule.

By using the total energy differences between the ground state (-146.860671054 a.u) and the ($C1s^{-1}$, $LUMO^{+1}$) excited state (-136.418870407 a.u), the energy of the carbon 1s → LUMO transition for C-H position in [3,3]PCP can be calculated as 10.441 a.u or 284.132 eV. This value obtained from the ΔK-S method is closer to the experimental value (285.0 eV) of the carbon 1s → π*(C-H) transition of [3,3]PCP (see **Chapter 4**).

3. Ionization Potential (IP) calculation: Like EHC calculation, MOMODIFY term puts a full-core hole (0.0) on the lowest energy MO, but no charge is included to the molecule to create configuration ((C1s^{-1}; π*). The IP can be obtained from the **Equation A.4** by using the total energy output in each first and third calculation.

IP = E (Ionized State) - E(Ground State) **Equation A.4**

The resulting energy can be used to determine the energy of the IP in TP-DFT XAS calculation.

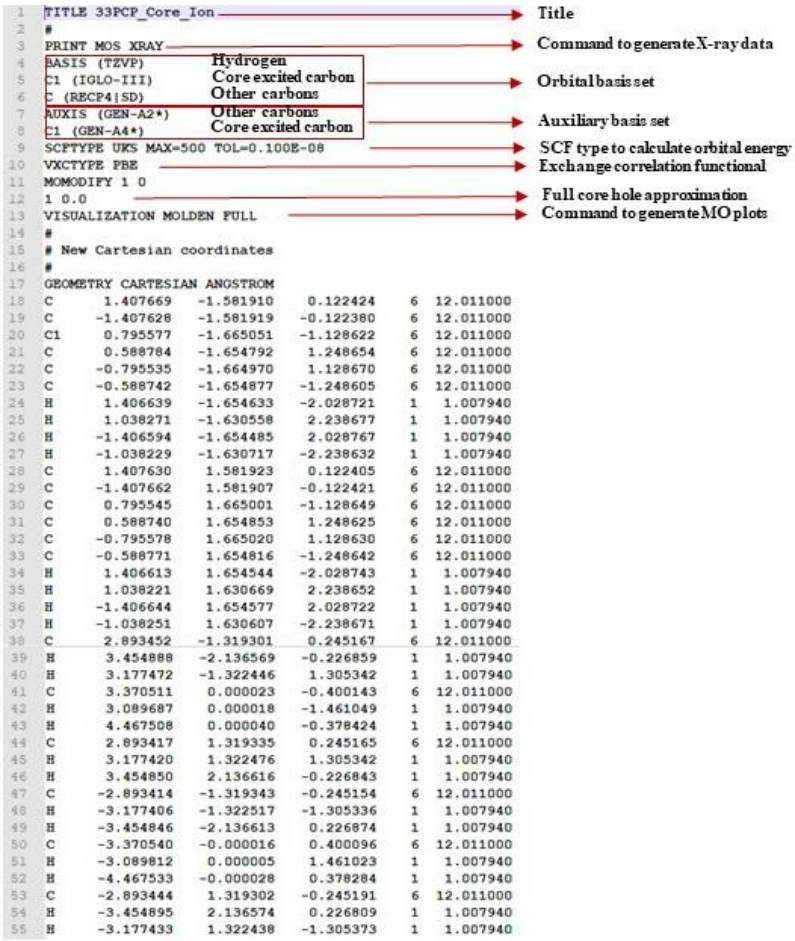

Figure A.13: Input file for IP calculations of [3,3]PCP aromatic C-H position.

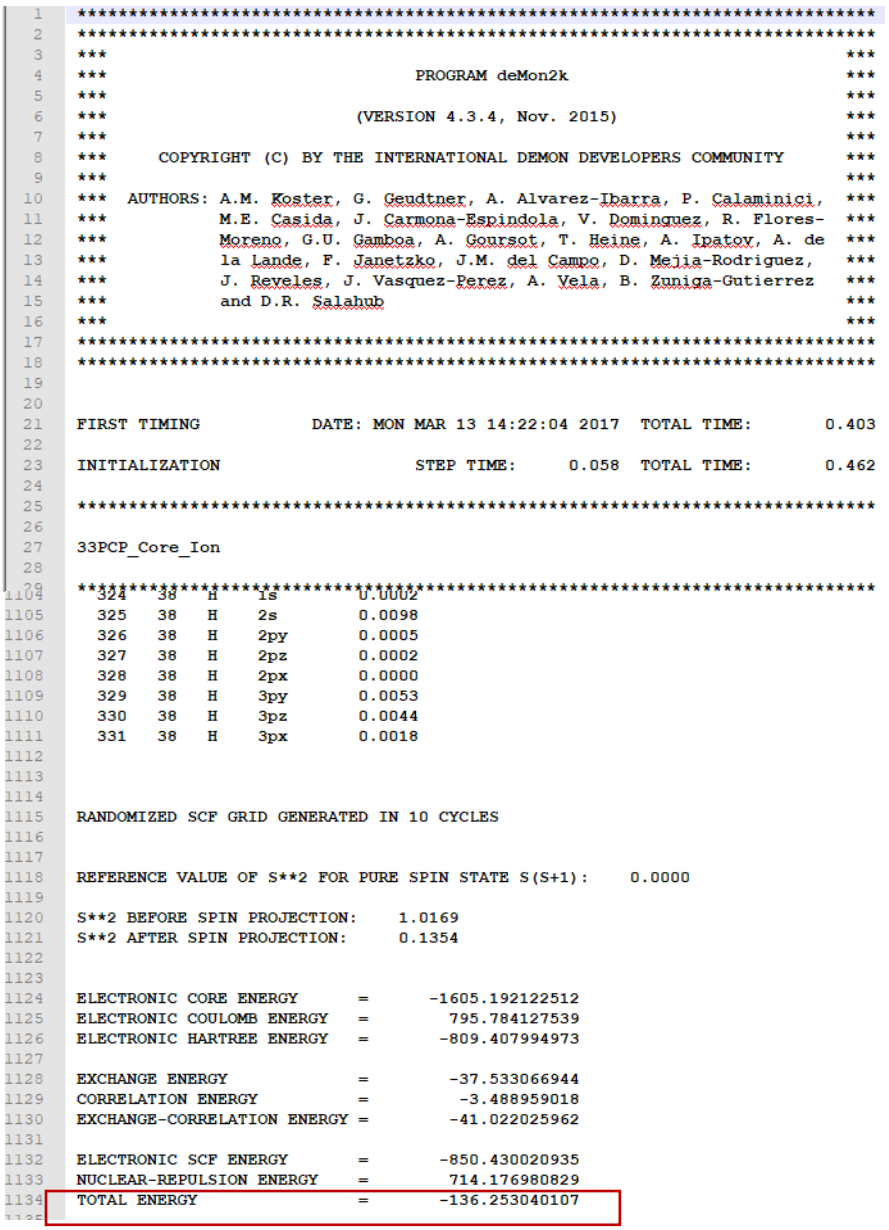

```
********************************************************************************
********************************************************************************
***                                                                          ***
***                              PROGRAM deMon2k                             ***
***                                                                          ***
***                         (VERSION 4.3.4, Nov. 2015)                       ***
***                                                                          ***
***     COPYRIGHT (C) BY THE INTERNATIONAL DEMON DEVELOPERS COMMUNITY        ***
***                                                                          ***
***  AUTHORS: A.M. Koster, G. Geudtner, A. Alvarez-Ibarra, P. Calaminici,    ***
***           M.E. Casida, J. Carmona-Espindola, V. Dominguez, R. Flores-    ***
***           Moreno, G.U. Gamboa, A. Goursot, T. Heine, A. Ipatov, A. de    ***
***           la Lande, F. Janetzko, J.M. del Campo, D. Mejia-Rodriguez,     ***
***           J. Reveles, J. Vasquez-Perez, A. Vela, B. Zuniga-Gutierrez     ***
***           and D.R. Salahub                                               ***
***                                                                          ***
********************************************************************************
********************************************************************************


FIRST TIMING           DATE: MON MAR 13 14:22:04 2017  TOTAL TIME:       0.403

INITIALIZATION                    STEP TIME:     0.058  TOTAL TIME:       0.462

********************************************************************************

33PCP_Core_Ion

********************************************************************************
  324   38    H     1s         0.0002
  325   38    H     2s         0.0098
  326   38    H     2py        0.0005
  327   38    H     2pz        0.0002
  328   38    H     2px        0.0000
  329   38    H     3py        0.0053
  330   38    H     3pz        0.0044
  331   38    H     3px        0.0018



RANDOMIZED SCF GRID GENERATED IN 10 CYCLES


REFERENCE VALUE OF S**2 FOR PURE SPIN STATE S(S+1):    0.0000

S**2 BEFORE SPIN PROJECTION:    1.0169
S**2 AFTER SPIN PROJECTION:     0.1354


ELECTRONIC CORE ENERGY      =      -1605.192122512
ELECTRONIC COULOMB ENERGY   =        795.784127539
ELECTRONIC HARTREE ENERGY   =       -809.407994973

EXCHANGE ENERGY             =        -37.533066944
CORRELATION ENERGY          =         -3.488959018
EXCHANGE-CORRELATION ENERGY =        -41.022025962

ELECTRONIC SCF ENERGY       =       -850.430020935
NUCLEAR-REPULSION ENERGY    =        714.176980829
TOTAL ENERGY                =       -136.253040107
```

Figure A.14: Output file for total ionized state energy calculations for the carbon 1s → $\pi^*_{(C\text{-}H)}$ transition of [3,3]PCP molecule.

By using the total energy differences between the ground state (-146.860671054 a.u) and the ionized state (-136.253040107 a.u), the energy of the carbon 1s → LUMO transition for C-H position in [3,3]PCP can be calculated as 10.608 a.u or 288.64 eV.

Appendix B: Effects of Rydberg Quenching on the Degree of Rydberg-Valence Mixing to the Carbon 1s NEXAFS Spectra of *n*-Alkanes

B.1 Attempts to Obtain Stable Carbon 1s NEXAFS Spectra of Short Chain *n*-Alkanes (*n*-$C_{23}H_{48}$ and *n*-$C_{24}H_{50}$)

The **Appendix B** presents work done as part of the approaches discussed in **Chapter 5**, but did not succeed to meet the intended research objectives. §**B.1** describes an attempts made to obtain stable carbon 1s NEXAFS spectra of short chain *n*-alkanes (*n*-$C_{23}H_{48}$ and *n*-$C_{24}H_{50}$) in our system. The initial *n*-alkane sample system had *n*-tricosane (*n*-$C_{23}H_{48}$) and *n*-tetracosane (*n*-$C_{24}H_{50}$) molecules, in addition to the *n*-octacosane (*n*-$C_{28}H_{58}$), *n*-dotriconatne (*n*-$C_{32}H_{66}$) and *n*-tetracontane (*n*-$C_{40}H_{82}$). This sample selection based on the chain length and the crystal structure of *n*-alkanes. According to the literature, *n*-alkanes (*n*-C_nH_{2n+2}) can exhibited three different solid state structures at room temperature: triclinic, 12≤ n (even) ≥26; monoclinic 28≤ *n* (even) ≥36; orthorhombic (*n* even) ≥36 and (*n* odd).[4]

Therefore, the initial sample selection not only expands the chain length variation, it also cover the whole crystal structure variation (orthorhombic, monoclinic and triclinic) possible for *n*-alkanes at room temperature. However, at room temperature, *n*-alkane chains can exhibit more than one crystal structures. This can occur because of contamination with the neighboring *n*-alkanes molecules such as slightly shorter chain lengths of alkanes.[4-5] Although each *n*-alkane shows multiple crystalline polymorphs at room temperature, the structure of *n*-alkane single crystals can be identified by measuring the interior angle of the crystals.[5] Therefore, based on the acute interior angle of the crystal, possible crystalline polymorphs of each *n*-alkane were found. However, unlike long chain *n*-alkanes (*n*-$C_{28}H_{58}$, *n*-$C_{32}H_{66}$, *n*-$C_{40}H_{82}$), crystals formed from the short chain *n*-alkanes are not stable at room temperature. The crystal shape of short chain *n*-alkane crystals undergo rapid distortion by losing the sharpness of their facet edges with the time (within 20 minutes).

The morphology variation in the *n*-$C_{23}H_{48}$ single crystals with the time at room temperature is shown in **Figure B.1**. According to **Figure B.1**, shapes of the *n*-$C_{23}H_{48}$ single crystals are distorted rapidly after the crystals formed on the silicon substrate. Same observation observed for *n*-$C_{24}H_{50}$ alkane. Both samples were stored inside the refrigerator in order to protect the crystal shape between preparation and measurement. Rapid shape distortion was not observed for longer

n-alkane (*n*-$C_{28}H_{58}$, *n*-$C_{32}H_{66}$, *n*-$C_{40}H_{82}$) crystals, they showed crystal stability at room temperature.

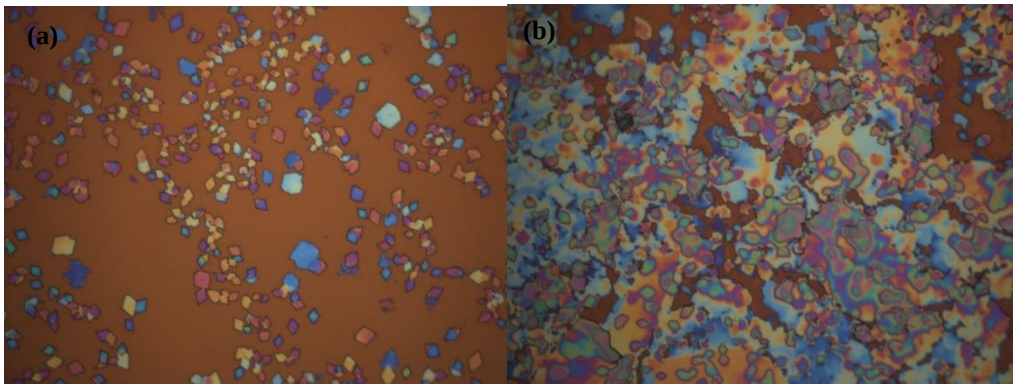

Figure B.1: The optical microscopy (OM) images of *n*-$C_{23}H_{48}$ at room temperature (a) crystal morphology soon after crystal deposited on the Si substrate and (b) crystal morphology after 20 minutes. The objective of the OM image is 50X with 4×4 binning.

This crystal distortion could be due to two reasons.

1. The higher vapour pressure of the shorter chain *n*-alkanes with respect to the longer chains.
2. Lower melting points of the shorter chains *n*-$C_{23}H_{48}$ and *n*-$C_{24}H_{50}$ relative to the other longer alkanes (*n*-$C_{28}H_{58}$, *n*-$C_{32}H_{66}$, *n*-$C_{40}H_{82}$) in the system.

For instance, vapor pressure and melting point of the *n*-$C_{24}H_{50}$ is ~ 50 °C and 4×10^{-6} mm Hg at 25 °C whereas melting point and vapour pressure of the *n*-$C_{28}H_{58}$ is ~ 62 °C and 1.6×10^{-9} mm Hg at 25 °C. The crystal shape is important to identify the crystal structure of *n*-alkanes, because without well-defined facet crystal edges, acute interior angle calculations are not trustworthy for crystal structure determination. Therefore, attempts were made to protect the shape of the short chain *n*-alkane crystals.

B.1.1 *In Situ* Rotatable Cooling Cell for Short Chain *n*-Alkanes

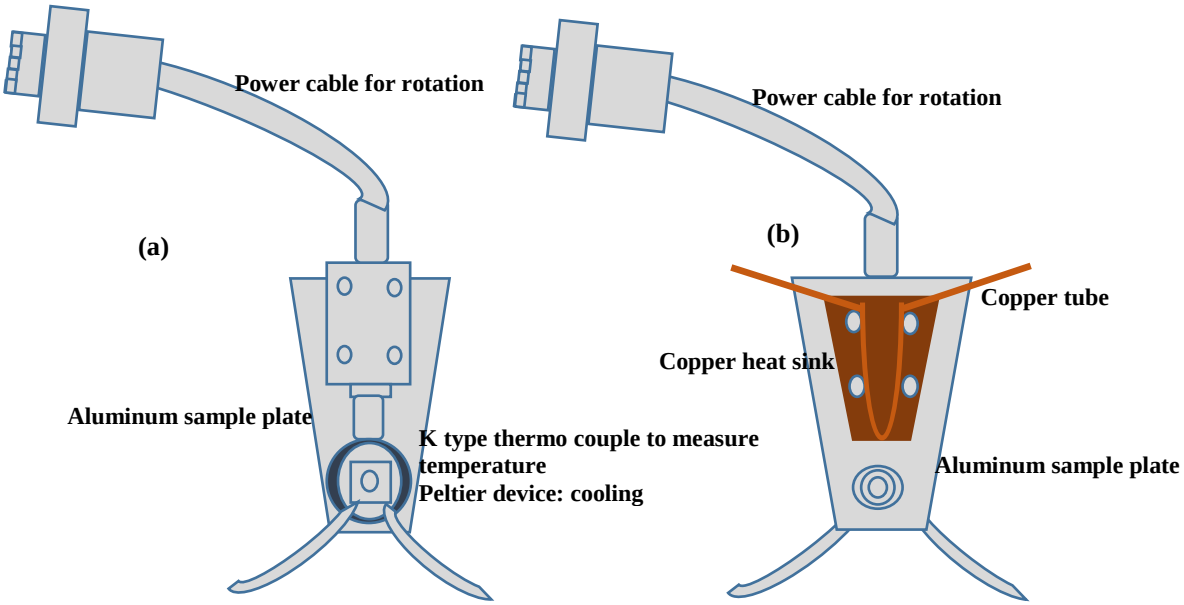

Figure B.2: Schematic diagram for the *in situ* rotatable cooling sample plate: a) top view, b) bottom view.

The goal of this *in situ* cooling cell is to decrease the vapour pressure of the short chain *n*-alkanes by cooling the sample substrate below the room temperature. By cooling the sample substrate, the sublimation process of the crystal is slow down and it should retain the crystal shape on the substrate while during the data acquisition.

This rotatable cooling cell is used to acquire angle dependent NEXAFS spectra of *n*-alkanes along the principle axes (X and Y) of the crystal. The reason behind using rotatable cooling cell for this purpose is explained below.

Although SM beamline's elliptically polarized undulator (EPU)[6] can produce arbitrarily inclined linear polarization to acquire angle dependent NEXAFS spectra of *n*-alkanes along the principle axes (X and Y) of the crystal, a small variations in the degree of linear polarization have been observed in the proximity of the carbon dip for horizontal and vertically polarized radiation. Therefore, to control for this variable, a fixed horizontal polarization was used so that the degree of polarization would be constant for all measurements. This was achieved by rotating the sample azimuthally around the photon propagation direction. From this way, fixed electric field vector is maintained throughout the angle dependent measurements and degree of linearity would be constant for all the measurements. Therefore, rotatable cooling cell was used for this purpose.

Figure B.2 shows the schematic diagram for the *in situ* rotatable cooling cell and **Figure B.3** shows the final setup of the cell device installed inside the STXM. According to **Figure B.2**, front side (top view) of the aluminum sample plate is equipped with Peltier device (1MD06-032-05111; Tec microsystems),[7] K type thermocouple (Fluke 52 II: accuracy 0.05% + 0.3°C),[8] and GPS 1850 digital power supply (0 - 18 V and 0 - 5A).[9] In this setup, sample is cooled by the Peltier, and the K type thermocouple (Fluke 52 II: accuracy 0.05% + 0.3 °C) attached to the aluminum sample plate is used to measure the temperature of the sample.[8] The temperature in the aluminum sample plate is controlled by the voltage provided by the power supply attached to the sample plate. When voltage is applied to the aluminium sample plate, one side of the Peltier device gets cold and other side gets hot. However, with the continuous supply of voltage, heating happened much faster than the cooling. The purpose of this *in situ* cell is to cool down the sample while taking the NEXAFS measurements. Therefore, in order to make the cold side cold during the data acquisition, back side of the aluminum sample plate is equipped with the copper heat sink, and it will take the heat away from the Peltier. However, the copper by itself is not enough to take all the heat generated from the hot side of the Peltier, therefore, device's water circulation used as an additional heat sink (see copper tubes in **Figure B.2**).

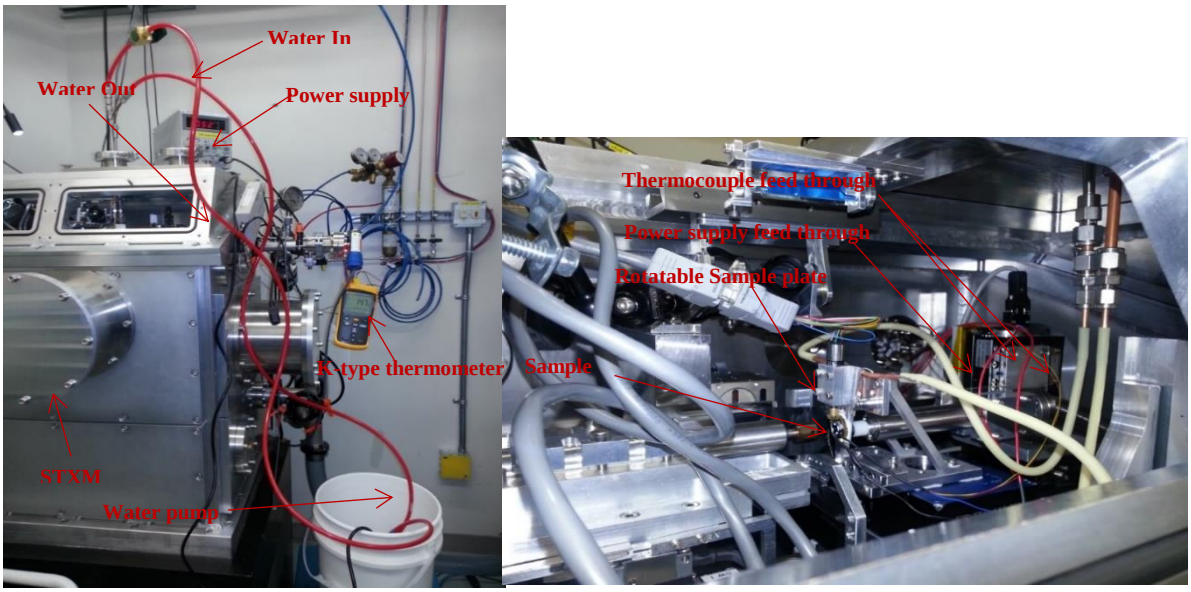

Figure B.3: Final setup of the *in situ* rotatable cooling cell installed inside the STXM.

The device's performance at different working environments are tabulated in **Table B.1**. According to the **Table B.1**, the lowest temperature achieved by the device is -1 ± 2 °C (in this case, ±°C represent the temperature fluctuation). However, cooling performance of the cooling

cell is strictly depends on the temperature of the water. Therefore, by adding more ice to the water circulation system will drop down the device temperature, and makes the device temperature more stable inside the STXM chamber.

Although this device was able to drop down the temperature below 0 °C, crystal shape was unable to be protected during the data acquisition.

Table B.1: Cooling cell performance at different working conditions.

Condition	**Voltage (Volts)**	**Temperature (°C)**
Device outside of the STXM without water circulation	0.00	22.0 ±2
	0.50	13.0 ±5
	1.00	10.0 ±5
Device outside of the STXM with water circulation	0.00	22.0 ±2
	0.50	13.0 ±5
	1.00	10.0 ±5
Device inside of the STXM without water circulation (under normal atmosphere)	0.00	24.0 ±2
	0.50	17.0 ±5
	1.00	15.0 ±5
Device inside of the STXM with water circulation (under normal atmosphere)	0.00	22.0 ±2
	0.50	12.0 ±5
	1.00	10.0 ±5
Device inside of the STXM with water circulation (under helium with more ice)	0.00	**20.0 ±2**
	0.50	**14.0 ±2**
	1.00	**5 ±2. But went down to -1 ±2 with more ice**

Conclusion

Despite the attempts, it was still not possible to protect the crystal shape of the *n*-$C_{23}H_{48}$ and *n*-$C_{24}H_{50}$ single crystals. The crystal shape was distorted during the data acquisition.

B.2 Experimental Challenges in Single Crystal *n*-Alkane NEXAFS Spectroscopy

B.2.1 Purity of the X-ray Polarization to Single Crystal *n*-Alkane Spectroscopy

The room temperature measurements of the carbon 1s NEXAFS spectra of *n*-alkanes shown in **Chapter 5** were initially recorded with the circular polarization. The spectra obtained from the circularly polarized radiation should not be sensitive to the in-plane (x,y) orientation of the crystal because electric field vector of the circularly polarized light should evenly probe the in-plane orientation of the crystal. However, *n*-alkane spectra obtained with the left circularly polarized light showed a slight angle dependence, i.e. a small linear dichroism effect was observed in the NEXAFS spectroscopy.

We hypothesized that the circular polarization is distorted into an elliptical polarization since it shows some linear dichroism effect to the NEXAFS spectra. To confirm that hypothesis, experiment was design in order to examine the purity of the circularly polarized light at the carbon energy range (280-300 eV). In this experiment, *n*-alkane single crystal was azimuthally rotated and compared the NEXAFS measurements with the in-plane orientation of the *same* crystal. This is shown in **Figure B.4**.

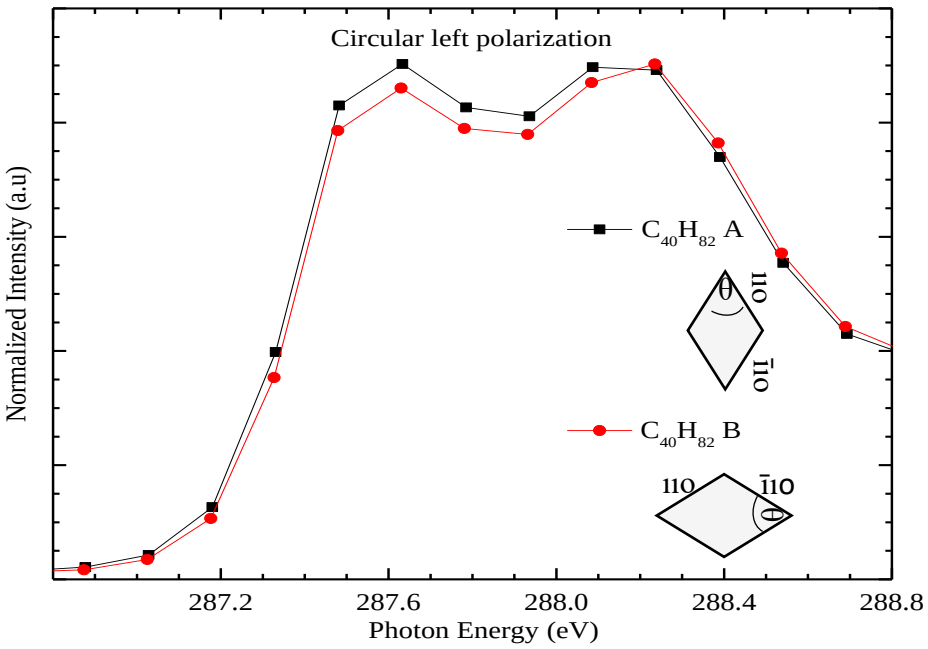

Figure B.4: Carbon 1s NEXAFS spectra of *n*-tetracontane (*n*-$C_{40}H_{82}$) recorded with left circularly polarized radiation for different orientations A and B of the same single crystal.

According to **Figure B.4**, shape of the C-H band changed with the in-plane orientation of the crystal. That is, the relative intensity of the two C-H peaks changed with the orientation of the same crystal with circularly polarized light. In one spectrum (crystal *n*-$C_{40}H_{82}$ A), intensity of the first C-H peak is higher than the second C-H peak and intensity relationship become reversed with the other spectrum (crystal *n*-$C_{40}H_{82}$ B).

Since the same crystal was examined for both measurements, this spectral change should not be due to the quality involve of the crystal, and but likely due to the purity of the circular polarization in the carbon energy range (287-300 eV). In SM measurements, X-ray beam produced by the EPU is directed and focused to the plane grating monchromator and STXM via stationary mirrors in the STXM setup (see **Figure 2.10** for STXM setup). Therefore, it has a higher probability of showing a linear polarization contamination in the carbon energy range (280-330 eV) due to the carbon deposition on the STXM optics. This explanation conclude that circular polarization is distorted into an elliptical polarization in the carbon energy range (280-320 eV). Since circular polarization can not be used to avoid the linear dichroism effects, orientation effects to the carbon 1s NEXAFS spectra of *n*-alkanes in **Chapter 5** and **7** were explicitly studied by angle dependent NEXAFS spectroscopy.

B.2.2 Effect of Crystal Thickness to the Single Crystal *n*-Alkane Spectroscopy

In a transmission measurement, thickness of the sample is important in order to have a decent transmitted signal for OD measurement (see **Equation 2.5**). The effect of crystal thickness to the *n*-alkane single crystal spectra is shown in **Figure B.5**.

Figure B.5 shows the variation in the carbon 1s NEXAFS spectra of *n*-$C_{28}H_{58}$ with different crystal thicknesses. According to this data, C-H peaks (287-288 eV) of the NEXAFS spectra are broader for thicker crystals, specifically for crystals that have a thickness greater than 1.8 OD. **Figure B.5** shows that thick crystals attenuate the strongest or more intense feature in the spectra. However, this effect is minimal with the crystals thickness lower than the 1.8 OD. The thickness effect can be explained as below.

When crystal is too thick, most of the light transmitted is from higher order photons (such as 2^{nd}, 3^{rd} order photons etc.). Although the fraction of higher order photons is relatively small, that fraction becomes significant to the transmitted signal (I) because first order photons are almost absorbed by the thicker crystal. Therefore, the majority of the remaining transmission spectrum is

contributed by the higher order photons and that makes the transmission spectrum (I) is somewhat larger than it should be for thicker crystals. As a result, OD (OD = -ln(I /I_0)) signal is decreased and causes the attenuation of the strongest features in the OD spectra. The NEXAFS spectra shown in **Chapter 5, 6** and **7** were carefully address the effect of crystal thickness to the NEXAFS spectra and use the crystals with thickness lower than 1.8 OD.

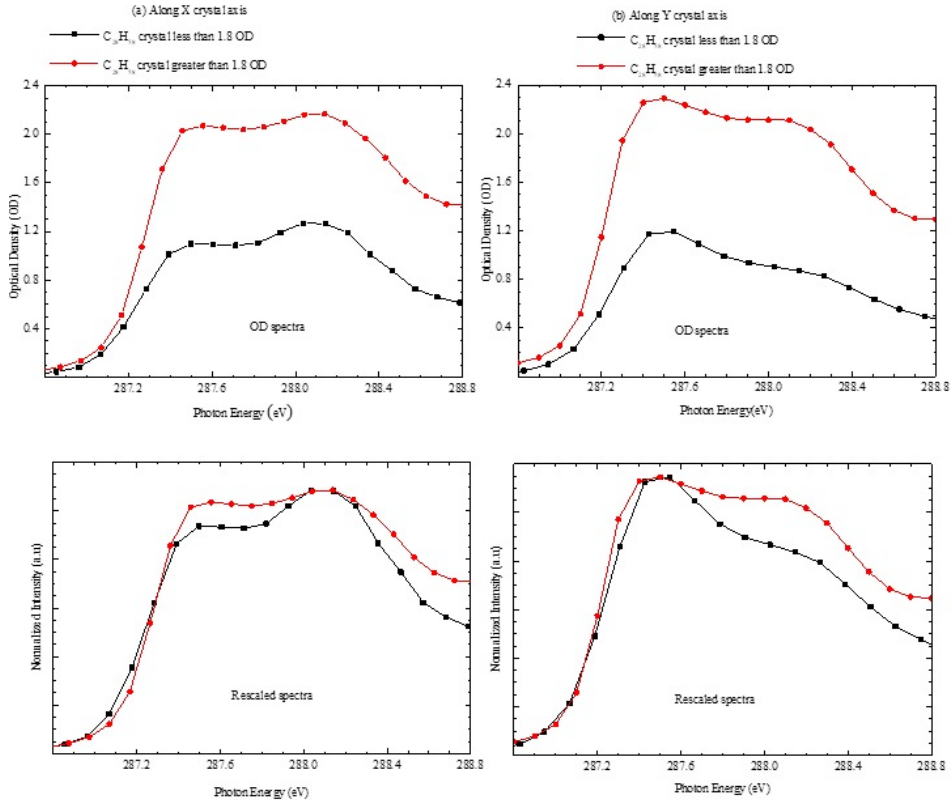

Figure B.5: Effect of crystal (*n*-$C_{28}H_{58}$) thickness to the carbon 1s NEXAFS spectra (a) along the long (X) crystal axis and (b) along the short (Y) crystal axis under linear horizontal polarization.

B.2.3 Effect of Misalignment of the Crystal to the Single Crystal *n*-Alkane Spectroscopy

In addition to the crystal thickness, misalignment of the crystal along its principal crystal axes (x,y) effect to the shape of the NEXAFS spectra. The relative intensity in the CH band of the single crystal *n*-alkane spectra is sensitive to the alignment of the crystal orientation with the electric field vector of the X-ray polarization. This effect is shown in **Figure B.6**.

According to the **Figure B.6**, common relative intensity of the two C-H peaks in a given crystal axes X and Y is slightly change with the crystal misalignment. Crystal misalignment alter the direction of the dipole moment. Since intensity of a given dipole allowed NEXAFS feature

depends on the angle between the electric field vector of the X-ray radiation and the dipole moment of the particular molecular transition, changing the angle by the crystal slightly will change the intensity of the NEXAFS feature.

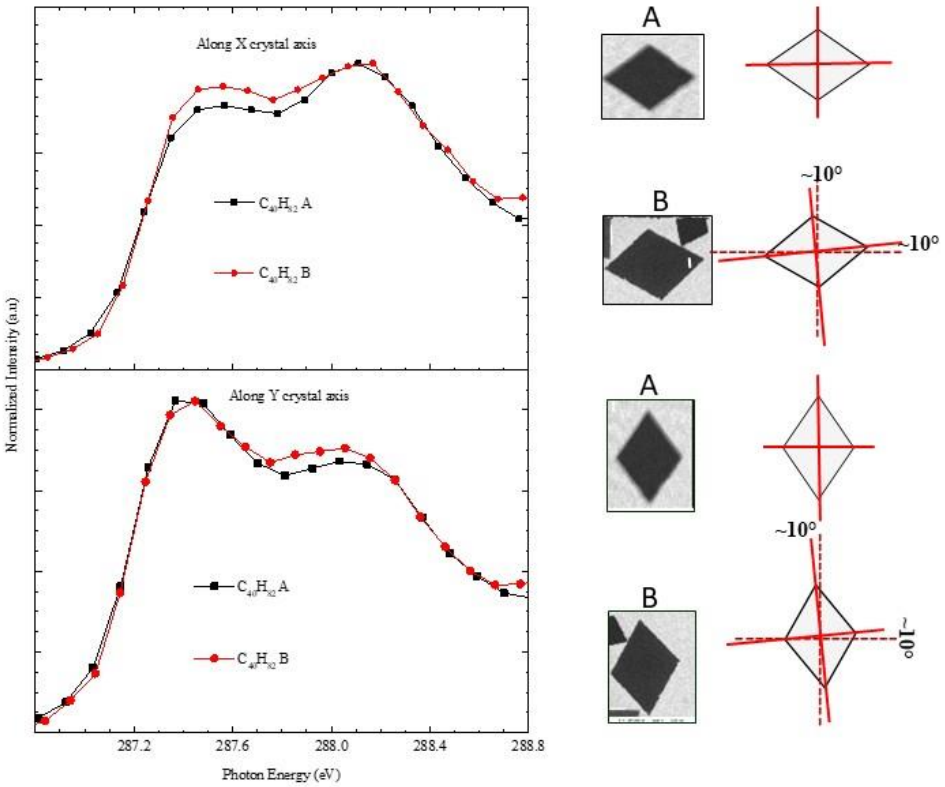

Figure B.6: Effect of misalignment of the *n*-alkane (*n*-$C_{40}H_{82}$) crystal to the carbon 1s NEXAFS spectra (a) along (X) crystal axis and (b) along the short (Y) crystal axis under linear horizontal polarization.

In **Chapters 5** and **7**, extra care was taken in order to make sure that the crystals are aligned with their principal crystal axes (x,y) before taking the measurement.

Appendix C: Effects of Nuclear Motion Contributions and Molecular Disorder to the Carbon 1s NEXAFS Spectra of *n*-Alkanes

C.1 Experimental Challenges in Single Crystal *n*-Alkane Raman spectroscopy

This section shows the effect of substrate thickness, laser damage, and laser power to the Raman signal. It is important to understand the individual contributions of these factors in order to isolate the contribution of the alkane disorder to the Raman signal. In here, CH_3 rocking vibration band (890 cm^{-1}) used as a model peak to optimize the experimental conditions. The laser source used in this experiment was 785 nm.

C.1.1 Effect of Substrate Thickness (Gold Layer) to the Raman Signal of *n*-Alkane Crystal

In our Raman measurements, a silicon wafer is used as a substrate to deposit the orthorhombic *n*-alkane crystals. In this regard, some of the Raman signals from the silicon wafer interfere with the alkane signals and decrease the intensity of the alkane signals in the Raman spectra. Therefore, a thick layer of gold was deposited on top of the silicon wafer in order to avoid the laser to penetrate into the silicon layer.

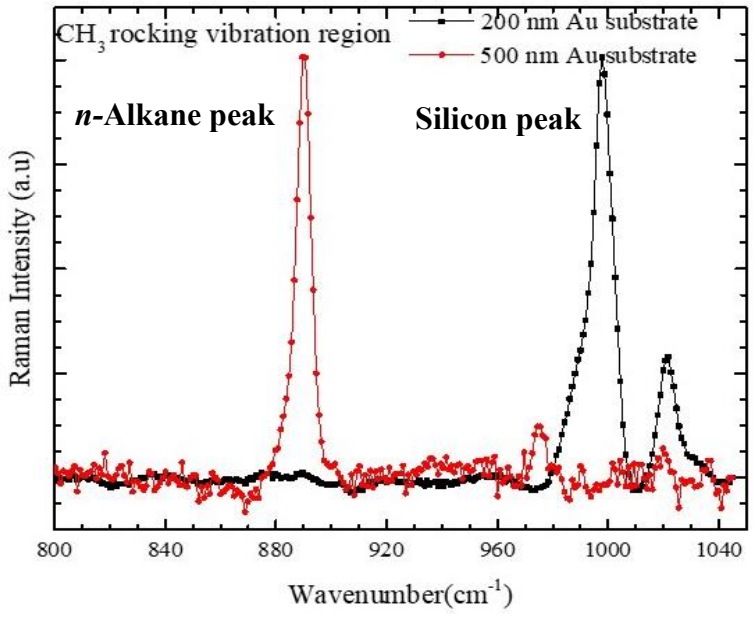

Figure C.1: Effect of gold substrate thickness on the *n*-alkane signal in the Raman spectra.

Gold is a good choice since gold signals are not observed within the alkane region (100 cm^{-1} – 3500 cm^{-1}), therefore, it does not interfere the alkane signals of the *n*-alkane samples. However, the thickness of the gold layer is important. Otherwise, the laser will penetrate into the

silicon substrate and give silicon signals instead of the alkane signals. **Figure C.1** showed the effect of gold layer thickness to the Raman signal of *n*-alkane crystal. According to the **Figure C.1**, a strong silicon peak was observed around 1000 cm^{-1} with the 200 nm gold layer. This means laser is penetrated into the silicon substrate and scanned silicon substrate instead of alkane crystals and that cause a weak signal for alkane (signal at 890 cm^{-1}). However, with the 500 nm gold layer, the CH_3 rocking vibration peak is resolved and strong peak observed at 890 cm^{-1}. In this case, the silicon peak is not strong as with the 200 nm gold layer. This suggests the laser is not penetrated into the silicon substrate with the 500 nm gold layer. Orthorhombic *n*-alkanes samples (crystals) were subsequently deposited on 500 nm gold coated silicon wafer for our Raman measurements.

C.1.2 Effect of Laser Heating to the Raman Signal of *n*-Alkane Crystal

To examine the effect of laser heating to the Raman signal, multiple Raman measurements were obtained at the same area of the *n*-alkane single crystal with 100% laser power and laser exposure time (dwell time) was set to 10 seconds. After each measurement, peak intensity and the crystal damage was examined by comparing the Raman spectrum and the Raman microscope image of *n*-alkane crystal (o-rh *n*-$C_{40}H_{82}$). This is shown in **Figure C.2**.

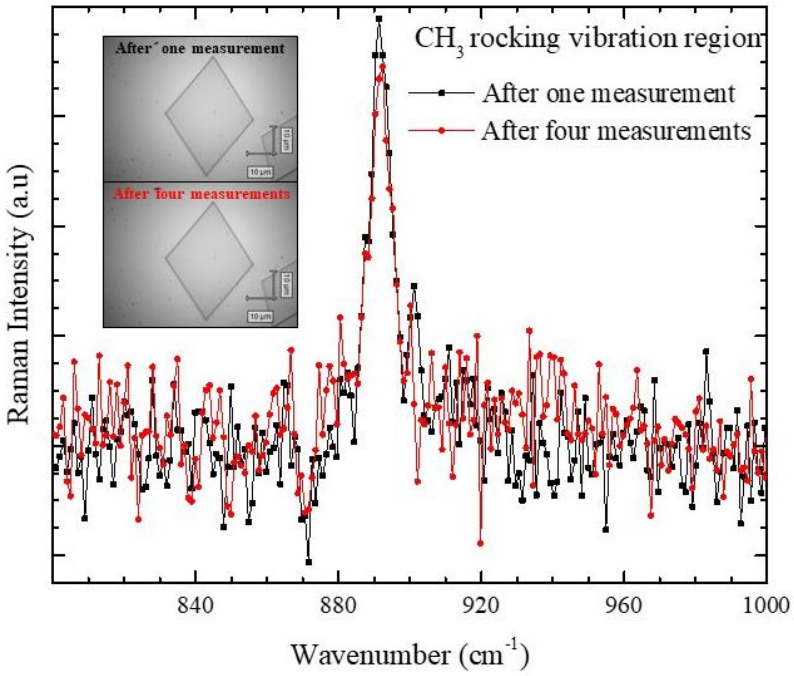

Figure C.2: Effect of laser heating on the *n*-alkane crystal and on the Raman signal.

According **Figure C.2**, intensity of the CH_3 rocking vibration peak is decreased with the number of Raman measurements, but it is not very significant. Moreover, Raman images of the *n*-alkane single crystal confirmed that multiple scans did not melt the *n*-alkane single crystal. Therefore, the shape of the *n*-alkane single crystals used in this experiment was survived with the 100% laser power.

C.1.3 The Effect of Focus Position of the Crystal to the Raman *n*-Alkane Signal

The variation in the Raman signal intensity across the crystal area is shown in **Figure C.3** According to the example shown in **Figure C.2**, the intensity of the CH_3 rocking vibration peak (890 cm^{-1}) is maximum when crystal scan is to the middle, and intensity drops at the crystal edges. All the Raman measurements were obtained by scanning the middle area of the crystal for maximum signal.

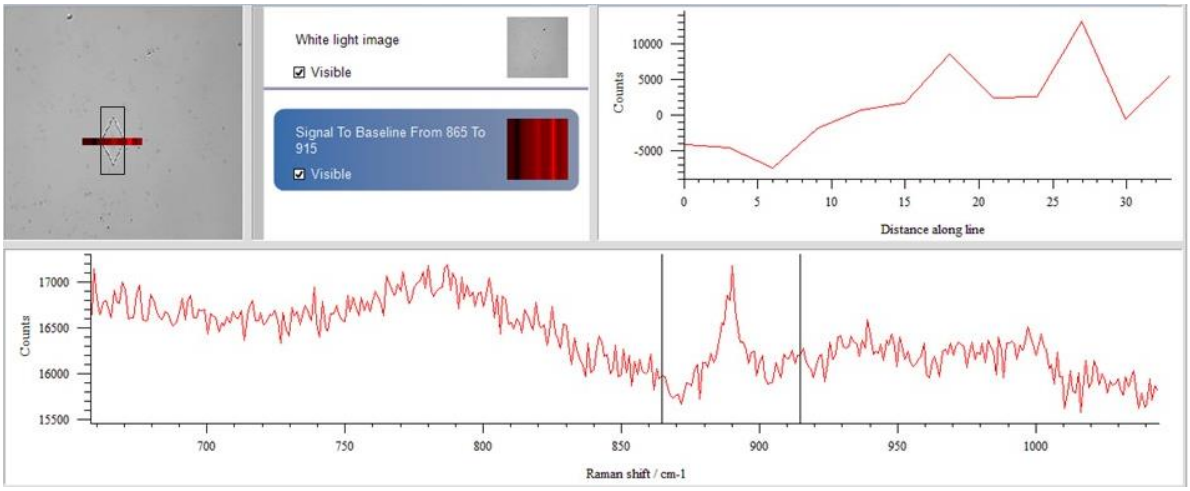

Figure C.3: Spectral variation across the crystal (line scan) across the CH_3 rocking vibrational mode.

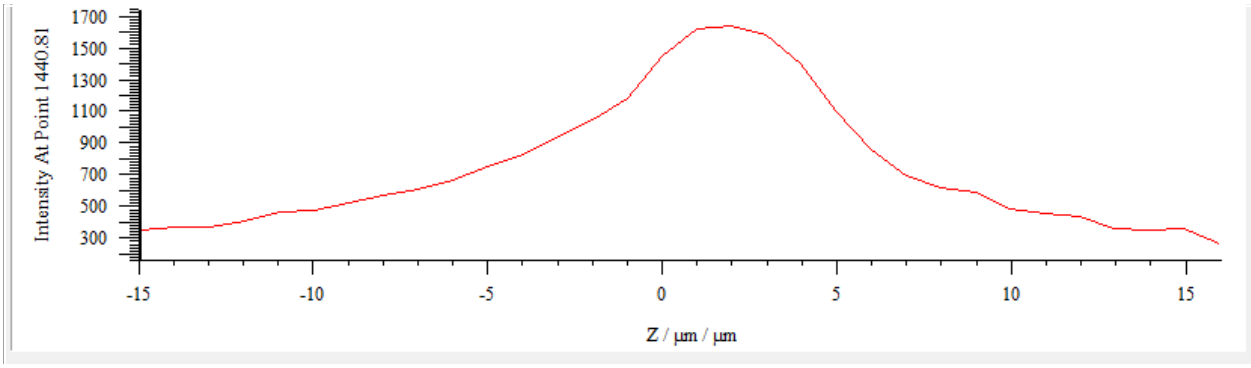

Figure C.4: Peak intensity vs sample depth plot for *n*-alkane crystal (*n*-$C_{40}H_{82}$)

The optimally positioned crystal can delivered the highest signal for a given Raman measurement. This optimum focus is varied from crystal to crystal, and can be identified by doing a depth scan to the given crystal. In **Figure C.4**, peak intensity is varied with the focus position of the alkane crystal, and two microns is the optimum focus for the crystal scanned in **Figure C.3**. Therefore, for each Raman measurement, Raman microscope focus was optimized to obtain the maximum intensity.

References

1. Dodziuk, H.; Szymański, S.; Jaźwiński, J.; Ostrowski, M.; Demissie, T. B.; Ruud, K.; Kuś, P.; Hopf, H.; Lin, S.T. Structure and NMR Spectra of Some [2,2] Paracyclophanes. The Dilemma of [2.2] Paracyclophane Symmetry. *The Journal of Physical Chemistry A* **2011,** *115* (38), 10638-10649.

2. Dodziuk, H.; Szymański, S.; Jaźwiński, J.; Marchwiany, M. E.; Hopf, H. Structure and Dynamics of [3,3] Paracyclophane As Studied by Nuclear Magnetic Resonance and Density Functional Theory Calculations. *The Journal of Physical Chemistry A* **2010,** *114* (38), 10467-10473.

3. Triguero, L.; Pettersson, L.; Ågren, H. Calculations of Near-Edge X-ray-Absorption Spectra of Gas-Phase and Condense- Phase Molecules by Means of Density-Functional and Transition-Potential Theory. *Physical Review B* **1998,** *58* (12), 8097-8110.

4. Craig, S. R.; Hastie, G. P.; Roberts, K. J.; Sherwood, J. N. Investigation into the Structures of Some Normal Alkanes Within the Homologous Series $C_{13}H_{28}$ to $C_{60}H_{122}$ Using High-Resolution Synchrotron X-ray Powder Diffraction. *Journal of Materials Chemistry* **1994,** *4* (6), 977-981.

5. Plomp, M.; Van Enckevort, W.; Van Hoof, P.; Van De Streek, C. Morphology of and Dislocation Movement in *n*-$C_{40}H_{82}$ Paraffin Crystals Grown From Solution. *Journal of Crystal Growth* **2003,** *249* (3), 600-613.

6. Kaznatcheev, K.; Karunakaran, C.; Lanke, U.; Urquhart, S.; Obst, M.; Hitchcock, A. Soft X-ray Spectromicroscopy Beamline at the CLS: Commissioning Results. *Nuclear Instruments and Methods in Physics Research Section A: Accelerators, Spectrometers, Detectors and Associated Equipment* **2007,** *582* (1), 96-99.

7. Peltier device (1MD06-032-05111). http://www.tec-microsystems.com/ (accessed 03rd March **2018**).

8. Fluke 52-2 Dual Input Thermometer. http://en-us.fluke.com/products/thermometers/fluke-52-ii-thermometer.html (accessed 03rd March **2018**).

9. Instek GPS-1850D Digital Power Supply, 0-18V, 0-5A. https://www.itm.com/ (accessed 04th March **2018**).